Multiscale modeling of lithium transport in solid and hybrid Li-ion electrolytes and their interfaces

Joël Martín Dalmas

To cite this version:

Joël Martín Dalmas. Multiscale modeling of lithium transport in solid and hybrid Li-ion electrolytes and their interfaces. Physics [physics]. Université Grenoble Alpes [2020-..], 2023. English. NNT : 2023GRALY098 . tel-04594398

HAL Id: tel-04594398
https://theses.hal.science/tel-04594398

Submitted on 30 May 2024

THÈSE

Pour obtenir le grade de

DOCTEUR DE L'UNIVERSITÉ GRENOBLE ALPES

École doctorale : PHYS - Physique
Spécialité : Physique des matériaux
Unité de recherche : Laboratoire d'Innovation pour les Technologies des Energies Nouvelles (LITEN - CEA)

Modélisation multi-échelle du transport du lithium dans des électrolytes Li-ion solides et hybrides et leurs interfaces

Multiscale modeling of lithium transport in solid and hybrid Li-ion electrolytes and their interfaces

Présentée par :

Joël MARTIN DALMAS

Direction de thèse :

Natalio MINGO DIRECTEUR DE RECHERCHE, CEA CENTRE DE GRENOBLE	Directeur de thèse
Stefano MOSSA DIRECTEUR DE RECHERCHE, CEA CENTRE DE GRENOBLE	Co-directeur de thèse
Ambroise VAN ROEKEGHEM CEA	Co-encadrant de thèse

Rapporteurs :

JESUS CARRETE MONTANA
SENIOR SCIENTIST, CSIC
MATHIEU SALANNE
PROFESSEUR DES UNIVERSITES, SORBONNE UNIVERSITE

Thèse soutenue publiquement le **18 décembre 2023**, devant le jury composé de :

BENOÎT COASNE, DIRECTEUR DE RECHERCHE, CNRS DELEGATION ALPES	Président
JESUS CARRETE MONTANA, SENIOR SCIENTIST, CSIC	Rapporteur
MATHIEU SALANNE, PROFESSEUR DES UNIVERSITES, SORBONNE UNIVERSITE	Rapporteur
MAYLISE NASTAR, DIRECTRICE DE RECHERCHE, CEA CENTRE DE PARIS-SACLAY	Examinatrice
NOEL JAKSE, PROFESSEUR DES UNIVERSITES, GRENOBLE INP	Examinateur

Abstract for the General Public

Hybrid Solid Electrolytes (HSEs) have emerged as a promising alternative for Li-ion batteries, offering advantages over traditional liquid electrolytes. While Solid Polymer Electrolytes (SPEs) are generally known for their lower ionic conductivity compared to liquid or ceramic electrolytes, there has been a long-standing debate in the scientific community about whether the incorporation of passive ceramic fillers, such as silica or alumina nanoparticles, can enhance the conductivity of SPEs. This debate is essential for optimizing battery performance.

To address this question, our research employs molecular dynamics simulations to investigate two hybrid systems: Polyethylene Oxide (PEO) as the polymer and LiTFSI as the salt, combined with either silica or alumina as ceramic components. We use the OPLS-AA force field to analyze the dynamics and interactions in these Hybrid Solid Electrolytes (HSEs over extended time scales. Our results provide valuable insights into how these ceramic nanoparticles affect ion mobility in solid polymeric electrolytes, helping to unravel this long-standing scientific enigma.

Résumé grand public

Les électrolytes solides hybrides (ESH) se présentent comme une alternative prometteuse aux batteries Li-ion, offrant des avantages par rapport aux électrolytes liquides traditionnels. Bien que les électrolytes polymères solides (EPS) soient généralement connus pour leur moindre conductivité ionique par rapport aux électrolytes liquides ou céramiques, un débat de longue date persiste au sein de la communauté scientifique quant à savoir si l'incorporation de charges céramiques passives, telles que des nanoparticules de silice ou d'alumine, peut améliorer la conductivité des EPS. Ce débat revêt une importance cruciale pour l'optimisation des performances des batteries.

Pour répondre à cette question, notre recherche utilise des simulations de dynamique moléculaire pour étudier deux systèmes hybrides : le polyéthylène oxyde (PEO) en tant que polymère et LiTFSI en tant que sel, associés à de la silice ou de l'alumine en tant que composants céramiques. Nous utilisons le champ de force OPLS-AA pour analyser la dynamique et les interactions au sein de ces électrolytes solides hybrides (ESH) sur des échelles de temps prolongées. Nos résultats fournissent des informations précieuses sur la manière dont ces nanoparticules céramiques affectent la mobilité des ions dans les électrolytes polymères solides, contribuant ainsi à résoudre cette énigme scientifique de longue date.

Abstract

Hybrid Solid Electrolytes (HSEs) offer a promising alternative to conventional liquid electrolytes in the field of Li-ion batteries. Whereas solid polymer electrolytes (SPEs) are poorer ionic conductors than liquid or ceramic electrolytes, early research from two decades ago suggested that incorporating passive ceramic fillers like silica or alumina nanoparticles enhances SPE conductivity. However, more recent literature demonstrates an adverse effect of ceramics on ionic mobility in SPEs, especially in the amorphous polymer phase

To clarify this debate, our thesis addresses the question: Does the inclusion of ceramic nanoparticles enhance or impede ion mobility in Solid Polymeric Electrolytes? To tackle this, we use molecular dynamics simulations to study two hybrid systems: Polyethylene Oxide (PEO) as polymer with LiTFSI as the salt, combined with either silica or alumina as ceramic components. Our simulations employ the OPLS-AA force field to analyze the dynamics and interactions of these Hybrid Solid Electrolytes (HSEs) over extended time scales, typically spanning tenths of nanoseconds. We carefully select force field parameters from validated literature sources.

This thesis analyzes the structural and dynamical properties of these materials while establishing correlations between dynamic changes and their structural characteristics. The results precisely replicate the temperature-dependent conductivity observed in experimental studies of pure SPEs and reproduce the salt solvation mechanisms on PEO. This serves as robust validation for our findings.

The results with silica nanoparticles show a significant conductivity decrease, independent of ionic concentration. This reduction is mainly due to the nanoparticle's occupation of space, interrupting ionic diffusion. We observe two concentration regimes: one above and one below a 2 mol/L threshold, coinciding with the maximum conductivity. These regimes display differing ionic distributions and coordination properties. In the low-concentration regime, lithium ions primarily bind to PEO oxygen atoms, saturating the polymer at 2 mol/L. In the second regime, excess lithium ions interact with TFSI, affecting the interactions among other types of atoms. The absence of conductivity enhancement aligns with recent experimental measurements, contradicting earlier reports on hybrid ceramic/polyethylene-oxide electrolytes. Similar outcomes are evident for alumina nanoparticles. In this case, we employed a new set of force field parameters, leading to significant changes in the internal organization of the electrolyte. Despite these variations, the simulations consistently indicate reduced conductivity with the addition of alumina nanoparticles.

Résumé

Les électrolytes solides hybrides (HSE) offrent une alternative prometteuse aux électrolytes liquides classiques dans le domaine des batteries Li-ion. Alors que les électrolytes polymères solides (SPE) sont de moins bons conducteurs ioniques que les électrolytes liquides ou céramiques, des recherches antérieures menées il y a deux décennies ont suggéré que l'incorporation de charges céramiques passives telles que des nanoparticules de silice ou d'alumine améliore la conductivité des SPE. Cependant, des publications plus récentes démontrent un effet négatif des céramiques sur la mobilité ionique dans les SPE, en particulier dans la phase polymère amorphe.

Pour clarifier ce débat, notre thèse aborde la question suivante : l'inclusion de nanoparticules céramiques améliore-t-elle ou entrave-t-elle la mobilité ionique dans les électrolytes polymères solides ? Pour aborder cette question, nous utilisons des simulations de dynamique moléculaire pour étudier deux systèmes hybrides : le polyéthylène oxyde (PEO) en tant que polymère avec LiTFSI comme sel, combiné à de la silice ou de l'alumine en tant que composants céramiques. Nos simulations utilisent le champ de force OPLS-AA pour analyser la dynamique et les interactions de ces électrolytes polymères solides hybrides (HSE) sur des échelles de temps prolongées, généralement de l'ordre de la dizaine de nanosecondes. Nous sélectionnons soigneusement les paramètres du champ de force à partir de sources de littérature validées.

Cette thèse analyse les propriétés structurales et dynamiques de ces matériaux tout en établissant des corrélations entre les changements dynamiques et leurs caractéristiques structurales. Les résultats reproduisent précisément la conductivité dépendant de la température observée dans les études expérimentales des SPE purs et reproduisent les mécanismes de solvatation du sel sur le PEO. Ceci sert de validation solide à nos résultats.

Les résultats avec les nanoparticules de silice montrent une diminution significative de la conductivité, indépendamment de la concentration ionique. Cette réduction est principalement due à l'occupation de l'espace par les nanoparticules, interrompant la diffusion ionique. Nous observons deux régimes de concentration : l'un au-dessus et

l'autre en dessous d'un seuil de 2 mol/L, coïncidant avec la conductivité maximale. Ces régimes présentent des distributions ioniques et des propriétés de coordination différentes. Dans le régime de faible concentration, les ions lithium se lient principalement aux atomes d'oxygène du PEO, saturant le polymère à 2 mol/L. Dans le second régime, les ions lithium en excès interagissent avec le TFSI, affectant les interactions entre d'autres types d'atomes. L'absence d'amélioration de la conductivité concorde avec les mesures expérimentales récentes, contredisant les rapports antérieurs sur les électrolytes hybrides céramique/polyéthylène-oxyde. Des résultats similaires sont évidents pour les nanoparticules d'alumine. Dans ce cas, nous avons utilisé un nouvel ensemble de paramètres de champ de force, ce qui a entraîné des changements significatifs dans l'organisation interne de l'électrolyte. Malgré ces variations, les simulations indiquent de manière constante une réduction de la conductivité avec l'ajout de nanoparticules d'alumine.

Contents

List of Tables

List of Figures

-

Chapter 1

Introduction

1.1 Motivation and purpose

In recent years, the imperative for sustainable energy solutions has intensified due to the escalating impacts of climate change and the alarming rise in carbon dioxide emissions [1]. Climate change is already manifesting through rising temperatures [2], increased flooding incidents [3], prolonged drought periods [4], and an alarming surge in forest fires [5], among other consequences. Furthermore, climate change poses additional threats, such as the reduction of ice surfaces in the Arctic pole [6] and the subsequent repercussions [7].

A significant contributor to climate change is the high CO_2 emissions, with the transportation sector responsible for approximately 30% of global emissions [8, 9]. To address this challenge, a shift towards more sustainable transportation options, particularly electric vehicles (EVs), has gained prominence [10]. Beyond reducing pollution, EVs offer advantages in energy efficiency and reduced dependence on fossil fuels [11].

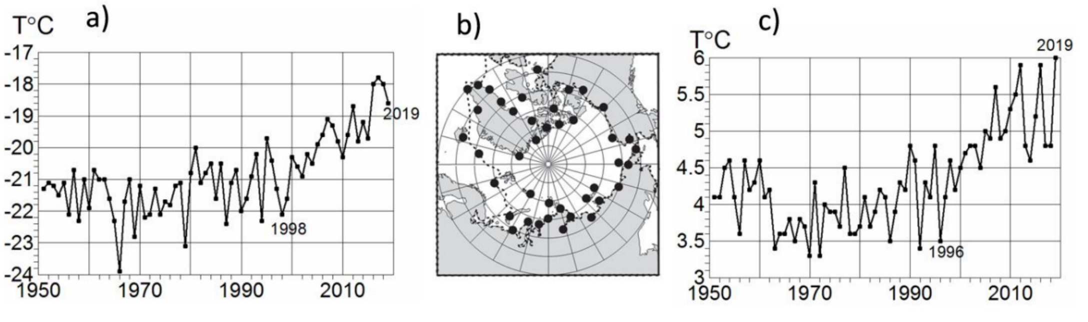

Figure 1.1: (a) Average surface air temperature in winter and (c) in summer at (b) meteorological stations in the marine Arctic for 1951–2019. From ref.[6].

The transportation sector plays a pivotal role in this climate change equation, contributing significantly to CO_2 emissions, accounting for approximately 30% of the world's total emissions [8, 9]. Recognizing the need for a more sustainable alternative, the industry has witnessed a notable shift towards electric vehicles (EVs) [10]. This shift is part of a broader strategy to mitigate emissions and address environmental challenges directly. EVs, powered by batteries, offer the potential to significantly reduce pollution and diminish our reliance on traditional fossil fuels [11].

Batteries serve as the linchpin in the transition to greener energy solutions. They are pivotal in storing and delivering electrical energy [12] and play a transformative role in various industries [13] towards a cleaner and more sustainable energy landscape. A battery functions as an electrochemical energy storage device, harnessing redox reactions to generate an electric current by facilitating the flow of electrons [12]. A battery consists of two electrodes (cathode and anode) immersed in an electrolyte solution. During discharge, the anode releases electrons, which flow through an external circuit to the cathode, where reduction reactions occur [14]. The electrolyte, often a liquid or solid medium, facilitates ion movement between the electrodes, enabling charge balance and sustaining the redox processes.

Developing safer and more efficient batteries has become a prominent research objective in the quest to reduce reliance on fossil fuels [17, 18, 19]. The efficiency of batteries relies on the conductivity of the electrolyte [20]. Ionic conductivity is a critical parameter, it measures the ease with which ions move through the electrolyte. It influences charge and discharge rates, power output, internal resistance and overall efficiency [21].

Among battery types, lithium-ion batteries stand out due to their high energy density, extended cycle life, and minimal self-discharge rates. Graphite anodes have been the standard choice for lithium-ion batteries, offering stability and reversible lithium intercalation. However, the pursuit of higher energy densities has led to interest in transitioning from graphite to lithium metal anodes , as the theoretical capacity of lithium metal surpasses that of graphite, promising greater energy storage capabilities [22].

The adoption of lithium metal anodes represents a promising avenue for enhancing the energy density and performance of batteries [23, 24]. However, integrating lithium-metal anodes with conventional liquid electrolytes (LE) poses significant challenges [23]. LEs struggle to prevent issues like Li plating and dendrite formation, which are intricate, finger-like crystalline structures. These dendrites have the potential to penetrate the separator within the battery, creating pathways for unintended electrical connections and leading to short circuits [25, 26, 27, 28, 29]. Furthermore, dendrites can compromise the safety of battery systems. As they grow, they can breach the separator, increasing the risk of internal short circuits, capacity loss, and, in extreme

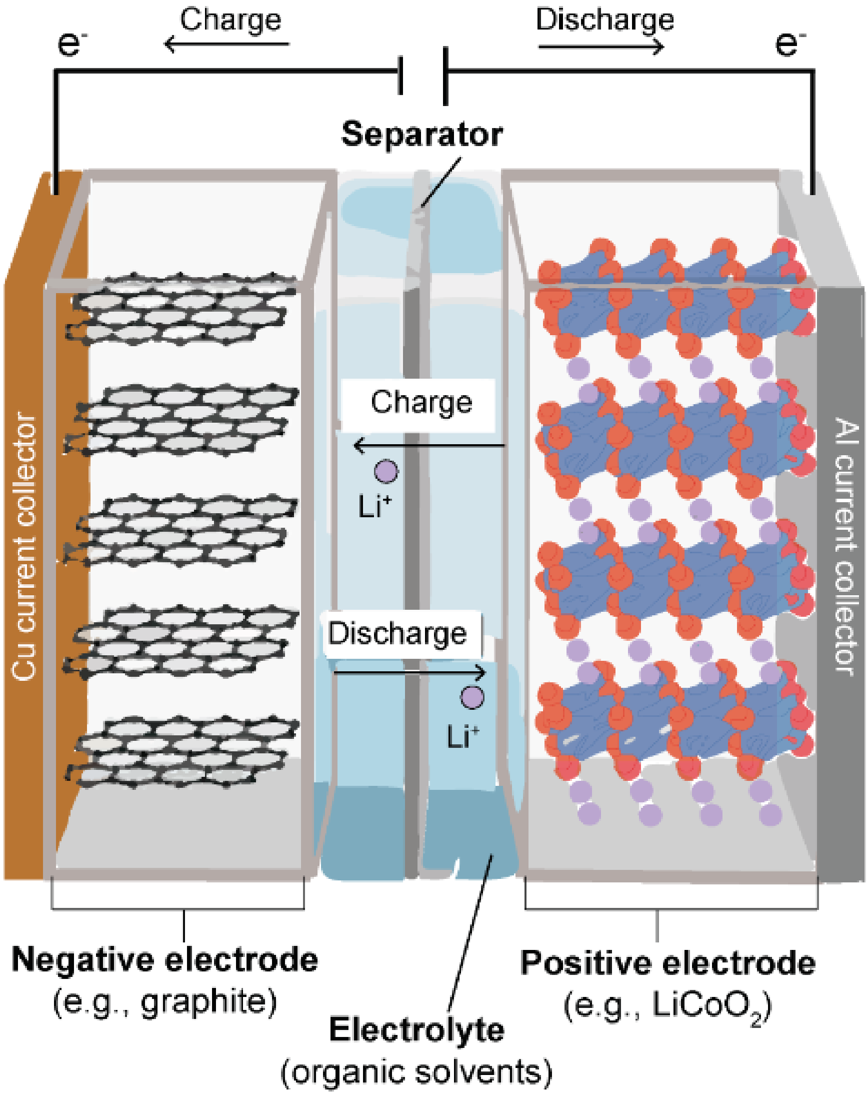

Figure 1.2: A lithium-ion battery's operation is shown schematically [15]. The negative electrode is composed of a low-potential material, such as graphite, whereas the positive electrode is composed of a transition metal that can release and receive lithium ions in its lattice. The electrolyte can be a liquid with a high ionic conductivity and a wide potential window that is created by dissolving a lithium salt in an organic solvent. From ref.[16].

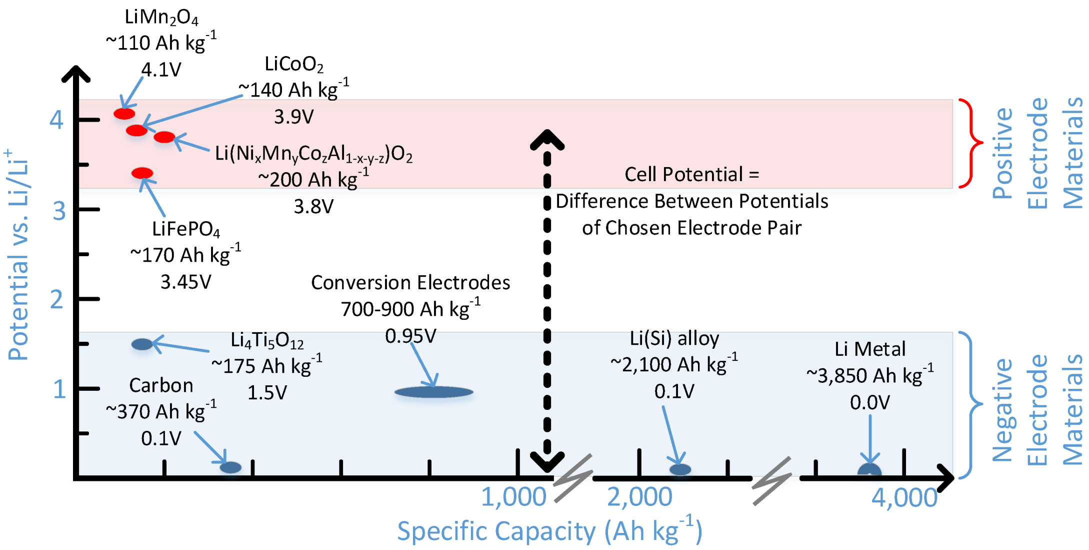

Figure 1.3: A summary of some present and future electrode chemistry options for Li-ion batteries. The proposed capacity of the Li(Si) is 50% of the theoretical capacity of the material, similar to the case found for some of the positive electrode materials [34].

cases, triggering catastrophic thermal runaway events within the battery [30, 31, 32, 33].

Solid-state electrolytes (SSEs) offer a compelling solution, circumventing the limitations associated with liquid electrolytes (LEs) in battery technology [32, 35]. SSEs encompass two primary categories: solid polymer electrolytes (SPEs) and ceramic electrolytes (CEs). CEs address safety concerns associated with LEs, exhibit high ionic conductivity at ambient temperature, and include materials such as oxides and sulfides. However, their inherent brittleness poses challenges in processing and raises susceptibility to electrode contact issues [36]. In contrast, SPEs offer an appealing alternative, known for their flexibility, cost-effectiveness, and improved electrode contact [37, 38]. Nonetheless, SPEs contend with reduced ionic conductivity compared to alternatives such as CEs and traditional LEs. This intriguing interplay between the attributes of CEs and SPEs propels exploration into a novel realm of solid-state electrolytes known as hybrid solid electrolytes (HSEs) [39].

HSEs combine the attributes of CEs and SPEs, offering benefits such as easier manufacturing, heightened safety measures, optimized electrode interfaces, and good ionic conductivity. Importantly, they address dendrite formation, enhancing battery integrity [40]. HSEs mark a significant shift in the landscape of energy storage systems, providing a foundation for a sustainable energy future [39, 41].

In the upcoming sections of this thesis, we will conduct a comprehensive exploration

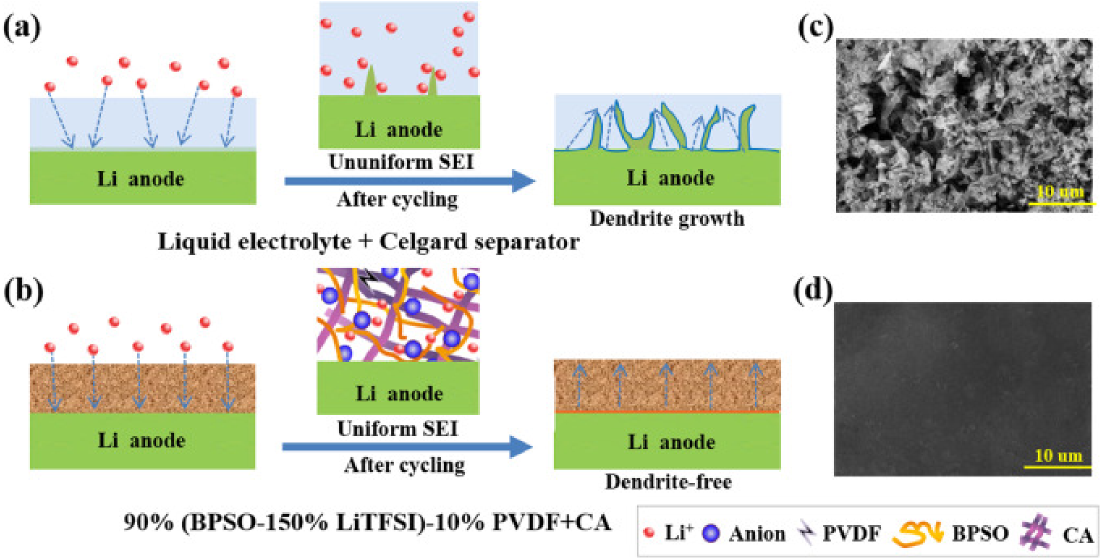

Figure 1.4: Schematic illustrations of Li dendrites formation in lithium symmetrical cells using (a) liquid electrolyte + Celgard separator and (b) 90% (BPSO-150% LiTFSI)-10% PVDF+CA, the 150% representing the mass ratio between BPSO and LiTFSI. SEM images of the Li surfaces obtained from lithium symmetrical cells assembled with (c) liquid electrolyte + Celgard separator and (d) 90% (BPSO-150% LiTFSI)-10% PVDF+CA after 300h cycling at 0.5mAcm-2 and 25°C, respectively [42].

of hybrid electrolytes tailored for batteries. Employing advanced molecular dynamics (MD) simulations, our primary aim is to unravel the complex behaviors and interactions within these hybrid solid electrolytes. Through meticulous computational analysis, we seek to enhance our understanding and contribute to the development of a more robust and sustainable energy future.

1.2 Solid Electrolytes

Solid electrolytes are emerging as promising candidates to fulfill the crucial role of electrolytes in advanced battery technology. One of their primary advantages lies in enhanced safety compared to traditional liquid electrolytes (LEs). Most solid-state electrolytes (SSEs) are non-flammable and eliminate leakage concerns often associated with LEs [43, 44].

While safety is an essential selling point, it's important to note that safety alone wouldn't drive significant investments in SSEs unless they also offered improvements in battery performance. The remarkable appeal of solid electrolytes largely stems from their remarkable ability to suppress dendrite formation [39, 30]. Dendrites significantly impact various battery properties and can render the use of lithium metal electrodes infeasible when liquid electrolytes (LEs) are employed [25, 42]. Lithium-metal anodes offer unmatched energy density and battery performance, making them a compelling choice in energy storage technology.

Another noteworthy advantage of SSEs is their suitability over an extended temperature range [45]. SSEs often demonstrate superior stability and performance across a broader temperature spectrum compared to LEs, making them suitable for demanding applications in extreme environments. Additionally, SSEs can contribute to prolonged cycle life by mitigating detrimental side reactions and preventing electrode degradation, resulting in overall improved battery longevity.

In this thesis, our primary research focus will be on solid polymer electrolytes (SPEs) as the starting point of our investigation, followed by an exploration of hybrid electrolytes. It's essential to acknowledge that SPEs, while promising, do exhibit a drawback in terms of ionic conductivity at room temperature compared to alternative electrolyte options. As an example, PEO based SPEs have a conductivity of about 10^{-7}-10^{-5} S/m at room temperature [46, 47], while the most commonly used CEs such as NASICON-type LATP ($Li_{1+x}Al_xTi_{2-x}(PO_4)_3$, and LAGP ($Li_{1+x}Al_xGe_{2-x}(PO_4)_3$ [48, 49], garnet-type CEs like LLZO ($Li_7La_3Zr_2O_{12}$) [50], and perovskite-type CEs as LLTO ($Li_{3x}La_{(2/3)-x}TiO_3$) [51], have an ionic conductivity of about 10^{-5}-10^{-3} S/m. Although these conductivity values remain below the ionic conductivity levels attained by liquid electrolytes (LEs), which can reach up to 1 S/m [52], they are considered acceptable for many practical applications. However, CEs encounter notable processing challenges, largely stemming from their mechanical properties, and often struggle to establish effective interfacial compatibility with electrodes.

Hybrid solid electrolytes (HSE) offer a solution to the limitations of both solid polymer electrolytes (SPEs) and ceramic electrolytes (CEs). By combining both materials, HSEs can potentially provide the advantages of each while overcoming their individual drawbacks [46, 41, 53, 54]. HSEs show great potential as electrolyte candidates due to their ability to combine the mechanical properties and processability of polymers with the enhanced ionic conductivity provided by ceramic fillers. Although research on these hybrid materials began two decades ago [53], it remains a subject of debate today due to the inconsistent and contradictory results found in the literature.

There are two main types of hybrid electrolytes: 'ceramic in polymer' and 'polymer in ceramic' [46]. The former combines a polymer framework with embedded ceramic material, offering strong mechanical properties and effective dendrite prevention. Additionally, it shows potential for improved ionic conductivity compared to the 'polymer in ceramic' approach. In contrast, 'ceramic in polymer' HSEs not only prevent dendrite formation but also exhibit robust mechanical properties, all without encountering the limitations of 'polymer in ceramic,' such as brittleness and challenges in achieving optimal contact with electrodes [55]. Our research primarily focuses on 'ceramic in polymer' HSEs, especially those featuring non-conductive ceramics.

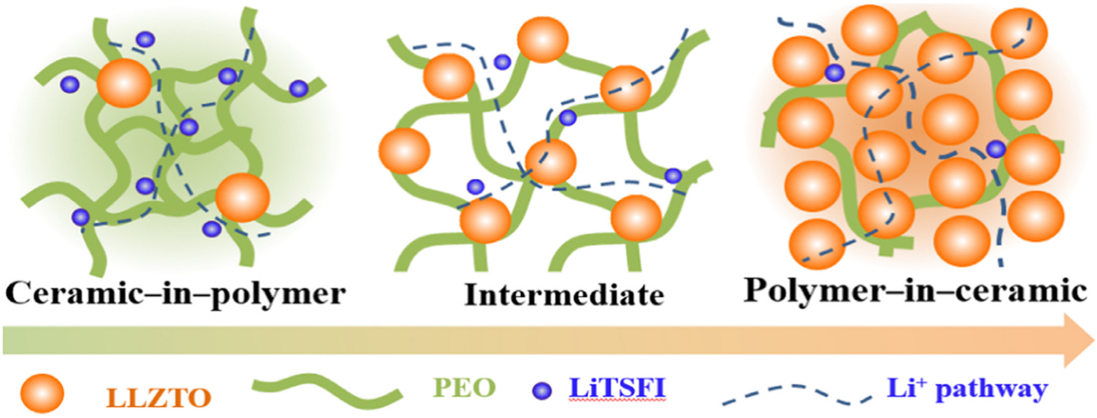

Figure 1.5: Schematic illustration for PEO-LLZTO CSE: (a) “ceramic-in-polymer”; (b) “intermediate”; (c) ”polymer in ceramic”. From ref.[55].

By studying structural changes at the nanoparticle-electrolyte interface, we aim to understand conductivity enhancements observed in some HSE systems. This research provides insights into the interplay between ion transport phenomena and the interface, shedding light on mechanisms that can improve electrolyte performance.

- *Active fillers* are components that directly participate in the ion conduction process within the hybrid electrolyte. These fillers are typically ion-conductive materials, such as ceramic oxides or sulfides, which can contribute to enhancing the overall ionic conductivity of the electrolyte matrix [56]. By introducing active fillers, researchers aim to create pathways for efficient ion movement, that can overcome the transport limitations of pure SPEs and ultimately boosting charge/discharge rates enhancing the overall performance of batteries [57].

- *Passive fillers* are ceramics that, while not inherently ion-conductive, produce a profound influence on the transport properties of the hybrid electrolyte [58]. Despite their inherent lack of conductivity, these fillers significantly impact the structural configuration of the electrolyte matrix. In theory, passive ceramics reduce the crystallinity of semi-crystalline polymers and inhibit ion clustering. They are believed to induce structural modifications in their vicinity that promote enhanced ionic conductivity [53] This structural adaptation enhances the overall performance of the electrolyte. The integration of passive fillers presents an intriguing pathway for optimizing ion mobility, shedding light on the intricate interplay between ion transport phenomena and the interface between the bulk polymer and the ceramic surface [57].

Our research will primarily focus on passive fillers due to their extensive use and simpler structural characteristics compared to most active fillers. This simplicity facilitates the modeling of these ceramics. In this thesis, our primary objective is to study structural

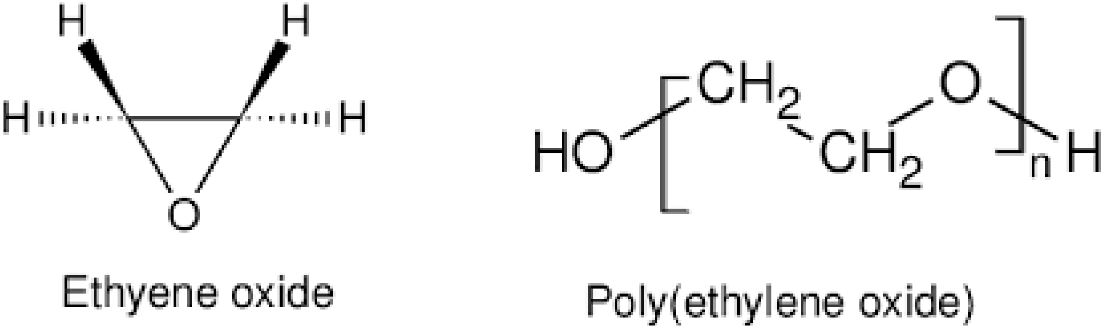
Ethyene oxide

Poly(ethylene oxide)

Figure 1.6: Chemical structure of ethylene oxide and poly(ethylene oxide). Poly(ethylene oxide) is synthesized by polymerizing ethylene oxide monomers, with the variable 'n' representing the number of repeating units, which can range from a few tenths to hundreds of thousands. From ref. [65].

modifications at the interface between nanoparticles and the electrolyte and assess their impact on ion mobility. As we will explore latter in Section 1.2.3, this hypothetical interfacial effect could potentially explain the observed conductivity enhancement in some references in the literature [53, 59, 54] within hybrid solid electrolyte (HSE) systems.

Active fillers conduct lithium within their structure, which could introduce additional factors that enhance conductivity. To isolate and thoroughly understand the pure effects of the interface, our focus on passive fillers is more suitable, ensuring that no other factors potentially boosting conductivity interfere with our investigation.

1.2.1 SPEs: The role of PEO

In the domain of polymers suitable for Solid Polymer Electrolytes (SPEs), some noteworthy candidates include polypropylene oxide (PPO) [60], polyvinylidene fluoride (PVDF) [61, 62], and poly(trimethylene carbonate) (PTMC) [63]. These polymers each offer distinct characteristics worth considering. However, it's clear that polyethylene oxide (PEO) [64] takes the lead as the most extensively researched polymer for fulfilling the role of an electrolyte. PEO stands out due to its inherent properties that collectively contribute to its prominence in the field of solid-state electrolytes.

Some of the properties that make PEO the most commonly used polymer in SPEs are:

- **Enhanced Ion Transport**: PEO exhibits exceptional ionic conductivity, a crucial feature for solid-state batteries. This conductivity arises from PEO's flexible polymer chain structure and its remarkable solvation properties with lithium salts containing large counterions. The flexibility of PEO's polymer chains and its ability to form complexes with lithium salts create favorable conditions for efficient lithium ion transport within the polymer matrix. This property ensures smooth energy storage and release in solid-state batteries [64, 66].

- **High Dielectric Constant**: PEO possesses a substantial dielectric constant due to its molecular structure, characterized by the periodic insertion of ethylene oxide units between every two carbon atoms along the polymer chain. This high dielectric constant plays a crucial role in effectively solvating lithium ions by separating them from their counterions within the salt, ultimately leading to improved ionic conductivity.
- **Low Crystallinity**: PEO offers advantages due to its relatively low crystallinity, which is achieved through specific synthesis methods. In materials that lack a highly ordered arrangement (amorphous) or contain regions of disordered arrangement (semi-amorphous), ions have more space to move freely, thus promoting higher conductivity [67]. In the case of partially crystalline materials like PEO, ion movement can be hindered within the crystalline regions, constraining their mobility and limiting the available pathways for ion flow. This lower degree of crystallinity in PEO can be advantageous for enhancing its ionic conductivity, a crucial factor in solid-state battery performance.
- **Ease of Processing and cost**: PEO's exceptional processability, which allows for diverse morphologies like thin films and membranes, is essential for solid-state battery construction. This feature simplifies interface formation and enhances battery performance. Additionally, PEO's widespread industrial use and simple synthesis methods make it cost-effective and appealing for various industries [22]. Its ease of production and broad industrial acceptance significantly contribute to its cost-effectiveness and widespread adoption.
- **Compatibility**: PEO is known to have good compatibility with other materials commonly used in battery systems, such as lithium metal anodes and cathode materials. This compatibility reduces the risk of unwanted side reactions and degradation [68]. It is also, as many polymers, a flexible material, which plays a significant role in facilitating the interfacial contact.
- **Well know material**: Extensive research on PEO-based solid electrolytes plays a crucial role in computational science and simulations [69]. These insights are particularly valuable when aligning computational projects with experimental data. Additionally, they prove advantageous in starting simulation research. In molecular dynamics simulations, using established bibliographic force field parameters significantly speeds up the initialization process, saving months of parameter optimization time. This wealth of knowledge simplifies PEO research and helps optimize its properties for solid electrolyte applications.

Polyethylene Oxide (PEO) serves as a prime candidate for our electrolyte due to its alignment with our research goals. PEO consistently plays a central role in our simulations.

Our investigation incorporates ceramic fillers into PEO to form a composite worthy of examination. We evaluate whether this hybrid electrolyte offers advantages compared to pristine PEO-based solid polymer electrolytes (SPEs). We also analyze PEO's interactions with neighboring atoms, including the ceramic surface and ions. This is pertinent because prior research suggests that hybrid solid electrolytes (HSEs) may enhance ionic conductivity through interfacial effects. Our structural analysis focuses on understanding interfacial dynamics at the nanoparticle surface.

While our primary focus revolves around hybrid electrolytes, we also conduct thorough investigations of pure SPEs. Rigorous comparison of our simulation results with experimental data validates our findings and ensures alignment between computational outcomes and real-world observations.

In summary, we choose PEO as our polymer due to its extensive research presence in PEO-based SPEs, owing to its low glass transition temperature (T_g), impressive solvation properties, and excellent compatibility with electrodes [70, 71, 72, 73, 74, 75].

1.2.2 Choosing the salt for Lithium-ion Batteries: LiTFSI and $LiClO_4$

Introduction

In Solid Polymer Electrolytes (SPEs), salt incorporation is crucial for enabling efficient charge transport. These ionic compounds dissociate upon dissolution, releasing ions with opposite charges, which, as previously discussed, are essential for conducting electric charges in batteries [76]. Similar to electrons that facilitate charge transfer through the circuit, ions serve a parallel role within the electrolyte.

Throughout a battery's charge and discharge cycles, ions migrate towards specific electrodes, as shown in Figure 1.2. This ion movement is a response to the potential difference between the positive and negative electrodes, ensuring effective charge transfer. This coordinated ion migration is essential for facilitating ionic transport and enhancing the battery's overall functionality [16].

Selecting an appropriate salt is a complex decision influenced by various factors. The multitude of options available for electrolyte components highlights the complexity of this decision-making process.

In our research, we focus on identifying suitable salt candidates for Lithium-ion batteries. Among the numerous possibilities, we specifically investigate one salt: LiTFSI

(Lithium bis(trifluoromethanesulfonyl)imide) [77, 68, 70, 78]. This choice is not arbitrary and we will explain it in the subsequent pages.

Li-Ion batteries

Lithium-ion (Li-ion) batteries are vital for contemporary energy storage due to their high energy density, low self-discharge rates, and long cycle life [79, 34]. They have revolutionized electronics, electric vehicles, and renewable energy systems, making them integral to various industries. Li-ion's superior energy density, especially compared to alternatives like sodium-ion technologies [80], makes it the preferred choice for high-energy applications [79]. Its enduring energy retention further cements its position in energy storage.

The selection of lithium as the preferred cation for electrolytes in lithium batteries is supported by its distinctive attributes that align with the core requisites of energy storage systems [22]. With its low atomic mass and efficient ion exchange capabilities, lithium promotes rapid charge transfer within battery cells, vital for achieving high energy density and swift energy conversion [34]. It possesses one of the highest electrochemical potentials among metals, approximately -3.04 volts concerning the standard hydrogen electrode (SHE), signifying its strong electron donation tendency and formation of positively charged ions (Li+).

This substantial electrochemical potential empowers lithium-ion batteries to deliver high voltage and energy density, making them efficient across diverse applications. Careful handling of lithium is essential due to its reactivity, especially when exposed to moisture or air.

While lithium exhibits a remarkable electrochemical potential, it's crucial to acknowledge that metals like sodium, potassium, and magnesium also possess relatively high potentials, which range from approximately -2.71 volts for sodium to -2.37 volts for magnesium. This warrants exploration for potential use in advanced batteries. The choice of metal for a specific battery system depends on factors like cost, availability, and specific application requirements.

Additionally, lithium's compact atomic size, with a radius of approximately 152 picometers, contributes to a stable solid-electrolyte interface, preventing dendritic growth during cycling and enhancing battery safety. Notably, lithium minimizes memory effect, where a battery's capacity diminishes upon repeated recharging without full discharge. These intrinsic traits establish lithium as a standout option for cation incorporation in lithium-ion batteries, facilitating the development of high-performance, efficient, durable, and lightweight energy storage systems for diverse applications.

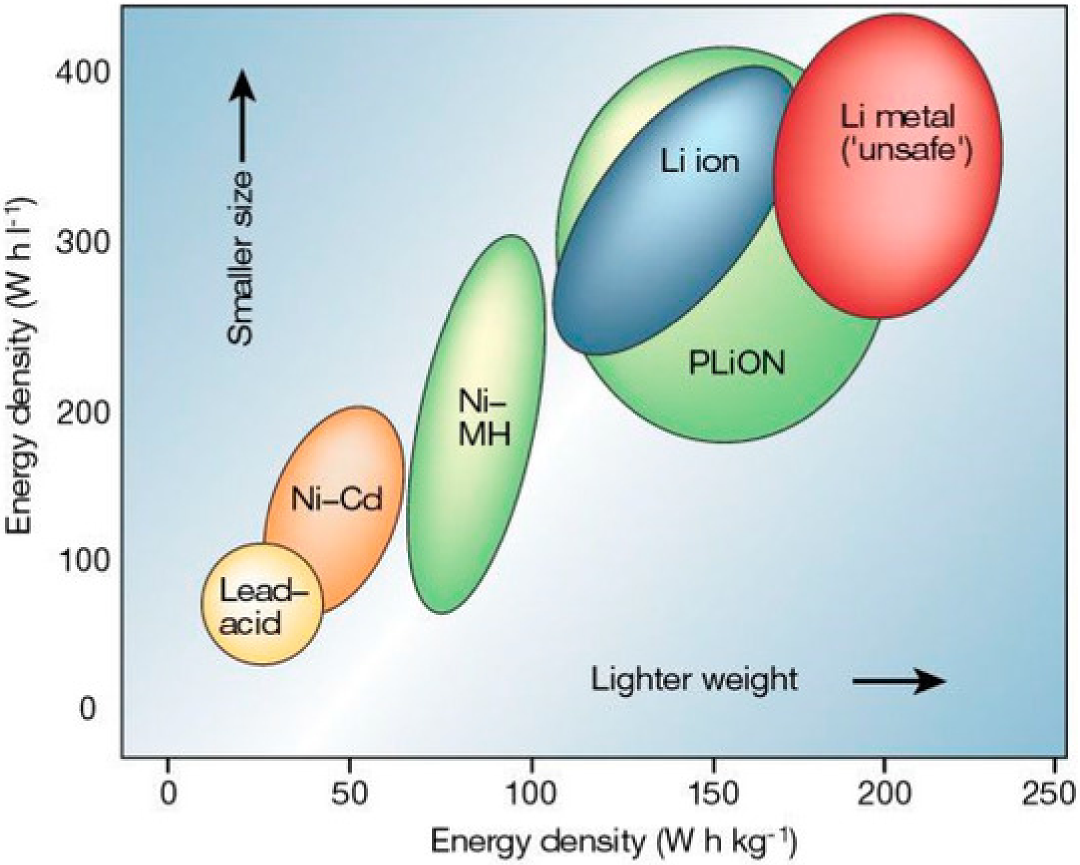

Figure 1.7: Comparison of the different battery technologies in terms of volumetric and gravimetric energy density. Li-ion technology and Li metal stand out as options that offer higher energy density [19].

Choosing the anion: TFSI

TFSI (bis(trifluoromethanesulfonyl)imide) stands out as a compelling counterion, known for its remarkable solvation properties, chemical stability, and low ionic coordination number, which have led to its widespread use alongside PEO in SPEs [66, 81, 82, 83, 84, 85]. When combined with PEO in solid polymer electrolytes (SPEs), TFSI forms strong Lewis acid-base interactions with oxygen atoms in PEO's chain, enhancing ion transport and improving ionic conductivity. Additionally, TFSI's reduced tendency for anion-cation association helps prevent ion clustering, reducing the accumulation of charges and boosting overall battery efficiency [77]. This behavior can be attributed to the large size of TFSI, which results in highly delocalized charge and makes it susceptible to breaking its association with the lithium counterion through electrostatic forces. The effective coupling of TFSI and PEO leads to a synergistic combination that enhances the electrolyte's performance and contributes to the advancement of solid-state battery technology.

While there are alternative candidates for lithium counterions in lithium-ion batteries, such as ClO_4^-, it's important to consider their specific properties. ClO_4^- has been explored for its good conductivity, but its use in batteries has been restricted due to safety concerns [86], as ClO_4^- can potentially lead to explosive reactions under certain conditions [87].

On the other hand, Lithium Hexafluoroarsenate ($LiAsF_6$) is another noteworthy option. $LiAsF_6$ exhibits a higher electrochemical stability window compared to some other lithium salts, making it suitable for high-voltage applications [88]. However, it may have limited stability under extreme conditions, so careful consideration is necessary.

While alternative lithium counterions like ClO_4^- and $LiAsF_6$ have been explored, TFSI remains the most promising and extensively studied counterion for lithium in our context. We focus on understanding the interaction between TFSI and PEO due to their well-documented compatibility and proven advantages [66, 81, 82, 83, 84, 85]. Our research aims to provide valuable insights that optimize solid polymer electrolytes and advance solid-state battery technologies, aligning with the central objective of our thesis.

1.2.3 Choosing a ceramic: SiO_2 and Al_2O_3

The final component essential for constructing a hybrid solid electrolyte is the ceramic material. In this thesis, our primary focus is on exploring passive fillers, which possess non-reactive and stabilizing characteristics, making them promising candidates for significantly improving the efficiency, durability, and overall performance of energy storage systems [89].

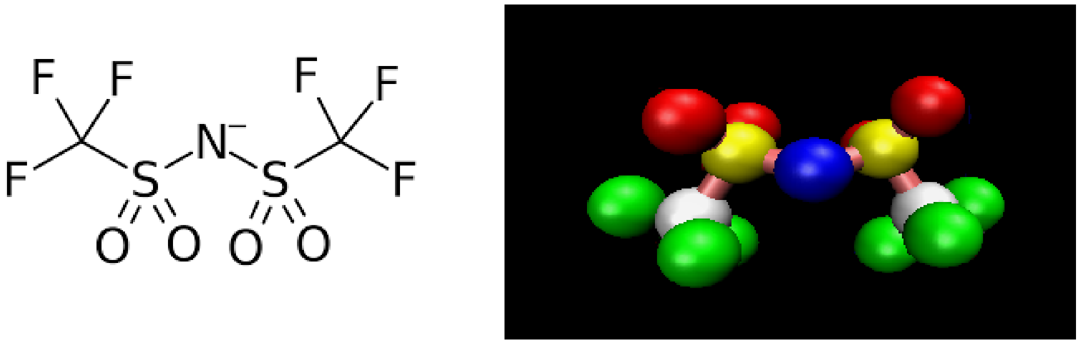

Figure 1.8: (left) Schematic representation of the TFSI molecule and (right) a snapshot of the simulated TFSI molecule displayed using the VMD visualization tool. In the visualization, atoms are color-coded as follows: nitrogen (blue), sulfur (yellow), oxygen (red), carbon (white), and fluorine (green).

While there exist varying viewpoints in the literature regarding the incorporation of ceramic fillers alongside polymers to enhance ionic conductivity, this section will outline some of the favorable studies that support their use in forming hybrid solid electrolytes. However, both positive and negative research findings will be thoroughly reviewed in the following section, labeled as Section 1.3.

Passive fillers, as demonstrated in experiments by Croce et al. [53] and Scrosati et al. [59], have a notable impact on ion conductivity and diffusivity in solid polymer electrolytes (SPEs). These studies employed similar methodologies, comparing the conductivity curves of various materials, including a pure SPE composed of PEO+$LiClO_4$ and different ceramic nanoparticles such as TiO_2 and Al_2O_3 in the case of Croce et al. [53], and SiO_2 in the study by Scrosati et al. [59]. In all instances, the addition of nanoparticles at a concentration of 10 wt% and an ion ratio of 8 PEO:Li resulted in a substantial increase in conductivity, ranging from one to two orders of magnitude.

This conductivity enhancement can be attributed to two main mechanisms. Firstly, the introduction of ceramic nanoparticles reduces the crystallinity of semicrystalline polymers like PEO, leading to a significant reduction in crystallinity [90, 91]. The interaction between ceramic particles and the polymer alters the polymer's structure, hindering crystallization in the vicinity. As a result, ion conductivity improves, resulting in reduced internal resistance and polarization effects during charge-discharge cycles.

However, this explanation alone cannot account for the increased conductivity observed above the melting point. To address this, an additional mechanism is proposed. The addition of ceramics modifies the electrolyte structure around the nanoparticles, facilitating ion movement through Lewis-acid interactions with the nanoparticle surfaces. The study suggests that nanoscale ceramic powders can function as solid plasticizers for PEO, kinetically inhibiting crystallization during annealing above 60ºC.

Several studies support the concept of enhanced conductivity attributed to both active and passive fillers [92, 93, 94]. More recent research builds upon the ideas presented in the earlier work [41] and provides a more detailed explanation for this conductivity enhancement.

For instance, the study by Zaman et al. [41] offers an extensive explanation of the previously mentioned hypothesis, expanding on the idea that nanoparticles modify the polymer's structure. This paper presents results that serve as a paradigm for hybrid solid electrolytes (HSEs). Zaman et al. investigated the use of Lithium lanthanum zirconium oxide ($Li_7.5La_3Zr_2Al_0.25O_{12}$), an active ceramic filler often referred to as Al-LLZO. They observed an enhancement in conductivity at low filler concentrations, reaching a maximum at 15% volume fraction. Beyond this point, conductivity gradually decreased.

The researchers explain this conductivity enhancement by proposing the formation of a space-charge region around the nanoparticles. Lewis-acid interactions between PEO and the counterion on the nanoparticle's surface reduce system crystallinity. However, this interaction also has other notable effects. It decreases the mobility of TFSI, but simultaneously exerts an attractive force on the PEO, diminishing their interaction with lithium. Consequently, lithium ions at the interface between bulk PEO and the ceramic present a faster ion movement. As more nanoparticles are added, ion percolation through the electrolyte becomes more efficient, reaching a maximum conductivity at 15%.

However, when exceeding this concentration, Zaman et al. employed Quantitative 3D morphological analysis using nanotomography techniques to demonstrate that particles tend to form large aggregates. This reduces the effective surface area of the nanoparticles, diminishing the effectiveness of the added material.

Experimental evidence shows that adding nanoparticles improves ionic mobility. This enhancement can boost energy conversion efficiency, allowing batteries to deliver more power with fewer losses. As a result, using passive fillers enhances both safety and overall battery performance [95].

Passive fillers significantly improve the mechanical properties of batteries. Some studies like ref. [94] demonstrate an ehancement of the mechanical properties. In their study they add SiO_2 to PEO ClO_4 and study the dependence of the tensile strength with the weigh fraction of ceramic content until 15% and it had a positive impact on the magnitude. Thus they concludeed that the addition of SiO_2 nanoparticles improves flexibility and mechanical stability of the elerctrolytes. The incorporation of these ceramic fillers can also help stabilize the electrode-electrolyte interface [94, 53, 59, 96], reducing undesired side reactions that can contribute to capacity fade over time [97].

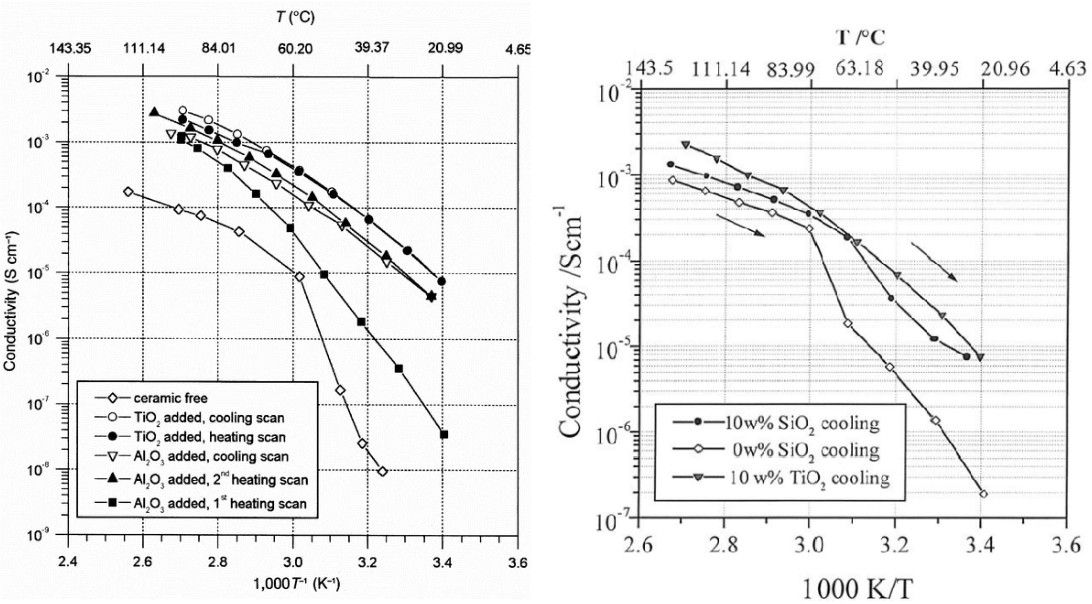

Figure 1.9: Arrhenius plots of the conductivity of ceramic-free PEO–LiClO$_4$ and of nanocomposite PEO–LiClO$_4$ 10%wt TiO2 [53] and PEO–LiClO$_4$ 10%wt Al$_2$O$_3$ polymer electrolytes [59] (PEO:LiClO$_4$ = 8:1 in all cases).

Furthermore, the introduction of passive fillers can also improve the thermal stability of the electrolyte [98, 99], showing results where the HSE is thermally stable until values of 220ºC. Also, in reference [99] they study the interfacial stability and the stability they show results for a 15% nanoparticle weigh in the system made of Li/PUA-SiO$_2$ and the results show a constant overvoltage for the samples containing more than 15 wt % SiO$_2$ additive polymer electrolyte even after 1500 cycles, indicative of high stability with metallic lithium. A stable interfacial layer in an electrolyte prevents unwanted chemical reactions, enhances battery durability, reduces internal resistance, and improves safety, ensuring efficient and long-lasting battery performance.

Among all the possible oxide materials suitable for electrolytes [100, 101, 95], SiO$_2$ (silicon dioxide) [59, 54, 102], TiO$_2$ (titanium dioxide) [103, 104, 105], and Al$_2$O$_3$ (aluminum oxide) stand out as the three most common options [53, 106]. These materials, traditionally employed around two decades ago, have recently regained research momentum due to ongoing investigations into their potential applications in hybrid electrolytes [106].

In this study, we specifically focus on exploring the properties and behavior of SiO$_2$ and Al$_2$O$_3$ as electrolyte materials, with a particular emphasis on SiO$_2$. Silicon dioxide, commonly known as silica, exhibits a remarkable combination of attributes that make it a compelling candidate for electrolyte applications. Its inherent chemical stability,

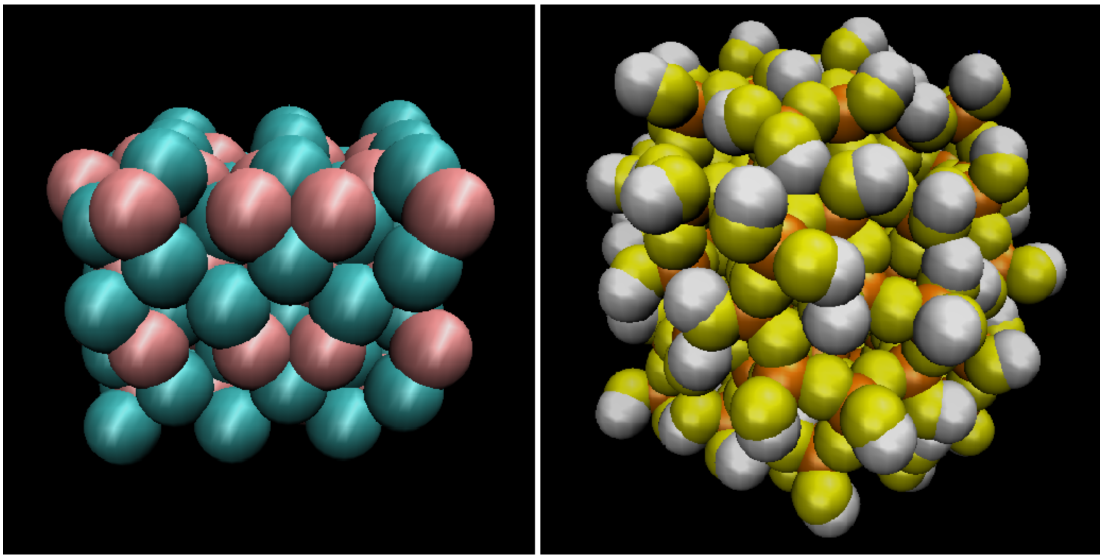

Figure 1.10: Snapshot of simulated Al_2O_3 represented by VMD visualization tool (left) and SiO_2 (right). The colocode for the alumina is: oxigen (cyan) and aluminium (pink). While for Silica the colorcode is: silicium (orange), oxigen (yellow) and hydrogen (white).

wide availability due to its abundance in nature, and ability to facilitate ion transport make it a material of significant interest for use as a ceramic in hybrid electrolytes [53, 107, 108]. Moreover, SiO_2 offers adjustable properties based on factors such as particle size, morphology, and surface modification, allowing for tailored electrolyte formulations to meet specific performance requirements. The incorporation of SiO_2 into the electrolyte matrix has shown promising results in mitigating dendrite formation, a significant challenge in rechargeable lithium-ion batteries. Importantly, some references [53, 59] clearly demonstrate an enhancement in the conductivity of PEO electrolytes with the addition of SiO_2 and Al_2O_3.

As for Al_2O_3 (alumina), it is another notable candidate to fulfill the role of a passive filler. Similar to SiO_2, Al_2O_3's surface characteristics and particle morphology can be tailored to suit specific battery configurations and performance requirements [53, 101].

The ceramic fillers under study are consistently at the nanometer scale, a practice rooted in research on hybrid electrolytes from over two decades ago. Croce et al. illustrated how nanometer-sized inert fillers enhance electrolyte ionic mobility and reduce crystallinity compared to pure SPEs [53]. One significant advantage of using small ceramic particles is the improved surface-to-volume ratio. Researchers attributed the observed conductivity increase to interactions between Lewis acidic sites on the nanoparticles' surfaces and both anions and PEO segments [101]. These interactions facilitate the release of more available lithium ions, generating additional amorphous regions that facilitate charge carrier movement. Hydroxyl groups on oxide nanoparticles' surfaces were thought to play a role in these interactions within hybrid polymer electrolytes (HPEs) [109]. Thus, working with nanoscale nanoparticles offers a distinct advantage over larger filler particles. Research in the field has primarily centered on ceramic nanoparticles [110, 102], and our study exclusively employs SiO_2 and Al_2O_3 nanoparticles.

This investigation encompasses both structural (explored in Chapter 3 for SiO_2 and Chapter 5 for Al_2O_3) and dynamical properties (examined in Chapter 4 for SiO_2 and Chapter 5 for Al_2O_3) of the two HSEs and the corresponding SPE electrolytes under various conditions. Our analysis delves into critical aspects such as the radial distribution function and coordination number to understand structural properties, while dynamical properties are analyzed through the examination of conductivity, mean squared displacement, and diffusion coefficients of ionic species. Through this research, our thesis aims to provide a conclusive assessment of the effectiveness of incorporating ceramics into the domain of solid electrolyte materials.

1.3 Precursor data

In this section, we will explore key studies in the field of Hybrid Solid Electrolytes (HSEs). The research on hybrid electrolytes finds its roots in the history of Li-ion batteries during the late 20th century, with significant developments occurring primarily in the 1970s and 1980s [111]. The emergence of Li-ion batteries also brought attention to solid-state electrolytes (SSEs). However, progress in this area was hindered by the challenge of finding materials that could simultaneously meet the mechanical and electrochemical requirements of SSEs, leading to initial setbacks [112].

1.3.1 Experimental data

Experimental exploration of hybrid electrolytes gained relevance around two decades ago, featuring influential researchers of that era such as Croce [53, 113, 101] and Scrosati [59, 54]. Nevertheless, research on hybrid electrolytes has gained momentum over the last decade, driven by an increased focus on identifying suitable material options to effectively contribute to hybrid configurations, encompassing ceramics and polymers [114].

On the experimental front, there is a wealth of literature supporting the hypothesis that the introduction of hybrid solid electrolytes significantly enhances ionic conductivity, both through the utilization of active [41] and passive fillers [115, 116, 117, 53, 118, 59, 113, 119, 96, 101]. These studies demonstrate promising and encouraging outcomes in this domain. Particularly, the integration of passive fillers into the system has been the subject of extensive investigation for approximately two decades, showcasing the enduring relevance of this area of study.

For passive fillers, researchers have proposed two main complementary hypotheses to explain the observed behavior [93]. It's widely accepted that the addition of ceramic nanoparticles to semicrystalline PEO reduces the crystallinity of the system [120, 121, 90, 91].

In reference [90], the researchers conducted an analysis of X-ray diffraction (XRD) patterns to investigate changes in the crystalline structure. They observed a significant reduction in the intensity of sharp peaks corresponding to the crystalline structure when SiO_2 nanoparticles were added. Additionally, they examined the thermograms obtained through differential scanning calorimetry (DSC) during both heating and cooling processes. Notably, even after the prior addition of $EMIHSO_4$, which already exhibits a plasticizing effect, the introduction of SiO_2 led to a substantial reduction in crystallinity. Figure 1.11 visually represents this observation, highlighting the usefulness of this common technique for assessing variations in crystallinity.

This deliberate reduction in the crystalline phase gives rise to an amorphous phase, a critical factor that promotes ion transport throughout the bulk, thereby enhancing the overall conductivity of the system. Fully amorphous solid polymer electrolytes (SPEs) can achieve conductivity values in the range of 10^{-5} to 10^{-4} S/cm at room temperature [120]. This is because lithium ions are unable to migrate through the crystalline phase, as demonstrated in reference [122]. In their study, the researchers conducted in-situ c-AFM characterization of a 50 wt.% LLZO-PEO($LiClO_4$) electrolyte at varying temperatures. They observed that conductivity occurred mostly in the amorphous regions, which they identified by analyzing the adhesion and Young's modulus of these regions within the material, as it can be seen in figure 1.12.

While the notion that adding fillers reduces conductivity is widely accepted in the literature, it alone cannot explain why nanoparticles enhance polymer conductivity above the melting temperature (T_m) [101]. Hence, while this initial hypothesis offers valuable insights, it falls short of fully explaining the conductivity-enhancing effects of nanoparticles, as observed in references such as [53, 113, 101, 59, 54].

The complementary hypothesis is that the addition of nanoparticles leads to the formation of an interface between the bulk SPE and the nanoparticle surface [41, 120, 123]. Within this interfacial zone, the structure of the PEO matrix undergoes

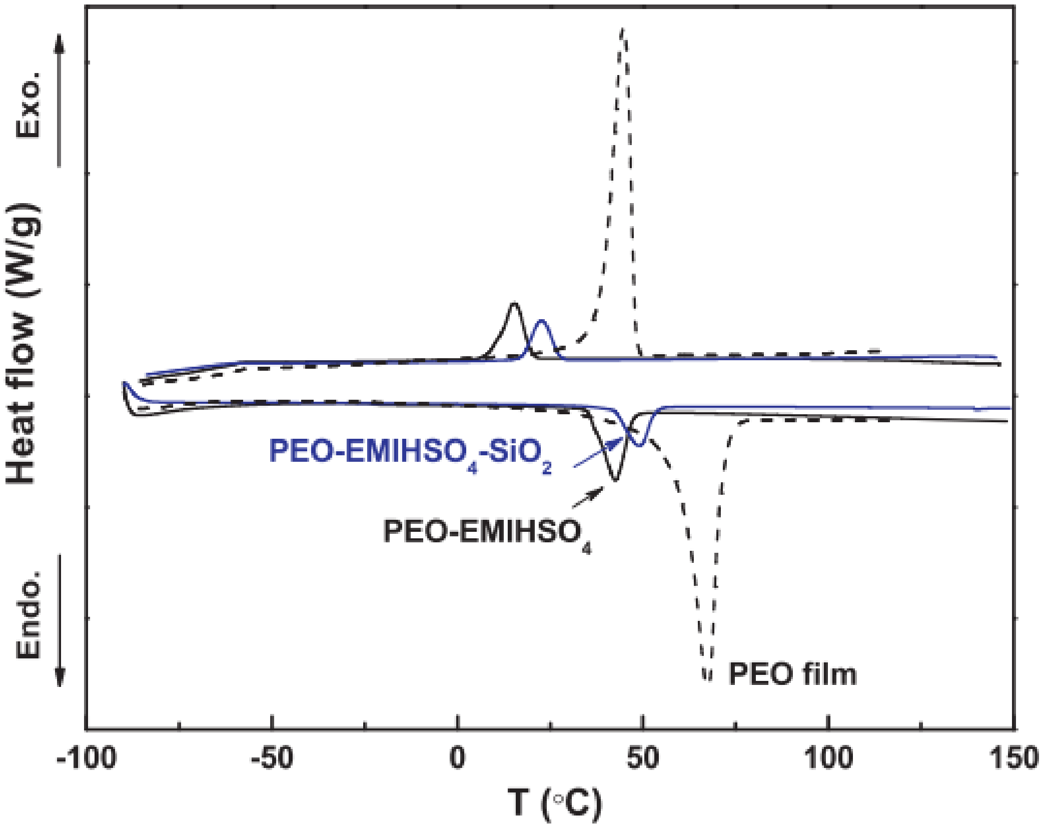

Figure 1.11: DSC heating and cooling thermograms of PEO film, PEO–EMIHSO4, and PEO–EMIHSO4–10% SiO$_2$. From ref. [90]

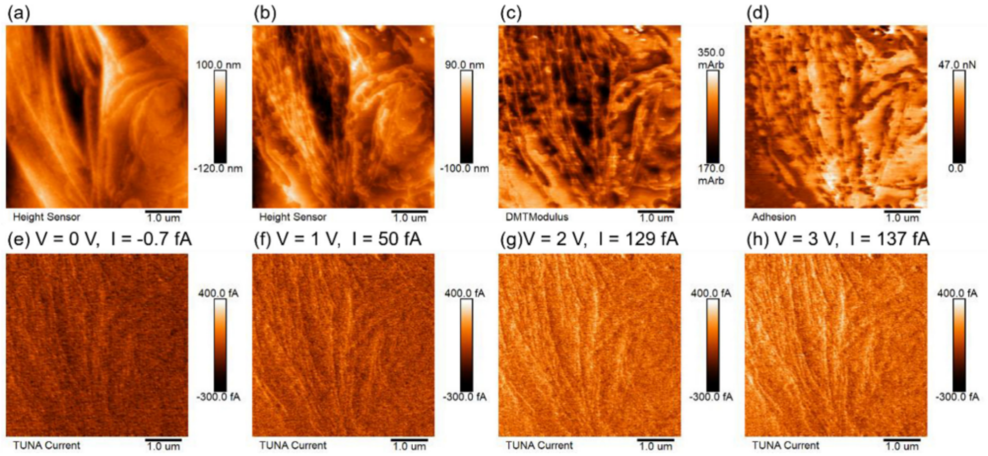

Figure 1.12: In-situ c-AFM characterization of Li-ion migration in pure PEO(LiClO4) at 30 °C and 55 °C: (a) topography at 30 °C; (b) topography, (c) Young's modulus and (d) adhesion at 55 °C; (e-h) c-AFM current under (e) 0 V, (f) 1 V, (g) 2 V and (h) 3 V at 55 °C. From ref. [122]

a reorganization, giving rise to vacant spaces that facilitate the movement of ions, subsequently leading to the development of a charge-rich space due to the interaction with the ceramic nanoparticle surface. This reorganization of the surface would further enhance the ionic conductivity in this surfacial region.

Recent studies have presented contrasting findings that question the established hypothesis regarding nanoparticle effects on electrolyte dynamical properties [124, 107, 125, 126]. These investigations have observed a detrimental impact on conductivity upon the addition of ceramic nanoparticles, initiating a debate within the scientific community. This debate centers on whether ceramic nanoparticles truly enhance the ionic conductivity of pure polymeric electrolytes and, if so, the underlying mechanisms driving any potential conductivity enhancement due to nanoparticle integration.

Moreover, empirical investigations conducted by Tekell [125] shed light on the significance of humidity-induced water absorption in altering conductivity. In their experiment, they note that well-dispersed silica nanoparticles lead to a decrease in ionic conductivity. Comparing their findings to numerous previous experiments conducted two decades ago, many of which have already been cited here [53, 113, 101, 54, 59, 96], Tekell's work acknowledges these differences and attributes them to two main factors: nanoparticle dispersion, as their well-dispersed study may differ from other studies, and the possible presence of trace amounts of water in other works, which can significantly affect the results.

Regarding the influence of humidity-dependent water uptake on conductivity, Fullerton and colleagues explored this phenomenon in ref. [126]. Their experiments demonstrate how the crystallinity of the polymer changes over time, eventually reaching equilibrium conditions. However, the time required to reach this equilibrium differs significantly between systems exposed to dry and humid conditions. Under dry conditions, crystallization takes three days, while under humid conditions, it extends to three weeks, as evidenced by corresponding DSC scans (Figures S3 and S5). Furthermore, DSC scans exhibit distinct shapes between filled and unfilled polymers in humid conditions, an effect absent in dry conditions. These early fluctuations in crystallinity, particularly in the initial days post-synthesis, critically impact the conductivity of these electrolytes.

Additionally, the timing of conductivity analysis is crucial, as illustrated in Figure 1.13. This figure reveals a substantial conductivity shift in dry conditions between samples synthesized for one day and those for fourteen days. High humidity conditions significantly prolong the time needed for the polymer to reach its final crystallization state while also enhancing electrolyte conductivity. Additionally, humidity tends to amplify the conductivity-altering effects of nanoparticles.

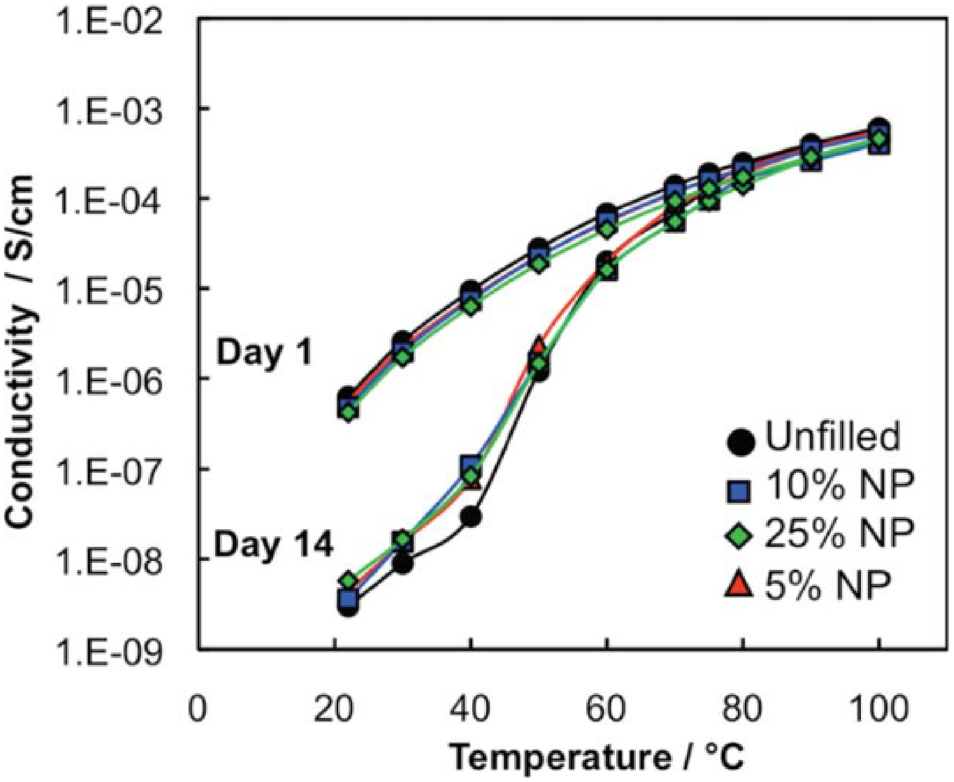

Figure 1.13: Conductivity vs. temperature 1 day after heating and14 days after heating for the 8:1 sample with and without NPs. From ref. [126]

.

This complexity underscores the critical role of humidity conditions in these systems, emphasizing the importance of conducting experiments under very dry conditions. Divergent results in the literature regarding the benefits of adding ceramic nanoparticles to solid polymer electrolytes may, in part, be attributed to variations in humidity levels during experimentation.

1.3.2 Computational data

In recent years, the application of computational methods has emerged as an indispensable tool for discerning the structural and dynamic properties inherent in polymeric systems [127]. While significant progress has been made through Molecular Dynamics (MD) simulations in the investigation of bulk PEO-LiTFSI systems, the research about incorporating fillers has remained relatively unexplored within this computational framework. Instead, MD studies have primarily focused into the dynamics of ions and polymers, as well as the atomic coordination within the PEO-LiTFSI matrix [128, 129].

Despite the substantial experimental literature in this field, computational studies are relatively scarce. The intricate nature of hybrid solid electrolytes presents a formidable challenge for computational modeling, contributing to this disparity. Notably, computational investigations have yielded varying results when assessing the impact of nanoparticle integration. While there are a few computational studies reporting increased conductivity with nanoparticle introduction [130], they remain limited in number. In contrast, in computational studies, it is more common to come across research indicating a negative impact resulting from nanofiller addition, as seen in refs. [131, 132, 133, 134]. These studies have shifted our previous understanding of nanoparticle effects, highlighting a complex interplay between nanoparticles and electrolyte behavior. Mogurampelly conducted three separate investigations [132, 133, 134] across various solid polymer electrolytes with differing ionic and thermal conditions, consistently demonstrating a detrimental impact on conductivity due to nanoparticle addition.

In this thesis we use molecular dynamics techniques to investigate the properties of PEO-matrix HSEs with SiO_2 and Al_2O_3 as a passive fillers, across a range of ceramic concentrations, geometries, ionic concentrations, and temperatures. By running molecular dynamics simulations at temperatures above the T_m of PEO we ensure that any possible effect from the polymer's crystallinity is eliminated.

While prior computational studies have explored hybrid solid electrolytes (HSEs), there appears to be a gap in the research regarding the use of SiO_2 as a filler. Existing studies have predominantly focused on other fillers such as TiO_2 and Al_2O_3 [135, 131, 130, 132]. Additionally, these previous investigations have primarily concentrated on lithium transport pathways due to its close interaction with PEO. In contrast, our research takes a comprehensive approach by examining both dynamical and structural properties across a wide range of ionic and ceramic concentrations. We also establish correlations between individual conductivities, transference numbers, and the coordination numbers of different atoms.

Furthermore, this study delves into the structural consequences of incorporating nanoparticles, specifically the interactions between the solid polymer electrolyte (SPE) and the ceramic nanoparticle surfaces. Through simulations, we gain atomic-level insights into the structure and dynamics of HSEs, shedding light on the intermediate phase that forms between the SPE and nanoparticle surfaces. These findings offer fundamental insights into HSE behavior, which can significantly contribute to the development of high-performance solid electrolytes for advanced energy storage systems.

1.4 Utility of HSEs: Contradictions in the literature and discrepancies between authors

In the preceding section of this thesis, we thoroughly reviewed the literature on Hybrid Solid Electrolytes (HSEs), encompassing both experimental and computational aspects. Our comprehensive examination unveiled a recurring theme of contradictions and discrepancies within the literature, particularly regarding the influence of nanoparticles on HSE conductivity.

Notably, there exists a considerable body of experimental research conducted over the past two decades, with prominent studies by Croce [53, 113, 101] and Scrosati [59, 54] that initially supported the notion that the inclusion of ceramic nanoparticles significantly enhances ionic conductivity. This positive trend in experimental findings persisted for quite some time and was further substantiated by various other researchers [115, 116, 117, 53, 118, 59, 113, 119, 96, 101, 54, 92, 136]. Correspondingly, fewer computational examples corroborate these findings, as seen in [130].

However, a more recent wave of research, particularly in computational studies, has introduced conflicting outcomes. These computational investigations, as exemplified by *Mogurampelly* [132, 133, 134, 125], have consistently demonstrated a detrimental impact on conductivity due to nanoparticle addition, thereby challenging the conventional understanding of nanoparticle effects in HSEs.

Another dimension of complexity arises from Fullerton and colleagues' research [126], which emphasized the role of humidity-dependent water uptake on conductivity. Their experiments revealed that the crystallinity of polymer electrolytes evolves differently under dry and humid conditions, ultimately impacting conductivity.

This complexity underscores the critical role of humidity conditions in HSE behavior and raises questions about the reproducibility and reliability of experimental results in various environmental settings.

In this thesis, we aim to address these contradictions and discrepancies in the literature by conducting a systematic exploration of HSEs. Our study centers on comprehending the impact of passive fillers, specifically silicon dioxide (SiO_2) and aluminum oxide (Al_2O_3), on HSE conductivity. By employing molecular dynamics simulations at temperatures above the melting point of polyethylene oxide (PEO), we eliminate potential inaccuracies stemming from polymer crystallinity. Our investigations encompass a wide range of ceramic concentrations, geometries, ionic concentrations, and temperatures.

This approach offers a unique opportunity to gain insights into the structural and dynamic properties of HSEs, shedding light on the behavior of the intermediate phase between the solid polymer electrolyte (SPE) and the nanoparticle surface. Our findings have the potential to contribute to the design of high-performance solid electrolytes for advanced energy storage systems.

In summary, this chapter has provided an overview of the contradictory nature of the HSE literature and has highlighted the need for a systematic investigation to bridge the gap between experimental and computational findings, offering a more comprehensive understanding of this intriguing area of study.

Chapter 2

Methodology and Simulations: Molecular Dynamics

2.1 Introduction

In recent decades, the integration of advanced computational methodologies with the progress in computing power, driven by significant advancements in electronics, has led to a noticeable increase in scientific research focused on computation [137, 138]. This growing trend highlights the significance of this innovative research approach as an essential complement to experimental investigations across diverse fields.

Computational science is a multidisciplinary field that employs advanced computing techniques to model, analyze, and solve complex equations representing real world systems and phenomena. It encompasses a range of numerical methods and algorithms, enabling researchers to gain insights and make predictions that might be impractical or impossible through traditional analytical approaches. It offers several distinct advantages over traditional experimental approaches and pure theoretical methods [139]. These advantages stem from the unique capabilities of computational techniques and their ability to bridge the gap between theory and experiment. Some key advantages of computational science are:

- **Cost and Resource Efficiency**: Computational simulations and modeling significantly reduce the need for expensive equipment, materials, and physical setups that are often required in experimental research [140, 141]. This leads to cost savings and allows researchers to explore a wider range of scenarios without the constraints of practical limitations.

- **Rapid Data Generation**: Computational methods can generate vast amounts of data in a relatively short time compared to the time-consuming nature of experimental data collection [142]. This speed facilitates the exploration of complex systems and the testing of hypotheses across various conditions.
- **Controlled and Manipulable Environments**: Computational simulations allow researchers to investigate phenomena under controlled conditions that might be challenging or impossible to achieve in experiments. Virtual environments enable the manipulation of parameters and variables to understand their individual and combined effects [140]. They also enable the exploration of extreme conditions, such as high temperatures, pressures, or energy levels, which might be dangerous or impractical to replicate in a laboratory setting [143].
- **In-depth Insights**: The ability to delve into microscopic or molecular scales offers researchers a high level of detail, enabling a deeper understanding of underlying mechanisms and properties within studied systems [144].
- **Prediction and Hypothesis Testing**: Computational models can serve as predictive tools to test hypotheses before committing resources to experimental research. This helps improve the efficiency and direction of experimental studies [140].
- **Reduced Ethical Concerns**: In certain fields, such as medicine and environmental science, computational models can replace the need for potentially ethically complex or harmful experiments. They also help mitigate environmental impacts associated with experiments [145].
- **Multiscale Modeling**: Computational methods excel at integrating analyses across various scales, from the molecular level to macroscopic systems, providing a comprehensive understanding of complex phenomena [146].

Computational science emerged in the mid-20th century to tackle increasingly complex scientific problems [147]. The advent of electronic computers revolutionized research by enabling large-scale data processing and analysis. In the latter half of the 20th century, computing technology advanced significantly, thanks to mainframe and personal computers. This progress was driven by the continuous development of advanced algorithms and powerful software tools, in line with Moore's law [148]. These tools empowered researchers to model complex phenomena, simulate real-world processes, and experiment with scenarios resembling actual situations.

In the present times, computational methods have become integral to scientific research. This marks a significant shift from an earlier era when research primarily depended on experiments and theories. The rise of computational science adds a new perspective, providing researchers with a fresh way to understand complex phenomena [149]. This shift reflects both the impressive progress in computational methods and a fundamental change in how we explore and expand our understanding of the natural world.

Contemporary research benefits from computer science techniques [150, 151], evident in the diverse tools that improve our understanding of complex phenomena and expedite problem-solving across multiple disciplines, including polymer science [152]. For instance, Monte Carlo simulations, initially used for particle interactions, now find applications in particle physics, statistical mechanics, and nuclear engineering [153]. Finite Element Analysis (FEA) assists engineers in simulating mechanical systems' behavior and optimizing designs without physical prototypes [154]. Molecular Dynamics (MD) simulations offer insights into microscopic behaviors in molecular systems, aiding drug discovery and materials design [155, 156]. Density Functional Theory (DFT) elucidates electronic properties of materials, guiding progress in electronics and materials science.

Computational science encompasses two main categories: modeling and simulations, each offering distinct approaches and methodologies.

Modeling entails the creation of simplified representations of real-world systems, capturing their essential characteristics while discarding finer details [157]. These models are typically expressed through equations or diagrams, aiding in conceptual understanding and hypothesis generation.

Simulations, on the other hand, go beyond abstraction, utilizing mathematical models as blueprints to recreate both dynamic and static behaviors in a digital format [158]. This approach is particularly powerful in methods like Molecular Dynamics (MD) or Density Functional Theory (DFT), where simulations explore the smallest scales of matter, delving into the domain of individual atoms and electronic structures. Simulations enable the observation of complex system evolution over small time scales, offering insights and illuminating phenomena across various domains.

Simulations are valuable tools in scientific research, approximating and replicating phenomena, providing dynamic representations of system behavior over time. However, they have limitations due to reliance on theoretical constructs that may lack precision in reproducing natural intricacies [159]. Researchers continually work to enhance simulation accuracy.

Computational science offers advantages but is not an all-encompassing solution and has constraints. It depends on model fidelity, requires empirical data validation, and can be computationally intensive. Comprehensive insights often involve a balanced integration of computational, experimental, and theoretical approaches, recognizing both strengths and limitations in simulations [160].

The pursuit of an absolutely precise description of natural phenomena remains ongoing, though it is often an elusive and likely unattainable objective. Simulations offer a valuable pathway, providing a closely approximated level of precision. The true significance of computational methodologies emerges when they align with empirical results, demonstrating reproducibility and expanding the scope for simulating various materials. The manipulation of positions, configurations, and parameters becomes routine in innovative research, a distinctive advantage of computational methods. Experimental techniques excel in revealing macroscopic attributes and quantifying measurements but fall short in understanding atomic-level intricacies due to inherent limitations. Fine details at the atomic scale evade direct experimental observation. In contrast, advanced simulations offer a solution to these limitations and provide a detailed scientific exploration. This section will delve into classical molecular dynamics techniques, one of the most widely used simulation methodologies [161].

2.2 Molecular Dynamics

Classical Molecular Dynamics (MD) is a computational simulation technique in the field of molecular modeling that investigates the temporal evolution of molecular systems by numerically solving Newton's equations of motion [162]. These systems typically comprise atoms, molecules, or larger aggregates, and MD seeks to emulate their behavior over time based on interatomic or intermolecular forces and energy potentials. In an MD simulation, a molecular system's initial state is defined by specifying the positions, velocities, and often initial forces on each atom or molecule [163]. Through iterative steps, the trajectories of these entities are calculated with the help of numerically solving equations of motion, accounting for forces arising from interactions with neighboring particles. By tracking the positions and velocities of individual atoms or molecules, MD enables us to understand complex processes that would be challenging or impossible to study experimentally [151].

The basis of Molecular Dynamics consists in treating atomic ions as objects that follow the laws of classical mechanics. Consequently, the method aims to solve Newton's equations to determine the motion of the ions based on the forces exerted on each of them, which will be explained and detailed in the next section. In essence, conducting Molecular Dynamics (MD) simulations entails resolving partial derivative equations (PDEs) of motion, often coupled with initial and boundary conditions, using finite difference methods. These PDE solutions provide the particles' positions and velocities as functions of time. Newton's second law equations are expressed as:

$$\frac{d\vec{r}}{dt} = \vec{v} \qquad\qquad \frac{d\vec{v}}{dt} = \vec{F}, \tag{2.1}$$

where $\vec{r}$ are the positions of the atoms, $\vec{v}$ corresponds to their velocities and $\vec{F}$ to their forces. At the same time, according to the relationship between force and potential energy:

$$F = -\nabla U, \tag{2.2}$$

where U is the potential energy of the system. And thus, we obtain the PDEs:

$$m\frac{d^2\vec{r}}{dt^2} = -\nabla U, \tag{2.3}$$

In order to solve equation 2.3 we make use of the Verlet algorithm [164]. This is a commonly used algorithm to solve PDEs and the basis of this method consists in defining $\vec{r}$ for a time infinitesimally greater than t and for a time infinitesimally lower than t.

$$\vec{r}(t+\delta t) = \vec{r}(t) + \vec{v}(t)\delta t + \frac{\vec{a}(t)\delta t^2}{2}, \tag{2.4}$$

$$\vec{r}(t-\delta t) = \vec{r}(t) - \vec{v}(t)\delta t + \frac{\vec{a}(t)\delta t^2}{2}, \tag{2.5}$$

Where δt is the timestep, equal to $1fs$ in our case. When both expressions are added, the value of $\vec{r}(t+\delta t)$ can be determined in terms of $\vec{r}(t)$ and $\vec{r}(t-\delta t)$, with a fourth order error. If one equation is subtracted from the other instead of adding them, the velocity value is obtained:

$$\vec{v}(t) = \frac{\vec{r}(t+\delta t) - \vec{r}(t-\delta t)}{2\delta t}, \tag{2.6}$$

This expression has a second order error and carries one of the main issues of this method: lower precision in velocity calculation. On the other hand, its significant advantage is that it exhibits excellent energy conservation for reasonably large time steps.

Molecular Dynamics offers a unique advantage by providing a detailed, time-dependent perspective on molecular systems. It can capture dynamic events and transient states. MD is one of the best suited techniques for simulations that require a large number of atoms and precision at the atomic level [163]. Other techniques like Coarse Grained models are much faster [165], as they simplify the representation of molecules by grouping multiple atoms into a single "bead" or particle, but by definition, it is not precise enough to get insight into the atomic level. Monte Carlo simulations are also faster to compute than molecular dynamics. Unlike MD, which tracks the trajectories of individual particles, Monte Carlo simulations use statistical sampling to estimate system behavior by generating random configurations and analyzing their properties. They are particularly useful for studying thermodynamic properties and equilibrium behavior, but they may not capture the same level of dynamic detail as MD.

Concerning the calculation of the forces, we encounter techniques like Density Functional Theory (DFT), a computational methodology focused on evaluating electronic structures and properties under equilibrium conditions. DFT represents the highest level of precision in simulations, delving deep into the complexities of materials at the electronic scale [166]. By solving the Hartree-Fock (HF) equations and incorporating the principles of quantum physics, it achieves significantly enhanced precision, reaching the electronic level of description. However, the elevated precision of DFT comes with a trade-off. It demands substantial computational resources, limiting its application to smaller systems and substantially shorter temporal scales by several orders of magnitude [167].

Another typical option for simulations is the use of polarizable force field (PFF) methods. These methods are a viable choice for systems like ours and closely resemble to classical molecular dynamics. Polarizable force field methods account for the changing electron distributions around atoms, leading to more precise representations of interactions involving significant charge transfer or polarization effects [168]. They capture subtle aspects of molecular behavior that fixed-charge force fields might overlook, especially in systems with strong electrostatic interactions. However, due to their complex treatment of electronic polarization, these methods demand more computational resources.

In our research context, we opt for using non-polarizable classical molecular dynamics (MD) due to its computational efficiency, which is essential for running large systems over extended periods.

Advances in computing technology have propelled MD to the forefront of molecular research. With specialized algorithms and high-performance computing, simulations encompassing millions of atoms and spanning nanosecond or milliseconds have become feasible. Such prowess enables scientists to scrutinize processes practically inaccessible through experiments alone.

In essence, Molecular Dynamics overcomes physical experimentation limitations, offering a window into molecules' dynamic world beyond naked eye or traditional techniques. Its numerical exploration of atoms and molecules in motion has reshaped our understanding and catalyzed breakthroughs across disciplines.

2.3 Description of the Force Field

Molecular dynamics simulations are fundamentally based on force fields, mathematical models that define how atoms and molecules interact within a system [163]. These force fields consist of equations and parameters that govern particle interactions, allowing simulations to calculate the system's potential energy based on the positions and types of particles. They encompass terms representing covalent bonds, non-bonded interactions (like van der Waals forces and electrostatic interactions), angles, dihedrals, and more [169].

Force fields are essential in molecular dynamics simulations because they determine how forces act on individual particles, influencing the system's temporal evolution. Many studies have been conducted to compare different options for specific materials [170]. In essence, the force field contains all the necessary information for running molecular dynamics simulations.

A force field (FF) comprises two main components: *equations* and *parameters*. Multiple sets of force fields are developed for atomic simulations, and the choice determines the specific set of equations employed. Some notable examples of optimized force field sets relevant to this study include CHARMM, AMBER, COMPASS, and OPLS-AA. These sets feature subtle differences in their equations, often tailored to specific material types. For instance, CHARMM [171, 172] and AMBER [173, 174] are well-suited for protein modeling, while [175, 172] and COMPASS [176] are designed for simulating organic molecules. Despite these distinctions, the central goal remains consistent: accurately simulating organic materials. In our research, we selected the OPLS-AA force field due to its compatibility with our case and the availability of force field parameters for all elements in our simulations. This choice was made for its precision and efficiency.

When using OPLS-AA, the potential energy function is given by the sum over five different terms:

$$U = E_{coul} + E_{LJ} + E_{bond} + E_{angle} + E_{dihedral}, \tag{2.7}$$

This potential energy is the one that drives the forces in Newton's equations 2.1 and 2.3, which describe the movement of the atoms. The interatomic potentials that describe the force field in OPLS-AA are the following:

$$E_{coul} = \frac{Cq_iq_j}{\epsilon r}, \tag{2.8}$$

$$E_{LJ} = 4\epsilon_{LJ}\left[\left(\frac{\sigma}{r}\right)^{12} - \left(\frac{\sigma}{r}\right)^{6}\right], \tag{2.9}$$

$$E_{bond} = K_b(\vec{r} - \vec{r}_0)^2, \tag{2.10}$$

$$E_{angle} = K_a(\theta - \theta_0)^2, \tag{2.11}$$

$$\begin{aligned} E_{dihedral} = \frac{1}{2}K_1\left[1 + cos(\phi)\right] + \\ \frac{1}{2}K_2\left[1 - cos(2\phi)\right] + \frac{1}{2}K_3\left[1 + cos(3\phi)\right] \\ + \frac{1}{2}K_4\left[1 - cos(4\phi)\right], \end{aligned} \tag{2.12}$$

In these equations, C represents an energy conversion constant, q_i and q_j denote the charges, ϵ is the dielectric constant, and ϵ_{LJ} and σ are the Lennard Jones (LJ) parameters for energy and distance, respectively. Regarding the bonding terms, K_b and K_a represent the bond and angle parameters, respectively. Here, θ signifies the angle, while K_1-K_4 are the parameters of the dihedral potential, and ϕ is the torsional angle defined by the quadruplet of atoms. Equations 2.8 and 2.9 correspond to the nonbonding terms, id est, the Coulombic interactions and Van der Waals interactions respectively, while equations 2.10, 2.11 and 2.12 correspond to the stretching, bending and dihedral torsions between atoms in the same molecule. We applied the Lorentz-Berthelot mixing rules to calculate the cross-terms of the Lennard-Jones coefficients:

$$\epsilon_{ij} = \sqrt{\epsilon_i\epsilon_j}, \tag{2.13}$$

$$\sigma_{ij} = \frac{1}{2}\left(\sigma_i + \sigma_j\right), \tag{2.14}$$

Molecular dynamics simulations were carried out using the LAMMPS simulation package, applying periodic boundary conditions in all three dimensions of space. We truncated the nonbonding terms in equations 2.8 and 2.9 with a cutoff distance of 10

Å, while long-range Coulombic interactions were computed using a particle-particle particle-mesh Ewald solver (PPPM) with a relative accuracy of 10^{-4}.

Atoms within macro-molecules interact with neighbors separated by up to three bonds via an intramolecular potential, $V_{\text{intra}} = V^b + V^a + V^d$, sum of a stretching 2.10, bending 2.11 and dihedral 2.12 torsion terms. The complete force fields used in this part of the research are available in the supplementary data. We used the standard method of excluding or reducing the pair interactions of Eqs.(2.8 and 2.9) by setting weighting coefficients $(w^b, w^a, w^d) = (0, 0, 1/2)$ for atoms involved in Eqs.(2.10, 2.11 and 2.12), while $w = 1$ for further atoms. Numerous examples of this technique can be found in the literature, as demonstrated by [177, 178].

The OPLS all-atom (OPLSAA) force field is an empirical, non-polarizable model that was originally developed for its use on organic molecules and peptides [175]. However, due to its accuracy and efficiency, this classical force field has been widely adopted in many areas of polymer science [179], ranging from battery applications to pharmacological research [180, 181]. The parameters of the FF rule the interactions between atoms which determine its movement at each timestep. The parameters of the force field have been optimized and reviewed several times, and the creation and optimization of force fields are active areas of research by themselves.

In addition to the equations, another fundamental aspect of force fields is the *atom parameters*. These parameters consist of specific numerical values assigned to each atom type within the simulation. These values are subsequently used in the equations as constants, providing unique identities to each set of atoms. Each atom type has its distinct set of parameters, which must be incorporated into the equations of the corresponding force field. It is important to note that even if certain atoms share the same element on the periodic table, they may still require different force field treatments. This distinction is necessary whether these atoms are part of different molecules or within the same molecule but involved in different bonds. This means that, for example, an oxygen atom within PEO has different force field parameters than an oxygen atom in SiO_2. This difference arises from variations in their surrounding environments and bonded atoms. These considerations are critical when calculating their respective parameters.

The accurate calculation and optimization of force field parameters represent a significant research pursuit in their own right, with examples like ref [182]. Some researchers dedicate their scientific efforts solely to this specific area of study, given its inherent complexity and time consuming nature. As this is a complex and time-intensive domain domain of research, we will not engage in the creation and optimization of our own force field parameters. Fortunately, there is an abundance of literature references and databases that detail their own meticulously optimized force fields, which we will

PEO			
atom type	q (e)	ϵ (kcal/mol)	σ (Å)
H1	0.092	0.03	2.5
H2	0.42	0	0
C	0.0072	0.066	3.5
O1	-0.38	0.14	2.9
O2	-0.59	0.17	3.12
TFSI			
N	-0.528	0.17	3.25
S	0.816	0.25	3.55
O	-0.424	0.21	2.96
C	0.28	0.066	3.5
F	-0.128	0.053	2.95
Lithium			
Li	0.8	0.166	1.506
SiO_2			
H	0.36	0.0	0.0
O1	-0.495	0.17	3.0
O2	-0.6075	0.17	3.12
Si	0.99	0.1	4
Al_2O_3			
O	-0.945	0.155	2.8
Al	1.4175	0.155	2.2

Table 2.1: Non-bonding coefficients of the force field of all the different types of atoms in the simulations.

use. Nevertheless, in a subsequent chapter of this thesis, we will also undertake minor force field modifications manually to explore how the original force field responds to slight variations.

The charges of the atoms used in the simulations are summarized in Table 2.1, and additional details regarding the force field parameters can be found in the Appendix.

2.4 Simulation procedure

To effectively solve Equation 2.3 and simulate atomic motion within our system, we must carefully define initial and boundary conditions. The initial conditions involve specifying particle coordinates, velocities, and external forces as the simulation begins. Meanwhile, boundary conditions encompass a broader set of considerations, including periodic boundary conditions, statistical ensembles, and external forces.

Periodic boundary conditions are often employed, allowing particles leaving one boundary to re-enter from the opposite side. This approach facilitates interactions across boundaries, effectively treating a small cell as a representative volume element for a much larger system, reducing computational demands to some extent. However, the use of periodic boundary conditions introduces translational periodicity, potentially conflicting with the behavior of amorphous materials and occasionally causing disparities between simulation and experimental outcomes [183].

To mitigate these periodicity-related effects, the simulation system must be sufficiently large, which, in turn, increases computational requirements. Striking the right balance between precision and computational cost is a critical consideration in our simulations. This balance ensures that our results align as closely as possible with experimental observations, addressing the challenges posed by periodic boundary conditions as we study atomic motion.

The thermodynamic ensemble is another crucial condition in MD simulations [184]. A thermodynamic ensemble refers to a collection of multiple microscopic states that share the same macroscopic properties like temperature, pressure, and volume. It represents a statistical framework for studying the behavior of a system in equilibrium. Some of the most important ensembles are the following:

1. **NPT Ensemble**: In the isothermal-isobaric ensemble, the simulation maintains a constant number of particles, pressure, and temperature within the system. The system's volume is allowed to change to accommodate variations in pressure and temperature. This ensemble is frequently employed when relaxing systems to their equilibrium state.

2. **NVT Ensemble**: The canonical ensemble keeps the number of particles, volume, and temperature constant during the simulation. It is commonly used for studying systems at a fixed temperature, making it suitable for investigating materials undergoing phase transitions. This ensemble is typically employed to collect data after the system has reached thermal equilibrium.

3. **NVE Ensemble**: In the micro-canonical ensemble, the number of particles, volume, and total energy of the system remain constant. This ensemble is used to model isolated systems where no exchange of particles or energy with the surroundings occurs. It's commonly employed to study the time evolution of a system without external influences.

In our case we are just going to use **NVT** and **NPT** thermodynamic conditions. The reason for not using NVE is simply that it does not suit the nature of our simulations, that want to reproduce a realistic system where what is constant is pressure and temperature or volume and temperature.

In the next subsections we will explain all the process of simulation and the different steps on it, as well as some explanations about the software that has been employed to run MD simulations during the research.

2.4.1 LAMMPS

In order to run molecular dynamics simulations, a suitable program is required to perform the necessary calculations. Among the available options, we have chosen LAMMPS [185]. LAMMPS (Large-scale Atomic/Molecular Massively Parallel Simulator) stands out as an extensively used open-source software package tailored for simulating and modeling molecular dynamics, as well as Monte Carlo simulations, at a microscopic or atomistic level. It is developed and distributed by Sandia National Laboratories and its primary purpose is to analyze the behavior, interactions, and properties of materials on atomic and molecular scales.

LAMMPS demonstrates remarkable versatility by enabling the simulation of diverse material types, including solids, liquids, gases, and biomolecules. This software empowers researchers to explore an extensive array of physical and chemical phenomena. These encompass the analysis of material properties, molecular interactions, chemical reactions, and phase transitions, among other notable examples. Our specific area of interest revolves around molecular interactions, which captures our attention due to both its extensive range of available options and its widespread application in the field of polymeric systems.

LAMMPS provides a simulation environment offering many tools for system manipulation, data restarts, and information extraction. Its user friendliness lies in its streamlined approach: a data file and an input file containing essential directives suffice for complex MD simulations. The input file covers vital details such as atom configurations, force fields, positions, and molecular topology. Even data from prior simulations can be utilized, allowing for a simple continuation. These conveniences, coupled with the extensive array of options for managing simulation data, establish LAMMPS as one of the most frequently employed tools in the field of MD simulation.

2.4.2 Initialization

The first step before simulation consist in setting all the initial conditions. This encompasses the establishment of initial positions and correct bonding arrangements for all elements within the system, as well as the acquisition of force field datasets for each atom type and the preparation of input files for the simulation software.

To facilitate the setup of initial positions and bonding within the system, we have employed a combination of our custom codes with CHARMM-GUI [186, 187, 188]. CHARMM-GUI is a versatile software application that facilitates precise initialization for various materials, including polymer systems and ceramic particles. In the following section, we will provide a detailed overview of this program and offer insights into the data initialization process.

CHARMM-GUI

CHARMM-GUI is an open-source program designed to assist scientists from various fields, particularly those engaged in atomic simulations, and more specifically, molecular dynamics. This program employs a range of algorithms to initialize different types of atomic structures.

When creating a melted polymer system, such as polyethylene oxide (PEO), CHARMM-GUI follows a systematic approach to set up the simulation [189]. It involves several essential steps:

1. Polymer Chain Construction: It begins by constructing the polymer chain, allowing users to specify the desired units and chain length.
2. Force Field Parameter Assignment: The program assigns force field parameters to ensure accurate modeling of the polymer's behavior.
3. Topology Generation: CHARMM-GUI generates the necessary connectivity information (topology) for the polymer, defining bonds, angles, dihedrals, and non-bonded interactions.
4. Solvation: Solvation is accomplished by introducing solvent molecules, usually water, into the system. This solvators can be eliminated in the final datafile.
5. Energy Minimization: To optimize atomic positions and eliminate steric clashes, an energy minimization step is performed, employing algorithms like the conjugate gradient method.
6. Equilibration: Equilibration ensures the system reaches a stable state. CHARMM-GUI employs the Nose-Hoover thermostat and barostat for this purpose.
7. Handling Long-Range Interactions: To efficiently manage long-range electrostatic interactions, methods like Particle Mesh Ewald (PME) or Particle-Particle-Particle-Mesh (PPPM) are employed.

CHARMM-GUI is primarily oriented towards simulating molecular systems, particularly biological macromolecules, including polymer gels, solvents, membranes, and solvated polymers. However, despite its primary focus on biomolecular simulations, CHARMM-GUI is also equipped to generate inorganic materials, such as nanoparticles and other types of inorganic systems [190]. This versatile tool allows users to generate, optimize energy states, and initialize systems independently, as well as combine different materials.

In our specific case, we employed CHARMM-GUI for simulating both pure polyethylene oxide (PEO) polymeric systems and hybrid systems involving ceramic nanoparticles. This was made possible through CHARMM-GUI's versatile multicomponent assembler package [191]. These hybrid systems often start with an initial hybrid input generated using CHARMM-GUI. However, in certain situations, such as when altering nanoparticle sizes, we directly incorporated these nanoparticles into LAMMPS. In those cases CHARMM-GUI provided us with initial files for the pure ceramic materials we studied. This adaptability of CHARMM-GUI makes it a valuable resource for researchers working on a wide range of materials and simulations, allowing for flexibility in material combination and simulation setup.

First steps of molecular dynamics

After settling the initial positions of the polymer or the hybrid electrolyte, the next step involves adding ions to the system. CHARMM-GUI offers a feature for including a salt within the system. However, their database does not always provide sufficient information to create complex anions like TFSI. Consequently, we must introduce the salt separately. To generate TFSI, we first gathered force field information and used this data to create an initial configuration with atoms placed at equilibrium distances [192]. We accomplished this using external programs, such as Python (further discussed later in this chapter). Subsequently, we optimized the energy of the TFSI molecule by allowing a single TFSI entity to evolve within LAMMPS.

Once we established the initial TFSI structure, we introduced both lithium ions and TFSI ions into the electrolyte. Their positions were randomized using tools available in LAMMPS. It is essential to note that when the electrolyte contains nanoparticles, it is imperative to define exclusion regions around the nanoparticles. This precaution prevents ions from being placed directly inside the ceramic material. Typically, the addition of ions constitutes one of the final steps in the initialization process.

A critical aspect of the system's initialization involves determining the number of atoms within the simulations. The number of atoms can vary significantly across different studies of the thesis. For some specific sections of the research, the atomic concentrations within the system are intentionally adjusted, ranging from high to low concentrations for ions and nanoparticles. The one constant element in all our simulations is the presence of 100 PEO molecules, equivalent to a total of 14,300 atoms. These PEO molecules consist of 20 ethylene oxide (EO) units and are terminated with two hydroxyl groups. To assign force fields and charges to these PEO molecules, we utilized LigParGen software [193, 194, 195], which is based on Jorgensen's OPLS potentials.

Another critical aspect to consider during system generation is the number of nanoparticles. This process is typically more straightforward to perform with LAMMPS than with CHARMM-GUI. Our typical approach involves replicating the system, removing any excess polymer, and then adjusting the system's volume isothermically until it reaches the desired volume.

Finally, prior to starting the actual simulations, we introduce controlled changes in the system's volume. This allows atoms plentiful space to move and exchange positions, helping to prevent the formation of potential metastable phases where atoms may become trapped. Additionally, we gradually raise the system's temperature and let it evolve in the NVT ensemble for 2 nanoseconds before proceeding towards the target volume.

In specific cases within this study, additional steps may be necessary, and these will be explicitly addressed in their respective sections. However, for the majority of simulations, the procedures mentioned above are enough to cover the essential steps.

In the following sections we will explain the details about the running steps of the LAMMPS program from the initialized system to the production run.

2.4.3 Running steps

Once all initial data and atom positions are set, the molecular dynamics (MD) simulations are conducted using a structured process. This process involves various steps, tailored to the specific research objectives. Our simulations utilize both the NPT (isothermal-isobaric) and NVT (canonical) ensembles, employing periodic boundary conditions to account for all three dimensions of space. The Nose-Hoover thermostat and barostat are applied with a timestep of 1 femtosecond (fs), and the simulation is run through the following sequential stages:

1. **Annealing phase**: The simulation begins with an annealing phase initiated at 1000 K using the NPT ensemble, lasting for 1 nanosecond (ns). Subsequently, over the next 1 ns, the temperature gradually decreases to reach the target value. During this cooling phase, temperature adjustments are controlled with a damping time of 100 timesteps, while pressure adjustments employ a damping time of 1000 timesteps. Annealing is a controlled temperature manipulation technique

used to modify or optimize a system's structure by subjecting it to cycles of gradual heating and cooling [196, 197]. The heating process always happens above the intended study temperature.

2. **Equilibration at high temperature**: Following the initial annealing, a second annealing phase elevates the temperature back to 1000 K over 1 ns. This is followed by an 4 ns period at 1000 K. This extended equilibration allows the system to overcome any remaining energy barriers at elevated temperatures. The repeated annealing process helps mitigating initial biases and promotes relaxation of the system's configuration.

3. **Thermalization and cooling**: After the equilibration at high temperature, the temperature is gradually reduced over a period of 2-4 ns. The final cooling is done slowly to avoid the development of metastable phases resulting from rapid equilibration outside the system's equilibrium state. This is followed by an additional equilibration phase lasting 8 nanoseconds, ensuring the system reaches a stable state before data collection.

4. **Production run at target temperature**: Upon reaching the desired temperature, the production run is initiated. During this phase, essential data is collected to analyze the behavior of the system. In the majority of simulations within this research, the production run spans 60 ns, during which data is gathered for subsequent analysis. Notably, results are averaged across various initial time points, specifically at intervals of 50 picoseconds (ps). This approach ensures the robustness of the conclusions drawn from the simulation.

Highlighting the time required for these simulations is essential, a frequently overlooked aspect in scientific research and particularly crucial for MD runs [198]. Data scientists using computational tools must meticulously plan and deeply consider the time investment necessary for their "computational experiments". Just as in traditional experiments, comprehensive organization and careful consideration of all relevant factors are imperative before starting any computations. On average, each simulation, spanning from the annealing phase to the end of the production run, demands approximately 1 week of computation on a supercomputer, employing 2 nodes with 40 cores each, making a total of 13440 hours of CPU time. However, this timeframe can vary significantly, primarily driven by the diverse sizes of systems, a crucial factor in this type of simulations.

For more insight into the methodologies employed, specific code examples utilized for simulating our systems are provided in the appendix section.

2.4.4 Analysis and Visualization

Simulation analysis was predominantly conducted using external programs rather than relying solely on LAMMPS. While LAMMPS offers automated tools for tasks like calculating centers of mass and radial distribution functions, external programs afford greater flexibility for precise and customizable analysis. This approach permits adjusting and restarting analysis codes as needed, contrasting with LAMMPS where everything must be predefined, and MD simulations are notably time-intensive compared to data parsing.

In this research, Python 3 was the primary tool for analysis. Python stands as a widely recognized high-level programming language known for its readability and adaptability [199, 200]. Its widespread adoption spans domains like web development, data analysis, and scientific research, facilitated by its intuitive syntax and extensive libraries.

Through Python, we have written numerous programs of diverse code to analyze our system's characteristics. Notably, an example showcasing the calculation of mean squared displacement and conductivity can be found in the appendix section.

Regarding the visualization, we have employed VMD as our primary tool for representing molecular structures. VMD is a versatile software tool capable of visualizing, analyzing, and modeling molecular structures and dynamics [201]. In Figure 2.1, you can observe visualization examples of the electrolyte under study in this thesis, as well as representations of individual simulation elements.

Visualization tools like VMD are essential in this type of research for elucidating complex molecular structures and dynamics, facilitating data interpretation, and helping in the discovery of insights that may not be apparent from raw data alone.

2.5 Transport properties

In the study of lithium-ion batteries, understanding transport properties is crucial, especially in the context of hybrid electrolytes. These properties, diffusion, conductivity and related phenomena, are vital for the performance of the batteries. The main objective of this research revolves around whether if the addition of nanoparticles enhance the SPE's conductivity. In this section, we delve into the intricacies of transport phenomena within these hybrids, leveraging computational methods and theoretical frameworks. By shedding light on these dynamics, we contribute to optimizing lithium-ion batteries,

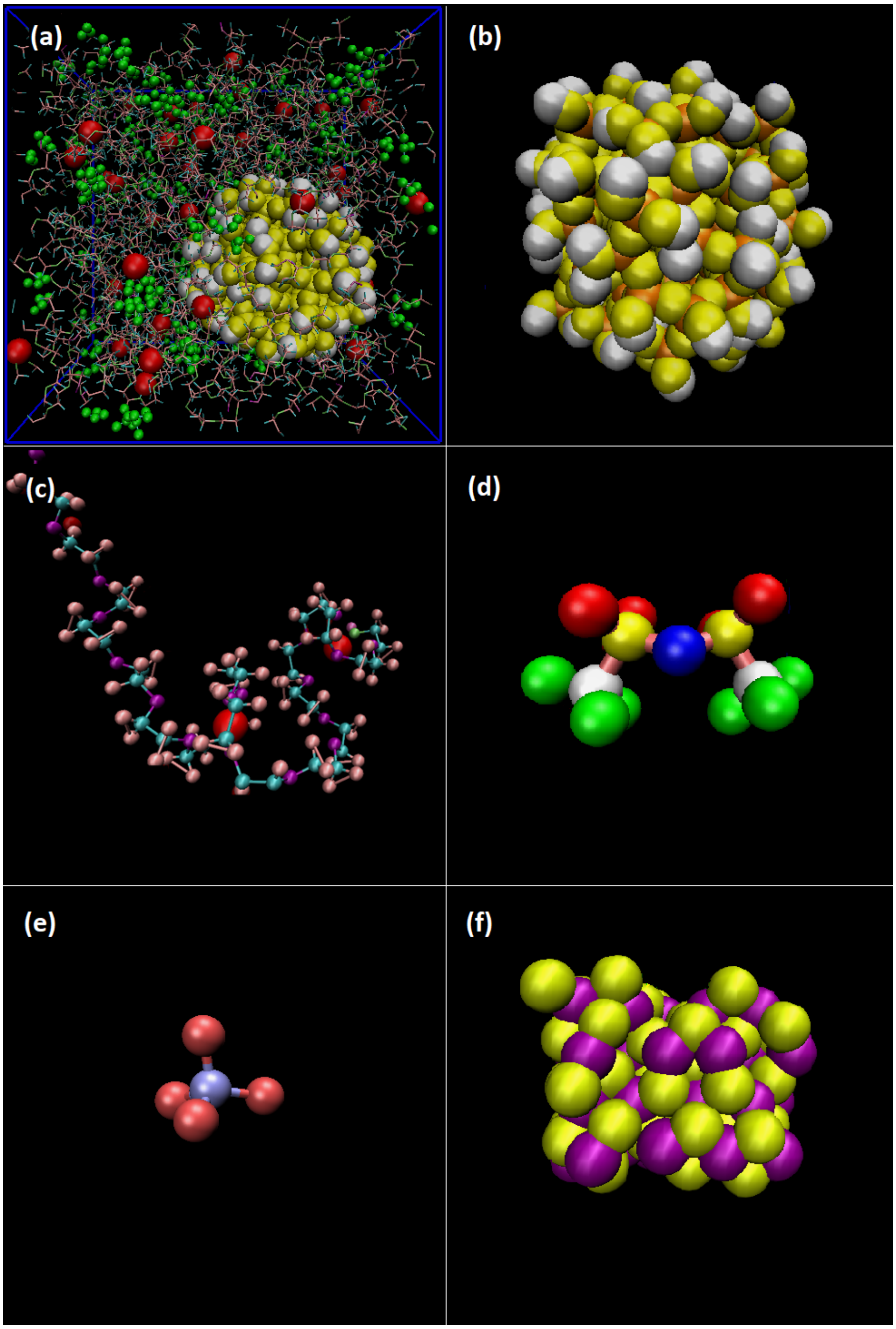

Figure 2.1: Images of the system of study visualized by VMD. (a) Snapshot of the full system showing four elements: lithium (red), TFSI (green), SiO_2 (yellow and white) and PEO (lines). (b) SiO_2 with hydrogen (white), oxygen (yellow) and silicon (orange). (c) Snapshot of the PEO surrounding the lithium (red) with its oxygens (purple). (d) TFSI molecule with nitrogen (blue), sulfur (yellow), oxygen (red), carbon (white) and fluor (green). (e) ClO_4^- anion with chlorine (violet) and oxigen (red). (f) Al_2O_3 with aluminum (purple) and oxigen (yellow).

in a search for more efficient and sustainable energy storage solutions.

In this thesis we are going to center our attention in 3 different properties: mean squared displacement, autodiffusion coefficient and conductivity.

The mean squared displacement (MSD) is our first dynamic parameter of interest. It quantifies the mobility with which atoms depart from their positions. By precisely tracking atomic trajectories and summing the squared positional deviations over time, MSD studies essential insights into diffusion processes and activation energies [202]. This analysis is essential for improving ionic conductivity and fine-tuning charge carrier pathways, highlighting its integral part in advancing battery materials' performance and design. The MSD is calculated by the following equation:

$$\langle r^2(t)\rangle = \frac{1}{N}\sum_{i=1}^{N} ||\vec{r}_i(t) - \vec{r}_i(0)||^2 \,, \tag{2.15}$$

where $\vec{r_i}$ is the position of atom i. This approach unveils two key phases. In early intervals, MSD displays a quadratic relationship with time, signifying a ballistic motion. Over time, a seamless shift occurs to the linear Fickian regime [203]. Operating as a measure of atom mobility, MSD embodies a complex interplay of forces governing atomic movement. In the initial phase, atoms move with minimal interaction-induced disruption, yielding quadratic trajectories. However, the forces arising from interactions with the surrounding atoms act on the ions, restraining them and interrupting their free movement.

This complex motion leads to the establishment of the Fickian regime, echoing the fundamental principles of random walk and Brownian motion. MSD analysis tracks the balance between free movement and collision-induced reorientation. Understanding atomistic mobility in different materials provides valuable insights into their transport properties, crucial for material design and technological advancement.

At long times, when the MSD gets to the Fickian regime, we can use it to calculate the self-diffusion coefficient of the atoms with the following equation:

$$D = \lim_{t\to\infty} \frac{\langle r^2(t)\rangle}{2dt}, \tag{2.16}$$

where d is the number of dimensions available for the movement of the atoms, 3 in our case. The self-diffusion coefficient is a crucial parameter for understanding transport phenomena in materials science and engineering. It quantifies how fast individual particles spread through a substance via random thermal motion, crucial for understanding molecular transport in various fields as it is a direct measure of the mobility of the particles. The conductivity of the system can be calculated using the Nernst-Einstein relation [204], which is a common approach in MD simulations as it is a good approximation at low concentrations [205]:

$$\sigma = \sum_{i}^{N} \frac{n_i q_i^2 D_i}{k_B T}, \tag{2.17}$$

where n_i is the concentration of ions i, q_i is their charge, k_B is the Boltzman constant and T is the temperature in kelvin. Conductivity measures a material's ability to transmit electric or thermal energy. It reflects the substance's capacity for efficient electron or heat flow. Conductivity in electrolytes profoundly influences battery performance by determining ion mobility and overall energy transfer efficiency. That is the reason why in this thesis we are so interested in studying this particular property.

The transference number measures the proportion of conductivity given by each sign of the charges either positive or negative, with respect to the total conductivity. It can be calculated by the equation:

$$t_i = \frac{\sigma_i}{\sigma_i + \sigma_{-i}}, \tag{2.18}$$

where t$_i$ is the transference number of charges i with $-i$ counterions. σ_i is the partial conductivity of the i type of ions. In our simulations this is equivalent to dividing the autocorrelation diffusion coefficient of the i ions by the sum of the individual diffusion coefficients of both ions.

2.6 Structural properties

Structural properties play a vital role in understanding the properties of matter. Through simulations, we gain the ability to explore the intricate details of these materials at the atomic level. This computational advantage allows researchers to directly assess material structural properties, which differs from relying solely on indirect experimental techniques. These structural features show strong connections with other material traits, often forming the basis for influencing various properties, including dynamic behaviors. This underscores the significant importance of investigating structural properties and establishing links between these and dynamic features, ultimately revealing how the system behaves as a whole.

2.6.1 Radial distribution function

The radial distribution function, also known as the pair correlation function or $g_{ij}(r)$, is a fundamental tool in the characterization of the local structure of liquids, where the absence of long-range order makes traditional crystallographic methods impractical. The $g_{ij}(r)$ quantifies the probability of finding a particle of type j at a distance r from a reference particle of type i. In essence, it measures the distribution of interatomic distances and is calculated by dividing the number of pairs of particles of types i and j separated by a distance r by the number of pairs that would be expected in a uniform distribution:

$$g_{ij}(r)4\pi r^2 dr = \frac{\langle N_{ij} \rangle}{\rho_j}, \tag{2.19}$$

where N_{ij} is the number of particles of type j in a spherical shell of thickness dr centered around a particle of type i, and ρ_j is the density of particles of type j in the system. The factor $4\pi r^2$ represents the surface area of the shell at a distance r from the reference particle and multiplied by dr it gives us the volume of the shell.

The radial distribution function is typically determined by computing the distances between all pairs of particles and binning them into a histogram. Even though the $g(r)$ contains information on both short and long-range correlations, the most useful information is often contained in the initial peaks of the function, which correspond to the first shell of neighboring atoms.

2.6.2 Coordination number

The coordination number (C_i^j) is another important measure of local structure, defined as the number of first-nearest neighbors of type j around particles of type i. The C_i^j can be calculated from the RDF by integrating the distribution of atoms up to the first minimum of the $g_{ij}(r)$, which corresponds to the first coordination shell:

$$\mathrm{C}^j(i) = \int_0^{r_{min}} 4\pi r^2 \rho_j g_{ij}(r) dr, \tag{2.20}$$

where r_{min} is the distance at which the first minimum of $g(r)$ occurs. The coordination number provides valuable insight into the packing and bonding of atoms in a material, and is particularly relevant in the context of solid electrolytes, where the coordination environment of the mobile ions can strongly affect the ionic conductivity.

2.6.3 Gyration radius

The gyration radius, often denoted as R_g, is a measure of the average distance of particles in a system from their center of mass while they are undergoing rotational motion. It is commonly used in the context of particles or molecules that have some sort of rotational symmetry, such as macromolecules or polymers like in our case.

In a polymer chain, the gyration radius helps characterize the overall size and shape of the molecule in a given solvent or environment. It is calculated based on the root mean square distances of individual particles within the molecule from the molecule's center of mass, based on this equation:

$$R_g = \sqrt{\frac{1}{N}\sum_{i=1}^{N} m_i(\vec{r}_i - \vec{r}_{\text{com}})^2}, \tag{2.21}$$

where N is the total number of particles in the system, $\vec{r}_i$ is the position vector of the i-th particle, m_i corresponds to its mass and $\vec{r}_{com}$ is the position vector of the center of mass of the system.

The gyration radius R_g, serves as a scalar measure that characterizes the size and shape of polymers. However, a comprehensive understanding and accurate representation of this value requires considering its orientation as well.In computer simulation programs like LAMMPS, when calculating the gyration radius, a R_g tensor is typically generated and stored as a 6-element vector. The formula of the components of the tensor is the same than 2.22 except that $(|\vec{r}_i - \vec{r}_{\text{com}}|)^2$ is replaced by the cross-terms:

$$R_{g,\alpha\beta} = \sqrt{\frac{1}{N}\sum_{i=1}^{N} m_i(\vec{r}_{i,\alpha} - \vec{r}_{\text{com},\alpha}) \cdot (\vec{r}_{i,\beta} - \vec{r}_{\text{com},\beta})}, \tag{2.22}$$

where α and β represent the x, y, z components.

In order to give orientation to R_g , a viable approach involves diagonalizing the R_g tensor. Upon diagonalization, the direction associated with the largest eigenvalue becomes the principal orientation of the polymer. By employing this principal eigenvector and multiplying it by the gyration radius, we can visualize the R_g of the polymer and amplify it, thus effectively depicting both the magnitude and orientation graphically. This pragmatic approach offers a more insightful perspective on polymer orientation compared to a straightforward R_g calculation.

2.7 Summary

In this chapter, we underscored the significance of computational methods, particularly Molecular Dynamics (MD), which serves as the foundation of our work. We gave an introduction to the theory behind MD and the use of the OPLS-AA force field. Minor alterations in these values can significantly impact system behavior, as they dictate interatomic forces and atom identity.

We also detailed the protocol tha we have used for simulating the HSE simulations by MD methods, highlighting the importance of proper initialization to mitigate issues and avoid potential meta-stable phases.

Lastly, we have discussed the crucial dynamical and structural properties essential for a comprehensive understanding and characterization of hybrid polymeric systems using MD techniques.

Chapter 3

Hybrid Solid Electrolytes: Silica Nanoparticles - Structure

3.1 Introduction

Hybrid solid electrolytes are a promising choice for future battery systems, particularly in the context of Generation 4a battery technology [46, 55, 206, 207]. Using solid materials like polymers and ceramics as electrolytes offers two significant advantages. Firstly, it enhances safety by eliminating the risk of flammability associated with liquid electrolytes. Secondly, solid materials effectively prevent dendrite formation, a critical issue in battery technology [46], as dendrites can severely impact battery performance.

However, solid polymer electrolytes introduce a new challenge: lower ionic conductivity compared to liquid electrolytes [25] and As we discuss in chapter 1.1, high ionic conductivity is a critical attribute for any electrolyte as it afects the speed of charging and discharging, the power density and the battery cycle life [207].

In the upcoming sections, we examine a specific category of materials: hybrid solid electrolytes comprising three components - PEO (polyethylene oxide) as the polymer, LiTFSI (lithium bis(trifluoromethanesulfonyl)imide) as the salt, and silica as ceramic nanoparticles. The objective of integrating ceramic fillers into the polymeric electrolyte to form hybrid materials is to enhance conductivity compared to pure SPEs. In the case of SiO_2, this ceramic serves as a passive filler, expected to contribute positively to conductivity despite its non-conductive behaviour.

The impact of ceramics on conductivity remains uncertain, as discussed in section 1.4, due to conflicting literature findings. Assuming passive fillers enhance conductivity, two potential mechanisms are proposed: Firstly, ceramic nanoparticles reduce the crystallinity of semi-crystalline polymers like PEO [53]. Secondly, nanoparticles may create a space-charge region at the interface between nanoparticles and the solid polymer electrolyte [41]. However, this second mechanism remains a hypothesis and requires further investigation for validation.

The main goal of this section is to confirm the existence of the hypothesized space-charge region and to explore the dependence of the system on various factors such as temperature, ionic concentration, and nanoparticle concentration.

This chapter focuses exclusively on the structural properties of the HSE:PEO+LiTFSI+SiO_2 systems. The next chapter will provide an analysis of the systems' dynamics and associated data.

3.2 Simulation Details

To investigate the structural features, we employed the LAMMPS software, applying periodic boundary conditions in all three spatial dimensions. Nonbonding terms in equations 2.8 and 2.9 were truncated with a cutoff distance of 10 Å. Long-range Coulombic interactions were computed using a particle-particle particle-mesh solver (PPPM) with a relative accuracy of 10^{-4}. Interactions within the macro-molecules were treated as described in section 2.3, employing weighting coefficients. The charges and LJ parameters of the force field are summarized in table 5.1, and the intramolecular terms can be found in the supplementary materials.

All simulations were run at 600K, unless otherwise specified. This temperature choice was motivated by the need to exceed the melting temperature (T_m) of PEO, which is approximately in the range of 55°C to 70°C [208]. There are two primary reasons for this temperature selection. The foremost reason is to simplify the analysis: we aimed to operate above the melting point to distinguish the influence of the nanoparticle at the interface and the possible formation of a space-charge region, while avoiding the effects of nanoparticles on the crystallinity, as discussed in this section's introduction

The second reason is technical. Molecular dynamics techniques encounter challenges when simulating semi-crystalline polymers. Typically, polymer research focuses on the amorphous phase because MD techniques are optimized for modeling liquid-like behavior and readily initializing disordered polymers. However, simulating semi-crystalline materials is more complex. One approach is to begin with a disordered material, lower the temperature, and allow it to reorganize [209]. However, this process requires macroscopic timescales, ranging from seconds to even longer, depending on the conditions, far exceeding the typical nanosecond timescales of classical MD simulations. Therefore, working with semi-crystalline materials poses challenges that are time-consuming, which is a crucial consideration in all computational studies.

The choice of 600K, well above T$_m$, was made to ensure a substantial margin from the melting point while permitting the system to diffuse into the Fickian regime as rapidly as possible.

3.3 Results

The radial distribution function (RDF) is a crucial structural property in liquid and amorphous materials (liquid-like systems), offering insights into atomic short-range order. It examines atomic organization around a specific element, revealing distances to neighboring atomic species, with the number of neighbors proportional to RDF intensity. This function is widely used in molecular dynamics simulations, especially in battery-related research involving polymeric materials [77, 210]. Equation 2.19 defines the RDF, quantifying the probability of locating atomic species 'j' at distance 'r' from central atomic species 'i,' normalized by $4\pi r^2\rho_j$.

The radial distribution function can be easily calculated in molecular dynamics and other simulation techniques. It is connected to experiments through the structure factor S(q) [211], which can be obtained by Fourier-transforming the g(r) function, as shown in equation 3.1.

$$S(q) = \rho \int h(r) e^{-i\vec{q}\vec{r} dr} \tag{3.1}$$

where $\vec{q}$ is the wave vector and $h(r)$ is equal to $g(r) - 1$. S(q) is an experimentally extractable quantity, typically obtained using techniques such as X-ray or neutron scattering. S(q) provides valuable information about the spatial arrangement of particles in the material, including details about interparticle correlations and density fluctuations. This relationship between RDF and S(q) is crucial as it allows researchers to bridge the gap between simulation data and experimental observations, providing a deeper understanding of the material's structural properties and aiding in the validation of simulation results.

The coordination number (CN) quantifies the count of first neighbors surrounding a particle, enabling comparisons of neighbor ratios around specific elements in the simulations [212, 213, 128, 77]. Like the RDF, CN is a well-established metric in computational investigations. It can be obtained directly from simulations by counting atoms around a particular species or deduced from the RDF by integrating the RDF curve from 0 to the first minimum and multiplying by the normalizing factor, $4\pi r^2\rho_j$, as shown in equation 2.20.

Both RDF's and their respective CN values can be directly computed using LAMMPS, thereby serving as the primary computational tool. However, LAMMPS inherently focuses on atom RDFs. To derive specific parameters, particularly those related to nanoparticle center-of-mass calculations, a custom Python program, developed inhouse, was employed.

In this chapter, we present the results related to the structural properties of the electrolyte, specifically the HSE:PEO+LiTFSI+SiO_2 system. The findings are organized into five sections:

1. Overview of the electrolyte's components.
2. Temperature-dependent structural changes.
3. Effects of nanoparticle concentration on structural properties.
4. Influence of ionic concentration on the structure of the electrolyte.
5. Detailed analysis of nanoparticle surface properties.

Finally, we will summarize the conclusions drawn from these results at the end of the chapter.

3.3.1 General structure of the electrolyte

Lithium

Lithium exhibits strong coordination with the oxygen atoms of PEO. The coupling between these two atom types prevents the addition of other atoms to the first shell of lithium's neighbors. Consequently, TFSI and lithium are nearly completely decoupled, underscoring PEO's high solvation capabilities for this salt. On the other hand, the interaction between lithium and silica is quite weak, as lithium does not tend to approach silica closely.

Figure 3.1 depicts the radial distribution function (RDF) describing lithium ion neighbors under the following conditions: 600K temperature, 10% SiO_2 volume fraction, and a 3.2 Li:PEO ion concentration, equivalent to 2 mol/L. These conditions will remain consistent throughout the subsection.

Notably, the two radial distribution functions of O_{PEO} centered around Lithium, $g^{O_{PEO}}Li(r)$ exhibit the shortest inter-atomic distances. Specifically, $g^{O_1}Li(r)$ displays a first maximum at $r = 1.95$, while $g^{O_2}Li(r)$ shows a similar peak at $r = 2.05$. These interactions also feature the highest intensity among all peaks, with values of $I = 35.1$

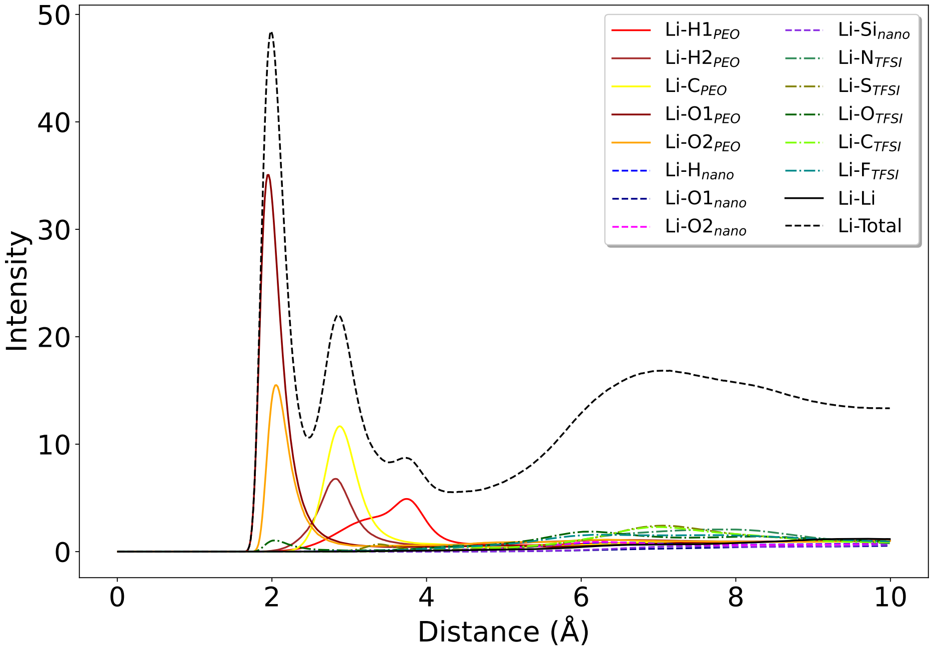

Figure 3.1: Radial distribution function depicting the distribution of all atomic species centered around Lithium. The black dashed line represents the cumulative distribution of all individual curves. The curves corresponding to different molecular components are represented by different line styles: PEO molecules (solid), SiO_2 (dashed), TFSI molecules (dash-dot), and lithium ions (solid black). Notably, the red and orange curves reveal the strong coordination between lithium and PEO oxygen atoms.

and $I = 15.5$, respectively, in line with previous studies like [77, 214]. These strong, sharp peaks suggest a significant coupling between lithium and O_{PEO}.

Additionally, the graph illustrates lithium's coordination with other atom types within the PEO structure, such as carbon and hydrogen, which also exhibit significant coordination with lithium, although at greater distances compared to oxygen. The coordination of lithium with its counterion is limited to a small peak involving O_{TFSI} in the first shell at a close distance of $r = 2.05$Å, but its intensity is negligible compared to the coordination with PEO.

In conclusion, lithium ions primarily associate with oxygen atoms from PEO, as evidenced by the pronounced peaks in their correlations. Furthermore, the presence of a smaller peak attributed to O_{TFSI} in close proximity to lithium suggests an affinity between lithium ions and oxygen atoms from TFSI. However, due to the preferential bonding of lithium ions to PEO, only a limited number of O_{TFSI} atoms can closely approach Li^+.

Polyethylene Oxide

PEO exhibits strong interactions with lithium ions, with its oxygen bonding tightly with them. While PEO also interacts with other polymeric atoms, it does not engage in significant interactions with elements other than lithium within the simulations.

Figure 3.2(a) shows the average RDF for all atoms in the PEO structure, while Figure 3.2(b) focuses on the RDF of oxygen atoms, which are highly coordinated in the electrolyte. In Figure 3.2(b), a sharp peak at a short distance with lithium ions is evident, confirming our previous observations in Figure 3.1. Other notable peaks correspond to oxygen atoms within the PEO chain, which are also closely associated with lithium ions. Hydrogen atoms show less intense peaks but remain in close proximity to the oxygen.

In Figure 3.2(a), oxygen curves are visible in the overall RDF functions. Notably, the intensity of the lithium-oxygen curve decreases significantly when viewed in the context of the entire RDF function $g_{\mathrm{PEO}}^{\mathrm{Li}}(\mathrm{r})$. This reduction is expected because PEO oxygens make up only a fraction, specifically 21/143, of the total PEO atoms. Nevertheless, this peak remains the most prominent and is located at the closest distance.

In the case of the $g_{\mathrm{PEO}}^{\mathrm{Li}}(\mathrm{r})$ curve, two extra peaks appear, likely due to hydrogen and carbon atoms near oxygen atoms. Other interactions in Figure 3.2(a) involve various PEO atoms, similar to the oxygen interactions.

In summary, the densely packed PEO structure primarily accommodates lithium ions, forming strong bonds with oxygen atoms. The other atom species within the polymer also make significant contributions to the PEO coordination sphere, as they account for over 5/7 of the simulation's atoms. In contrast, the other molecules in the simulation, TFSI and SiO_2, do not exhibit close coordination with PEO.

The connection between PEO and lithium can be explained by considering how PEO solvates TFSI, a concept supported by relevant literature [212, 213, 128, 77]. A visual analysis in Figure 3.3 further clarifies this mechanism. Essentially, the ionic bonding between lithium and TFSI is relatively weak due to TFSI's larger molecular size and charge delocalization. This characteristic allows PEO to surround lithium with its oxygen atoms, creating a stronger binding than the one between lithium and TFSI oxygen atoms. As a result, PEO effectively separates lithium from its counterion and becomes attached to it.

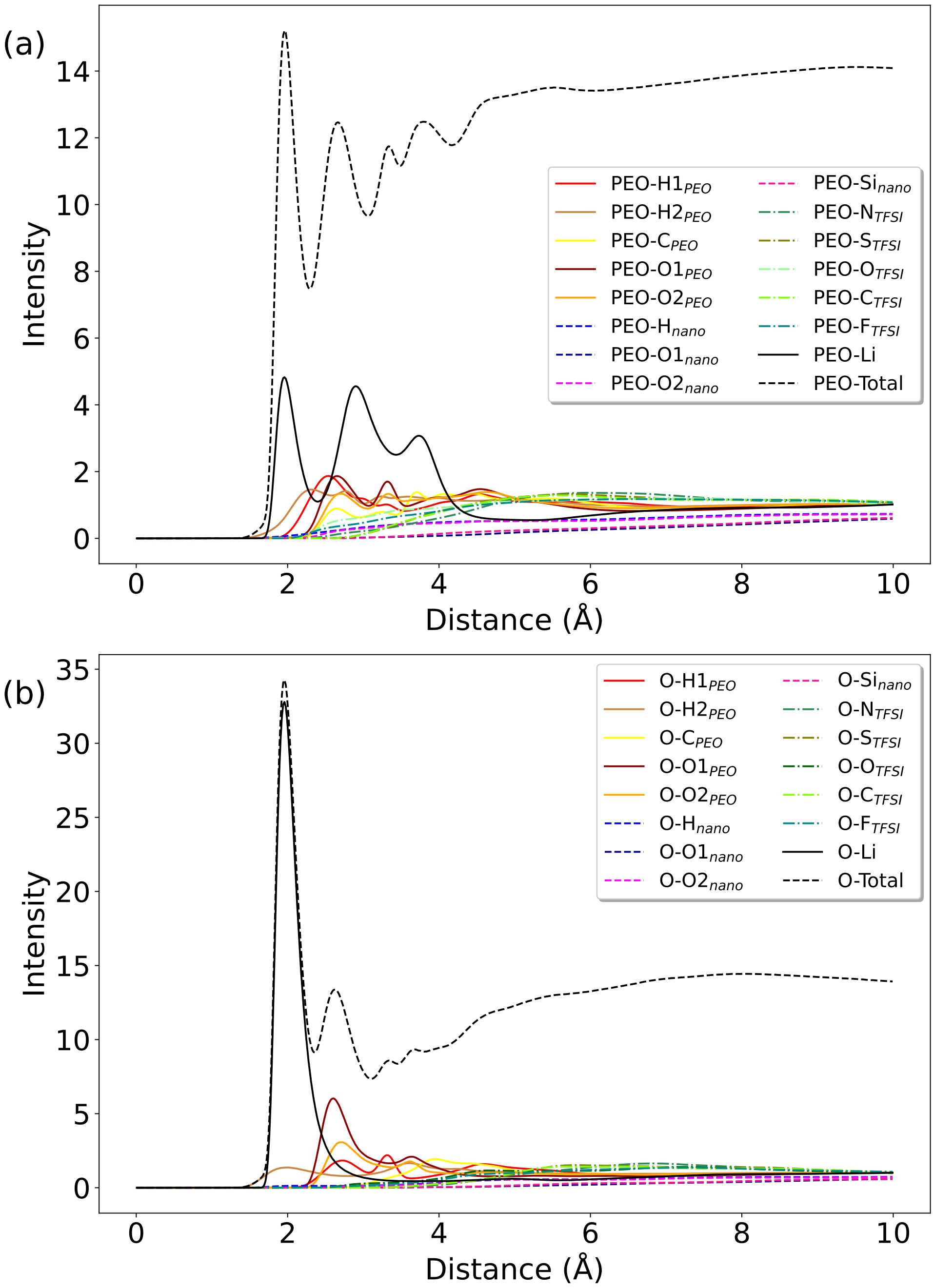

Figure 3.2: (Top) Radial distribution function depicting the distribution of all atomic species centered around PEO atoms, and (Bottom) centered around $O1_{\mathrm{PEO}}$. The black dashed line represents the cumulative distribution of all individual curves. The curves corresponding to different molecular components are represented by different line styles: PEO molecules (solid), SiO_2 (dashed), TFSI molecules (dash-dot), and lithium ions (solid black). Notably, in the lower case, the solid black curve stands out, corresponding to the lithium ions. This observation complements what was observed in Figure 3.1 and demonstrates a strong interaction between Li and O_{PEO}.

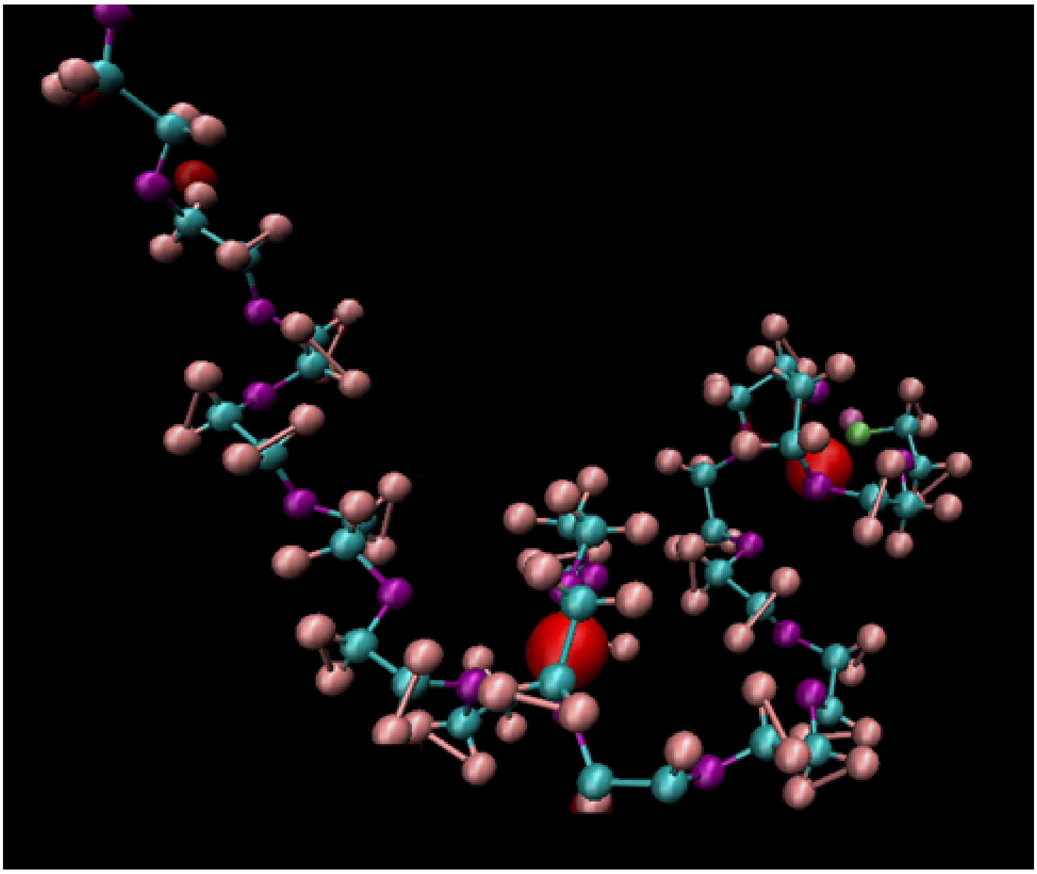

Figure 3.3: Visual representation created using VMD software, showing a single PEO chain and two Lithium atoms. The snapshot illustrates the PEO chain surrounding the two Lithium ions with its oxygen atoms, highlighting the solvation of LiTFSI salt in PEO. The elements represented in the figure are lithium (red), oxygen (purple), carbon (cyan), and hydrogen (pink).

Silica

The surface of silica is primarily coordinated with TFSI molecules, but these interactions are relatively weak, indicated by the small peak intensities. PEO molecules also cover the silica surface, although their interactions with silica are weaker than those between silica and TFSI.

Figure 3.4 displays the radial distribution function (RDF) curves illustrating the interactions of silica with other atoms present in the simulation. The figure comprises two distinct graphs: Figure 3.4(a) represents the average RDF in the silica surface, made up with the two types of surface atoms in silica, while Figure 3.4(b) exclusively portrays the RDF functions of hydrogen atoms on the silica surface.

Figure 3.4(b) reveals that the most intense peaks are associated with TFSI, indicating a specific interaction order with the nanoparticle: oxygen atoms first, followed by sulfur and nitrogen, while carbon and fluor atoms show more dispersed coordination. This observation suggests a preferred orientation of TFSI when interacting with and enveloping SiO_2. Additionally, interactions involving hydrogen ($g^{H_{PEO}}SiO_2(r)$) and oxygen ($g^{O_{PEO}}SiO_2(r)$) atoms from PEO also exhibit significant coordination within the first shell of neighboring H_{SiO_2}.

In Figure 3.4(a), the TFSI curves exhibit slightly lower intensity and greater delocalization compared to Figure 3.4(b). The closest peaks, representing oxygen atoms, are depicted by $g^{O_{PEO}}_{SiO_2}(r)$ and $g^{O_{TFSI}}_{SiO_2}(r)$. Notably, lithium is situated farther from the surface of the silica nanoparticles in comparison to other atoms.

The findings suggest that silica primarily forms bonds with oxygen atoms, whether they originate from TFSI or PEO molecules. However, oxygen atoms from PEO, denoted as O_{PEO}, predominantly coordinate with lithium ions, as shown earlier, resulting in stronger coordination compared to TFSI interactions. This preference for oxygen atoms can be attributed to the acidic properties of silica. Since the outermost atoms are hydrogen, which carries a positive charge, they tend to bond with the most electronegative atoms in the system, specifically oxygen, while repelling positively charged species like lithium. Additionally, it's important to note that TFSI molecules exhibit a preferred orientation when approaching the silica surface. Most computational studies on PEO-SiO_2 coordination have focused on non-acidic surfaces [215, 216], with limited literature available for direct comparisons in this specific context.

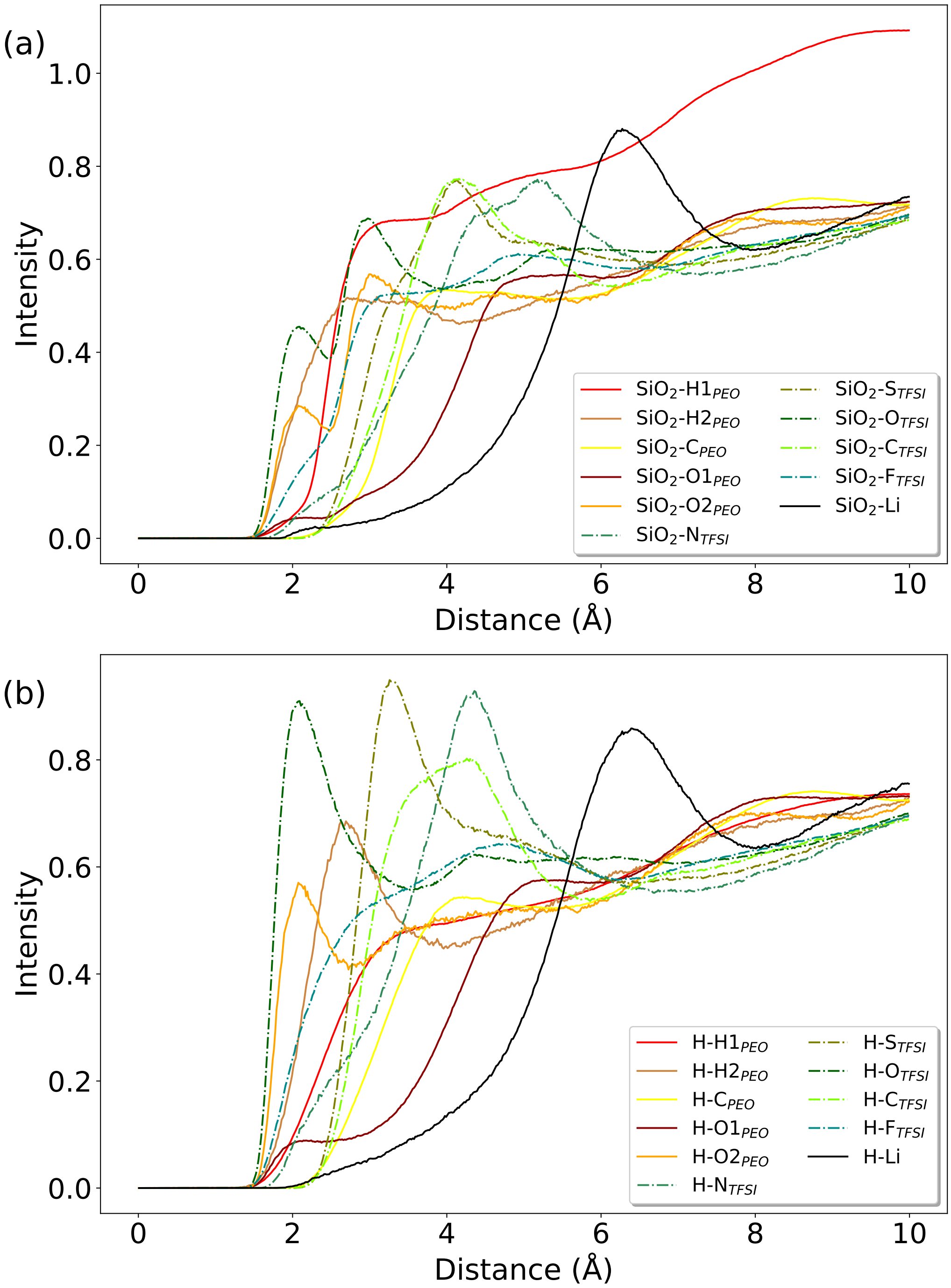

Figure 3.4: (Top) Radial distribution function centered around $H_{SiO_2} + O2_{SiO_2}$ and (Bottom) centered around H_{SiO_2} for all other types of atoms in the simulation. The curves corresponding to different molecular components are represented by different line styles: PEO molecules (solid), TFSI molecules (dash-dot), and lithium ions (solid black).

TFSI

TFSI is mostly coordinated to hydrogen atoms from PEO, as they constitute the matrix of the electrolyte, however, the anions are also coordinated to the hydrogens on the surface of the nanoparticles as well as to the Lithium ions.

Figure 3.5 presents the radial distribution function (RDF) curves illustrating the interactions of TFSI elements with other atoms within the simulation. This figure comprises two distinct graphs: Figure 3.5(a) represents the RDF encompassing all atoms within the TFSI molecule, while Figure 3.5(b) exclusively portrays the RDF functions associated with oxygen atoms within the TFSI molecule.

In Figure 3.5(b), we observe three distinct peaks in the first shell of neighbors at close distances: $\mathrm{g}_{\mathrm{O_{TFSI}}}^{\mathrm{H_{PEO}}}(\mathrm{r})$, $\mathrm{g}_{\mathrm{O_{TFSI}}}^{\mathrm{Li}}(\mathrm{r})$, and $\mathrm{g}_{\mathrm{O_{TFSI}}}^{\mathrm{H_{SiO_2}}}(\mathrm{r})$, positioned at $r = 2.00$Å, $r = 2.05$Å, and $r = 2.10$Å, respectively. The remaining peaks in the graph correspond to atoms bonded to those in the first shell. Notably, there is a second, significantly higher peak representing lithium at a distance of $r = 6.10$Å. This coordination at a further shell of neighbors surpasses the intensity of all other interactions, indicating a secondary-order coordination.

Figure 3.5(a) presents a notably diffuse structure in comparison to pure $\mathrm{O_{TFSI}}$.While the order of the peaks in the curves remains consistent, they appear more delocalized. However, Lithium stands as an exception, demonstrating a distinct organization into various coordination shells. It shows a small but clear and sharp peak at short distances, suggesting a noticeable yet not very intense binding. Additionally, a second shell at greater distances is marked by a significantly more intense peak.

Understanding the structural organization of these materials is a complex task, especially in the case of TFSI. TFSI is a molecule characterized by a triangular structure with atoms exhibiting substantial charge disparities, resulting in a polar structure. Analysis of its RDF curves suggests that TFSI tends to approach positively charged atoms, such as the hydrogen atoms on the silica surface ($\mathrm{g}_{\mathrm{O_{TFSI}}}^{\mathrm{H_{SiO_2}}}(\mathrm{r})$) and those within the polymer ($\mathrm{g}_{\mathrm{O_{TFSI}}}^{\mathrm{H_{PEO}}}(\mathrm{r})$). However, the sharpness of the $\mathrm{g}_{\mathrm{O_{TFSI}}}^{\mathrm{Li}}(\mathrm{r})$ curve highlights the strong preference for the $\mathrm{O_{TFSI}} - \mathrm{Li}$ interaction, particularly with oxygen atoms within TFSI. Nonetheless, due to the strong correlation between lithium atoms and the oxygen atoms of PEO, TFSI molecules have limited access to lithium ions. The presence of a second peak in the $\mathrm{g}_{\mathrm{O_{TFSI}}}^{\mathrm{Li}}(\mathrm{r})$ curve indicates that TFSI molecules are typically intertwined within the PEO matrix, primarily surrounded by them. Since lithium atoms are typically bonded to the PEO structure, as illustrated in Figure 3.3, they form a second coordination shell approximately 6Å away from the TFSI molecules, consistent with findings in ref [217].

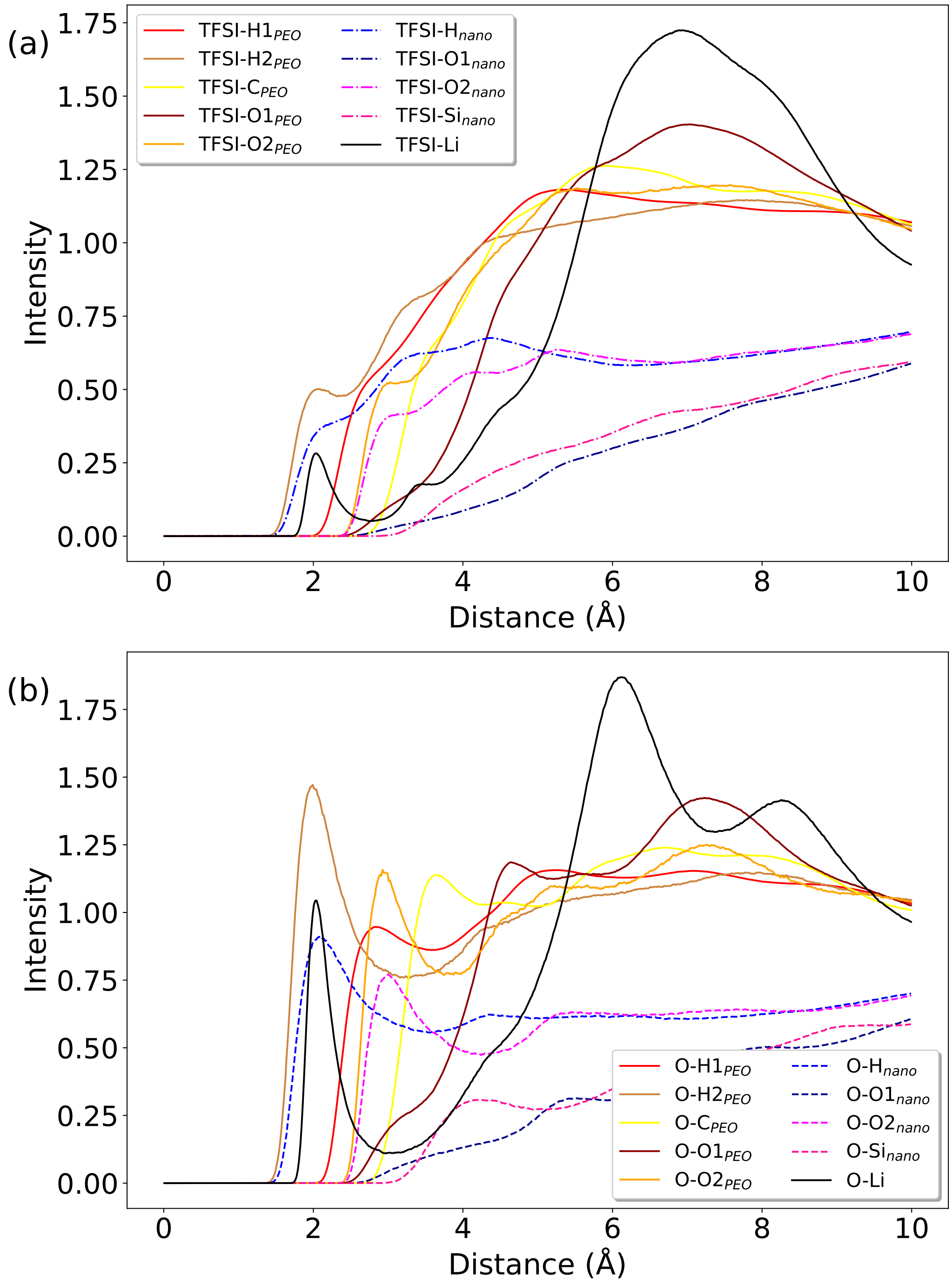

Figure 3.5: Radial distribution function (Top) centered around the atoms of TFSI, and (Bottom) around O_{TFSI} of all the other types of atoms in the simulation. The curves corresponding to different molecular components are represented by different line styles: PEO molecules (solid), SiO_2 (dashed) and lithium ions (solid black).

Detailed analysis: Following sections

In the following sections, we will conduct a detailed analysis of the structure from key atomic interactions within the simulation. This includes an examination of the mean square displacement (MSD) and coordination number (CN) functions for essential structural interactions.

Certain atoms in the system, such as silicon and and carbon atoms in the PEO chain, have passive roles and limited engagement with other particles due to their positions within their respective entities and weak Coulombic interactions. These atoms are not prominently featured in the earlier RDF curves. Therefore, our focus will be on the most relevant atoms, such as lithium, oxygen atoms within TFSI and PEO, as well as surface hydrogen atoms on the nanoparticles.

Analyzing the structural characteristics of these key elements will provide deeper insights into the organization of different molecular species and their specific interactions. These interactions are illustrated in Figure 3.6, representing the following pairs: (a) Li-$\mathrm{O_{PEO}}$, (b) $\mathrm{O_{TFSI}}$-$\mathrm{H_{PEO}}$, (c) Li-$\mathrm{O_{TFSI}}$, (d) $\mathrm{O_{TFSI}}$-$\mathrm{H_{SiO_2}}$, (e) Li-$\mathrm{O_{SiO_2}}$, and (f) $\mathrm{O_{PEO}}$-$\mathrm{H_{SiO_2}}$.

3.3.2 Temperature dependence of the structural properties

Radial distribution function

Figure 3.7 describes the variation with temperature of the radial distribution function of the most relevant interactions in the system. Each graph within the figure corresponds to a distinct interaction, with temperatures ranging from 300K to 1000K at an ionic concentration of 3.2 Li:PEO and with a nanoparticle concentration of 10% Vol.

Temperature alters the lithium coordination shell, diminishing its bonding with PEO in favor of strengthening lithium's coordination with TFSI. This interaction between the two ionic species is the only one that intensifies with temperature, while all other interactions decrease in intensity.

In Figure 3.7(a), we zoom in on the RDF of PEO oxygen atoms centered around Lithium, specifically focusing on the first shell. As temperature increases, the intensity of the first maximum in $\mathrm{g_{Li}^{O_{PEO}}}$ decreases consistently. The highest intensity decreases from 37.1 at 300K to 29.8 at 1000K, and the distance shrinks from 1.98Å at 300K to 1.94Å at 1000K.

In Figure 3.7(b), we analyze the $\mathrm{g_{H_{PEO}}^{O_{TFSI}}}$ functions and their temperature-dependent changes. A notable trend is the increased delocalization as temperature rises. At 300K, the RDF exhibits three distinct maximums at distances of 2.7Å, 5Å, and 7Å. However, with higher temperatures, the system becomes more disordered. By 500K,

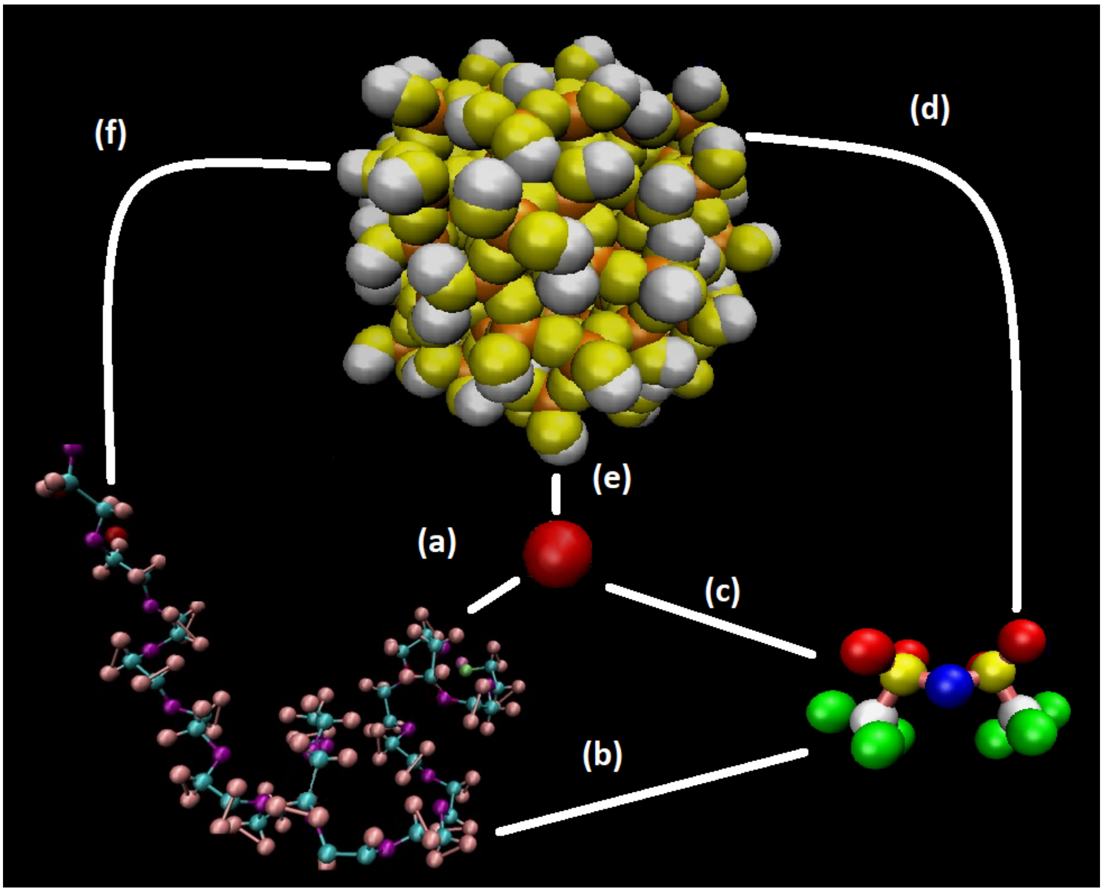

Figure 3.6: Schematic representation in VMD software displaying the four types of molecules and their respective coordinations. Lithium-PEO/Li-O_{PEO} (a), TFSI-PEO/O_{TFSI}-H_{PEO} (b), lithium-TFSI/Li-O_{TFSI} (c), TFSI-SiO_2/O_{TFSI}-H_{SiO_2} (d), lithium-SiO_2/Li-O_{SiO_2} (e) and PEO-SiO_2/O_{PEO}-H_{SiO_2} (f). These 6 interactions are the ones that we are going to focus on during the whole thesis.

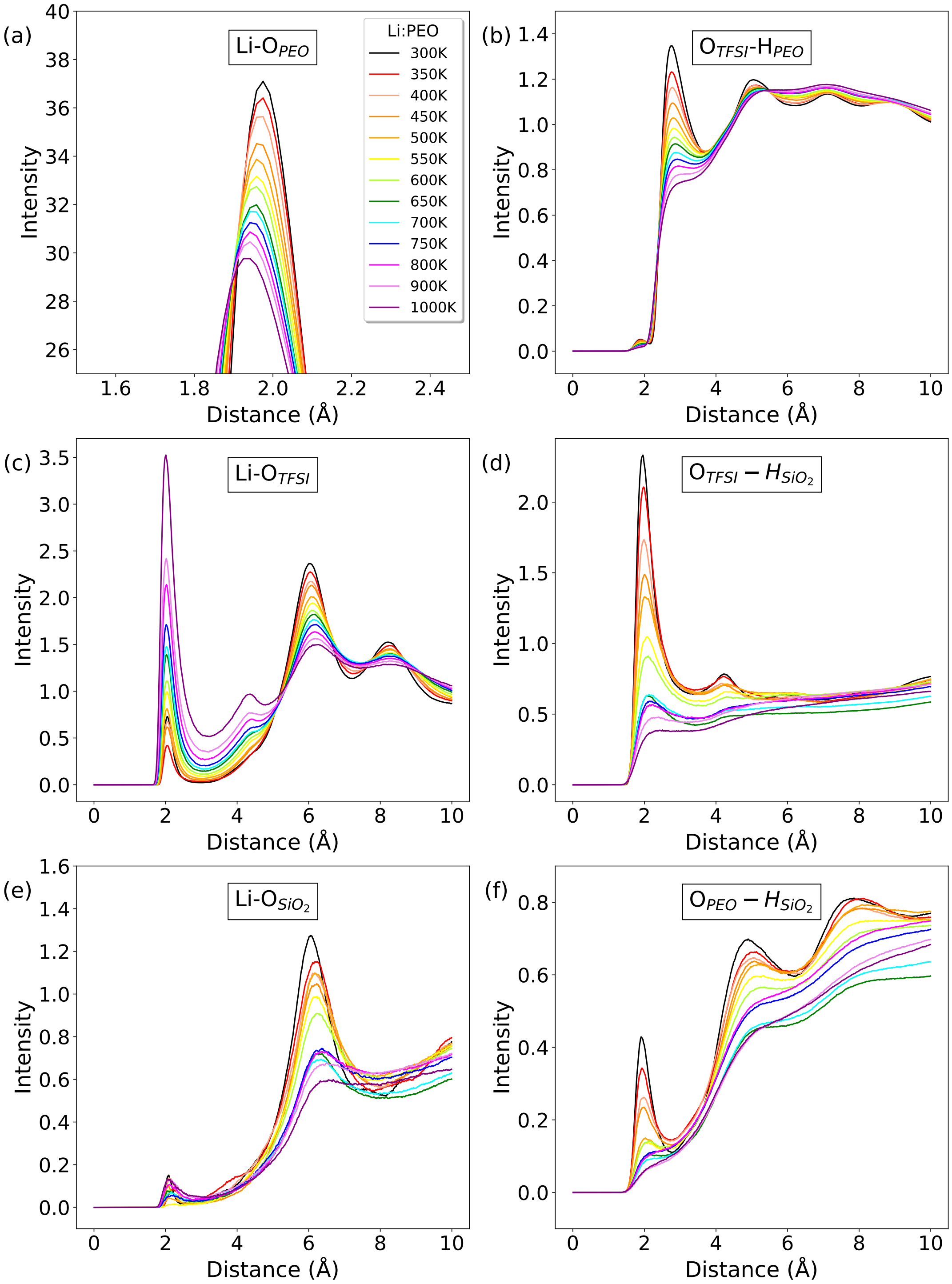

Figure 3.7: Radial distribution function curves were computed for the interactions shown in figure 3.6, including: (a) lithium and O_{PEO}, (b) O_{TFSI} and H_{PEO}, (c) lithium and O_{TFSI}, (d) O_{TFSI} and H_{SiO_2}, (e) lithium and O_{SiO_2}, and (f) O_{PEO} and H_{SiO_2}. These calculations were performed over a temperature range spanning from 300K to 1000K at an ion concentration of 3.2 Li:PEO and with a nanoparticle concentration of 10% Vol.

it's challenging to distinguish the second and third peaks, and the intensity of the first coordination shell decreases significantly. At 1000K, the interaction becomes highly delocalized.

Figure 3.7(c) displays the $\mathrm{g_{Li}^{O_{TFSI}}(r)}$ interaction. Unlike the lithium-polymer RDF, here, the first peak of $\mathrm{g_{Li}^{O_{TFSI}}}$ strengthens with rising temperature, while the second peak at $r = 6$Å weakens. This indicates an increased number of $\mathrm{O_{TFSI}}$ ions on the first lithium coordination shell. This change can be attributed to increased ion mobility at higher temperatures. As temperature rises, ions gain kinetic energy, making it easier for the TFSI to diffuse and approach lithium ions. This results in a reorganization of oxygen atoms in the first lithium coordination shell, with less $\mathrm{O_{PEO}}$ and more $\mathrm{O_{TFSI}}$ shifting from a distance of $r = 6$Å to $r = 2$Å. Notably, temperatures above 750K reveal a new peak between the first and 6Å shell, likely due to oxygen atoms within the same molecule unable to approach lithium ions due to increased atomic spacing.

Regarding the $\mathrm{g_{O_{TFSI}}^{H_{SiO_2}}(r)}$ interaction, Figure 3.7(d) exhibits a behavior similar to that of $\mathrm{g_{H_{PEO}}^{O_{TFSI}}(r)}$. At low temperatures there is a strong coupling between the silica surface and $\mathrm{O_{TFSI}}$, but this coupling diminishes significantly with increasing temperature, with near decoupling occurring at 550K. At 1000K, no clear first minimum is evident, indicating complete decoupling between TFSI ions and the silica surface, a contrast to the behavior observed at lower temperatures

In Figure 3.7(e), we examine the lithium-$\mathrm{H_{SiO_2}}$ interaction centered around lithium. The weak interaction at low distances remains stable in intensity and position with temperature changes. However, the second shell at around $r = 6$Å decreases to less than half its initial value and shifts slightly outward, consistent with repulsive interactions.

In Figure 3.7(f), we investigate the interaction between $\mathrm{O_{PEO}}$ and $\mathrm{H_{SiO_2}}$. As temperature rises, we observe increased delocalization in the second and third shells. In the first shell, we initially see a weak but discernible coupling at low temperatures, but, similar to Figure 3.7(d), this coupling disappears at higher temperatures. This indicates that the PEO-silica attachment weakens with increasing temperature.

We will summarize these results together with the coordination number analysis in the conclusions subsection.

Coordination Number

The coordination number, denoted as $\mathrm{C^j(i)}$, quantifies the number of first neighbors surrounding a central particle. It encompasses the particles within the sphere extending from distance zero to the first minimum of the $\mathrm{g}_i^j(r)$ curve. To maintain consistency, we use the same first minimum distance for all $\mathrm{C^j(i)}$ values with identical i and j elements. This approach is necessary because the first minimum distance can vary across temperatures, and at high temperatures, some curves lack a well-defined first minimum.

Figure 3.8 displays coordination numbers for the atomic interactions analyzed in the radial distribution function (RDF) study. It provides quantitative insights into first-shell atomic coordinations, corroborating our earlier RDF findings. Temperature primarily enhances the coordination between lithium and TFSI, whereas coordination decreases in most other cases.

In Figure 3.8(a), $\mathrm{C}^{\mathrm{O}_{\mathrm{PEO}}}(\mathrm{Li})$ shows a gradual decline in coordination number as temperature increases. The coordination reduces from approximately 5.5 atoms at 300K to around 4.75 at elevated temperatures, suggesting a sustained attachment between lithium ions and PEO despite temperature variations.

In Figure 3.8(b), $\mathrm{C}^{\mathrm{H}_{\mathrm{PEO}}}(\mathrm{O}_{\mathrm{TFSI}})$ is depicted, revealing a significant decrease in coordination number with increasing temperature. Starting at 6 coordinated atoms at 300K, it declines to approximately 2.5 at higher temperatures. This decline implies a weakening interaction between $\mathrm{H}_{\mathrm{PEO}}$ and $\mathrm{O}_{\mathrm{TFSI}}$ as kinetic energy rises, enabling greater mobility for TFSI ions.

In contrast to the previous curves, Figure 3.8(c) shows a significant increase in the coordination number for $\mathrm{C}^{\mathrm{O}_{\mathrm{TFSI}}}(\mathrm{Li})$ data. Although the coordination numbers in this graph are smaller than those in 3.8(b), it is worth noting that PEO atoms are the most abundant in the system. What is crucial here is the approximately 4.5-fold enhancement in the coordination value. This substantial increase in coordination between these two atoms stems from the reduction in the $\mathrm{C}^{j}(i)$ of both ions when interacting with the polymer. The elevated temperature weakens the bonding between Li and $\mathrm{O}_{\mathrm{PEO}}$, making it easier for TFSI to interact with lithium ions. While lithium ions are primarily bound to PEO, the marginal 0.5 reduction in their coordination with PEO is nearly compensated by their enhanced coordination with TFSI.

The curve in Fig. 3.8(d) represents $\mathrm{C}^{\mathrm{H}_{\mathrm{SiO}_2}}(\mathrm{O}_{\mathrm{TFSI}})$. It shows a reduction of the coordination intensity as temperatures rise. The weak interaction between these components enables TFSI ions to decouple from the nanoparticle's surface at higher temperatures, aided by enhanced coordination among ionic species.

The $\mathrm{C}^{\mathrm{O}_{\mathrm{SiO}_2}}(\mathrm{Li})$ interaction, shown in Figure 3.8(e), remains negligible across the entire temperature range, indicating that lithium ions do not exhibit a tendency to approach the silica surface.

Finally, Figure 3.8(f) highlights a fast loose of coordination between oxygen atoms of PEO and the silica surface. Similar to Figure 3.8(d), the interactions between oxygen atoms and the silica surface lack the strength to maintain coordination at high

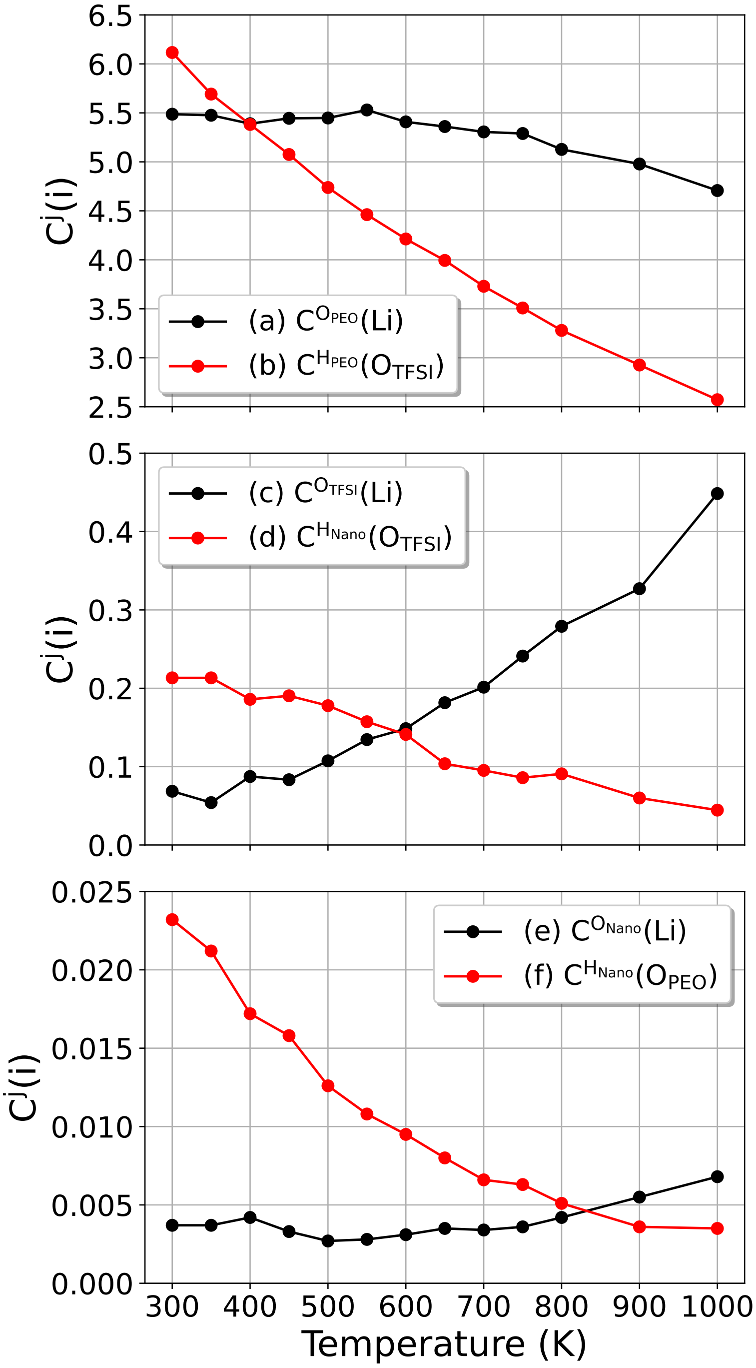

Figure 3.8: Coordination number curves ($C^j(i)$) as a function of temperature for various interactions: (a) Li-O_{PEO}, (b) O_{TFSI}-H_{PEO}, (c) Li-O_{TFSI}, (d) O_{TFSI}-H_{SiO_2}, (e) Li-O_{SiO_2}, and (f) O_{PEO}-H_{SiO_2}. The analyses were conducted at temperatures ranging from 300K to 1000K with 3.2 Li:PEO ion concentration and 10% Vol nanoparticle concentration. All coordinations, except (c) $C^{O_{TFSI}}(Li)$, decrease with rising temperature due to increased kinetic energy. Curve (c) compensates for a coordination loss, similar to that observed in curve (a)."

temperatures.

Conclusions

As temperature rises, excess kinetic energy leads to a delocalization effect among the interactions that define the electrolyte's structure. Weaker atomic couplings vanish at higher temperatures as atoms overcome their energy barriers. Only the stronger interactions endure throughout the temperature range. silica attracts negatively charged particles, mainly oxygens from PEO and TFSI. However, the forces that bind these oxygens to the positively charged hydrogens on the silica surface are relatively weak. This is due to the small individual charge of hydrogen and its inflexible structure, limiting efficient atom capture. Consecuently, silica interactions weaken, leading to reduced coordination numbers with temperature. Regarding PEO, all coordination numbers decrease except for lithium, which maintains a high coordination due to its strong interaction force with O_{PEO}

As kinetic energy increases, PEO becomes more mobile, creating additional free space around it and reducing coordination with other elements. Lithium ions maintain strong interactions with PEO while also attracting TFSI molecules. With increased available space due to PEO's enhanced mobility, anionic molecules replace PEO in the first coordination shell around lithium ions. This shift brings TFSI molecules closer to lithium, reducing their coordination numbers with other molecules in the system.

The number of atoms in the first coordination shell around lithium remains nearly constant across the entire temperature range. At low temperatures, only the stronger coordinations with PEO oxygens appear in this shell. However, as kinetic energy increases, the higher mobility of all elements in the simulation allows relatively weaker but still strong interactions to play a more significant role. These interactions replace lost atoms in the lithium coordination shell (O_{PEO}) with other nearby high-energy interacting atoms (O_{TFSI}).

3.3.3 Nanoparticle Concentration dependence of the structural properties

Radial distribution function

Figure 3.9 illustrates the radial distribution function of the interactions depicted in Figure 3.6, with the sole variable being the concentration of silica nanoparticles in the system. Each graph corresponds to a distinct interaction and includes five curves, representing varying nanoparticle concentrations from 0% Vol to 5% Vol.

The interactions between the atoms in the electrolyte show no significant dependence on nanoparticle concentration for low-volume nanoparticle content. The only interactions affected by this variable are the coordinations involving SiO_2.

Generally, the radial distribution functions exhibit only a minor dependency on SiO_2 concentration. Figures 3.9(b) and 3.9(c) demonstrate this trend, where both of them show almost an absence of dependence.

In contrast, other RDFs exhibit more significant variations. Figure 3.9(a) showcases a noticeable enhancement in the intensity of the first maximum, rising from $I = 29.8$ to $I = 31.5$ with increasing nanoparticle concentration. However, Figures 3.9(d), (e), and (f) do not present a clear trend, showing apparent disorder when comparing peak heights and nanoparticle quantities. A more detailed understanding of these variations will be addressed once we complement this analysis with the examination of coordination numbers.

Coordination Number

In Figure 3.10, we analyze the coordination numbers ($\mathrm{C}^{\mathrm{j}}(\mathrm{i})$) for the same interactions previously investigated in the radial distribution function analysis and described in figure 3.6. The coordination numbers serve as an additional structural metric, clarifying our understanding of the system's architecture. Each curve depicts the dependence of the respective $\mathrm{C}^{\mathrm{j}}(\mathrm{i})$ on the volume fraction of silica nanoparticles.

The coordination numbers yield similar conclusions to the RDF curve analysis. We find no significant changes in the number of atoms in the first coordination shell for many interactions. The only increased coordination numbers are those counting the SiO_2 atoms in their first shell, which is expected as the number of nanoparticles in the system increases.

Figure 3.10(a) depicts $\mathrm{C}^{\mathrm{O_{PEO}}}(\mathrm{Li})$, which shows a constant coordination number. It's important to note that $\mathrm{C}^{j}(i)$ is influenced by various factors and is proportional to the integral of the first peak multiplied by the density rather than the maximum intensity as observed in the RDF function.

In Figures 3.10(b) and (c), representing the interactions between (b) anions and the polymeric matrix and (c) lithium with anions, both interactions show minimal variations in their structural functions. However, the coordination numbers exhibit a slight decrease with increasing nanoparticle concentration. This difference is likely due to the limited coordination of these elements with the surface of the nanoparticles.

Figures 3.10(d), (e), and (f), which correspond to SiO_2 atoms, are the only ones showing any notable enhancement related to nanoparticle concentration. Nevertheless, this effect is primarily a result of the increased quantity of nanoparticles, as these $\mathrm{C}^{j}(i)$ functions are directly proportional to the density of SiO_2 atoms.

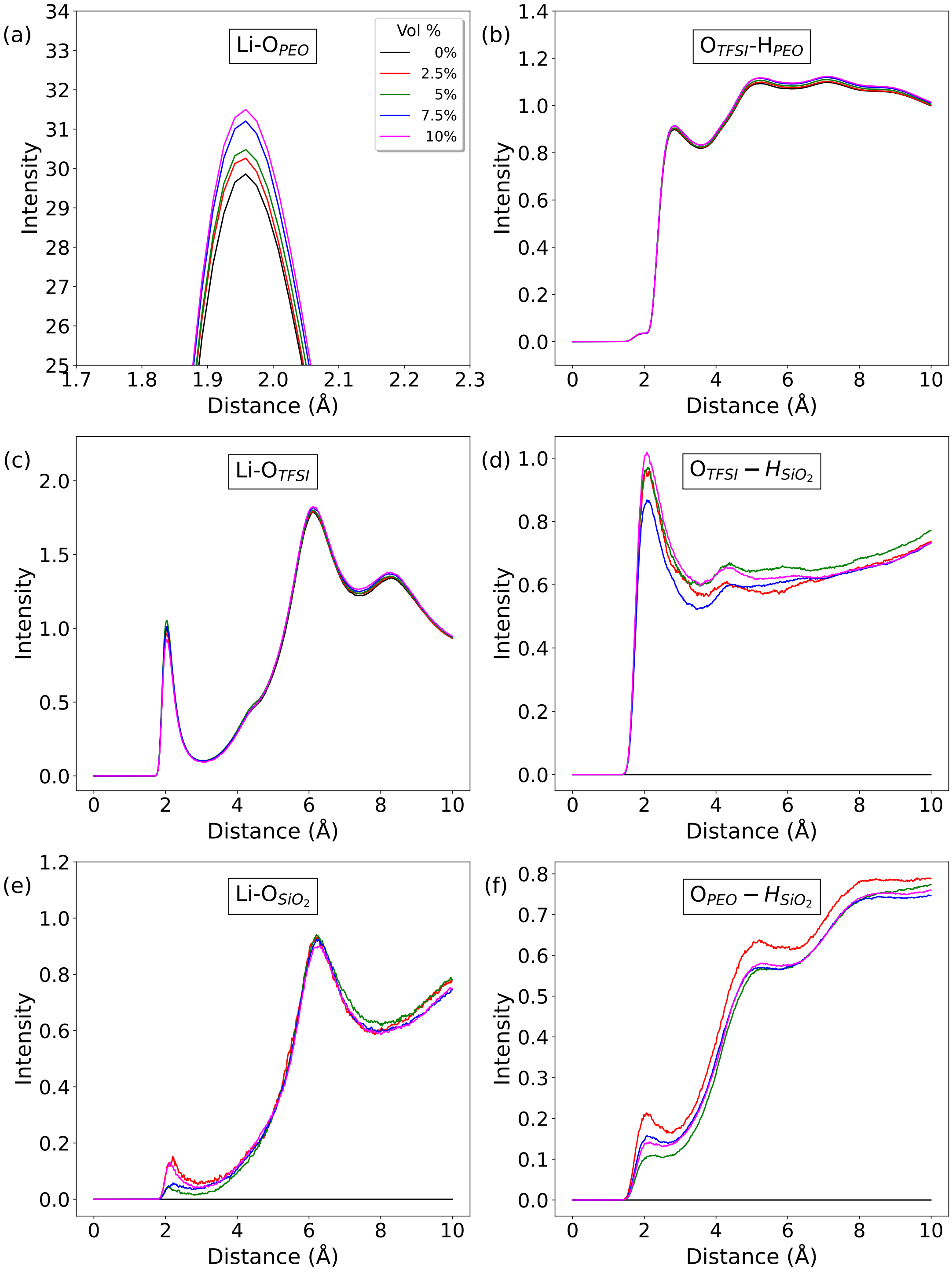

Figure 3.9: Radial distribution function curves were computed for various atom pairs, including: (a) lithium and O_{PEO}, (b) O_{TFSI} and H_{PEO}, (c) lithium and O_{TFSI}, (d) O_{TFSI} and O_{SiO_2}, (e) lithium and H_{SiO_2}, and (f) O_{PEO} and H_{SiO_2}. These calculations were conducted over a range of nanoparticle concentrations, from 0% Vol to 5% Vol, at a temperature of 600K and with an ionic concentration of 3.2 Li:PEO.

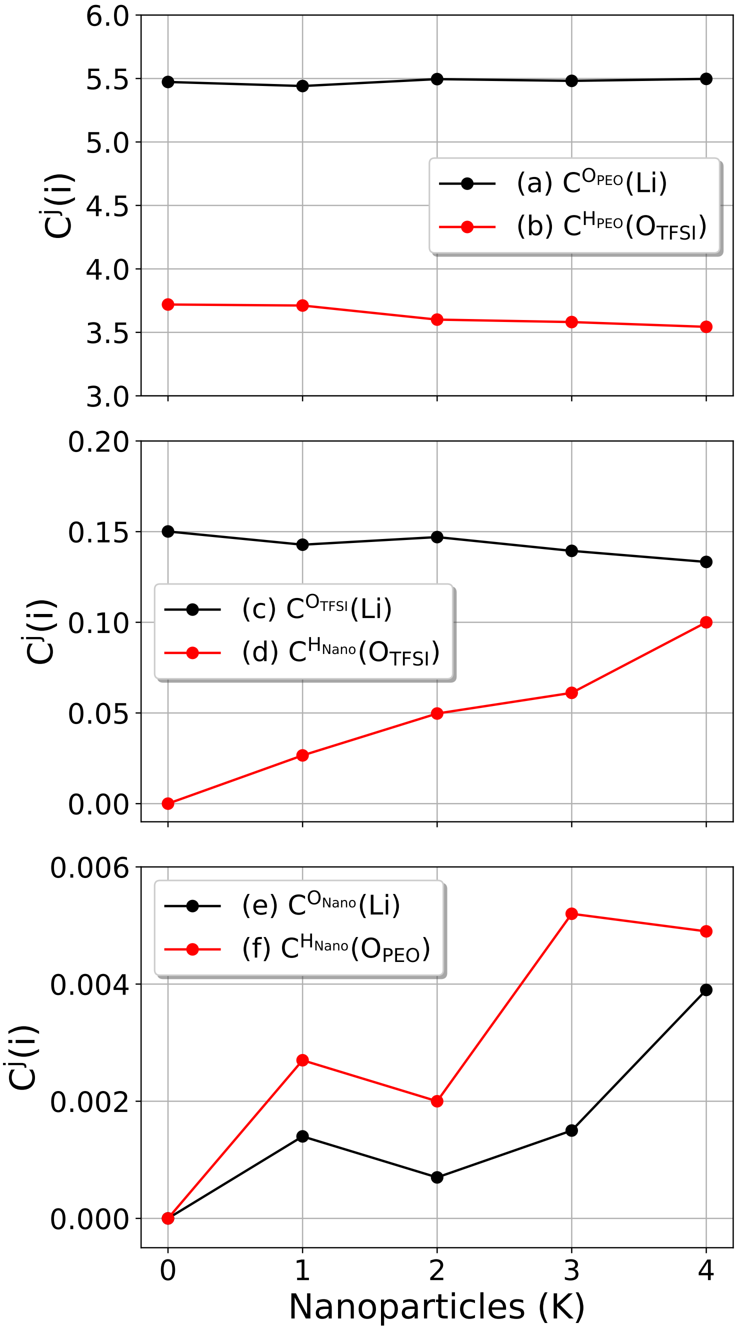

Figure 3.10: Coordination number curves ($C^j(i)$) were analyzed as a function of nanoparticle concentration for various interactions, including: (a) lithium and O_{PEO}, (b) O_{TFSI} and H_{PEO}, (c) lithium and O_{TFSI}, (d) O_{TFSI} and H_{SiO_2}, (e) lithium and O_{SiO_2}, and (f) O_{PEO} and H_{SiO_2}. These analyses were conducted over a range of nanoparticle concentrations, from 0% Vol to 10% Vol, at a temperature of 600K and with an ionic concentration of 3.2 Li:PEO.

Conclusions

Upon examining the impact of nanoparticle concentration on the system's structural properties, we find that at a 3.2 Li:PEO concentration, nanoparticles do not significantly affect the binding between lithium and TFSI in the bulk polymer, nor the binding between the ions and PEO. However, certain elements in the electrolyte, like TFSI, do interact with the surface of the silica nanoparticles. As a result, the surface of the silica exhibits a different structural organization than the pure bulk electrolyte, although this does not impact the interactions in the bulk.

3.3.4 Ionic concentration dependence of the strcutural properties

Ionic concentration strongly influences the structural and dynamic properties of electrolyte systems [218]. In the following sections, we will investigate the impact of ionic concentration on our system's structural properties, examining its effects on the short-range organization of our electrolyte and its potential consequences for ion mobility within the system.

Radial distribution function

Figure 3.11 illustrates the dependence of the radial distribution function (RDF) for the system's most relevant interactions on ionic concentration. We varied the ionic concentration by introducing LiTFSI into the electrolyte, starting from 20 ionic pairs, which is equivalent to a concentration of 0.2 Li:PEO, this is equivalent to 0.2 mol/L. The notation Li:PEO denotes the number of lithium atoms or ionic pairs per PEO chain, with the number of PEO molecules consistently set at 100. This notation facilitates comparisons between systems of different volumes in the coordination number analysis, and we will just use the mol/L notation to identify some specific points.

The interactions in the system exhibit a significant dependence on ionic concentration. Some atomic interactions that are unremarkable at low concentrations show a clear binging between the atoms at higher concentrations, such as the interactions between lithium and TFSI, and lithium and $\mathrm{O_{SiO_2}}$. Notably, the interactions between the two ions in the system and the polymer matrix display their maximum intensities at intermediate concentrations, setting them apart from other interactions.

Figure 3.11(a) shows the RDF function for PEO oxygen atoms centered around lithium. Notably, the $\mathrm{g_{Li}^{O_{PEO}}(r)}$ function exhibits a particular pattern. The maximum intensities are observed within the intermediate range of ionic concentrations, typically between 3.2 Li:PEO and 4 Li:PEO, while the lowest values for the first peak correspond to the systems with the higher or lower concentrations. In all concentration ranges, strong coordination is evident, with the maximum occurring at a distance of approximately

$r = 1.95$Å.

Moving to the second graph, Figure 3.11(b) represents the $g_{H_{PEO}}^{O_{TFSI}}$ functions. These curves share a similar shape but vary in intensity. Similar to Figure 3.11(a), the curves corresponding to intermediate concentration ranges display more pronounced first peaks. Additionally, we observe the emergence of a distinct second shell at a distance of approximately 5Å from the central oxygen, becoming prominent beyond the 3.2 Li:PEO ratio This second maximum indicates a structural change at these concentrations, suggesting the formation of a second shell, likely driven by oxygen atoms within the same molecules as the central one.

The curves in Figure 3.11(c) provide valuable insights into these electrolytes, highlighting distinct differences between highly concentrated and low-concentration systems. At low ionic concentrations, the ions are not bonded, resulting in long-distance coordination with the second neighbor shell at a distance of $r = 6$Å from the central lithium, featuring an intensity of $I = 5.2$. However, as the concentration increases, the coordination in the second shell diminishes, with a significant reduction observed at intermediate values between 3.2 Li:PEO and 4 Li:PEO. Within this range, the ions begin to couple, with the atoms in the second shell moving to closer distances. At these concentrations, an intermediate shell starts to emerge at approximately $r = 4.2$Å from the central atom, a result of the closer packing of other O_{TFSI} ions within the same molecules as those in the first shell. At elevated concentrations, the shell at $r = 6$Å nearly disappears, and the ions exhibit clear coupling with a maximum intensity of $I = 13.7$.

Turning to the $g_{O_{TFSI}}^{HSiO_2}$ curves depicted in Figure 3.11(d), we observe two distinct curve shapes, primarily distinguishable between highly concentrated and lowly concentrated systems. At lower concentration some anions are bound to the silica surface, while at higher concentrations, the O_{TFSI} detaches from the nanoparticles.

Figure 3.11(e) mirrors the behavior seen in Figure 3.11(c). In low-concentration systems, there are no lithium ions neighboring the surface of silica, while there is a clear concentration of ions in a second coordination shell at a further distance of $r = 6.2$Å with an intensity of $I = 1.0$. However, at around the 3.6 Li:PEO ratio, the lithium ions start binding to the silica surface with a sharp and intense peak in the first shell, reaching a maximum intensity of $I = 2.7$. The coordination in the second shell diminishes as a result.

The final plot, Figure 3.11(f), shows a complete detachment of the PEO from the silica as ionic conductivity increases. At low concentration, there is a small coupling between the atoms, with intensities reaching up to $I = 0.5$. However, this attachment disappears entirely at the highest concentrations.

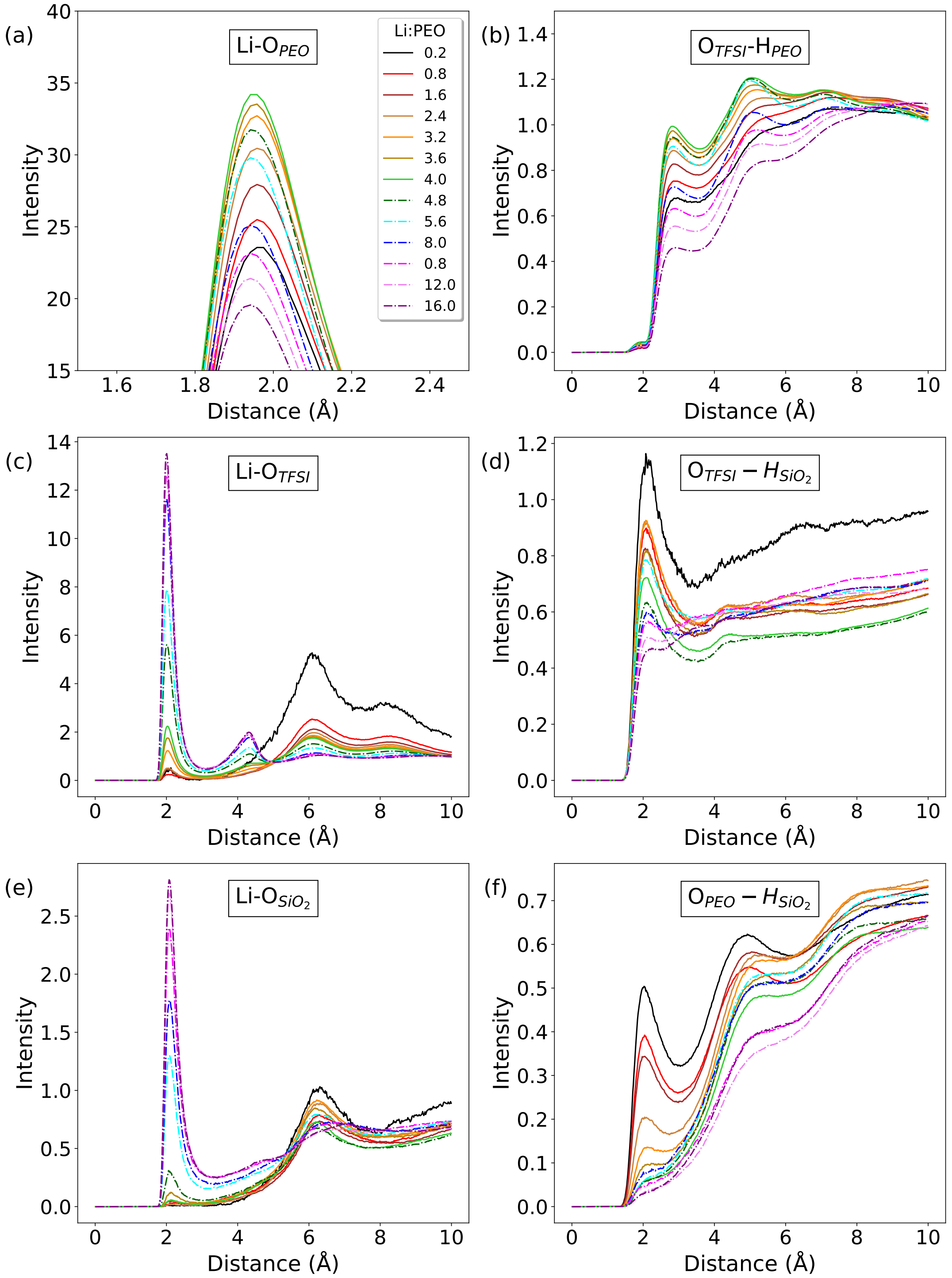

Figure 3.11: Radial distribution function curves were computed for various atom pairs, including: (a) lithium and O_{PEO}, (b) O_{TFSI} and H_{PEO}, (c) lithium and O_{TFSI}, (d) O_{TFSI} and H_{SiO_2}, (e) lithium and O_{SiO_2}, and (f) O_{PEO} and H_{SiO_2}. These calculations were performed over a range of ionic concentrations, spanning from 0.2 Li:PEO to 9.6 Li:PEO, at a temperature of 600K, and with a nanoparticle concentration of approximately 10% Vol for a 3.2 Li:PEO concentration.

Our calculations identify two distinct concentration regimes, separated by a threshold at 3.2 Li:PEO. These two phases are evident in all RDF functions and will be further analyzed in the upcoming subsection on coordination numbers. From now on, we will refer to these phases as the low-concentration (LC) and high-concentration (HC) regimes. The distinction between these distinct regimes also exerts a profound influence on the dynamic properties of the electrolyte.

The presence of two concentration regimes and the 3.2 Li:PEO threshold align with findings in previous computational studies, such as the work by Kang et al. [218]. Kang and colleagues investigated the structural properties of solid polymer electrolytes (SPE) composed of PEO and LiTFSI, specifically examining the impact of ionic concentration.

In their study, Kang et al. analyzed the radial distribution function (RDF) of oxygen atoms centered around lithium, distinguishing between oxygen atoms originating from PEO and TFSI for varying ionic concentrations. Their results revealed a notably higher maximum intensity in $\mathrm{g}_{\mathrm{Li}}^{\mathrm{O}_{\mathrm{PEO}}}(\mathrm{r})$ compared to the $\mathrm{g}_{\mathrm{Li}}^{\mathrm{O}_{\mathrm{TFSI}}}(\mathrm{r})$ curve, which parallels our own observations. Additionally, they documented a slight decrease in the intensity of the $\mathrm{g}_{\mathrm{Li}}^{\mathrm{O}_{\mathrm{PEO}}}(\mathrm{r})$ curve and a significant increase in the intensity of the $\mathrm{g}_{\mathrm{Li}}^{\mathrm{O}_{\mathrm{TFSI}}}(\mathrm{r})$ curve as the concentration exceeded the 3.2 Li:PEO ratio, mirroring the trends we've observed.

Coordination Number

We have calculated the coordination number for the interactions depicted in figure 3.6 across a wide range of ionic concentrations for four systems with varying content of ceramic fillers, ranging from 0% to 10% in volume. This approach allows us to determine if the minimal impact of nanoparticles observed in the preceding section of this chapter is attributed to suboptimal ion concentration conditions.

Following a trend akin to that of Figs. 3.11, the $\mathrm{C}^{j}(\mathrm{i})$ curves also present a sudden change of slope at 3.2 Li:PEO. Coordination of Li^{+} around the oxygen in PEO $\mathrm{C}^{\mathrm{Li}}(\mathrm{O}_{\mathrm{PEO}})$ increases in the LC regime, saturating at 3.2 Li:PEO (fig. 3.12(e)).This indicates that in the LC regime, the introduction of additional lithium ions results in their attachment to the PEO. This means that, at low concentration, newly introduced Li atoms attach to PEO. However, once every oxygen atom in PEO is coordinated with one lithium ion, the PEO becomes saturated, and any further increase in concentration will make the Li and TFSI ions form ionic pairs again. Consequently, additional salt introduced thereafter remains undissociated free ions, impacting the conductivity.

This can also be seen in the reciprocal coordination number, $\mathrm{C}^{\mathrm{O}_{\mathrm{PEO}}}(\mathrm{Li})$ (Fig. 3.12(a)). Initially, in the LC regime, this coordination value starts at approximately 6, in line with the values reported in the literature [77, 128, 213, 219], reaching the HC regime at 3.2 Li:PEO. From there on, the coordination decreases much faster, since the new

Li^+ atoms cannot attach to the PEO. These Li^+ ions, not being able to form strong interactions with the PEO, begin to coordinate with their counterions as the curves in Figs.3.12(b) and (c) show. At low ionic concentrations, the coordination numbers between the two ions are nearly negligible. However, after surpassing the 2 mol/L threshold, the C_i^j between lithium and TFSI begin to rapidly increase.

The TFSI coordination behavior as a function of concentration is not so different from that of Li. Figure 3.12(d) shows how in the LC regime, TFSI is mainly interacting with the PEO, but in Figure 3.13(b) we can observe that in contrast with lithium, it is also coordinating with the SiO_2, which was a much smaller partial density and thus, the numbers are considerably lower. In the HC regime, TFSI starts coordinating with lithium while the coordination with PEO decreases. This is again a result of the saturation of oxygens sites of PEO, causing the Li ions to coordinate with TFSI. We note in Fig. 3.12(f) that there is even a decrease of the coordination of TFSI with PEO at high concentrations. This does not happen in the case of lithium because it is more strongly binded to PEO, as already seen in the temperature dependence of coordination numbers.

Regarding SiO_2, at LC the ceramic is mainly surrounded by PEO, while at HC this PEO is totally replaced by TFSI and its coupled lithium ions (Fig.3.13(c)). This higher coordination indicates that there is a stronger interaction between the ions and the nanoparticles than between the nanoparticles and the PEO. Whereas there is no noticeable change in the coordination properties of the matrix upon addition of silica nanoparticles (Fig.3.12), differences are noticeable in the coordination of the SiO_2 filler atoms, depending on the nanoparticle size (Fig.3.13). The nanoparticles employed in the 10% volume case were bigger than in the other cases. This smaller curvature means that they have less available surface on their effective range of coordination, explaining the lower value of the blue curve.

Conclusions

We observe a significant dependence of the structural properties on the ionic concentration of the system. Notably, many RDF functions exhibit a change in behavior at intermediate ionic concentrations, approximately 2 mol/L or 3.2 Li:PEO. The maximum height of the first peak in the RDF functions is most pronounced in curves 3.11(a) and 3.11(b) at concentrations near 3.2 Li:PEO. Furthermore, all the graphs in Figure 3.11 demonstrate a shift in behavior at this concentration, signifying a transformation in the system's properties driven by changes in its composition.

This transformation is reflected in the coordination numbers ($C^j(i)$) as abrupt changes. This threshold is marked by black dashed lines in Figures 3.12 and 3.13. Upon closer examination of $C^{Li}(O_{PEO})$, we deduce that at 3.2 Li:PEO, PEO becomes saturated

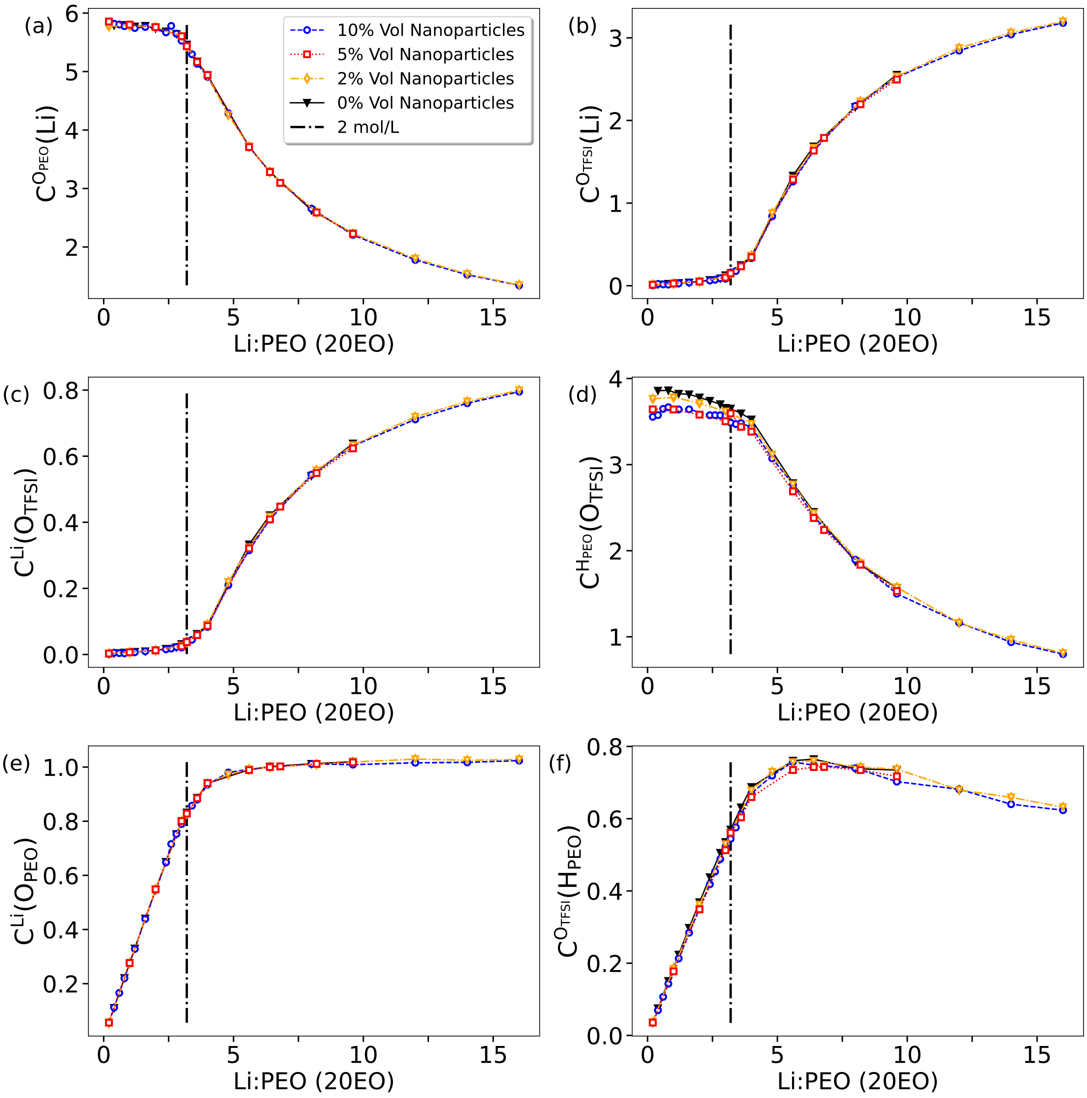

Figure 3.12: Coordination numbers determined for various atom pairs, including: (a) lithium and oxygen of PEO, (b) lithium and oxygen of TFSI, (c) oxygen of TFSI and lithium, (d) oxygen of TFSI and hydrogen of PEO, (e) oxygen of PEO and lithium, and (f) hydrogen of PEO and oxygen of TFSI. These calculations were conducted across a range of ionic concentrations, spanning from 0.2 Li:PEO to 16.6 Li:PEO, at a constant temperature of 600K. The data presented here corresponds to four distinct systems, each representing different nanoparticle loadings ranging from 0% to 10% Vol (see inset).

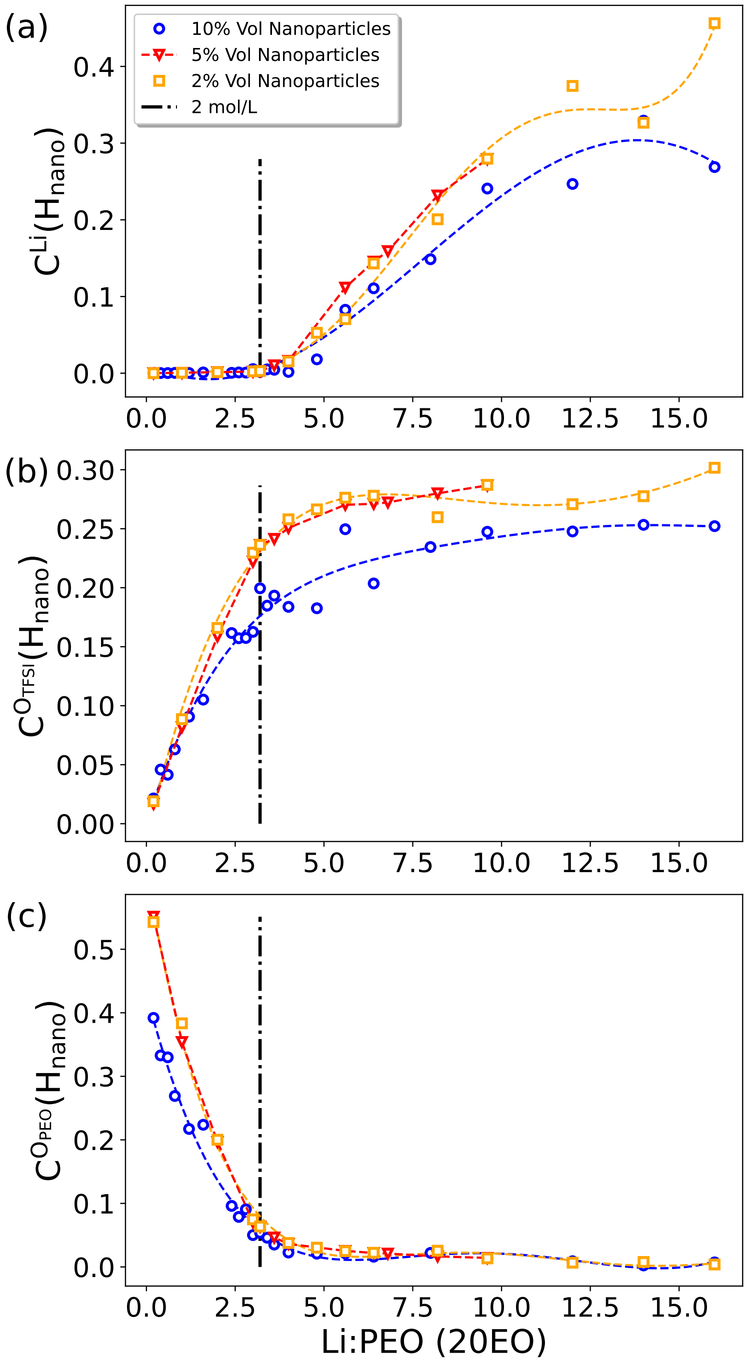

Figure 3.13: Coordination numbers determined for various species within the coordination sphere of the surface hydrogens of the SiO_2 nanoparticles: (a) lithium, (b) oxygen of TFSI, and (c) oxygen of PEO. Dashed lines have been included as interpolations to serve as visual guides. These calculations were conducted across a range of ionic concentrations, spanning from 0.2 Li:PEO to 16.6 Li:PEO, at a constant temperature of 600K. The data presented here corresponds to four distinct systems, each representing different nanoparticle loadings ranging from 0% to 10% Vol (see inset).

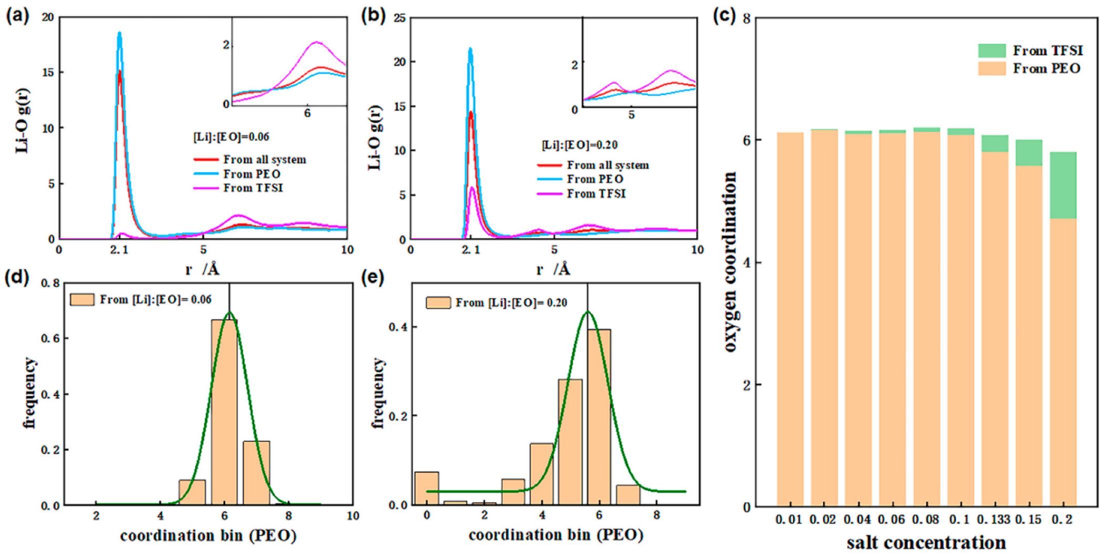

Figure 3.14: (a,b) Representative RDF and (d,e) distribution of CNs from EO at r = 0.06 and 0.20. (c) Average CNs at various salt concentrations, on the one hand for PEO, and on the other hand for TFSI$^-$. From reference [218].

with lithium ions. Consequently, from this point onward, some lithium ions can move more freely within the system due to reduced interactions with PEO. This phenomenon triggers subsequent changes in interactions among other atoms, ultimately altering the overall performance and structure of the electrolyte.

The most significant impact of these alterations is observed in the correlations between lithium and PEO, as well as TFSI. We notice that as we transition into the high concentration (HC) regime, the coordination of lithium with oxygen atoms from PEO, denoted as $C^{O_{PEO}}(Li)$, decreases rapidly. In contrast, the coordination of lithium with oxygen atoms from TFSI, denoted as $C^{O_{TFSI}}(Li)$, grows at a similar rate to the decrease in $C^{O_{PEO}}(Li)$. This ultimately results in lithium ions being coordinated by approximately the same number of oxygen atoms, effectively replacing O_{PEO} with O_{TFSI} in their coordination spheres. This behavior aligns with the findings of Kang et al. [218], who conducted simulations with different ionic concentrations, one in the low concentration (LC) and another in the HC. Their results, shown in Figure 3.14, exhibit coordination numbers similar to ours, supporting the conclusion that this substitution of oxygen atoms in the first coordination shell of lithium occurs between PEO and TFSI.

The value of the inflection point becomes evident when we analyze the data in Figure 3.12(a). The number of oxygen atoms in the coordination shell of PEO is approximately 6, and there are 21 oxygen atoms per PEO chain. Therefore, if we divide 21 by the number of oxygen atoms required for a single PEO chain, we obtain that the threshold is $21/6 = 3.5$, which is approximately equal to 3.2 Li:PEO.

The influence of nanoparticles on the system has also been explored. Figure 3.12 compares four different concentrations of nanoparticles, ranging from a simulation without SiO_2 to a 10% volume content. All curves overlap, indicating that the presence or absence of nanoparticles has no discernible impact on the coordination numbers between the atoms in the bulk matrix of the system. We will discuss this further in the dynamics section. However, not all the $C^j i$ values centered around the silica in Figure 3.13 overlap: the curve representing 5% volume (blue) is slightly lower than the others. This is because the nanoparticles employed in the 5% volume case were larger than in the other cases, resulting in less available surface area for coordination within their effective range.

In conclusion, the $C^j i$ curves centered on SiO_2 are primarily influenced by the local concentrations around the nanoparticles but have no significant impact on the coordination in the bulk polymer matrix.

Concerning the adsorption of ionic species onto silica, TFSI exhibits a higher degree of coordination with the ceramic initially. This is attributed to the larger size of TFSI molecules, which are not strongly bound to PEO. However, once the PEO becomes saturated with lithium ions at approximately 2 mol/L, the behavior of TFSI molecules towards the nanoparticle surface becomes similar to that of other ions.

3.3.5 Structure around the Nanoparticle

In the preceding sections, we investigated the structural properties of several significant interactions within the system, some of which involved atoms on the surface of silica nanoparticles. Now, we will delve further into the nanoparticle's structure by examining the radial distribution functions (RDF) of the entire nanoparticle. We accomplish this by calculating RDFs with respect to the center of mass of the nanoparticles.

Radial Distribution Function

Figure 3.15 displays the RDF functions for interactions involving lithium (Li), TFSI oxygen ($\mathrm{O_{TFSI}}$), and PEO oxygen ($\mathrm{O_{PEO}}$) with the SiO_2 nanoparticle. We also compare the results for two different nanoparticle sizes: $\mathrm{R}_{nano} = 6$Å on the left and $\mathrm{R}_{nano} = 12$Å on the right and side.

In the initial two graphs, 3.15(a) and (b), illustrating $\mathrm{g^{Li}_{Nano}(r)}$, a distinct first shell of lithium ions becomes evident at sufficiently high concentrations. For concentrations below 4 Li:PEO, only one occupied shell exists at greater distances from the nanoparticle. However, the intensity of this peak diminishes in favor ofthe first shell at higher concentrations. This pattern remains consistent across both scenarios, although the distances at which it occurs differ due to the different nanoparticle radii.

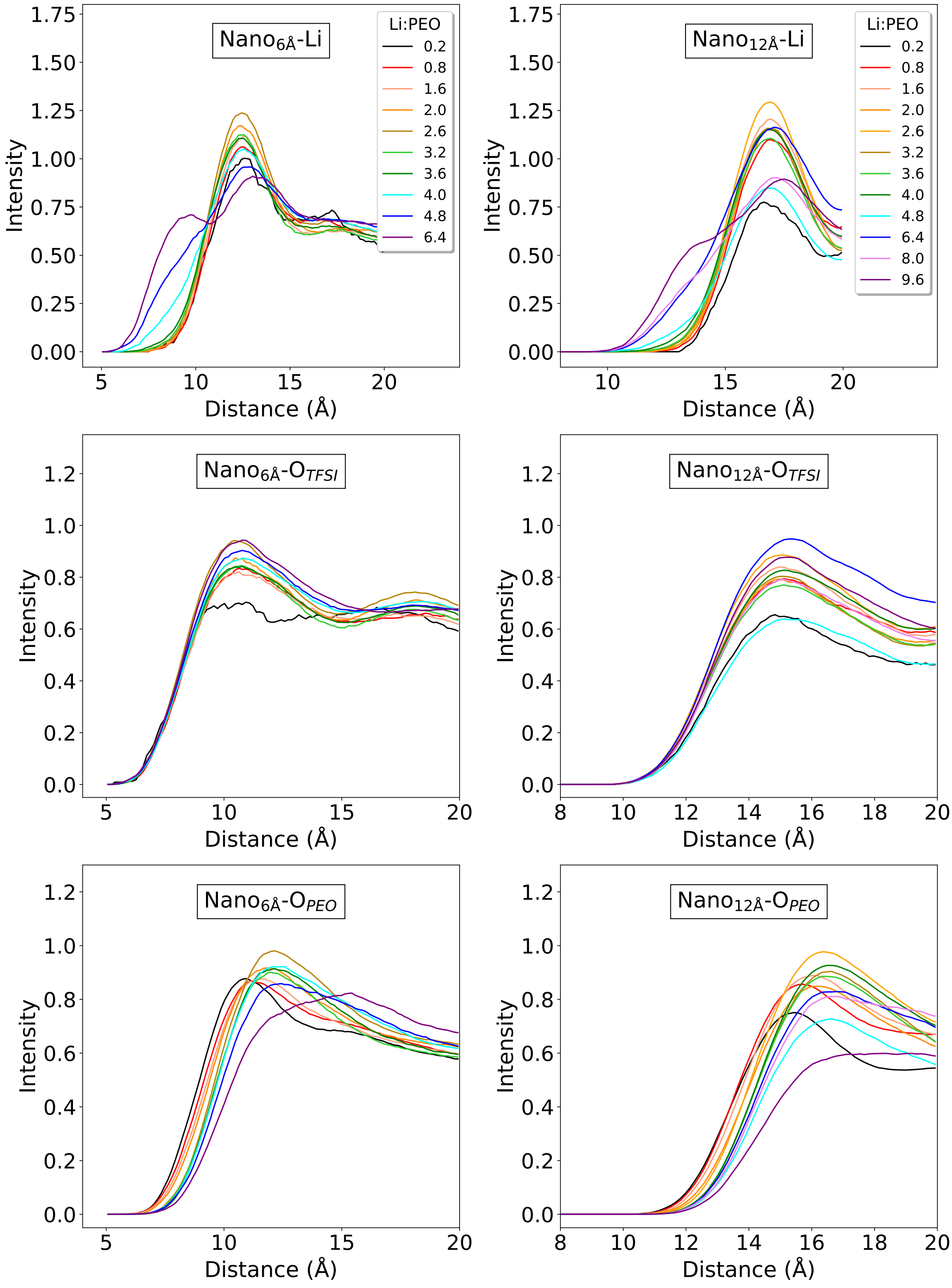

Figure 3.15: Radial distribution functions determined for various species (a-b) lithium, (c-d) oxygen of TFSI, and (e-f) oxygen of PEO, centered around the nanoparticle's center of mass (COM). These calculations were performed over a range of ionic concentrations, varying from 0.2 Li:PEO to 9.6 Li:PEO, while maintaining a constant temperature of 600K.

Figures 3.15(c) and (d) analyze the $g_{\mathrm{Nano}}^{\mathrm{O_{TFSI}}}(r)$ curves, revealing a clear attachment of the atoms throughout the entire concentration range, in contrast to the $g_{\mathrm{Nano}}^{\mathrm{Li}}(r)$ curves. When comparing the two nanoparticle sizes, the curves exhibit less variation around the nanoparticle at $r = 6$Å, likely due to its closer proximity to the center of mass.

Similar behavior can be observed in the $g_{\mathrm{Nano}}^{\mathrm{O_{PEO}}}(r)$ curves for the LC regime. Both nanoparticles exhibit some coordination with the nanoparticle in their first shell of neighbors, as well as happens fort $\mathrm{O_{TFSI}}$. However, in this case, the higher concentration regime shows a clear detachment from the nanoparticle's surface.

Conclusions

The analysis of ion distribution around the entire nanoparticle structure confirms the observations made in the analysis of surface atoms. In summary, the positive charges on the silica surface create a coating of the surface with the most electronegative atoms in the bulk electrolyte at the LC regime, which are the oxygen atoms from both TFSI and PEO. However, this changes in the HC regime, where $\mathrm{O_{PEO}}$ detach from the filler's surface because when all the $\mathrm{O_{PEO}}$ sites are saturated with lithium, they can no longer coordinate with silica. Conversely, as more TFSI molecules are introduced, they maintain their proximity to the silica surface. When the silica concentration is high enough, lithium ions also approach the filler's surface, forming strong interactions with the oxygen atoms on the outside of silica. Thus, the nanoparticles are coated by both TFSI and lithium ions in the HC regime.

3.3.6 Planar Nanoparticles

After exploring HSEs with spherical ceramic nanoparticles, we now turn our attention to a system featuring a flat nanoparticle. This change in molecular geometry offers distinct advantages. Spherical ceramics help us investigate the volumetric impact of silica on the system's conductivity, while flat nanoparticles allow us to study potential surface effects. We achieve this by analyzing anisotropic dynamic properties, as explained in Chapter 4.3.3. To do so, we introduce a single flat nanoparticle at the simulation box's center, introducing anisotropy to the system. Our focus on studying dynamic properties parallel to the nanoparticle's surface allows us to easily examine surface effects by excluding the plane perpendicular to the nanoparticle, thus avoiding any disruption to ion movement.

In this section, we will concentrate on examining the polymer's organization in a system characterized by the presence of flat nanoparticles. Through a visual analysis of polymer orientation within the electrolyte, we can draw the following conclusions: in the vicinity of the nanoparticle, the polymers exhibit a significant reorientation, aligning strongly parallel to the SiO_2 surface and adsorbing onto it. However, polymers located farther

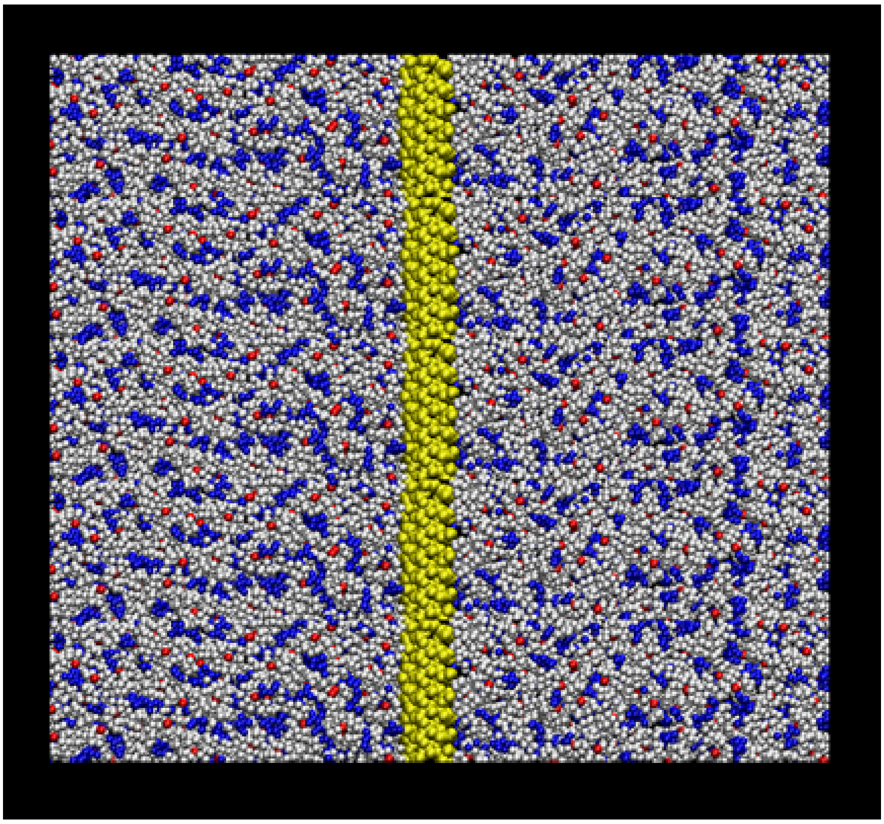

Figure 3.16: Visual representation created using VMD, illustrating the arrangement of the electrolyte with a planar nanoparticle at the center. The depicted molecules include SiO_2 nanoparticles (yellow), lithium ions (red), TFSI ions (blue), and PEO polymer chains (white).

away show a slight preference for the perpendicular direction, although this effect is minimal.

As depicted in Figure 3.16, the flat nanoparticle is positioned at the center of the simulation box, creating an "infinite plane" due to the periodic boundary conditions. This arrangement prevents PEO or ions from passing through it. To maintain this structure, the lengths of the x and y components of the simulation box are kept constant, while the pressure is adjusted in the NPT ensemble by varying the length of the z dimension. This adjustment continues until the system reaches equilibrium, following which the damping simulations are conducted in the NVT ensemble.

The initialization of these new systems begins with the generation of the planar SiO_2 structure. In this case, we employed VMD, the visualization software, along with a plugin that allows SiO_2 crystal generation. Subsequently, we introduced additional atoms using an ad-hoc Python script. The nanoparticles exhibit an approximate thickness of 14 Å and variable lengths for different systems.

Following the SiO_2 creation, we placed it at the center of a simulation box, aligning the perpendicular direction with the z-axis. We then incorporated two SPEs electrolyte simulations previously thermalized on either side of the plane. To maintain the position of the central nanoparticles' atoms (Si and inner oxygen), we conducted the annealing and thermalization process before proceeding to the subsequent damping steps under NVT conditions.

To perform these calculations, we utilized an anisotropic simulation box. In this setup, the box is elongated, featuring a greater z-axis length compared to the other two dimensions (x and y). Given that the x and y components must remain fixed to preserve the "infinite surface" nanoparticle, we applied an anisotropic barostat during the NPT simulation. This allowed us to constrain the x and y components while permitting movement solely in the z direction.

After establishing the new systems, we proceeded to analyze the system's structure using the gyration radius.

Gyration Radius

Figure 3.17 visually presents the gyration radius mapping of the polymers within the simulation, color-coded for clarity. This mapping is projected onto three spatial planes, reflecting the gyration radius accordingly. As mentioned earlier in the modeling chapter, the gyration radius is closely associated with polymer orientation. Therefore, the lines observed in Figure 3.17 can be interpreted as indicators of polymer orientation.

The color code signifies the balance between the two displayed coordinates in each plane. A vertical alignment is represented by blue, while a horizontal orientation is depicted in red, with intermediate colors indicating varying degrees in between.

In the top left corner, along with the color code, we present an average ratio between the two components of the gyration radius projection. This average is computed across all polymers in the system using the following formula:

$$R_{ij} = \sum_{n}^{N} \frac{|Rg_i|}{|Rg_i| + |Rg_j|} \tag{3.2}$$

where, R_{ij} represents the ratio between components i and j, n corresponds to each polymer or individual vector, and Rg_i, Rg_j represent the i and j coordinates of each individual vector. In an entirely isotropic system, this ratio would equal 0.5. A ratio below 0.5 indicates a greater average projection along the vertical axis compared to the horizontal axis, while a ratio above 0.5 signifies the opposite, a higher average projection along the horizontal axis.

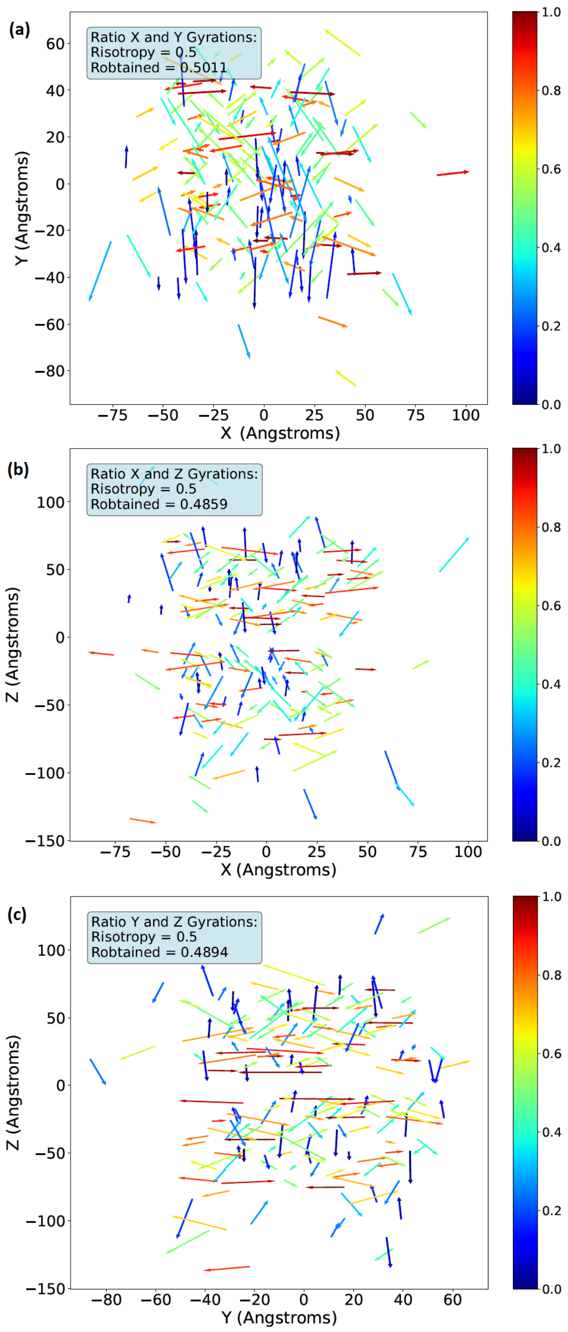

Figure 3.17: Vector map illustrating the gyration radius of the polymer molecules within the electrolyte featuring a planar nanoparticle at the center. The length of the vectors is proportional to the molecular elongation, with longer vectors indicating greater elongation. The color code within the vectors serves as a visual aid, with the most horizontally oriented vectors represented in dark red and the most vertically oriented vectors in blue. In the second and third figures, a noticeable gap can be observed at the center, corresponding to the space occupied by the nanoparticle.

From the analysis of the vectors in Figure 3.17, we observe a high degree of organization in the polymers near the nanoparticle. These polymers align themselves parallel to the nanoparticle's surface and demonstrate a clear affinity for the silica fillers. Additionally, we note that the z-component of the vectors is slightly larger on average than the other two components, as indicated by the ratios in graphs (b) and (c) being less than 0.5. This visualization method not only offers a clear depiction of polymer organization but also simplifies visual analysis. While the anisotropy in this case is not highly pronounced, such a visual representation can provide initial insights into more anisotropic systems.

Figure 3.18 presents a histogram of the y and z components of different vectors, illustrating their distribution on quantity and orientation. This complements the data from Figure 3.17 with a more numerical analysis. Thanks to the histogram, we can confirm that the polymer in direct contact with the nanoparticle adopts a preferential orientation parallel to its surface. As we move away from the nanoparticle, the polymer orientation progressively switches to become more perpendicular to the nanopaticles surface.

In summary, despite the planar nanoparticles introducing some directional tendencies in the system, their impact remains relatively subtle. Furthermore, we have demonstrated that this method of representing gyration radii proves to be a valuable and visually intuitive tool for analysis. To the best of our knowledge, this innovative approach to gyration radius visualization has not been explored in previous literature.

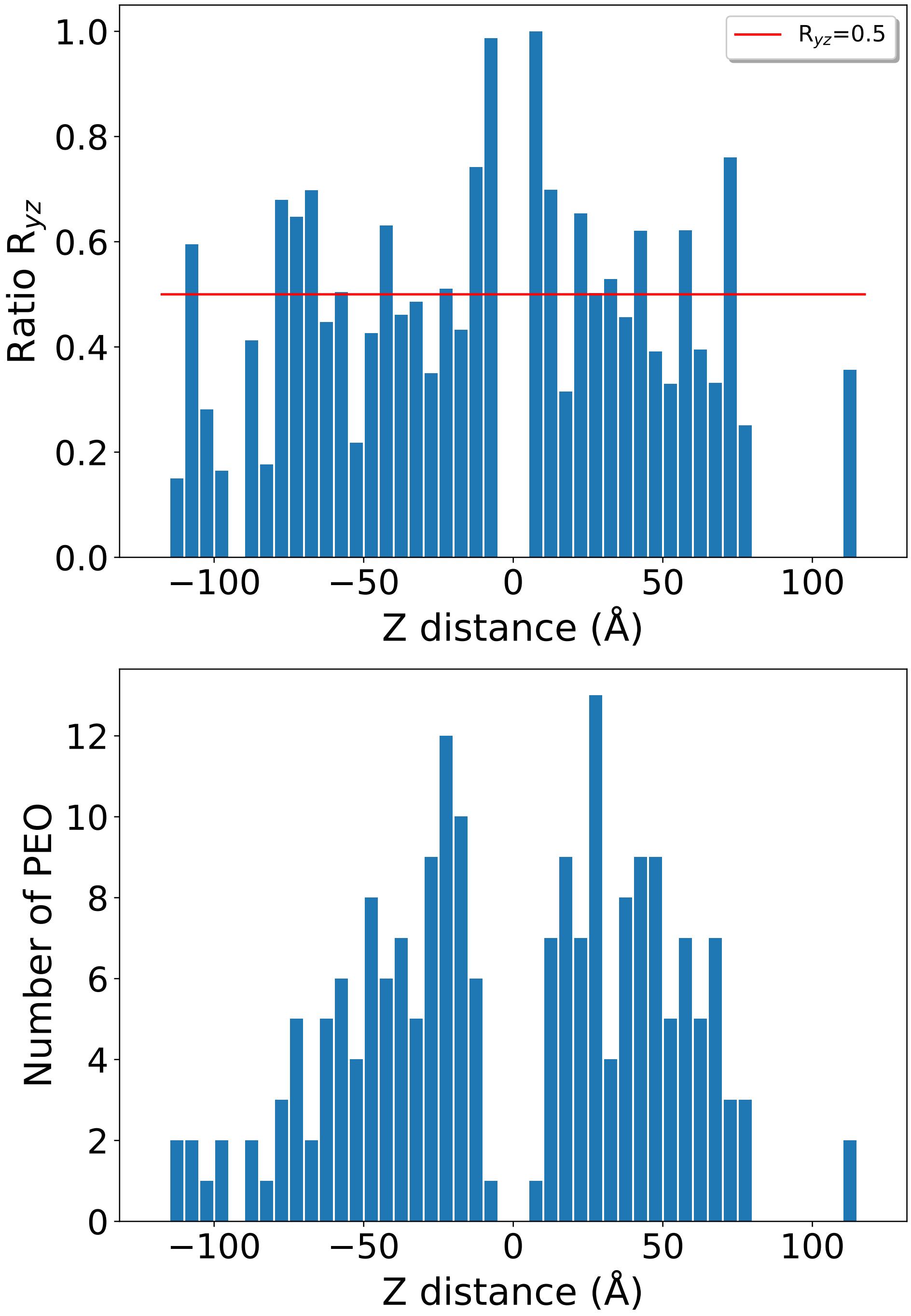

Figure 3.18: Histogram representation, where (Top) shows the mean ratio of the vectors by sections, and (Bottom) illustrates the distribution of the positions of the PEO center of masses corresponding to the third graph in Figure 3.17. Notably, a gap in the middle corresponds to the space occupied by the nanoparticle, while there is an accumulation of high-ratio vectors in the area surrounding the nanoparticle. The red line represents the ideal isotropic value, $r = 0.5$.

Chapter 4

Hybrid Solid Electrolytes: Silica Nanoparticles - Dynamics

4.1 Introduction

This chapter shifts focus from the structural aspects of HSE: PEO+LiTFSI+SiO_2 to the dynamic properties of the same material system. We aim to explore how its constituents: PEO (polyethylene oxide), LiTFSI (lithium bis(trifluoromethanesulfonyl)imide), and silica nanoparticles collectively influence dynamic behaviors, including mean squared displacement, diffusion coefficients, and conductivity. Our goal is to understand the complex interplay between these factors.

Dynamic properties are crucial for battery performance, especially ionic conductivity, which directly impacts factors like charge time. High ionic conductivity reduces internal resistance, leading to minimal energy losses, less heat generation, and quicker charge and discharge cycles. Therefore, we aim to clarify how this HSE influences the dynamic parameters, with a particular emphasis on the effect of nanoparticles. These insights complement the structural analysis from the previous chapter, offering a comprehensive understanding of the dynamics within HSE: PEO+LiTFSI+SiO_2.

4.2 Simulation Details

In contrast to our structural examination, where we primarily studied atomic arrangements, our present objective is to delve into the evolving behavior of this hybrid solid electrolyte over time. To accomplish this, we maintain the use of periodic boundary conditions, ensuring that our simulated system remains a representative miniature replica of the actual material.

We use a cutoff distance of 10 Ångströms for nonbonding interactions, encompassing both terms, Coulombic and Lennard-Jones. We employ a particle-particle particle-mesh solver (PPPM) with a relative accuracy of 10^{-4} to faithfully account for long-range Coulombic forces. This treatment of interactions is essential to capture the dynamics within our HSE.

Our simulations are carried out at 600K, unless otherwise stated. This choice was motivated by two key factors. First, it surpasses the melting point of PEO, approximately 65°C. Operating above the melting point we ensure that any possible effect from the polymer's crystallinity is eliminated, as discussed in section 1.3.1. This way we can focus on studying the hypothesis of the formation of a space-charge region at the interface.

Second, simulating semi-crystalline polymers is challenging due to slow phase transitions and reorganization on macroscopic timescales. MD techniques are generally optimized for amorphous or purely crystalline materials, making it more efficient to study the properties of the melted electrolyte when focusing on liquid-phase behaviors.

In the following sections, we present the results of studying the mean squared displacement, diffusion coefficients, and conductivity of our HSE to better understand this electrolyte system's dynamic behavior.

4.3 Results

We initiate our analysis by investigating the Mean Squared Displacement (MSD), which measures the average particle displacement over time and quantifies their mobility within the solid electrolyte. By tracking the trajectories of ions and particles under different conditions of temperature, nanoparticle concentration, and ionic content, we gain insights into their dynamic behavior within the material. Molecular dynamics (MD) simulations, commonly used for precise atomic-scale diffusion and MSD calculations, play a crucial role in understanding nanosecond-scale phenomena that are challenging to study with experimental techniques.

An essential parameter for analyzing atomic dynamics is the diffusion coefficient (D), which quantifies ion mobility and provides insights into the rate at which species move through the electrolyte. The D coefficient can be derived directly from MSD data once it reaches the Fickian regime. Experimental determination of D can be challenging, making MD techniques a practical alternative. It's worth noting that the D coefficient is closely linked to conductivity, which can be readily measured experimentally.

We use the Nernst-Einstein approximation to calculate the ionic conductivity of the simulated electrolytes. This approximation relates ion mobility, described by the diffusion coefficient, to ionic conductivity, as shown in Equation 2.17. Electrical conductivity is essential for charge conduction in the electrolyte. High electrical conductivity results in lower internal resistance, reduced energy losses, and faster charge-discharge cycles. This is crucial for applications like electric vehicles and portable electronics.

4.3.1 Temperature dependence of the dynamical properties

In this section, we explore the temperature dependence of the dynamic properties of the HSE:PEO+LiTFSI+SiO_2 electrolyte. We initiate our analysis by examining the Mean Squared Displacement (MSD), from which we derive the self-diffusion coefficient and subsequently calculate the electrical conductivity.

Mean Squared Displacement

Figure 4.1 depicts the temperature-dependent variations in Mean Squared Displacement (MSD) for the two types of ions: lithium (Li) and Bis(trifluoromethanesulfonyl)imide (TFSI). We examine three systems: one with 10% SiO_2 nanoparticles, another with 5%, and a third without any SiO_2. The latter two systems have an ionic concentration of 0.8 Li:PEO, while the 10% volume system has a higher concentration of 3.2 Li:PEO, equivalent to 2 mol/L. This is the concentration threshold that distinguishes the LC regime from the HC regime, affecting ion mobility.

Figures 4.1(a) and 4.1(b), show the MSD profiles for lithium and TFSI ions, respectively, in the electrolyte with 10% volume fraction of SiO_2 nanoparticles. Both lithium and TFSI exhibit a pronounced sensitivity to temperature, resulting in several orders of magnitude difference across the temperature range. At 300K, the MSD values at 30 nanoseconds are approximately 0.042nm^2 for Li and 0.061nm^2 for TFSI. In contrast, at 1000K, these values increase by four orders of magnitude, to approximately 575nm^2 for Li and 1497nm^2 for TFSI. Additionally, the MSD is consistently higher for TFSI than for lithium, a phenomenon we will elaborate on further in the diffusion subsection.

The behavior of the other systems in Figures 4.1(c), (d), (e), and (f) mirrors that of the first case. In all instances, TFSI exhibits higher MSD values than lithium, and there is a substantial four-order-of-magnitude increase in MSD with temperature across the board.

When comparing the three distinct systems, we observe that the system containing 10% volume fraction of SiO_2 nanoparticles exhibits a clearly smaller MSD for both lithium and TFSI ions. This difference mainly commes from the difference in salt concentrations. As this system is much concentrated, the ions have less space to move freely and thus, their mobilities are expected to be smaller as well. Moving to the 5%

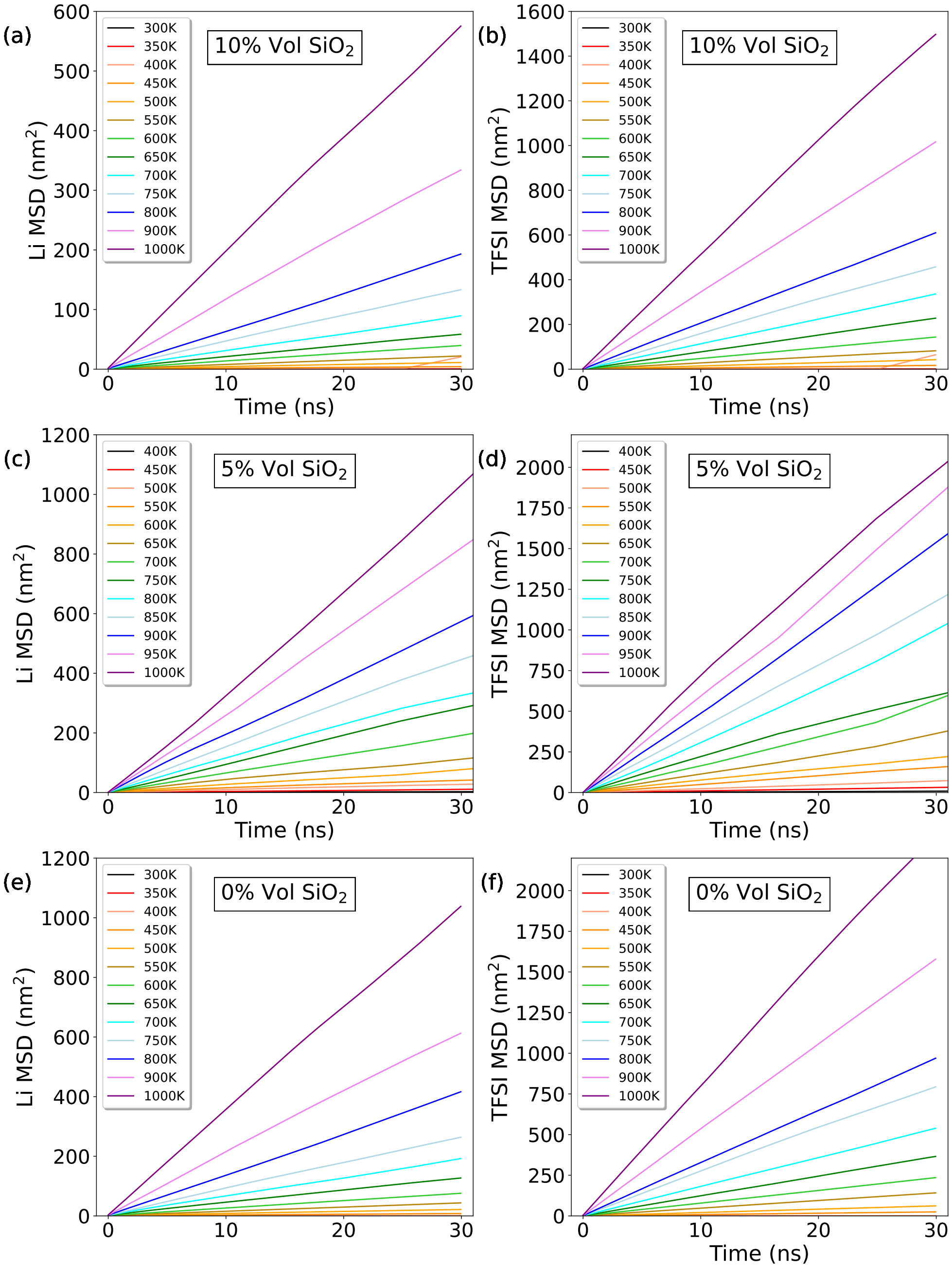

Figure 4.1: Mean Squared Displacement (MSD) of the two ionic species: (left) Lithium and (right) TFSI, investigated across three systems with varying nanoparticle concentrations: (a and b) 10%, (c and d) 5%, and (e and f) 0%. The system with a 10% nanoparticle concentration exhibits an ionic ratio of 3.2 Li:PEO, while the other two systems maintain an ionic ratio of 0.8 Li:PEO. Each plot displays the MSD over a temperature range spanning from 300K to 100K (see input).

SiO_2 system, we find that its MSD is lower than the 0% SiO_2 system. In the case of lithium, the difference is quite small, whereas a slightly more noticeable distinction is observed for TFSI ions.

To gain further insights into atom mobility, we will now examine the diffusion coefficients.

Self-diffusion

The diffusion coefficient, also known as self-diffusion, is determined by analyzing the Mean Squared Displacement (MSD) at long time intervals using Equation 2.16. This analysis is conducted at large timeframes because the MSD must reach the Fickian regime, characterized by a linear dependence on time. In our case, we start collecting data to calculate the diffusion coefficient at 5 ns.

The resulting diffusion coefficients for three systems featuring different ionic concentrations and quantities of nanoparticles are presented in Figure 4.2.

Figure 4.2(top) and Figure 4.2(bottom) display the diffusion coefficients for Li and TFSI ions, respectively. These curves exhibit an exponential dependence on temperature, consistent with typical Arrhenius behavior observed in these polymers [220].

Comparing the three systems, the 10% case, with higher ion density due to greater ionic concentration, exhibits lower diffusion coefficients for both lithium and TFSI ions, indicating reduced mobility. The 0-nanoparticles system shows slightly higher D values compared to the 5% system, despite having the same ionic concentration, suggesting that nanoparticles influence ion diffusion. These results align with previous studies, such as the one referenced in [129].

Conductivity

Applying Equation 2.17 to the previously determined diffusion coefficients, we establish the conductivity dependencies for the three systems under investigation. Figure 4.3 provides a comparative analysis of our calculated conductivities for these systems and experimental data from Maurel et al. [47], focusing on completely melted PEO.

Above the melting temperature (T_m), our calculations exhibit both qualitative and quantitative agreement with Maurel's experimental conductivities for the case without nanoparticles. It is essential to note that the PEO chain sizes in our simulations are considerably smaller ($\sim 10^3$ g/mol) than those in the experiments ($> 10^6$ g/mol). This disparity could account for the slight deviation in conductivity since smaller chains tend to exhibit higher mobilities, resulting in a factor of approximately 2 difference in diffusion [221].

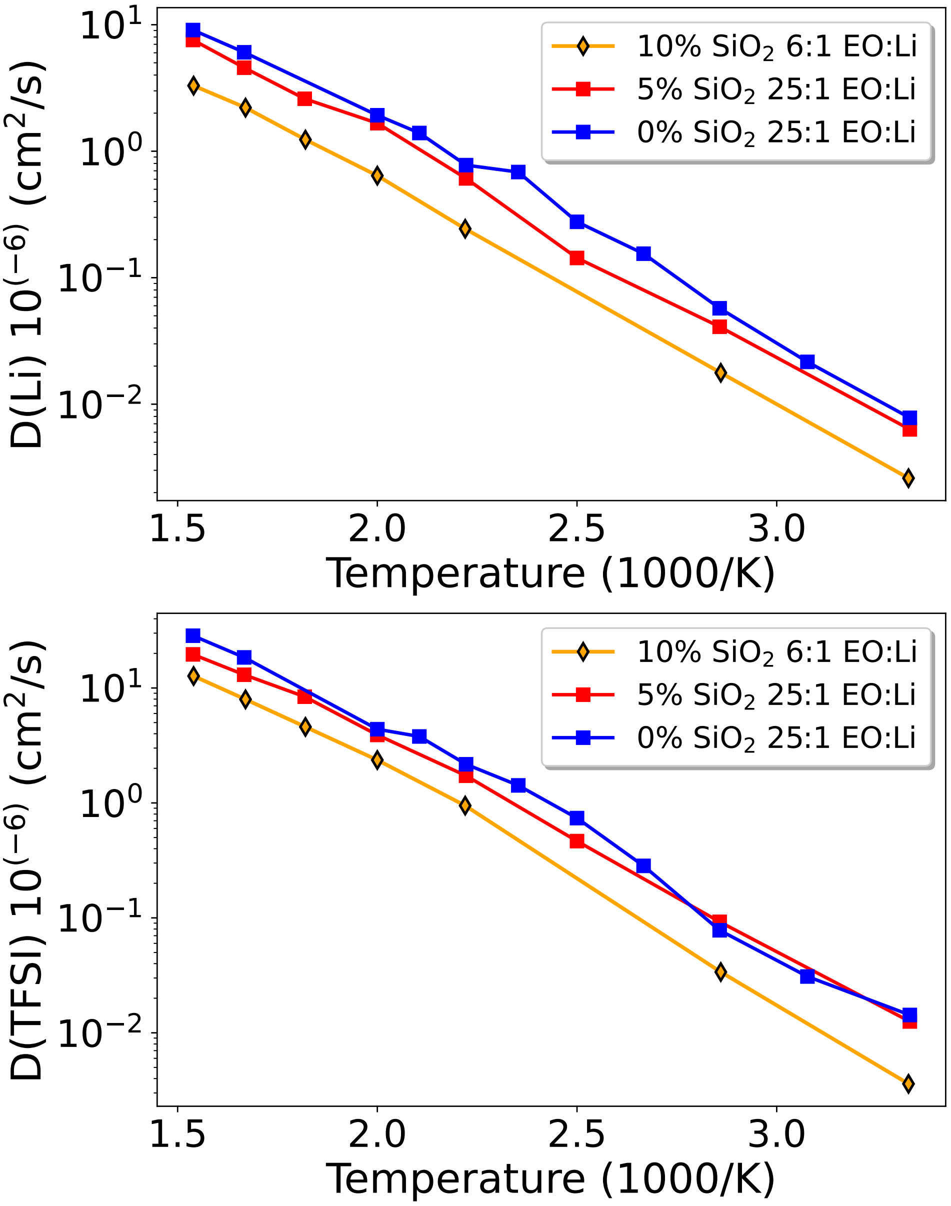

Figure 4.2: Diffusion coefficients for the two types of ions, with (top) Lithium and (bottom) TFSI, investigated across the same three systems as in Figure 4.1. Each curve represents the evolution of the diffusion coefficient across a temperature range from 300K (corresponding to 3.3 on the x-scale) to 1000K (corresponding to 1 on the x-scale). Notably, the red and blue curves exhibit closer proximity in both graphs compared to the orange curve.

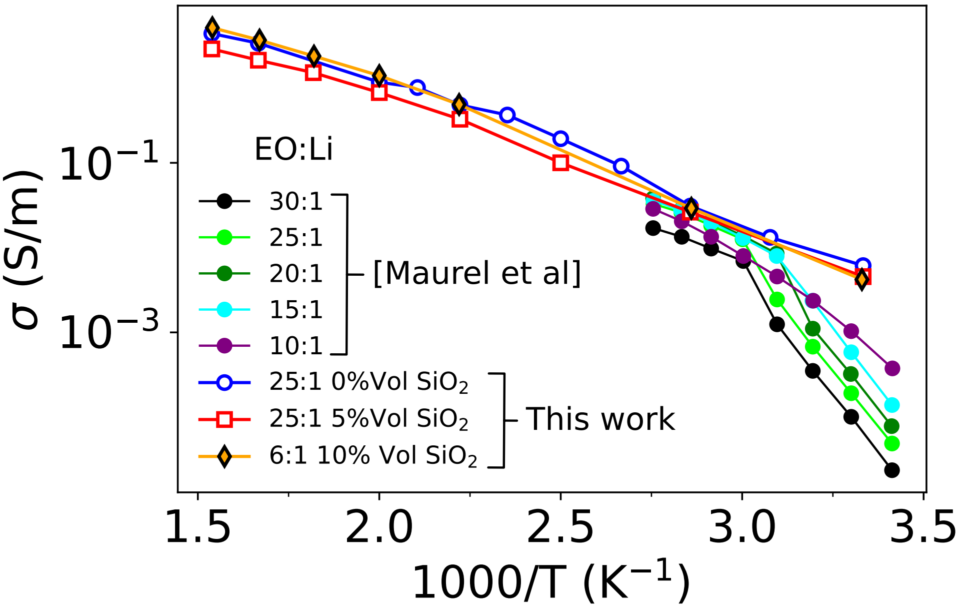

Figure 4.3: Ionic conductivity as a function of temperature within a range spanning from 300K (corresponding to 3.3 on the x-scale) to 1000K (corresponding to 1 on the x-scale). We compare the conductivity of eight different systems: The first five correspond to the data of Maurel et al. [47] for a pure solid polymer electrolyte (SPE) of PEO LiTFSI with various ionic concentrations (see inset), and the last three correspond to the systems previously studied in Figure 4.2. Notably, the computational curves closely align with the experimental results.

In contrast, below T_m, our simulations demonstrate a significant deviation from experimental values. This deviation was anticipated, as MD simulations are inherently limited in timescale and struggle to accurately capture the freezing process, leading to a liquid-like behavior even at temperatures below T_m. The inclusion of nanoparticles in our simulations introduces a similar temperature dependence.

When focusing on our dataset, the relationship between the red and blue curves remains consistent, but a noticeable difference appears in the 10% Vol case compared to pure diffusion coefficients. At higher temperatures, the 10% Vol case shows the highest values, influenced by its distinct ionic concentration. We will delve into this topic further in the upcoming section on ionic concentration dependency (Section 4.3.4). This observation is in line with findings in Maurel's experimental data [47], where different ionic concentrations led to varying conductivities. Our calculations reinforce the significant impact of ionic concentration on conductivity.

Conclusions

The comparison between our data and the references from the bibliography demonstrates a remarkable level of agreement. This validation is particularly noteworthy as molecular dynamics (MD) simulations, while valuable, are inherently limited in precision, potentially resulting in minor disparities between simulated and real-world behavior. MD simulations heavily rely on the selected force field to construct the model, introducing the possibility of numerical discrepancies. However, in our study, we not only achieve good qualitative agreement but also quantitative alignment, providing validation for our model and results.

4.3.2 Nanoparticle Concentration dependence of the electrolyte dynamics

In this subsection, we investigate how ion dynamics in the electrolyte are affected by varying nanoparticle concentrations.

Mean Squared Displacement

Figure 4.4 presents the mean squared displacement (MSD) curves of three independent systems with different ionic concentrations at 600K.

As discussed in Section 3.3.4, the concentration of 3.2 Li:PEO represents the threshold dividing the LC and HC concentration regimes, indicating PEO saturation with lithium ions. This concentration also aligns with the 'optimal concentration' for ionic conductivity, as discussed in Section 4.3.4. Figure 4.4(a) and (b) depict the dependence of the MSD with the nanoparticle concentration for the optimal concentration threshold . Systems with slightly higher concentrations, namely 3.9 Li:PEO (Figures 4.4(c) and (d)) and 4.2 Li:PEO (Figures 4.4(e) and (f)), are also studied.

Across all the cases, a consistent trend emerges. Both lithium and TFSI ions exhibit decreased MSD values with increasing nanoparticle concentrations. While minor deviations exist, such as the comparison between the red and black curves in fig.4.4(b), these variations can be attributed to statistical fluctuations. Overall, the systems presented here display a similar trend, highlighting the decrease in MSD for both ion types with the addition of nanoparticles.

Self-Diffusion

Figure 4.5 presents the diffusion coefficients extracted from the MSD analysis in the previous subsection. It showcases the self-diffusion coefficient data for three systems at 600 K, each with fixed ionic concentrations: 3.2 Li:PEO or 6.25 EO:Li, 3.9 Li:PEO or 5.12 EO:Li, and 4.2 Li:PEO or 4.17 EO:Li, along with increasing nanoparticle concentrations.

Figure 4.5(a) shows the diffusion of lithium ions, while figure 4.5(b) illustrates TFSI ion diffusion. Both figures reveal a consistent reduction in diffusion coefficients with

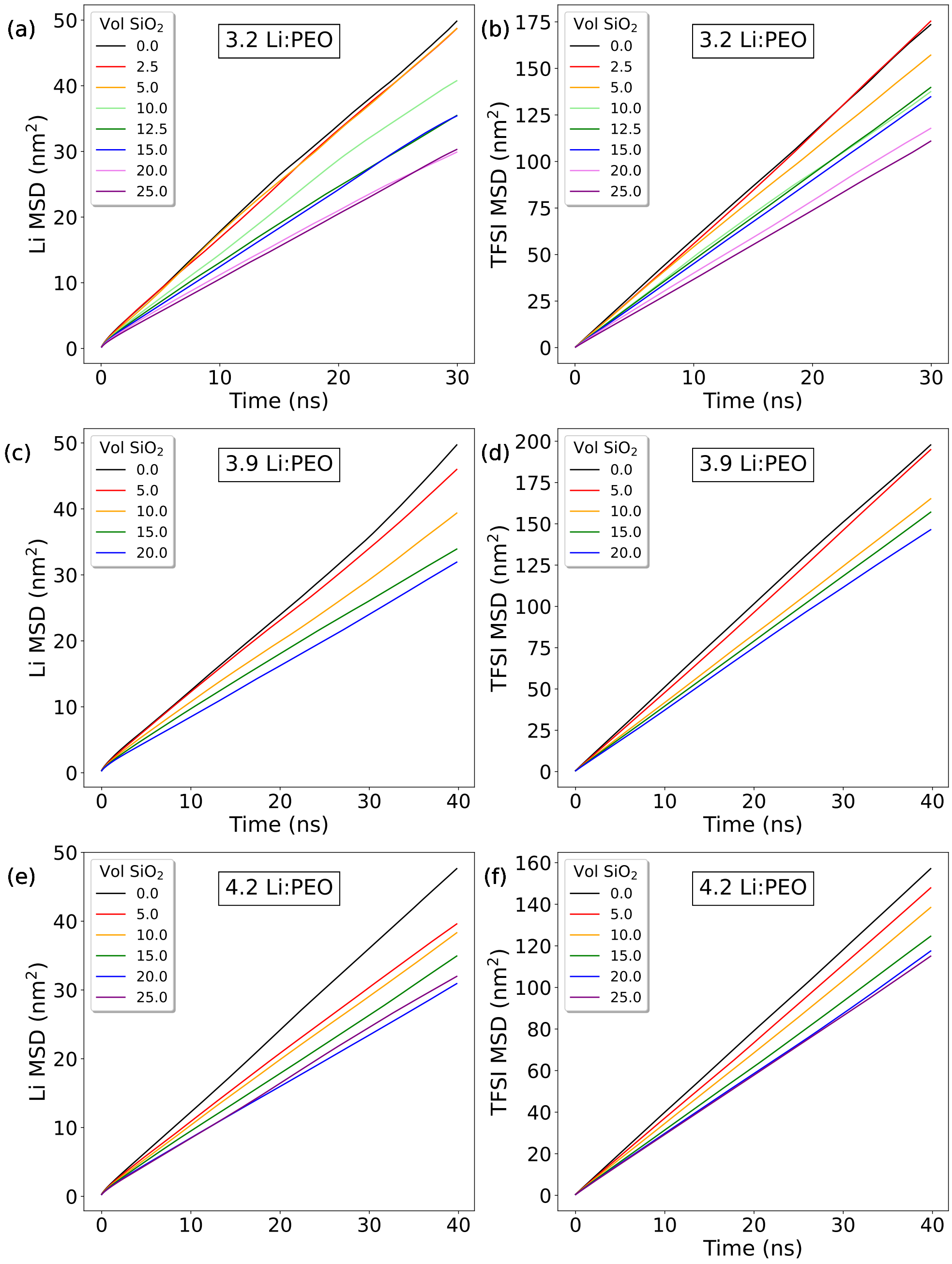

Figure 4.4: Mean Squared Displacement (MSD) of the two ionic species: (left) Lithium and (right) TFSI, for three different systems with varying ionic concentrations: (a and b) 3.2 Li:PEO, (c and d) 3.9 Li:PEO, and (e and f) 4.2 Li:PEO. Each plot displays the MSD over a range of nanoparticle's concentrations from 0% Vol to 20% vol at 600K.

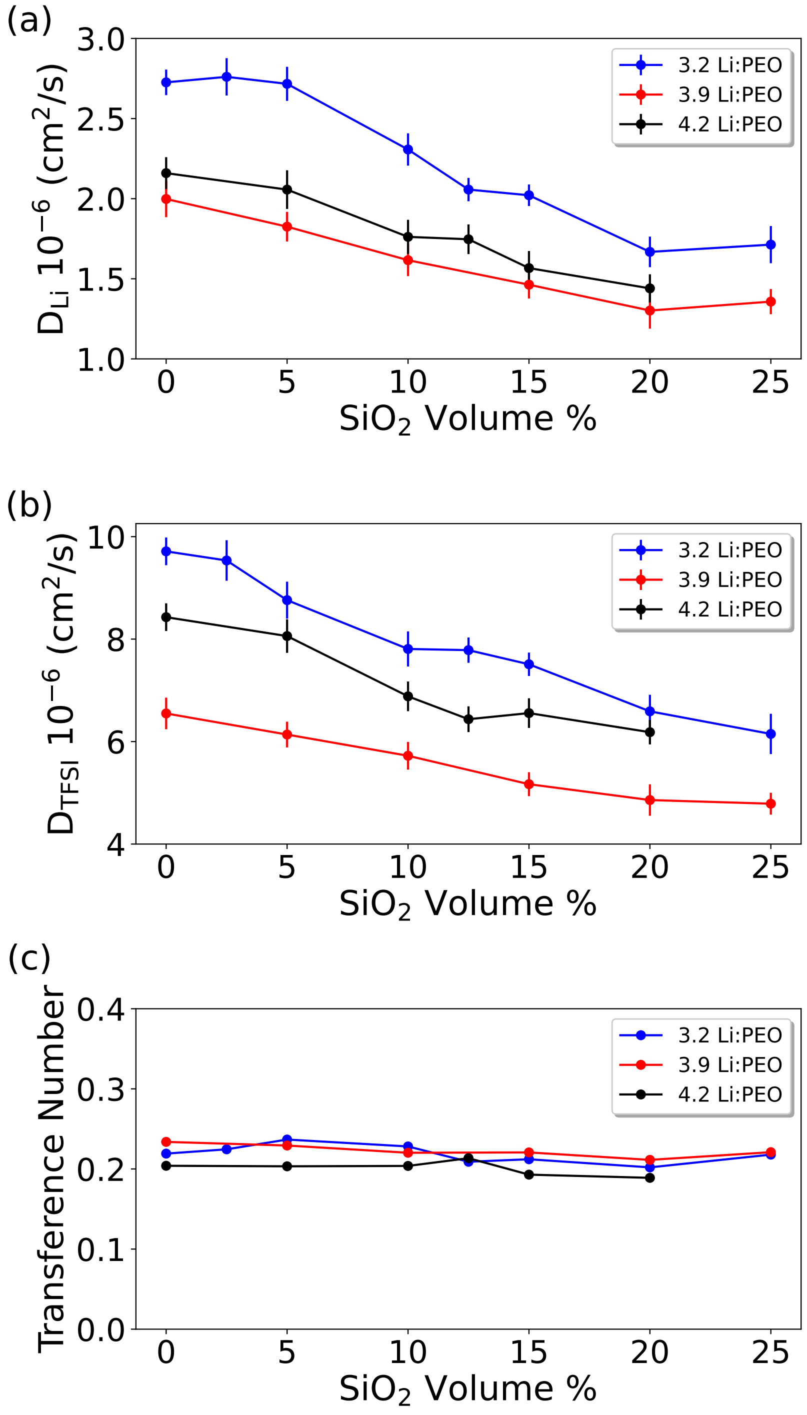

Figure 4.5: Diffusion coefficients for the two types of ions, namely (a) lithium and (b) TFSI, are examined in the same three systems as presented in Figure 4.4. Each curve illustrates the relationship between the diffusion coefficient and the concentration of nanoparticles, spanning from 0% to 25%. Additionally (c) we present the lithium's transference number corresponding to these data. Notably, all three curves exhibit a negative dependence on SiO_2 concentration, except for the blue curve, which shows an exception at the 2% nanoparticle content point for lithium.

increasing nanoparticle concentration, with minor exceptions, such as the 2.5% volume fraction point in the blue curve, which falls within the range of error, calculated after averaging over 5 runs. A similar trend is observed for TFSI, with a consistent reduction in diffusivity as nanoparticles are added.

We also calculate the transference number of lithium from the diffusion coefficient between the two species. Contrary to observations in other studies, such as [107], our results show no significant variation in the transference number, remaining approximately constant with the addition of SiO_2 nanoparticles, similar to other literature like [108].

Conductivity

Figure 4.6 shows the dependence of the electrolyte conductivity on silica content based on the results of Fig. 4.5. The addition of nanoparticles does not improve the conductivity; instead, it leads to a consistent decrease of ionic mobilities. This trend holds true for all three studied concentrations, showing a similar dependency on silica content. An additional subplot in the top right corner of the figure displays the normalized results, providing further clarity on the observed pattern. The dashed line represents a finite element solution of the diffusion equation, where we treat the SiO_2 nanoparticles as "empty space" inaccessible to ions, in the shape of spherical cavities arranged as a simple cubic lattice inside the diffusive medium. Remarkably, this simple model exhibits a similar trend to our MD simulation curves. The actual MD simulated values lie slightly below the diffusion equation solution. Other analytical and numerical approximations for the conductivity of a suspension of empty spheres yield similar results [222]. Experimentally, recent measurements on well-dispersed polymer nanocomposites have reported reductions below the Maxwell or Bruggeman models [125], which suggest an additional effect related to hindered segmental motion of the polymer in the proximity of the nanoparticles. This is in also in line with the MD simulations of ref.[131]. In our simulations, the nanoparticle's main effect on the conductivity stems from the fact that the space it occupies becomes unavailable for diffusion.

This finding is also in line with some of the most recent literature such as reference [124], which presents an experimental research on several active ceramics and gets to the conclusion that the nanoparticles do not enhance the conductivity of the polymeric electrolyte. We can also find examples of some other studies on passive ceramics, such as references [223, 224]. Dudney et al. found that incorporating a 30% volume fraction of ceramic nanoparticles resulted in a conductivity decrease of 60% from the original value. This result is similar to what we can expect in our system for 30% volume content of SiO_2.

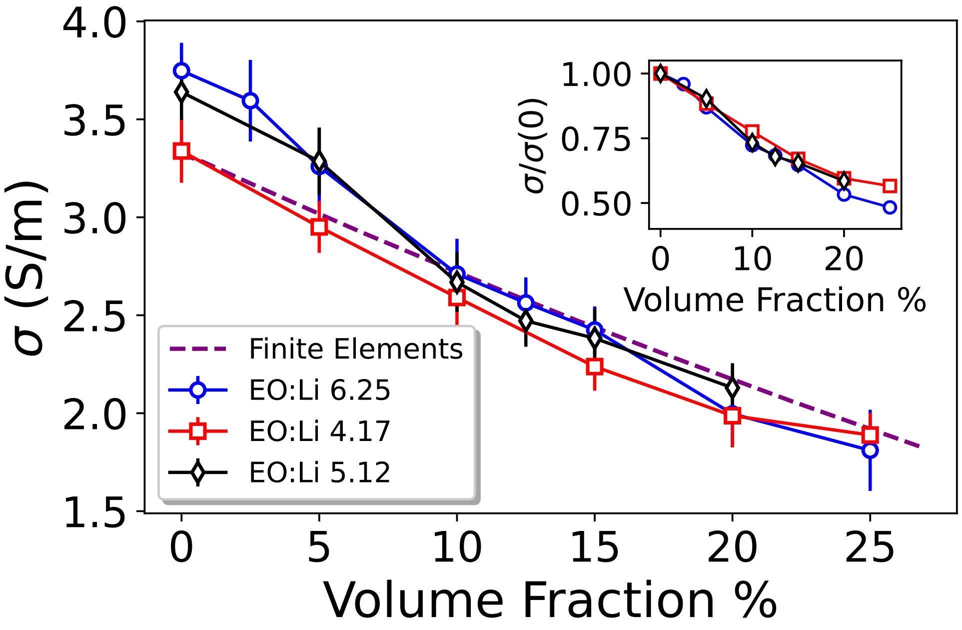

Figure 4.6: Ionic conductivity as a function of volume fraction of nanoparticles, ranging from 0% to 20%, for the same three systems studied in Figure 4.5. The dashed line corresponds to a finite element solution where the nanoparticles are considered as empty space, with an ionic concentration equal to the red curve. Notably, all the curves exhibit a negative dependence on the volume fraction of nanoparticles.

Conclusions

The conclusion drawn from this analysis is that the addition of nanoparticles does not enhance the conductivity of the polymeric system; instead, it hinders ion mobility and introduces additional volume that behaves as empty space, further impeding ion movement. Overall, the inclusion of silica has a detrimental effect on the conductivity of these electrolytes at temperatures above T_m, contradicting previous studies [41, 53, 54] that postulated the existence of a space-charge region at the interface between bulk PEO and nanoparticles.

4.3.3 Geometry effect on the dynamical properties

In this subsection, we explore the influence of nanoparticle geometry on ionic dynamics. While the previous section emphasized the significant impact of nanoparticle volume, we now investigate various sizes of spherical nanoparticles and the introduction of planar nanoparticles. The goal is to determine whether surface effects result from the addition of silica or if the observed effects are solely due to volumetric considerations.

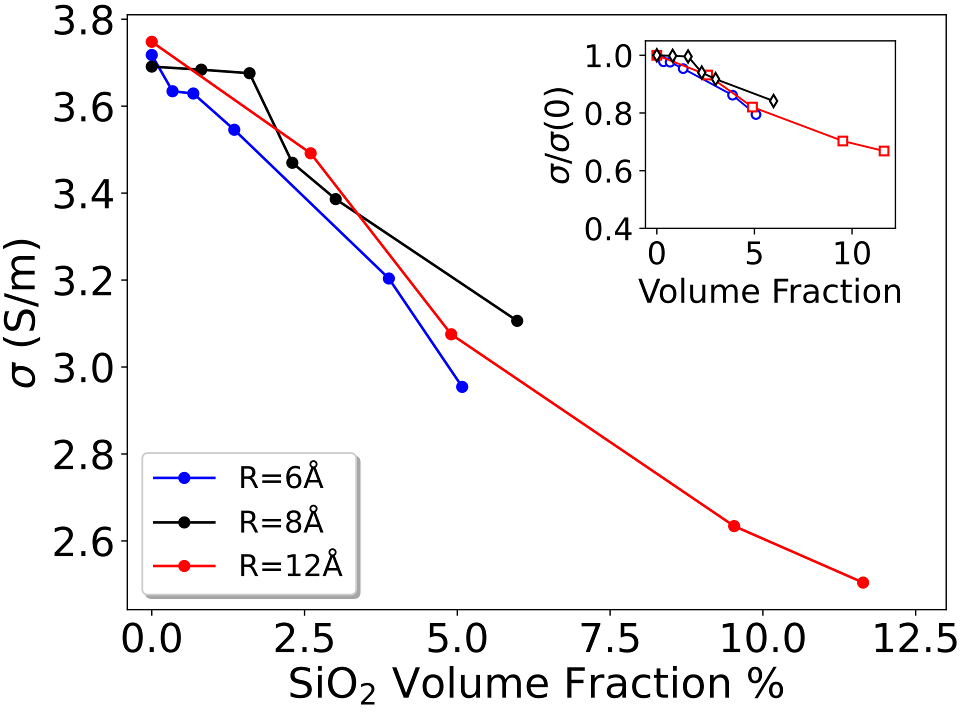

Figure 4.7: Ionic conductivity as a function of silica volume fraction for three distinct systems employing spherical nanoparticles of varying sizes, ranging from $r = 6$Å to $r = 12$Å. In all three cases, the ionic concentration is $3.2 Li : PEO$, and the temperature is maintained at 600K. A normalized data subplot is presented in the top-right corner of the figure.

Size of the nanoparticles

In Figure 4.7, we present an examination of three distinct systems, each characterized by nanoparticles of varying sizes. This graphical representation depicts the relationship between conductivity and the nanoparticle volume fraction within the electrolyte at a temperature of 600K. Additionally, an upper right subplot provides a normalized view of the three curves.

We employ CHARMM-GUI to generate smaller nanoparticles, following the same method used previously. To expedite the initialization process, we opted to remove the preexisting nanoparticles and replace them with the newly generated smaller ones in the positions originally occupied by the $r = 12$Å nanoparticles. Following a period of 12 ns of annealing and thermalization, the system achieves complete equilibration.

The red curve corresponds to data already analyzed in Figure 4.6, featuring nanoparticles with a radius of $r = 12$Å. All three systems contain an equivalent number of ions, corresponding to the optimal concentration of 3.2 Li:PEO or 2 mol/L at 0% nanoparticle content. Observations indicate that the other two curves exhibit comparable behavior to the initial nanoparticles. The blue curve, corresponding to nanoparticles with a radius of $r = 6$Å, also exhibits a negative correlation with the volume fraction of nanoparticles. This becomes evident in the normalized plot, where the two curves closely align.

The black curve corresponds to the use of nanoparticles with a radius of $r = 8$Å. The black curve features an outlier point at approximately 2.5% volume of SiO_2. This value is notably higher than that observed in the other two curves. However, this discrepancy may be attributed to statistical deviations, as for higher values, the black curve exhibits conductivity values that closely resemble those observed in the cases of $r = 6$Å and $r = 12$Å nanoparticle radii.

In summary, it appears that the size of the nanoparticles does not have a significant influence on the ultimate outcome of the simulation. In this context, the critical parameter of interest is the volume fraction of nanoparticles, rather than the individual sphere sizes themselves. The results point out that volume effects dominate over surface effects.

Planar nanoparticles

The introduction of planar nanoparticles offers a new perspective in the examination of dynamics. Since these new nanoparticle types are non-isotropic, our study of dynamics must shift away from isotropy. Due to the confinement along the z-axis by the silica wall, our analysis excludes this dimension, focusing solely on two-dimensional diffusion involving the x and y components of ion movement.

While the previous section (Section 4.3.2) revealed changes in diffusivity due to the volume effect, it remains unclear if surface effects influence it as well. To investigate this, we introduce a planar nanoparticle with a significantly higher surface-to-volume ratio. Calculating diffusivity in the parallel plane allows us to isolate the surface effect from the volume effect.

Figure 4.8 presents a comparative analysis of the diffusion coefficients for two ion types across various systems, including simulations without nanoparticles, simulation with spherical nanoparticles, and with planar nanoparticles. The first three scenarios pertain to a cubic simulation box geometry, namely, without nanoparticles (C 0N), with spherical nanoparticles at 2.5% volume content (C S-2.5%), and with a planar nanoparticle (C P-Nano) wich corresponds to a 16.6% volume content. Additionally, we provide simulation results for two elongated simulation box cases, one without nanoparticles (E 0N) and another with a planar nanoparticle (E P-Nano). The process to get this elongated systems is explained in section 3.3.6. To compare the surfaces of spherical and planar nanoparticles, we examine the number of hydrogen atoms present. The spherical C S-2.5% has 88 surface hydrogen atoms, while the planar C P-Nano has 578. The planar nanoparticle, C P-Nano, measures around 60Å in length and 14Å in thickness.

The outcomes with planar nanoparticles in a cubic box closely resemble those with spherical nanoparticles, both showing reduced conductivity. However, the error bars are wider, likely due to one less degree of freedom. Planar nanoparticles are chosen to minimize interference and focus solely on coordination parallel to them. Nonetheless, our findings suggest that the reduction in mobility persists, indicating that the decrease is not solely due to the interruption of movement caused by the volume effect. It is also influenced by subtle alterations induced by the nanoparticle surface on the interface atoms. However, the surface effect is relatively minimal, as the reduction observed with a 16.6% volume planar nanoparticle is equivalent to that seen with a 2.5% volume spherical nanoparticle, where volumetric effects are considered..

Elongated systems show higher lithium ion mobility compared to cubic ones, but this difference may be a simulation artifact rather than a physical effect. In the elongated simulation, the x and y coordinates are halved to approximately 34 Å, which can significantly affect outcomes due to periodic boundary conditions and interactions with molecular images. However, this difference is minimal and falls within the error range. The observed decrease in ion mobility in elongated systems remains significant.

In conclusion, the use of planar silica nanoparticles exerts a negligible impact on ion mobility, comparable to the effects observed with spherical SiO_2 nanoparticles. This points out that volume effect dominate over surface effects when using SiO_2 as the nanoparticles.

4.3.4 Ionic concentration dependence of the dynamical properties

Ionic concentration plays a critical role in PEO-based electrolytes, as highlighted in our previous study on structural properties (Chapter 3.3.4). This concentration marks a clear division between two regimes: the Low Concentration (LC) regime, characterized by lithium ion adsorption by PEO, and the High Concentration (HC) regime, characterized by PEO saturation with lithium ions. This distinction occurs at a threshold concentration of 3.2 Li:PEO, equivalent to 2 mol/L. We will refer to these regimes as LC and HC, with the threshold concentration termed the "optimal concentration," as we will explain later in this subsection.

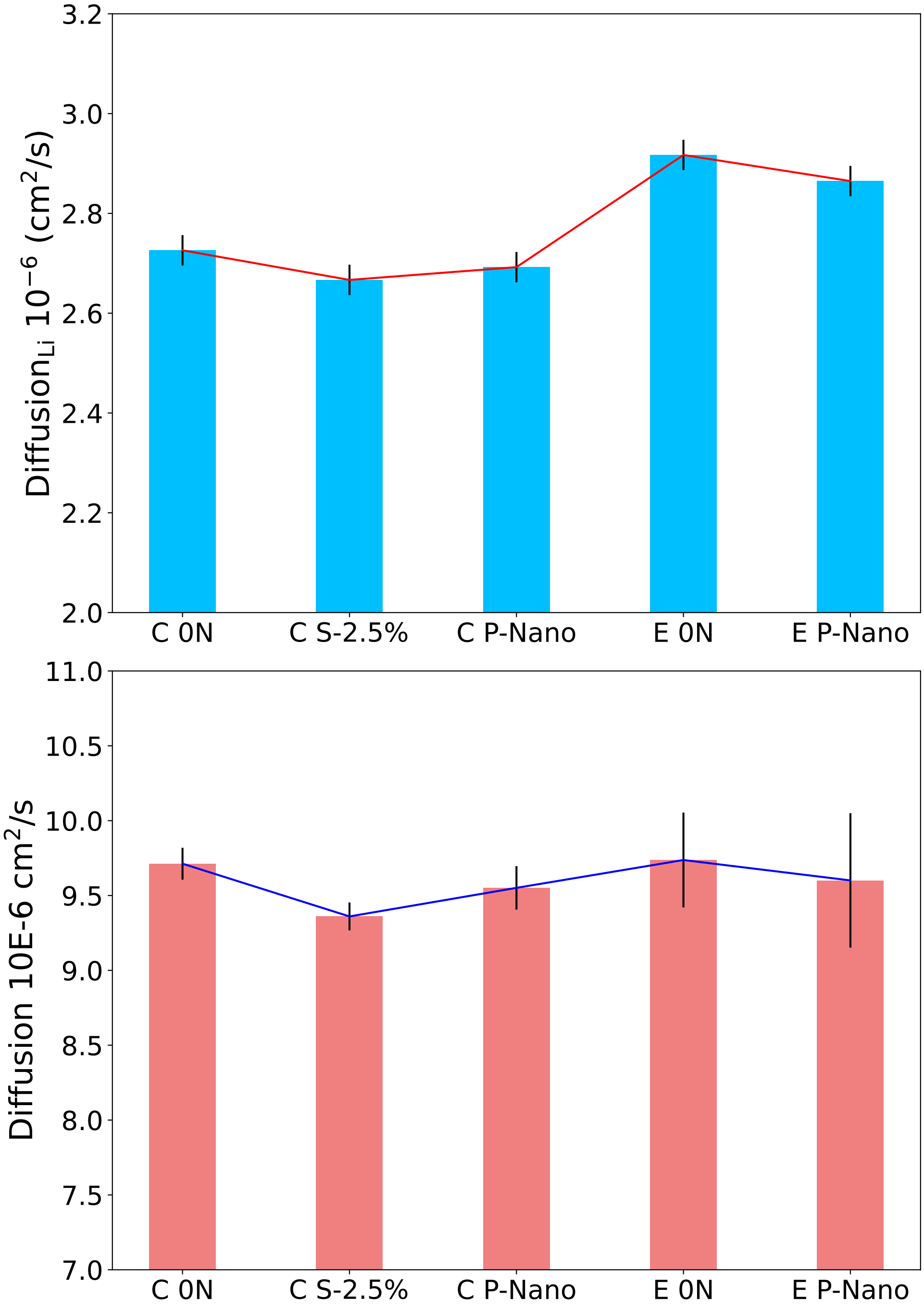

Figure 4.8: Diffusivity of (top) lithium and (bottom) TFSI compared across five different systems with varying box and nanoparticle geometries. The red (top) and blue (bottom) lines represent the different diffusivities, while the black segments denote the corresponding error bars.

Mean Squared Displacement

Figure 4.9 illustrates the correlation between Mean Squared Displacement (MSD) and ionic concentration for lithium and TFSI ions in our systems. We examine four different systems, varying in nanoparticle content from 10% volume fraction of SiO_2 nanoparticles to 0%. All simulations are conducted at a constant temperature of 600K and span a wide range of ionic concentrations, from approximately 0.15 mol/L or 0.2 Li:PEO to high concentrations around 4.5 mol/L or 9.6 Li:PEO.

Figures 4.9(a) and 4.9(b) display the MSD profiles for lithium and TFSI ions in the system with a 10% volume fraction of SiO_2 nanoparticles. In both cases, there is a clear negative correlation between MSD and ionic concentration, resulting in decreasing MSD values as ion concentration rises. Additionally, it is noteworthy that TFSI consistently exhibits higher diffusion coefficients than lithium across all systems.

This trend persists in the other systems depicted in Figures 4.1(c), (d), (e), (f), (g), and (h). In each instance, TFSI demonstrates higher MSD values compared to lithium, and there is a consistent inverse relationship between MSD and ionic concentration.

When comparing the four systems, the one with 10% volume fraction of SiO_2 nanoparticles consistently exhibits lower MSD values for both lithium and TFSI ions than the 5% system. This pattern is maintained when comparing other systems, with MSD generally increasing as nanoparticle content decreases.

To gain a more comprehensive understanding of atom mobility, we will now focus on the examination of diffusion coefficients.

Self-diffusion

Figure 4.10(a) displays the dependence of the diffusivities of both ions with respect to the ionic concentration. In the LC regime, both elements show a constant decrease of the diffusivity, with the TFSI diffusing much faster than the lithium. However, at 1.5 mol/L for the Li^+, or 2 mol/L for the TFSI, there is a marked change in slope, where the D coefficient starts decreasing faster. In addition, after surpassing the 2 mol/L point, the diffusivity of Li^+ changes again its behavior and starts a transition to a very slow decrease, while that of TFSI keeps decreasing all the way to 4.5 mol/L.

The earlier change in slope observed in lithium diffusivity, preceding a similar change in TFSI behavior, suggests a causal relationship between the two. It is likely that the alterations in lithium behavior, such as expansion throughout the system, drive the subsequent structural changes that occur at approximately 2 mol/L. However, it's possible that these effects become more pronounced when the concentration of "free" ions is sufficiently large, allowing lithium's influence to become more noticeable before

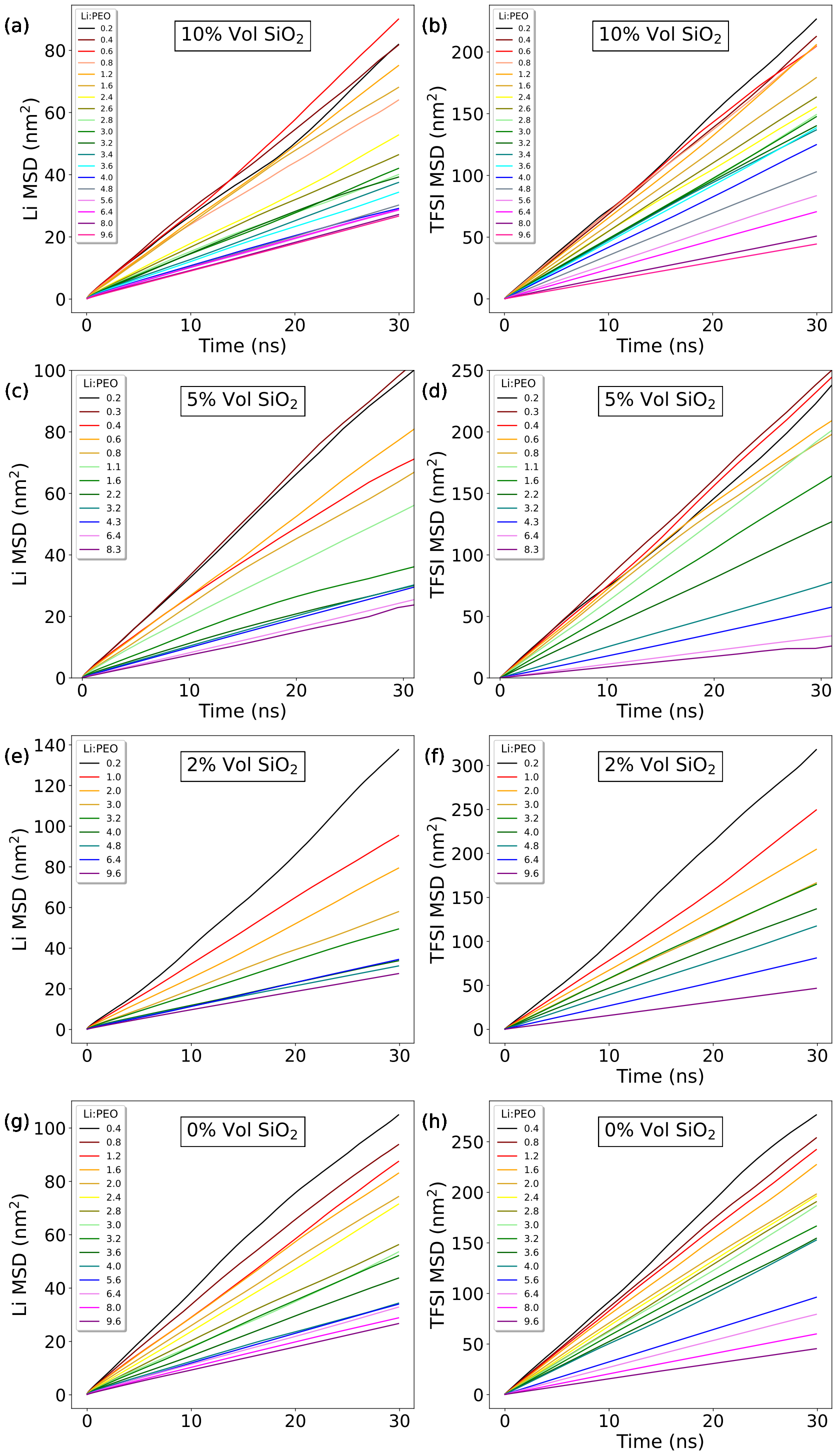

Figure 4.9: Mean Squared Displacement (MSD) of the two ionic species, namely (left) Lithium and (right) TFSI, investigated across four systems with varying nanoparticle concentrations: (a and b) 10%, (c and d) 5%, (e and f) 2%, and (g and h) 0%. All systems are maintained at a constant temperature of 600K. Each plot displays the MSD over a range of ionic concentrations, ranging from $0.2 Li : PEO$ to $9.6 Li : PEO$ (see input).

affecting other species.

In Figure 4.10(b), we present data on the transference number, which is derived from the diffusion coefficient data. In the low concentration (LC) regime, there is a slight decrease in the transference number, reaching its minimum at a concentration close to 2 mol/L. Beyond this point, as we transition into the high concentration (HC) regime, the transference number begins to steadily increase. This can be understood by looking at the individual contributions to the conductivity from lithium and TFSI in Fig. 4.10(a).

The transference number, defined in Equation 2.18, plays a critical role in battery electrolytes. A lithium ion's transference number close to 1 signifies that a significant portion of the charge transport within the electrolyte is carried by lithium ions, rather than counterions. This high transference number is crucial for battery efficiency because it ensures efficient charge transport by lithium ions, which is essential for battery performance.

Hence, it is crucial to examine not just overall conductivity but also the changes in the transference number. Molecular dynamics (MD) techniques offer a valuable tool for in-depth exploration. A pertinent example of such research is presented in [225], which observes a similar trend, confirming the validity of our findings.

Conductivity

In figure 4.11 we present the conductivity driven by the two ions of the system. Figure 4.11 (a) represents the partial conductivity of the individual species and 4.11 (b) represent the total conductivity of the system, calculated by using the Nerst-Einstein equation 2.17. We study 4 systems with varying concentration of nanoparticles, from 10% to 0% as in the previous pages.

In the previous page we have studied the dependence of the diffusion coefficient of the two species with ionic concentration and observed a change in the slope at 3.2 Li:PEO $\approx$ 2 mol/L. The combination of this change in the slope, added to a constant increase in the number of ions translates to the conductivity curves (Fig. 4.11) as a maximum in the conductivity at this points. That is the reason why we refer to this concentration as the "optimal conductivity" as it is the one in which we can obtain the maximum conductivity of the system.

Figure 4.11 illustrates the dependence of conductivity on ionic concentration for four systems with increasing ceramic content. We can see that the ionic and nanoparticle concentrations both impact the transport properties. The black line represents the conductivity obtained from a simulation without nanoparticles. As previously mentioned, the maximum conductivity is achieved at a concentration of 2 mol/L, in agreement with the findings of Molinari et al. [77]. The optimal concentration remains constant

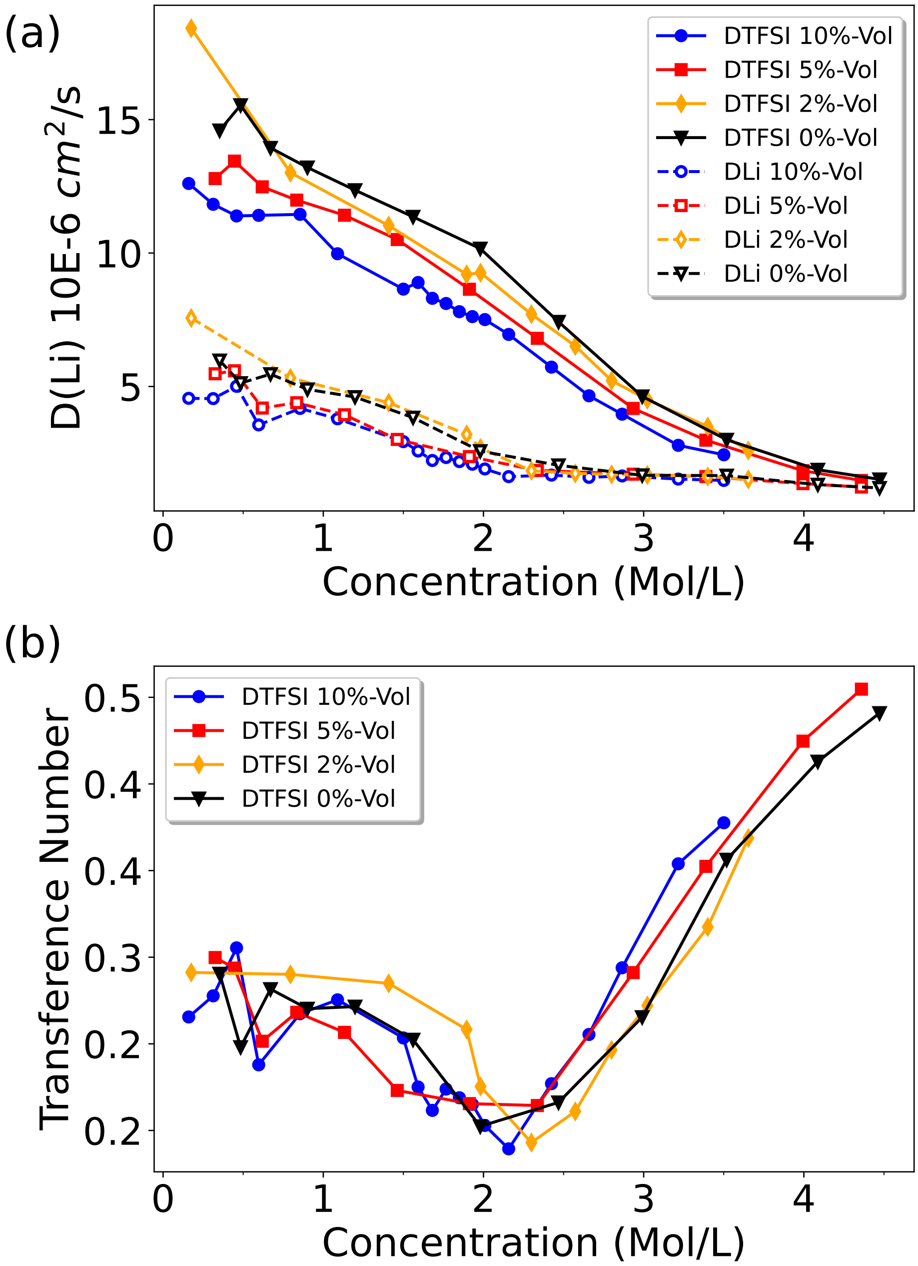

Figure 4.10: (Top) Diffusion coefficients for the two types of ions and (bottom) transference number of lithium ions are examined in the same four systems as presented in Figure 4.9. Each curve illustrates the dependence of the self-diffusion coefficients (top) or transference number on the ionic concentration, expressed in mol/L. Notably, around 2 mol/L, there is a change in the slope of the diffusion curves and a minimum in the transference number.

while the nanoparticle content is gradually increased up to 10% volume. However, despite following the same trend in all cases, the conductivity values consistently exhibit a decrease with silica content.

The TFSI partial conductivity is very similar to the total conductivity curve in Fig.4.11(b). This means that the total conductivity is dominated by the behavior of TFSI. In contrast, the lithium conductivity displays a much softer peak, at a lower ionic concentration around 1.5 mol/L. We attribute this difference in the optimal ionic concentrations between Li and TFSI to the fact that oxygen atoms of PEO are saturated by Li before the hydrogens of PEO are saturated by TFSI, as will be shown in the next section. Slightly before the oxygen of PEO are fully saturated, less oxygen sites become available for lithium hopping, and diffusivity is already impacted at 1.5 mol/L. In contrast, the diffusivity of TFSI changes due to the presence of non-solvated Li ions, only after the full saturation of the oxygen atoms of PEO at 2 mol/L. Above 1.5 mol/L, σ_{Li} decreases slightly and then rises again and keeps a constant value.

Surprisingly, the transference number shows the opposite trend as the conductivity, as shown for various nanoparticle loading values on fig. 4.10. The curves present a minimum at the concentration that maximizes $\sigma \sim 2$, roughly mol/L and display the same trend as obtained in a recent simulation for bulk PEO [225], which itself re-analyzed earlier experimental results from ref. [226]. The quantitative differences of about 10% with respect to that simulation may stem from the neglect of the Onsager cross terms by the Nernst-Einstein approximation.

Conclusions

Our findings highlight the presence of distinct concentration regimes, namely, the low concentration (LC) and high concentration (HC) regimes, with a critical transition occurring at approximately 2 mol/L. the difference between these two regimes is observed in various key properties, including conductivity (Fig.4.11), diffusion, and transference number (Fig.4.10).

In the LC regime, we observe a minor reduction in transference number accompanied by an increase in conductivity, eventually reaching a minimum around a concentration close to 2 mol/L. Transitioning beyond this point leads to the HC regime, characterized by a steady increase in the transference number while the conductivity experiences a decline. This behavior can be understood by examining the individual contributions to conductivity from lithium and TFSI, as illustrated in Fig. 4.10(a).

The transference number's minimum at 2 mol/L arises from σ_{TFSI} exhibiting a distinct peak, while σ_{Li} remains relatively stable, given that transference number $t_{Li} = \frac{\sigma_{\mathrm{Li}}}{\sigma_{\mathrm{Li}}+\sigma_{\mathrm{TFSI}}}$ in agreement with the findings from ref [225].

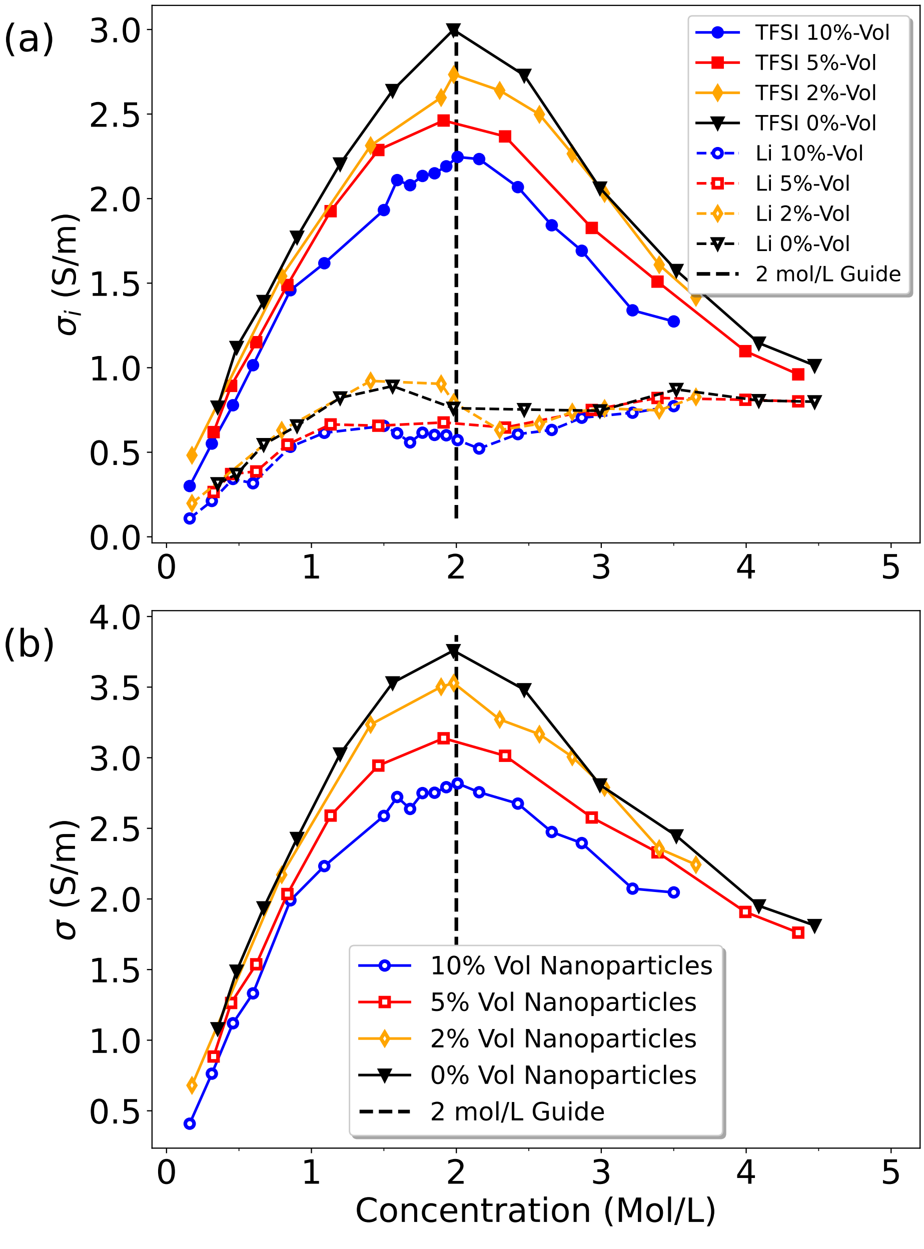

Figure 4.11: (Top) Partial conductivity of the two ionic species and (bottom) total conductivity of the system as a function of ion concentration within the system. The same four different systems as presented in Figure 4.10 are studied. Notably, as the concentration of nanoparticles increases, the conductivity decreases for all partial and total conductivity curves. The total conductivity and partial TFSI conductivity exhibit a distinct maximum at 2 mol/L, while a less pronounced maximum appears at 1.5 mol/L in the case of the partial conductivity of lithium.

Notably, our research has identified an optimal conductivity concentration at 2 mol/L, a finding that holds true even when nanoparticles are introduced into the system. This observation aligns with previous literature, such as the study conducted by Molinari et al. [77]. In their research, they investigated the pure solid polymer electrolyte (SPE) system composed of PEO and LiTFSI, specifically analyzing the relationship between conductivity and ionic concentration. Their findings also revealed a peak conductivity at the concentration of 2 mol/L, in agreement with our results.

It is noteworthy that we calculate a different optimal concentration for lithium's partial conductivity than for the total conductivity, which appears at 1.5 mol/L. This unexpected finding has significant implications for practical applications, as the conductivity of lithium takes precedence over that of TFSI.

Regarding the influence of nanoparticles, our examination of dynamic properties across a range of ionic concentrations corroborates our earlier observations in the preceding section (Sec. 4.3.2). There, we identified a negative impact stemming from nanoparticle addition, comming from a volumetric effect. In this section, we have extended our analysis to encompass a variety of nanoparticle concentrations, reaffirming the conclusion that nanoparticles do not enhance the electrolyte's conductivity. Instead, they exert an adverse effect on ion mobility and overall system conductivity.

Chapter 5

Al2O3

Abstract

In this chapter, we replace our previous silica nanoparticles with alumina, resulting in significant structural differences. This change has a profound impact on lithium behavior. Unlike silica, our results show that alumina exhibits strong coordination with lithium, causing some lithium ions to adhere to the nanoparticle's surface. Consequently, there is a notable decrease in lithium diffusivity, as those ions attached to the nanoparticle's surface no longer diffuse freely.

On the other hand, TFSI behaves differently. It does not coordinate with alumina, in contrast to its behavior with silica. The presence of alumina causes Li^+ ions and PEO to coordinate with its surface, drawing them closer to the nanoparticles. This, in turn, reduces their influence on TFSI, allowing it to move more freely within the electrolyte. As a result, TFSI's diffusivity slightly increases, while the transference number of the electrolyte decreases.

The analysis of dynamic properties reveals a decrease in lithium diffusivity and an increase in TFSI diffusivity. Notably, we initially adopted the alumina force field parameters from reference [130]. Our findings diverge from the results presented in this paper, as they observed an enhancement in lithium diffusivity when alumina was added. Consequently, in light of this disparity, we decided to employ their entire force field, rather than solely integrating the alumina parameters.

The new force field introduces minor changes in most parameters, with the most significant differences found in the charges of TFSI, which are, on average, much larger. These alterations in the force field result in a strong coordination between lithium and TFSI. Consequently, both ions experience a substantial decrease in diffusivity, and the presence of nanoparticles negatively affects both diffusion coefficients.

Our findings with the second force field exhibit similar structural results compared to the reference [130]. However, the dependence of dynamical properties on the alumina content is still very different.

In summary, our comparison of the two employed force fields indicates that the first force field (FF) provides a notably more accurate description of the electrolyte's structural properties in the same system. This is because in these conditions, LiTFSI should be fully decoupled due to PEO's effectiveness as a solvent for this type of salts. This decoupling is evident in our observations within the first force field, while the second force field demonstrates clear coupling between the ionic species. This distinction is also noticeable in Wang's reference, further emphasizing the suitability of the first force field for characterizing PEO's electrolytes.

5.1 Introduction

Within the domain of passive hybrid fillers for electrolytes, three prominent ceramics emerge as promising fillers: SiO_2, TiO_2, and Al_2O_3. The preceding two chapters have analyzed PEO+LiTFSI+SiO_2 hybrid solid electrolytes, aiming to uncover any potential enhancements in their dynamical properties resulting from the inclusion of SiO_2. However, our deep analysis revealed no discernible improvements.

In order to validate the generalizability of our findings across other passive filler materials, we shift our attention to an additional ceramic. The research done by Wang and coworkers [130] has conducted a computational study on PEO+LiTFSI+Al_2O_3, employing a methodology closely aligned with our approach for silica. They too have employed Lammps and the OPLS-AA force field, incorporating standard parameters for PEO and LiTFSI to simulate the electrolyte system. They have provided in their paper the parameters required for simulating alumina. Wang et al. obtained an enhancement in conductivity akin to the results reported by Croce et al. in their investigations involving Al_2O_3 and TFSI[53], as well as Scrosati's work on silica[59].

This chapter delves into the hybrid solid electrolyte comprising PEO+LiTFSI+Al_2O_3. We analyze its properties, drawing comparisons between this system and our prior work on silica. Additionally, we juxtapose our findings with the computational investigations in reference [130] and experimental studies conducted by Croce and Scrosati[53, 59, 54].

5.2 Simulation Details

To investigate the system involving Al_2O_3, we use the LAMMPS software, maintaining consistency with our previous simulations. In line with Wang et al.'s approach [130], we choose an ionic concentration different from our previous settings of 3.2 Li:PEO or 6.25

EO:Li ratios. Instead, we shift to a concentration of 20 EO:Li to ensure direct comparability with Wang's reference data. Our simulation framework retains a configuration of 100 PEO molecules, each comprising 20 monomers per chain.

The initialization process for the system involves several steps. First, we remove the existing ions and nanoparticles from the simulation box. Then, we introduce the new Al_2O_3 nanoparticles to occupy the spatial voids left by the silica nanoparticles. Afterwards, we randomly position the new ions within the simulation box. The system then goes through an annealing and thermalization process to reach equilibrium.

The geometry of the new nanoparticles closely resembles that of Wang et al.'s reference [130], featuring rectangular prism-shaped structures. To initialize these nanoparticle structures, we emplyed CHARMM-gui, as we did to generate the SiO_2 initial structure. We then externally incorporated the force field parameters through a Python script. It's important to mention that Wang's reference provides only non-bonding parameters for Al_2O_3 and specifies that the positions of Al_2O_3 nanoparticles were held fixed. We also maintain this constraint in our simulations.

We apply periodic boundary conditions in all three dimensions of space, truncating the nonbonding terms in equations 2.8 and 2.9 with a cutoff distance of 10 Å, while the long-range part of the Coulombic interactions have been computed with a particle-particle particle-mesh solver(PPPM) [227], with a relative RMS error in the per-atom forces of 10^{-4}.

Atoms within macro-molecules interact with neighbors separated by up to three bonds via an intramolecular potential, $V_{\text{intra}} = V^b + V^a + V^d$, sum of a stretching 2.10, bending 2.11 and dihedral 2.12 torsion terms. The complete force fields used in this part of the research are available in the supplementary data. We will refer to the initial force field as "FF1," and the second one as "FF2" in table 5.1. We used the standard method of excluding or reducing the pair interactions of Eqs. (2.8 and 2.9) by setting weighting coefficients $(w^b, w^a, w^d) = (0, 0, 1/2)$ for atoms involved in Eqs. (2.10, 2.11 and 2.12), while $w = 1$ for further atoms.

We considered three temperatures, 300K, 333K, and 363K to compare with litterature data.

5.3 Results: Structural Properties

We will first focus our attention on the structure of the electrolyte with a particular emphasis on the changes driven by the alumina into the overall system. We will start by analyzing the radial distribution function of each of the individual components of the electrolyte. After that we will analyze the temperature dependence of the system and the dependence of the RDF with the concentration of alumina.

5.3.1 General structure of the electrolyte

Lithium

Figure 3.1 presents the radial distribution function (RDF) providing a detailed view of the spatial arrangement of atoms surrounding lithium ions. This analysis is conducted under specific conditions, including a temperature of 363K, a 5% volume fraction of Al_2O_3, and an ionic concentration of 1 Li:PEO or equvalently, 20 EO:Li. These conditions will remain constant throughout the subsequent parts of this subsection.

Lithium exhibits strong coordination with the oxygen atoms of both PEO and the nanoparticles. However, lithium's coordination with TFSI is minimal. Unlike with silica nanoparticles, lithium in this context not only coordinates with PEO but also tends to adhere to the nanoparticle's surface, which marks a distinct difference from the previous ceramic.

The RDF graph highlights two prominent RDF functions. The first, denoted as $g_{Li}^{O_{\mathrm{Nano}}}(r)$, exhibits a distinct first maximum at $r = 1.88$, with an intensity of $I = 26.6$. The second, represented by $g^{O1_{\mathrm{PEO}}}Li(r)$, displays a peak at $r = 2.18$, with a maximum intensity of $I = 20.7$. These large coordinations on the first shell indicate the preferential distances at which lithium ions are most likely to interact with the surrounding oxygen atoms.

With Figure 3.1 at our disposal, we can gain valuable insights into the spatial distribution of lithium ions under the specified conditions. Notably, lithium ions exhibit a strong affinity for oxygen atoms in both PEO and alumina, as evidenced by the prominent peaks in their distribution functions. In contrast, the $\mathrm{O_{TFSI}}$ species show no significant coordination with lithium ions in this scenario. The biggest variation comparing to the electrolytes with silica comes from the strong interaction between the cations and the nanoparticles, suggesting that the ions may form strong interactions with the $\mathrm{O_{Nano}}$ and thus they adhere to it surface, as figure 5.2 shows. This highlights a distinct preference for certain ion-atom interactions under the influence of Al_2O_3 nanoparticles, shedding light on the complex dynamics of this hybrid system.

Polyethylene Oxide

Figure 5.3 illustrates radial distribution functions (RDFs) centered on the oxygen and hydrogen atoms within polyethylene oxide (PEO).

Polyethylene oxide atoms exhibit strong coordination with Li^+ ions, similar to what

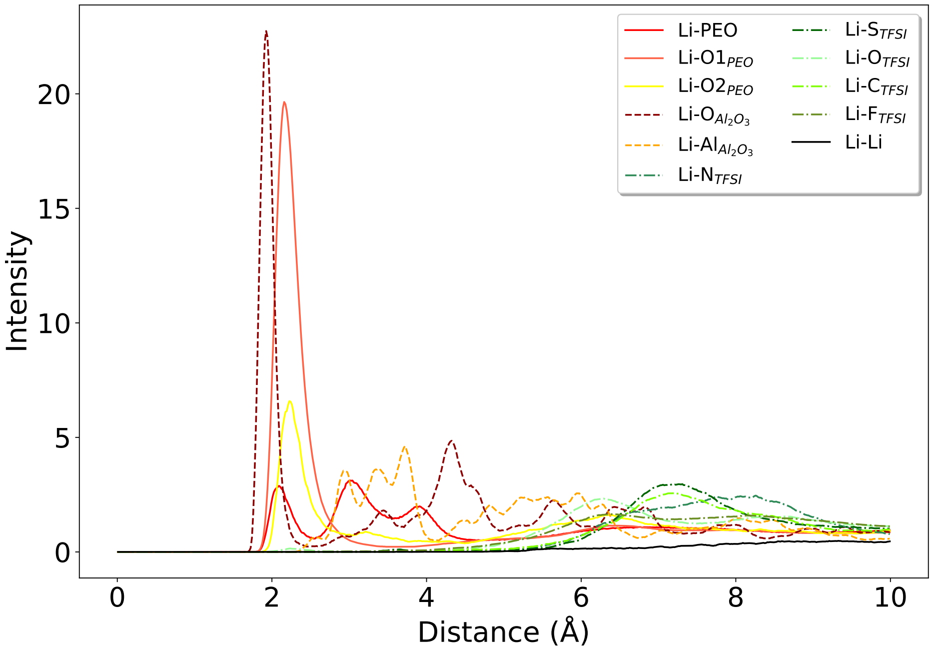

Figure 5.1: Radial distribution function depicting the distribution of some atomic species in the simulation centered around Lithium. The dashed red curve outstands, indicating a strong interaction between lithium and $O_{Al_2O_3}$. The red and yellow solid curves correspond to the oxygen atoms within the PEO, demonstrating as well alumina, a high coordination with lithium.

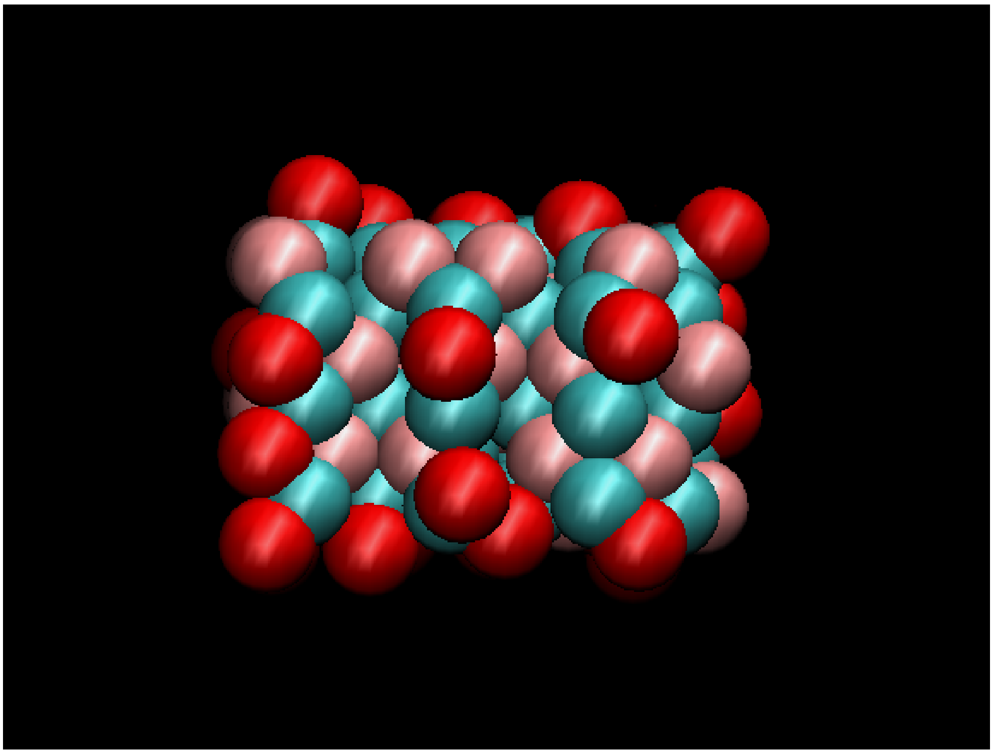

Figure 5.2: Visual representation created using VMD software, showing a single alumina nanoparticle. The snapshot illustrates how the lithium ions are adsorbed at the alumina surface. The elements represented in the figure are lithium (red), oxygen (cyan), and aluminum (pink).

occurs when using silica nanoparticles. Additionally, PEO displays a significant coodination with the nanoparticles, in contrast to its previously weaker interaction with silica.

In Figure 5.3, one RDF curve stands out, the one representing the correlation with lithium. It exhibits the highest intensity, surpassing all other RDF distributions centered on PEO atoms. At a distance of 2.11Å, within the first coordination shell, this curve reaches its maximum intensity at $I = 20.8$. This observation aligns with the results presented in Figure 5.1, underscoring the importance of the interaction between lithium and PEO. It is worth mentioning that this peak correspond to one of the two types of oxygen atoms in PEO, however, the second more intense curve, in red, corresponds to the other oxygen.

Additionally, we observe other significant interactions in the RDFs. The purple curve represents the coordination between oxygen atoms in PEO and aluminum atoms ($\mathrm{g}_{\mathrm{O}_{\mathrm{PEO}}}^{\mathrm{Al}_{\mathrm{Nano}}}(\mathrm{r})$). It peaks at $r = 2.29$Å within the first shell, with a maximum intensity of $I = 4.1$.

The next most intense curve is in blue and signifies the correlation between oxygen atoms of the nanoparticle and oxygen atoms of PEO. However, it is important to note that this coordination arises due to the proximity of oxygen atoms in PEO to aluminum atoms in the nanoparticle.

Additionally, a distinct but much weaker peak appears at extremely close distances in the RDF, with a maximum intensity of $I = 0.62$ at $r = 1.50$Å, a very close proximity. This represents the coordination between hydrogen atoms in PEO and oxygen atoms in the nanoparticle ($\mathrm{g}_{\mathrm{H}_{\mathrm{PEO}}}^{\mathrm{O}_{\mathrm{Nano}}}(\mathrm{r})$). Despite its lower intensity, the proximity at such a short distance highlights the coordination between hydrogen and alumina oxygen atoms.

In summary, lithium ions remain the primary contributors to PEO's coordination, consistent with previous observations in the absence of nanoparticles and when using silica, as discussed in the previous chapters. However, a notable difference in this simulation is the pronounced influence of alumina nanoparticles on the $\mathrm{g}_{\mathrm{PEO}}^{\mathrm{j}}(\mathrm{r})$ curves. This signifies a close coordination between PEO and alumina nanoparticles, distinguishing it from the less significant interactions observed with silica nanoparticles (see Section 3.3.1).

Alumina

Figure 5.4 presents radial distribution function (RDF) curves, offering insights into the interactions between alumina and other atoms in the simulation. It displays the most significant $g_i^j(r)$ curves for the two types of atoms within the nanoparticles.

Alumina exhibits strong coordination with lithium, leading to the adherence of lithium

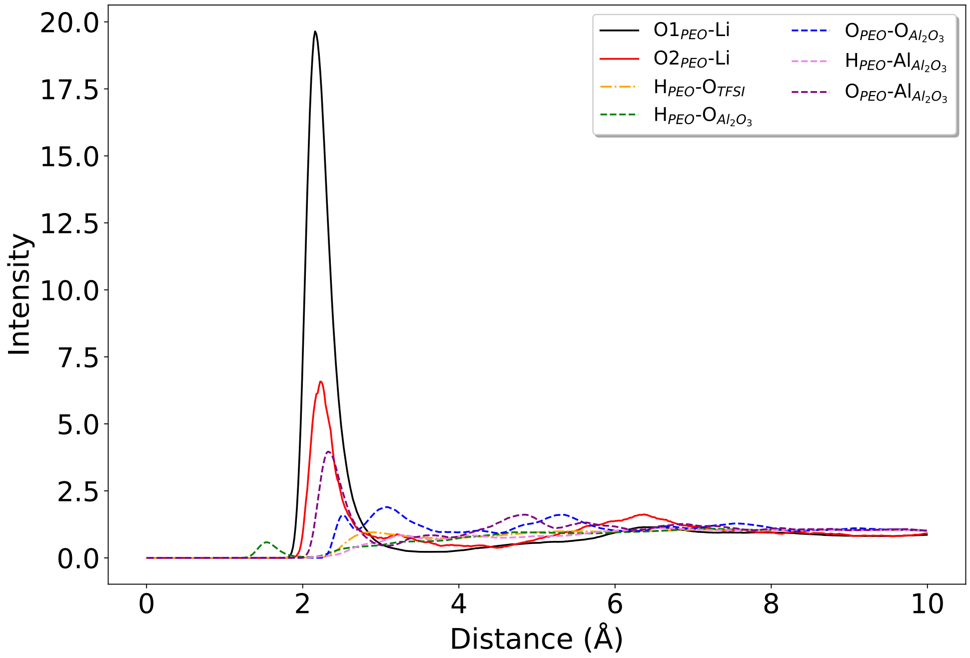

Figure 5.3: Radial distribution function depicting the distribution of some atomic species in the simulation centered different PEO atoms. The dashed line represents the cumulative distribution of all individual curves. Notably, the black curve stands out, corresponding to the lithium ions, indicating a strong coordination between the ions and the oxygen of the PEO. This observation complements what was observed in Figure 5.1

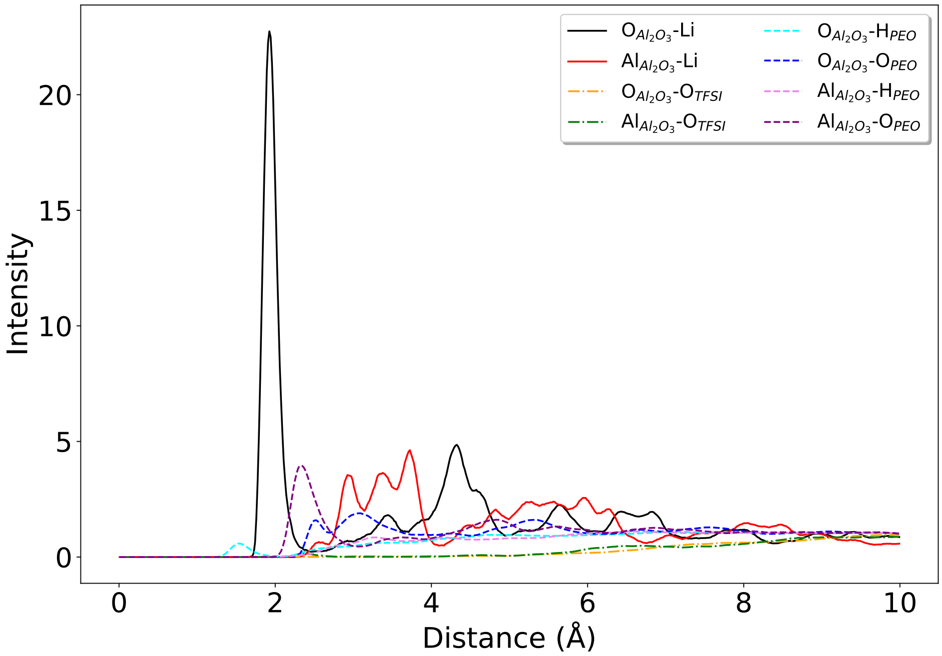

Figure 5.4: Radial distribution function centered around the alumina atoms. The black solid curve, corresponding the oxygen interaction with lithium shows a high intensity, as it happened in the corresponding figure 5.1

ions to its surface. Additionally, it shows notable coordination with the oxygen atoms of PEO, with hydrogen atoms from PEO being its closest coordinating atoms.

In Figure 5.4, we observe several key interactions. The most prominent peak in the first shell corresponds to the coordination between oxygen atoms of alumina and lithium ($g^{Li}_{O_{Nano}}(r)$), consistent with our previous discussion on lithium's structure. Another significantly strong interaction is evident between aluminum atoms and oxygen atoms of PEO ($g^{Al_{Nano}}_{O_{PEO}}(r)$), as previously mentioned. Additionally, a smaller yet noticeable coordination exists between the oxygen atoms of alumina and the hydrogen atoms of PEO ($g^{O_{Al_2O_3}}_{H_{PEO}}(r)$).

However, it is important to emphasize that there is no strong interaction between alumina and TFSI ions, in contrast to the alumina interactions observed with the other elements in the electrolyte.

These findings indicate that alumina primarily interacts with lithium ions. As the strong an sharp peak indicates that lithium ions tend to adhere to the surface of Al_2O_3 upon reaching it, which differs from the patterns observed in the chapter involving SiO_2 as the electrolyte. Additionally, alumina exhibits significant interactions with

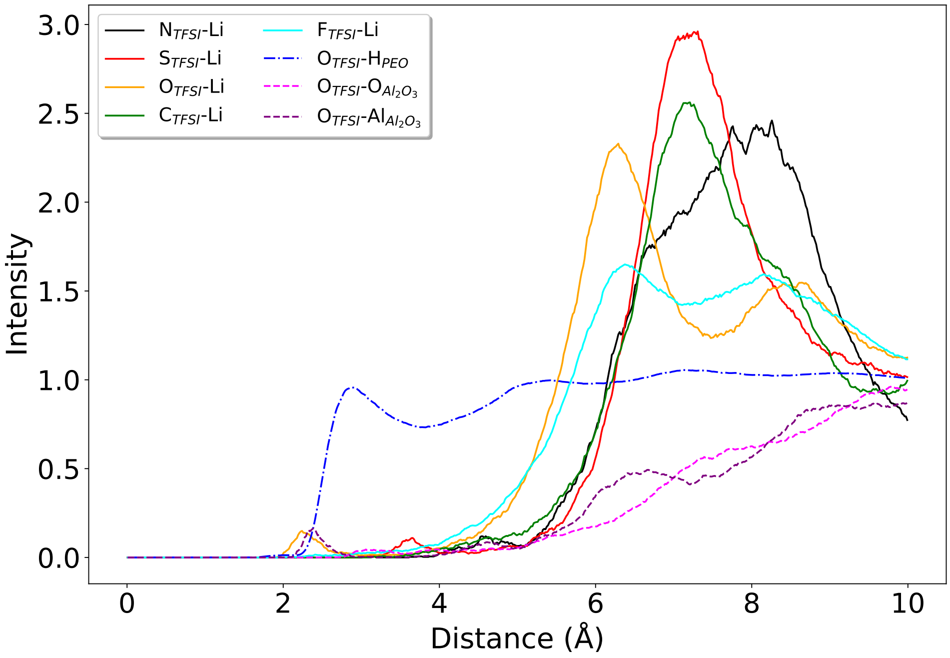

Figure 5.5: Radial distribution function centered around the atoms of TFSI. The figure indicates low coordination with other atoms apart from $\mathrm{H_{PEO}}$.

PEO, although these interactions have less pronounced intensity compared to lithium. Notably, unlike silica, there is no observable correlation between TFSI ions and the alumina nanoparticles in this simulation.

TFSI

Figure 5.5 illustrates the radial distribution function (RDF) curves, offering insights into the interactions of TFSI elements with other atoms within the simulation.

TFSI does not exhibit significant coordination in its first coordination shell. It is primarily surrounded by hydrogen atoms from PEO, without any distinct ordering or clear shell structure. There is a second coordination shell at distances around $r = 6-8$Å consisting of lithium, but with no relevant coordination at short distances.

In Figure 5.5, the most significant RDF corresponds to the blue curve, representing the interaction between $\mathrm{O_{TFSI}}$ and $\mathrm{H_{PEO}}$, $\mathrm{g^{H_{PEO}}_{O_{TFSI}}}$ at a distance of $r = 2.92$Å, which is relatively large for a first shell, with a low intensity of $I = 0.98$.

The most intense peaks correspond to the interaction between different atoms from TFSI and lithium. These maximum intensities appear at distances ranging from 6 to 8 Å, similar to what was observed in the case without nanoparticles.

In summary, the analysis indicates that TFSI does not establish strong coordination with the other molecules in the simulation. TFSI ions appear to move freely, with their closest coordination being with the abundant hydrogen atoms of PEO. In contrast to the case of silica nanoparticles, TFSI has minimal contact with alumina. The robust interaction between alumina and lithium keeps these ions separated from TFSI, preventing their coordination at close distances.

Conclusions

The structure of the new electrolyte is significantly influenced by the strong charges of the atoms comprising the alumina nanoparticles. These substantial charges result in powerful interactions with atoms in proximity to the filler's surface, ultimately leading to structural alterations when compared to the SPE-equivalent system.

Lithium atoms, carrying a positive charge of +0.8e, form strong bonds with the oxygen atoms of alumina, which bear a charge of -0.945e, resulting in their attachment to the alumina surface. Similar interactions occur between O_{PEO} and aluminum. However, due to the larger size of the PEO molecule and its numerous other interactions, it does not readily adhere to the alumina surface.

TFSI does not engage in strong interactions with any specific atom, primarily because of its highly delocalized charge.

5.3.2 Temperature Dependence

The question we want to answer is: does temperature has a significant effect on the structure of the electrolyte?

Figure 5.6 provides an overview of the temperature-dependent radial distribution functions (RDF) for the most relevant interactions within the system. Each graph in the figure corresponds to a distinct interaction, at three temperatures 300K, 333K, and 363K. These simulations maintain other properties constant, such as a nanoparticle volume content of 5% and an ionic concentration of 20 EO:Li.

Most of the atomic coordinations do not show a strong variation with temperature, although there are some exceptions that are worth mentioning, specially the RDF curves corresponding to the Li-$O_{\mathrm{Al_2O_3}}$ interaction.

Figure 5.6(a), displays the radial distribution function of PEO oxygen atoms centered around lithium. The $\mathrm{g_{Li}^{O_{PEO}}(r)}$ function consistently exhibits a small decrease in the intensity of the first peak with increasing temperature. The highest intensity drops from $I = 20.7$ at 300K to $I = 19.6$ at 363K, and the peaks get slightly closer with rising temperature, varying from $r = 2.20$Å at 300K to $r = 2.18$Å.

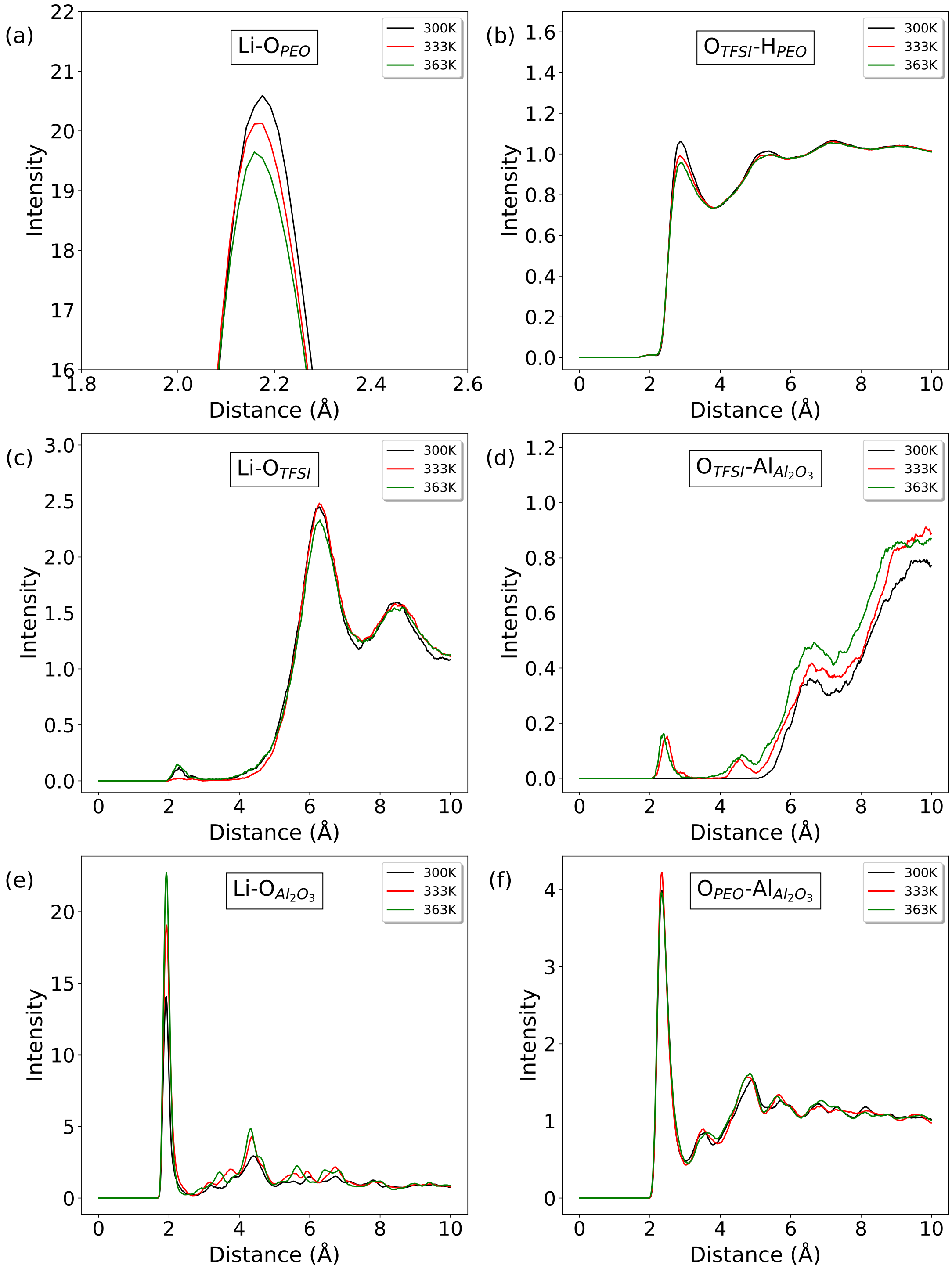

Figure 5.6: Radial distribution function curves computed for various atom pairs, including: (a) lithium and O_{PEO}, (b) O_{TFSI} and H_{PEO}, (c) lithium and O_{TFSI}, (d) O_{TFSI} and H_{SiO_2}, (e) lithium and H_{SiO_2}, and (f) O_{PEO} and H_{SiO_2}. These calculations were performed over a temperature range spanning from 300K to 363K at an ion concentration of 1 Li:PEO.

Figure 5.6(b) and (c) explore the $g_{H_{PEO}}^{O_{TFSI}}(r)$ and $g_{Li}^{O_{TFSI}}$ functions respectively. Both of them show a small dependence with temperature with not substantial variations.

In Figure 5.6(d), the $g_{O_{TFSI}}^{Al_{Nano}}$ interaction reveals two new peaks emerging at 333K at close ($r = 2.3$Å) and medium ($r = 4.6$Å) distances, absent at 300K. This suggests that at the lower temperature, TFSI molecules were farther from the aluminum, but at higher temperatures, increased kinetic energy allowed TFSI to overcome energy barriers and approach the alumina surface. However, the correlation between TFSI and alumina remains weak at all distances, indicating no strong interaction between them in the simulation.

Figure 5.6(e) highlights the interaction between lithium and $O_{Al_2O_3}$. The peak from the first shell stands out across all temperatures, reaching its highest intensity at 363K, surpassing even the Li-O_{PEO} maximum intensity in Figure 5.6(a). This peak's intensity exhibits a strong temperature dependence, increasing from $I = 14$ at 300K to $I = 23$ at 363K. This contrasts with the low temperature dependence observed for the other most relevant peak in Figure 5.6(a). One plausible explanation is that elevated temperatures enhance Li mobility, facilitating its approach to the surface, surpasing the energy barriers. Consequently, more lithium atoms become attached to the nanoparticles as the temperature increases.

Figure 5.6(f) shows the interaction between O_{PEO} and $Al_{Al_2O_3}$. The three curves display minimal temperature dependence, with slight variations at 333K. The correlations show little change with temperature, and no significant temperature dependence is observed.

In summary, temperature significantly affects interactions with alumina nanoparticles but has minimal influence on other interactions such as (a), (b) and (c). With increasing temperature, more TFSI and, especially, lithium ions can approach the alumina surface due to the large charges on the surface. The alumina structure consists of a repetitive arrangement of aluminum and oxygen atoms, as depicted in Figure 5.2. These atoms have opposite charges, causing positively charged ions to be attracted to oxygen atoms while being repelled by aluminum atoms, and vice versa. This results in strong interactions when ions approach their preferred atom types, as particularly evident with lithium (see Figure 5.6(e)). However, when ions try to approach the surface they also experience repulsive forces from the other type of alumina atoms. This interplay creates an energy barrier that can be more easily overcome with increased kinetic energy. Consequently, as the temperature increases from the lowest to the highest setting, both lithium and TFSI ions exhibit enhanced coordination in the first shell.

5.3.3 Nanoparticle Concentration

Figure 5.7 illustrates the radial distribution function at 363K and how it responds to varying nanoparticle concentrations. Each graph in the figure corresponds to a distinct interaction and includes three curves representing nanoparticle concentrations from 0%Vol to 5%Vol.

The introduction of nanoparticles decreases the coordination between PEO and lithium, mainly because many lithium ions become attached to the nanoparticle surface, making them unavailable for PEO coordination. However, no other significant structural changes result from the nanoparticle addition.

Figure 5.7(a) demonstrates a clear nanoparticle concentration dependency. The black curve, representing 0% nanoparticle content, displays a peak in the first shell with a maximum intensity of $I = 23.9$ at a distance of $r = 2.08$Å. Introducing a 2.5% nanoparticle content results in reduced coordination between lithium and PEO, as the peak significantly drops to $I = 20.4$ and shifts to a greater distance of $r = 2.12$Å. At a 5% alumina concentration, the intensity further decreases to $I = 19.7$, with a distance of $r = 2.18$Å.

Figures 5.7(b) and (c) exhibit no discernible dependency on nanoparticle concentration.

This lack of dependency persists in the subsequent figures, 5.7(d), (e), and (f), with the black curve naturally reaching zero in the absence of nanoparticles in that system.

In summary, the introduction of nanoparticles has a significant impact on the coordination between lithium and PEO oxygen, reducing it due to lithium adsorption on the alumina surface, preventing those lithium atoms from being fully surround by PEO.

However, these results differ from those reported by J. Wang et al. in their study, as shown in Figure 5.8. Wang and colleagues presented radial distribution functions (RDF) depicting spatial correlations between lithium and O_{PEO}, as well as between lithium and O_{TFSI}. In contrast to our findings, their data indicates a considerably higher coordination between Li and O_{TFSI}, while our data shows a near absence of this correlation. Conversely, the correlation between Li and O_{PEO} is notably stronger in our simulations, approximately twice as intense as observed by Wang's team.

As a result, we conducted additional simulations with a modified force field, available in the supplementary information. The charges and LJ parameters can be seen in table 5.1. The primary changes in this force field involve adjusting ion charges to ±1 from their previous ±0.8. Additionally, the charges of the individual TFSI atoms are enhanced. These modifications significantly impact TFSI, enhancing both the overall charge and individual atom charges, thereby increasing polarity and leading to substantial changes in their interactions. We sourced these force field parameters from the Moltemplate

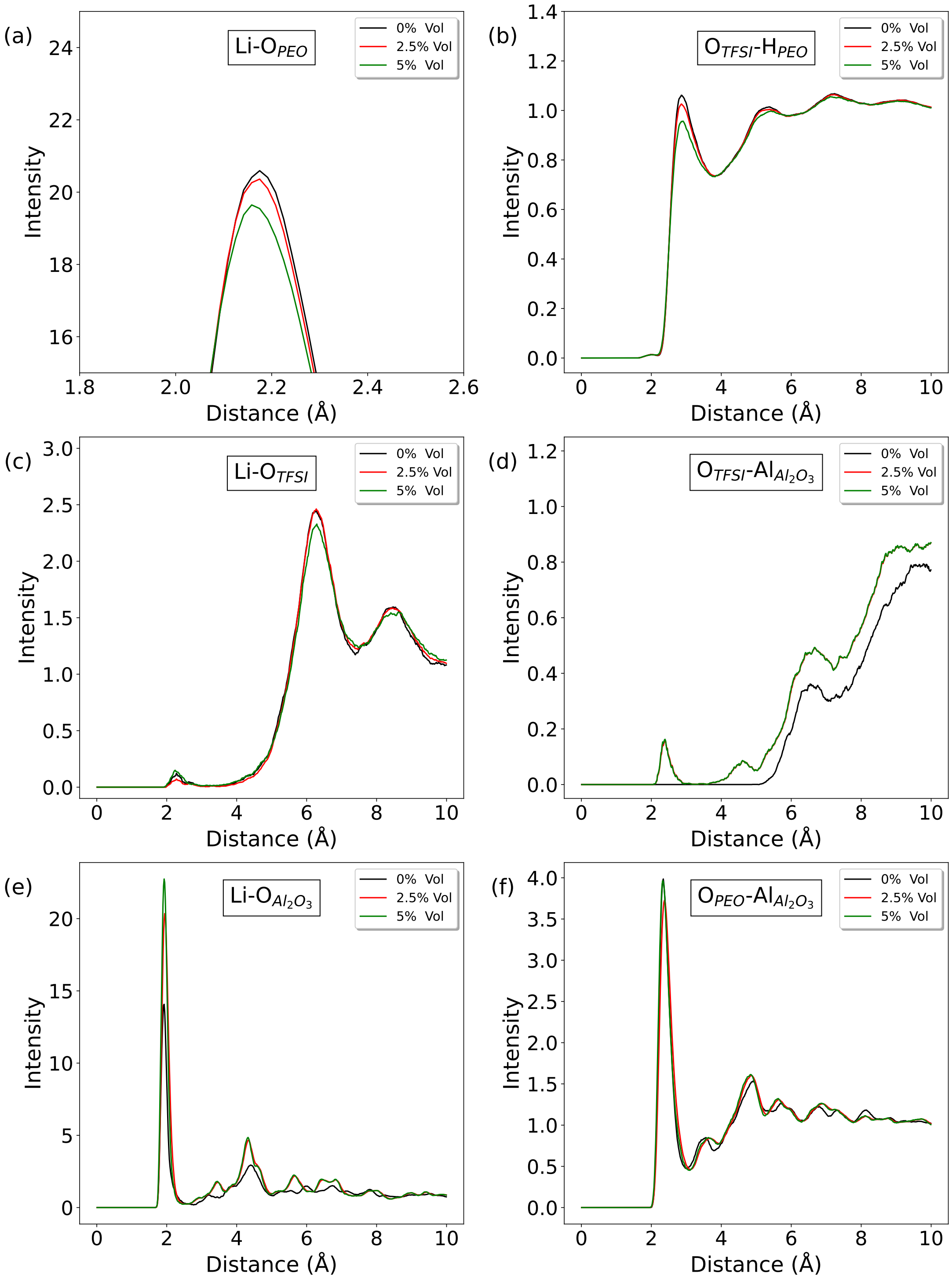

Figure 5.7: Radial distribution function curves computed for various atom pairs, including: (a) lithium and O_{PEO}, (b) O_{TFSI} and H_{PEO}, (c) lithium and O_{TFSI}, (d) O_{TFSI} and H_{SiO_2}, (e) lithium and H_{SiO_2}, and (f) O_{PEO} and H_{SiO_2}. These calculations were performed at 363K with an ion concentration of 1 Li:PEO and varying nanoparticle concentrations from 0% to 5% Vol.

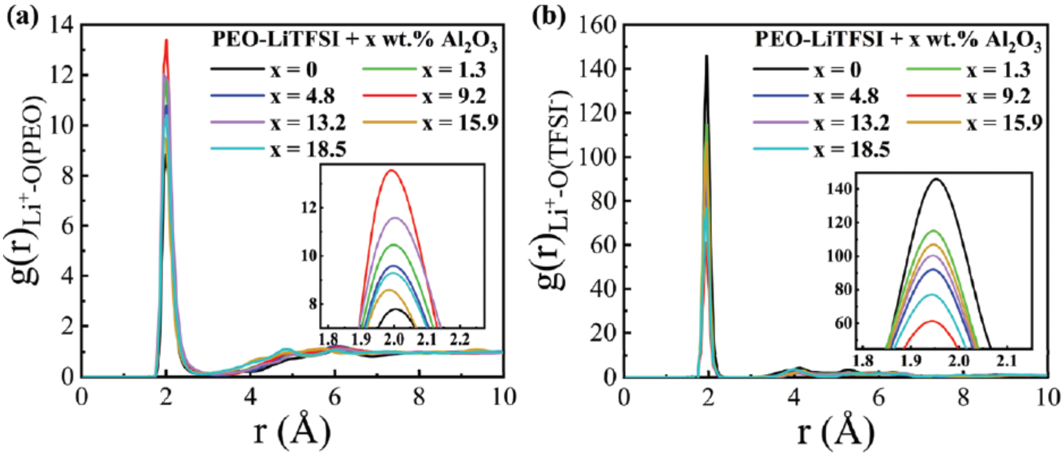

Figure 5.8: RDFs of (a) Li^+–O(PEO) at 333K, (b) Li^+–O(TFSI) at 333 K. PEO-LiTFSI + x wt% Al2O3 represents PEO-LiTFSI with x wt% Al2O3. x is the mass fraction of Al2O3. The insets show an enlargement of the first coordination shell. Image from ref.[130].

database [228], as recommended in reference [229]. You can find the RDF curves for the new simulations using this modified force field (FF2) in the following section.

5.3.4 Force field 2

Figure 5.9 compares the radial distribution function's response to temperature changes for two nanoparticle concentrations in the electrolyte using the new force field (FF2). We examine the same six interactions previously analyzed with the original force field (FF1), while maintaining a fixed ionic ratio of 3.2 Li:PEO.

The results obtained with the new force field differ significantly from those calculated with FF1. Notably, there is a much stronger coordination between lithium and alumina, indicating a coupling between these two ions. As a consequence, the interactions of lithium with other components in the electrolyte, such as $g_{\mathrm{Li}}^{\mathrm{O_{PEO}}}(\mathrm{r})$ and $g_{\mathrm{Li}}^{\mathrm{ONano}}(\mathrm{r})$, are notably reduced because many lithium atoms are coupled to TFSI.

In Figure 5.9(a), significantly lower values are observed compared to the previous force field. The interaction $g_{\mathrm{Li}}^{\mathrm{O_{PEO}}}(\mathrm{r})$ exhibits negative temperature dependence when nanoparticles are absent. Specifically, lithium binds more strongly to $\mathrm{O_{PEO}}$ at lower temperatures, but this trend becomes less distinct in the presence of nanoparticles.

In contrast, the correlation $g_{\mathrm{O_{TFSI}}}^{\mathrm{H_{PEO}}}(\mathrm{r})$ in Figure 5.9(b) and $g_{\mathrm{Li}}^{\mathrm{O_{TFSI}}}(\mathrm{r})$ in Figure 5.9(c) show minimal temperature dependence. The black curve, representing the 0% Vol and 300K system, exhibits well-defined peaks due to its lower temperature and the absence of nanoparticles. These conditions promote greater ordering, a phenomenon observed in previous studies like [230] and [231], highlighting the dependence of PEO crystallinity

PEO			
atom type	q (e)	ϵ (kcal/mol)	σ (Å)
H1	0.03	0.03	2.5
H2	0.435	0	0
C	0.14	0.066	3.5
O1	-0.4	0.14	2.9
O2	-0.635	0.17	3.09
TFSI			
N	-1.0	0.17	3.25
S	1.374	0.25	3.55
O	-0.687	0.17	2.96
C	0.36	0.066	3.5
F	-0.12	0.053	2.95
Lithium			
Li	1.0	0.0005	2.87
Al_2O_3			
O	-0.945	0.155	2.8
Al	1.4175	0.155	2.2

Table 5.1: Non-bonding coefficients of the force field 2 (FF2) of all the different types of atoms in the simulation.

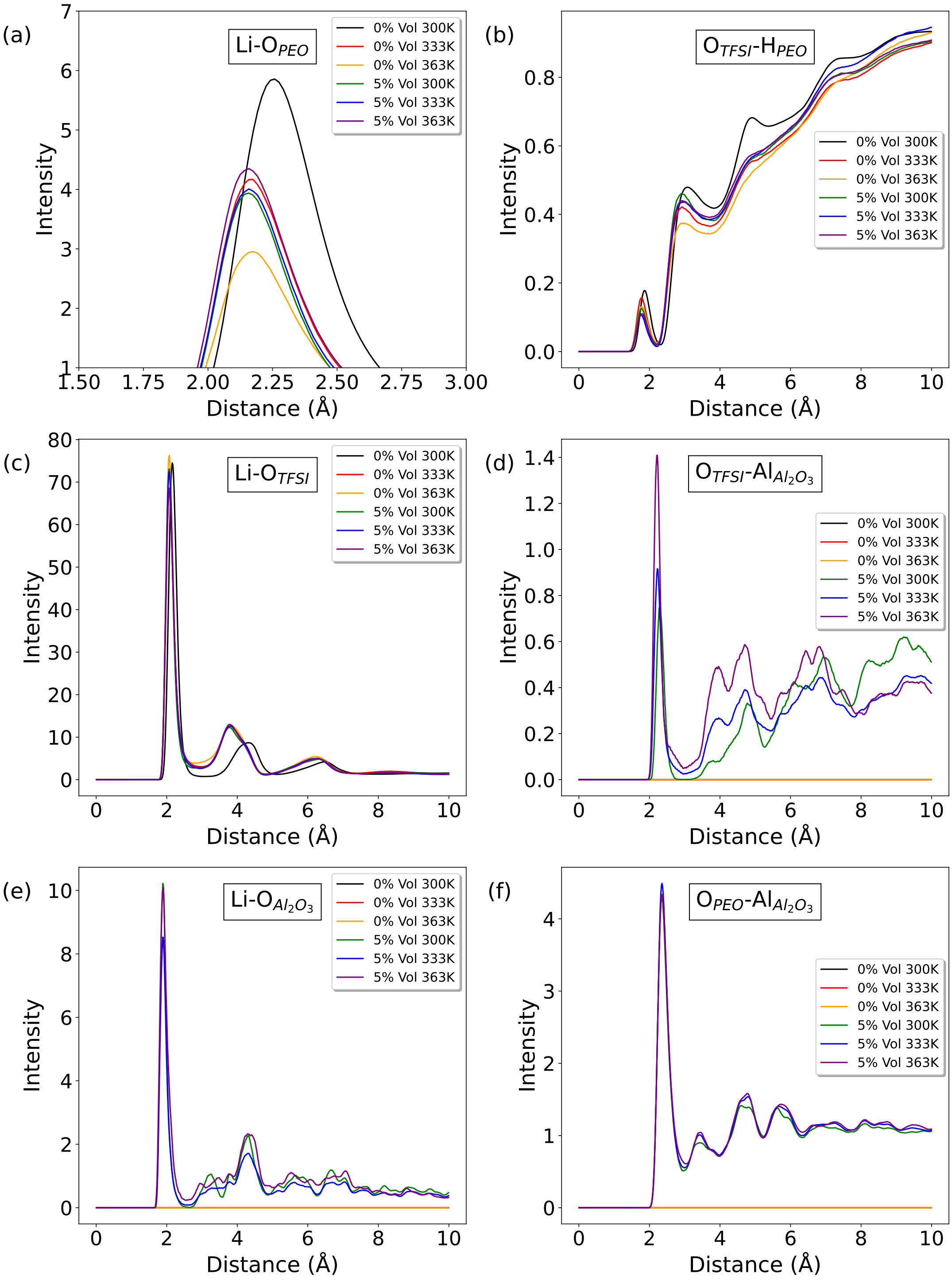

Figure 5.9: Radial distribution function curves computed using the FF2 for various atom pairs, including: (a) lithium and O_{PEO}, (b) O_{TFSI} and H_{PEO}, (c) lithium and O_{TFSI}, (d) O_{TFSI} and H_{SiO_2}, (e) lithium and H_{SiO_2}, and (f) O_{PEO} and H_{SiO_2}. These calculations were performed over a temperature range spanning from $300K$ to $363K$ with an ion concentration of 1 Li:PEO and for two different nanoparticle concentrations, 0% and 5% in volume.

on nanoparticle content.

Figure 5.9(c) demonstrates a significant increase in the intensity of the first peak compared to the previous force field. This sharp peak suggests a strong coupling between the two ionic species, which contrasts with the behavior observed with the previous force field, where they were almost completely decoupled. However, this interaction does not display any significant dependence on temperature or nanoparticle concentration.

In Figure 5.9(d), depicting the interaction between $\mathrm{O_{TFSI}}$ and $\mathrm{Al_{Nano}}$, there is a noticeable increase in coordination with increasing temperature. The intensity nearly doubles, going from $I = 0.72$ to $I = 1.41$. This significant enhancement in the binding strength between alumina and TFSI, as indicated by the sharp peak, suggests that some TFSI molecules adhere to the alumina surface. This contrast with the behavior observed with the previous force field, where the ions were totally decoupled.

Figures 5.9(e) and 5.9(f) exhibit almost no temperature dependence. Figure 5.9(e) experiences a significant reduction to less than half of its value with the initial force field, while Figure 5.9(f) remains unchanged.

In conclusion, the new force field drives significant changes in the structure of the electrolyte, making the TFSI closer to the nanoparticles but especially, coupling most of the TFSI molecules to lithium, thus less lithium is coupled with PEO and attached to the $\mathrm{Al_2O_3}$ surface.

This new force field aligns more closely with the results presented in Wang's paper [130], emphasizing a high correlation between lithium and TFSI. However, this outcome, which shows lithium's higher coordination with TFSI than with PEO, contradicts other simulation studies, such as Kang et al. [218], where a larger intensity of the $\mathrm{g_{Li}^{O_{PEO}}(r)}$ first peak compared to $\mathrm{g_{Li}^{OTFSI}(r)}$ was observed, as well as it contradicts experimental studies like [232]. These references [218, 232], in line with existing literature, exhibit behavior more akin to our previous force field, while contradicting Wang's results and our own results with the new FF regarding the structure of the electrolyte.

5.4 Results: Dynamical Properties

We now shift our focus from the radial distribution functions to ion dynamics. Specifically, we will examine the diffusion coefficients of lithium and TFSI ions in the hybrid electrolyte with alumina nanoparticles, using both force field 1 and force field 2. Our investigation will consider how temperature and ionic concentration affect these diffusion coefficients.

5.4.1 Temperature Dependence

Figure 5.10 illustrates the temperature-dependent variations in the diffusion coefficient within three distinct systems, each featuring different concentrations of alumina nanoparticles: approximately 0% Vol, 2.5% Vol, and 5% Vol. These systems maintain an ionic concentration equal to 3.2 Li:PEO.

In Figure 5.10(a), we present the diffusion coefficient of lithium ions, while Figure 5.10(b) showcases the diffusion coefficient of TFSI ions. Both curves exhibit an exponential dependence with temperature, mirroring the behavior observed in the equivalent curves for the electrolyte with silica discussed in the previous chapter in Figure 4.2.

At 300K, the temperature is below the polymer's melting point. However, as explained in Section 4.3.1, our simulations do not replicate the usual crystallization process seen in experiments. Therefore, we don't see a significant change in the curve's slope at this temperature.

Comparing the three nanoparticle concentrations, a clear trend emerges. For lithium ions, regardless of temperature, diffusion decreases with increasing nanoparticle concentration. However, the pattern for TFSI ions is different. At the lowest temperature, the trend is reversed, with the system containing higher alumina content exhibiting higher diffusivity. As the temperature rises, this difference diminishes, and at the highest temperature, the three cases converge to yield very similar diffusion values

5.4.2 Concentration of nanoparticles

Figures 5.11(a) and (b) illustrate the dependence of the autodiffusion coefficient on the nanoparticle content at 363 K, maintaining an ionic concentration of 3.2 EO:Li. We omitted the diffusion coefficient results for other temperatures for clarity, due to significant order of magnitude changes. Figure 5.11(c) extends this analysis to examine the transference number's dependence on nanoparticle concentration at three distinct temperatures: 363K, 333K, and 300K.

We observe a rapid decrease in lithium ion diffusion with increasing filler concentration, as shown in Figure 5.11. This decline is more pronounced compared to the case with silica nanoparticles in Figure 4.5. However, the situation changes when we analyze the diffusion of the anion, TFSI. In this case, the presence of alumina results in a slight improvement in their diffusion values.

These differences in ion behavior can be explained by examining their structural characteristics. In Figure 5.7, we observe that lithium ions strongly bind to alumina, significantly reducing their mobility and conductivity. Those lithium ions attached to the alumina surface tend to have very limited diffusion. However, alumina's introduction

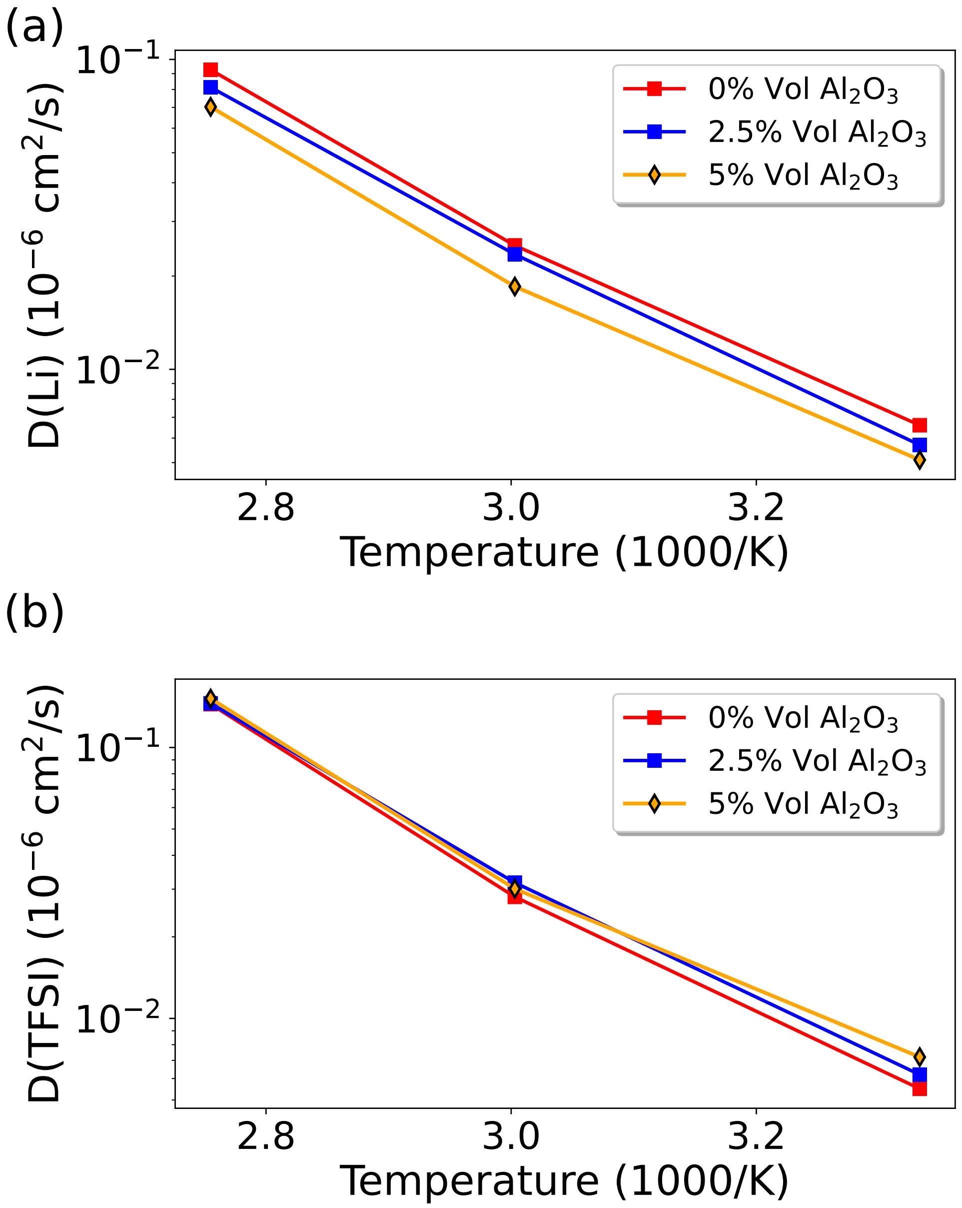

Figure 5.10: Diffusion coefficients dependence with temperature of the two types of ions, with (top) lithium and (bottom) TFSI. Each curve represents the evolution of the diffusion coefficient across a temperature range from 300K (corresponding to 3.3 on the x-scale) to 1000K (corresponding to 1 on the x-scale). Both curves show an exponential dependence with temperature.

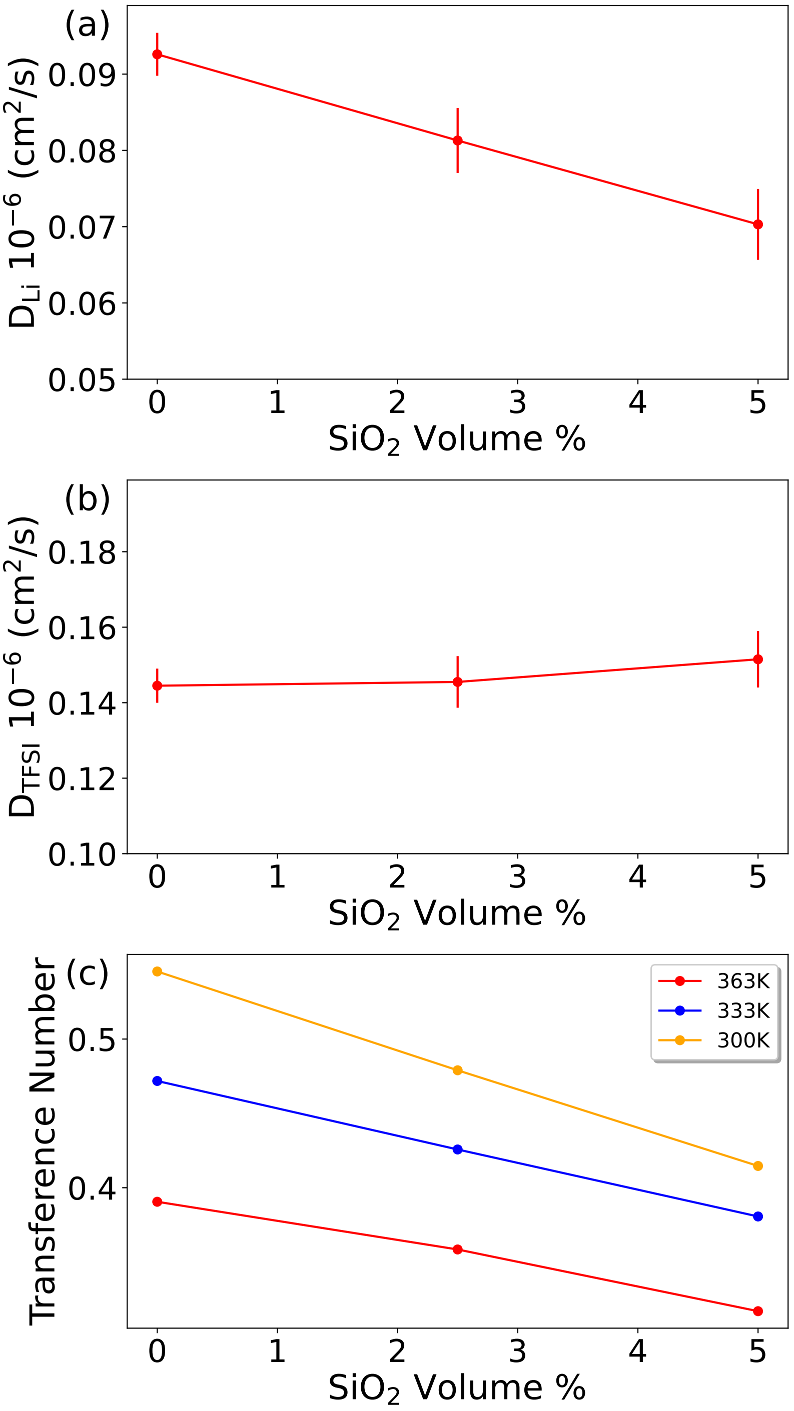

Figure 5.11: Diffusion coefficient dependence with alumina content for the two types of ions, namely (a) Lithium and (b) TFSI. Additionally, figure (c) displays the corresponding lithium transference number. Each curve illustrates the relationship between the diffusion coefficient and the concentration of nanoparticles, spanning from 0% to 5%. Remarkably, all three curves display a negative correlation with SiO_2 concentration when it comes to lithium diffusion, while showing a slight improvement in TFSI diffusion.

has a less pronounced effect on the coordination of TFSI ions with other atoms. Unlike with silica nanoparticles, TFSI ions do not form strong correlations with alumina, allowing them to move more freely without substantial interactions hindering their diffusion.

The analysis of the transference number confirms our earlier findings and shows a consistent pattern across various temperatures. With the inclusion of more nanoparticles, the diffusion of lithium ions decreases, whereas that of TFSI ions slightly rises. Consequently, the transference number experiences a notable decline as the nanoparticle concentration increases.

However, it's important to highlight that our findings diverge from those reported in reference [130]. In their study, they observed an increase in lithium and TFSI ion diffusivity. Due to these discrepancies, as well as the variations observed in the radial distribution function (RDF) in section 5.3.3, we conducted additional simulations employing a modified force field. The new force field parameters were sourced from the Moltemplate database [228], following the recommendations in ref [229]. Consequently, we adjusted our force field using these updated coefficients, and the results of these simulations are presented in the following subsection.

5.4.3 Force field 2

Figure 5.12 presents the dependence of diffusion coefficients on nanoparticle concentration under the same conditions as the curves shown in Figure 5.11, but employing the updated Moltemplate force field available in the appendix. The charges and LJ parameters of the force field are presented in table 5.1.

With the implementation of the force field 2, we observe a significant reduction in ionic diffusivity for both species as the nanoparticle volume fraction increases. In Figure 5.12(a), Li^+ ion diffusivity decreases as the ionic concentration rises, exhibiting a similar trend to the diffusivity observed in Figure 5.11(a) in relative terms, but much lower absolute values. Additionally, Figure 5.12(b) illustrates how the diffusivity of TFSI ions diminishes as the alumina concentration increases with the newly implemented force field, in contrast to the results obtained with force field 1.

Furthermore, it's worth noting that the introduction of the new force field results in significantly lower values for the diffusion coefficients of both ions. In Figure 5.12(a), we observe a reduction of lithium ion diffusion coefficients to less than one-third of their values with the previous FF (FF1). Similarly, in Figure 5.12(b), the diffusion coefficients of TFSI ions experience an even more substantial reduction, dropping to less than one-fifth of their previous levels with FF1. This pronounced decrease is particularly notable for TFSI ions.

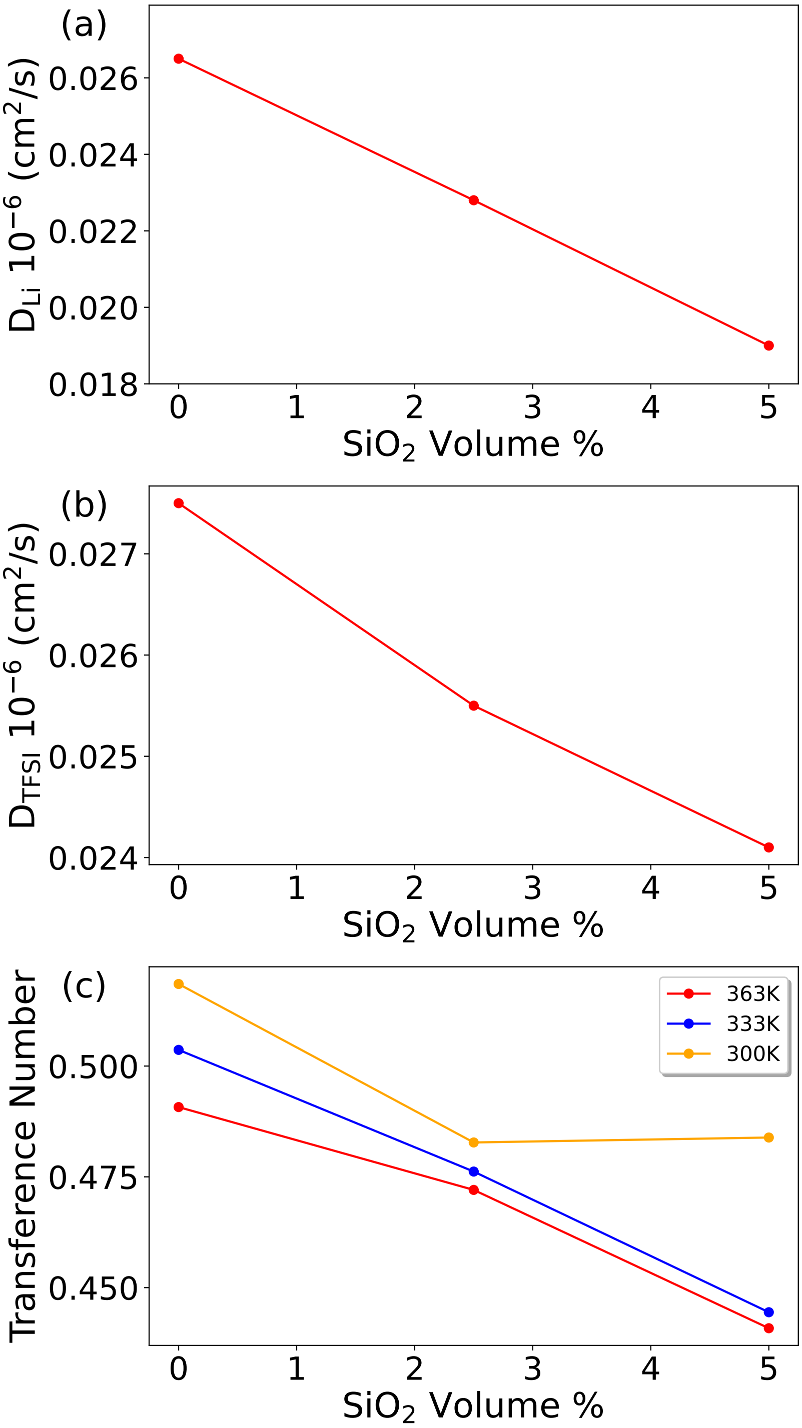

Figure 5.12: The figures illustrate the dependence of diffusion coefficients on alumina content using the FF2 for both ions: (a) Lithium and (b) TFSI. Additionally, figure (c) displays the corresponding lithium transference number. Each curve illustrates the relationship between the diffusion coefficient and the concentration of nanoparticles, spanning from 0% to 5%. All the calculation were performed at 1 Li:PEO content. Curves (a) and (b) correspond to the 363K data, while curve (c) shows the results obtained at three temperatures, ranging from 300K to 363K.

The reason behind this decline becomes evident when analyzing their radial distribution functions (RDF), as shown in Figure 5.9. It is clear that the two ionic species are strongly attached, forming bonds that restrict their individual mobility. Consequently, TFSI ions, which previously exhibited relatively independent mobility, are now constrained due to their attachment to alumina and the strong interactions with other elements, such as oxygen atoms within the polymer.

The transference number, depicted in Figure 5.12(c), exhibits smaller variations with the new force field compared to the previous one. TFSI ion diffusivity decreases moderately with increasing alumina content in the new force field.

In summary, adopting the new force field FF2 results in a significant reduction in ion mobility, which further decreases with higher filler content. This contrasts with the findings in [130], although our structural measurements align with Wang's data.

5.5 Conclusion

In this chapter, we examined the dynamic behavior of a hybrid solid electrolyte consisting of polyethylene oxide (PEO), lithium bis(trifluoromethanesulfonyl)imide (LiTFSI), and alumina nanoparticles (Al_2O_3). Our investigation focused on understanding how temperature and nanoparticle concentration affect both structural features, represented by radial distribution functions (RDF), and dynamic properties, particularly ion diffusion coefficients. Additionally, we explored the use of an alternative force field (FF2), similar to the one employed by Wang et al. [130, 229], in an attempt to replicate their findings suggesting a positive impact of nanoparticles on ionic dynamics.

We initially employed force field 1 (FF1), which included the non-bonding terms for alumina as provided in reference [130], along with our previous force field parameters used in chapters 3 and 4. In this setup, we kept the positions of the alumina nanoparticles fixed. With FF1, we observed that lithium ions exhibit an exceptionally strong attraction to the alumina surface, showing very intense and sharped peaks on the first shell at any given condition, as depicted in Figure 5.6. This strong interaction resulted in lithium ions becoming tightly bound to the nanoparticle surfaces, leading to either very slow diffusion or complete immobilization. Consequently, the diffusivity of lithium ions experienced a significant reduction. In contrast, TFSI ions display weaker coordination with nanoparticles, and their diffusion is only marginally enhanced by the addition of nanoparticles. As a result, the transference number exhibits a rapid decrease as nanoparticle content increased, indicating an overall adverse impact on the dynamical properties of the electrolyte

However, our results diverge from the findings of Wang et al. In our simulations, we observe discrepancies in both dynamical and structural aspects compared to their research. While Wang's work suggested an enhancement in the lithium ion diffusion coefficient and revealed strong correlations between lithium and TFSI ions, our observations reveal a strong coupling between lithium and the fillers, with no coordination between lithium and TFSI ions.

To address the differences, we employed an alternative force field (FF2), following the suggestions in reference [229], which should be similar to the one employed in Wang's research [130]. The use of the new force field parameters results in a strong coordination between lithium and TFSI. This coupling of the ions results in a big decrease in their diffusivities, as their charges are enhanced, and this stronger interaction reduces their mobility. The presence of nanoparticles has a negative impact on the mobilities of both ions.

This contrasts with Wang's reference, and we do not have a clear explanation for this inconsistency. In Wang's experiment, the two ions are coupled, but the addition of nanoparticles decreases this coupling in favor of lithium bonding with PEO. The cations attached to PEO exhibit higher mobility than those attached to TFSI, resulting in enhanced diffusivity when nanoparticles are added. However, in our case, the addition of nanoparticles does not reduce the coordination between lithium and TFSI. We believe that making subtle adjustments to the charges of TFSI to place them in between the charges in FF1 and FF2 could potentially yield results similar to Wang's. However, determining the exact values for these minor charge adjustments remains challenging, as there is no consistent trend or clear guidance on which direction to pursue.

In summary, our study highlights the influence of alumina nanoparticles on the structural properties of the electrolyte, but this influence varies notably depending on the chosen force field. While the second force field closely aligns with Wang et al.'s structural findings, it significantly diverges in terms of ion dynamics. However, considering the structural differences between the two force fields, the first one remains more reliable. This reliability is attributed to the expected full decoupling of LiTFSI due to PEO's efficacy as a solvent for such salts [218, 232]. The first force field indeed exhibits this decoupling, while the second one demonstrates clear coupling between the ionic species.

In all of these scenarios, the incorporation of alumina nanoparticles did not yield any discernible improvement in the electrolyte's lithium conductivity. Therefore, we did not find any evidence of the utility of alumina as a filler for hybrid electrolytes in molten conditions. We recommend careful consideration when evaluating its practical applications.

Chapter 6

Conclusion

In this thesis, we have examined the structural and dynamic properties of hybrid polymer electrolytes. Specifically, we aimed to understand how the addition of ceramic nanoparticles impacts pure polymer electrolytes. To this aim, we applied molecular dynamics techniques to investigate two different electrolytes: one featuring silica and the other alumina. A notable distinction is that the silica nanoparticle has a surface coated with hydrogen atoms, whereas the alumina fillers does not present this coating. This investigation involved an analysis of the electrolyte's response to various parameters, including temperature, nanoparticle concentration, ionic concentration, nanoparticle shape, and filler size.

1. The hybrid electrolyte's general structure, comprising Li, TFSI, PEO, and silica, was analyzed through the calculation of the radial distribution function in our simulations. Our findings reveal that lithium exhibits a strong affinity for the oxygen atoms within the electrolyte. This behavior aligns with the proposed solvation mechanism for LiTFSI salt in PEO, supported by experimental evidence **??**, as well as previous simulation studies **??**. Consequently, the TFSI ions do not closely associate with lithium but instead form coordination bonds primarily with the hydrogen atoms of PEO, which are the most abundant in our simulation. TFSI ions also engage with the silica surface in a polar orientation, with their oxygen atoms facing the silica. Notably, silica interactions with lithium are minimal when the system is not highly concentrated.

2. We explored the structural dependencies of the electrolyte by analyzing the radial distribution function and coordination numbers, specifically examining six primary interactions between the four different molecules in the system.

   Temperature significantly impacts the structural characteristics of the electrolyte. As temperature rises, the structure becomes more delocalized, and coordination numbers decrease. However, a notable exception arises in the interaction between lithium and TFSI. The lower coordination between lithium and PEO creates additional space, enabling TFSI to approach and enhance its coordination with lithium.

3. These structural changes are accompanied by alterations in the system's dynamics. We study the ionic dynamics using metrics like mean squared displacement, diffusion coefficients, and conductivity. Comparing the temperature-dependent conductivity with Maurel's experiments [47], our results align closely both qualitatively and quantitatively. This demonstrates the effectiveness of our force field in reproducing experimental trends. Our conductivity exhibits Arrhenius behavior with temperature, although it doesn't replicate the curvature shift at the melting point (Tm) since our simulations lack the necessary time to model the polymer's crystallization.

4. The nanoparticle concentration, in contrast to temperature, has no significant impact on the electrolyte's structure. Introducing silica fillers leads to an increase in coordinations with silica, but this has no significant impact on other coordinations. This indicates that the addition of silica affects its immediate surroundings but does not notably influence the bulk electrolyte.

5. The filler content has a negative effect on the dynamic properties of the ions. Silica reduces the mobility of both lithium and TFSI, resulting in a decrease in the electrolyte's conductivity. We have also observed that the decrease in conductivity due to the addition of fillers can be explained by a pure volumetric effect. This contradicts the initial experiments in this field, led by Croce's works around 20 years ago, which were corroborated by several other experimental and computational studies [53, 113, 101, 59, 96] [**empty citation**]. However, it aligns with a more recent trend in research that demonstrates the detrimental impact of nanoparticles on ion mobility in the electrolyte. [**empty citation**]

6. We also analyzed the impact of ionic content on the system's structure. We observed the existence of two distinct concentration regimes: the Low Concentration regime (LC) and the High Concentration regime (HC). These regimes are divided by a threshold content of 3.2 Li:PEO, equivalent to 2 mol/L. This threshold concentration marks the point at which PEO becomes saturated with lithium ions. In the LC regime, lithium ions are adsorbed by the PEO, while in the HC regime, there is an excess of lithium ions that are not trapped by the PEO. This release of lithium ions through the electrolyte has a significant impact on all the other interactions.

7. The changes in the structure significantly affect the dynamic properties. In the

Low Concentration (LC) regime, conductivity increases with ionic concentration, whereas in the High Concentration (HC) regime, it exhibits a negative dependence on ionic concentration. The maximum conductivity is achieved at the optimal concentration of 3.2 Li:PEO. Notably, the optimal concentration differs for TFSI and lithium. When examining lithium's partial conductivity, it reaches a maximum at around 2.4 Li:PEO or 1.5 mol/L, while the total conductivity is primarily influenced by TFSI. The divergence in optimal concentration for lithium may have practical implications for industrial applications.

8. The influence of the geometry of silica nanoparticles has been explored. Analyzing particles of different sizes and the diffusivity in the parallel direction to a planar nanoparticle, we find that surface effects of silica have minimal impact on ion mobility, and variations in conductivity due to nanoparticle addition are primarily driven by volumetric effects. However, it's noteworthy that while surface effects do not significantly affect ionic mobility, the region surrounding the nanoparticle exhibits a distinct molecular distribution compared to the bulk electrolyte, with a higher proportion of TFSI molecules on its surface. Additionally, in the vicinity of the nanoparticle, polymers exhibit different spatial organization compared to the bulk, as observed in the case of planar SiO_2.

9. The electrolyte containing alumina nanoparticles has been investigated using two distinct force fields: FF1, which was employed in our prior studies with LiTFSI, PEO and silica to which we added the alumina parameters, and FF2, which introduces several changes, including higher ionic charges and enhanced TFSI dipole. In our simulations with FF1, alumina nanoparticles demonstrated distinct behavior compared to silica, primarily attributed to their different surface terminations. Despite this distinction, both materials had an adverse impact on the electrolyte's conductivity. The introduction of alumina altered the coordination and properties of the electrolyte. It resulted in increased binding of lithium ions to the alumina surface, diminishing lithium's coordination with PEO, and adversely affecting diffusivity. Additionally, with FF2, the biggest difference was comming from a strong coupling between the ions, in agreement with Wang's structure [130] but contradicting the experimental evidences on the solubility of LiTFSI salt [**empty citation**]. Overall, the alumina also shows a negative impact on the ions mobility with FF2.

In summary, our findings do not demonstrate any beneficial effect resulting from the addition of nanoparticles to the electrolyte, improving its conductivity for use as an electrolyte under the conditions we investigated. We do not observe any evidence of improved conductivity or the creation of a space-charge region at the interface that enhances ion mobility. However, our study does not exclude the possibility that nanoparticles could still have a positive effect when used to reduce the crystallinity of the electrolyte at low temperatures.

Appendix I:
FF1 including PEO, LiTFSI and SiO_2

Masses

1 1.008 # H1-PEO
2 1.008 # H2-PEO
3 1.008 # H-SiO_2
4 12.011 # C-PEO
5 15.999 # O1-SiO_2
6 15.999 # O2-SiO_2
7 15.999 # O1-PEO
8 15.999 # O2-PEO
9 28.086 # Si-SiO_2
10 14.007 # N-TFSI
11 32.065 # S-TFSI
12 15.999 # O-TFSI
13 12.011 # C-TFSO
14 18.998 # F-TFSI
15 6.941 # Li-TFSI

Pair Coeffs

1 0.03 2.5 # H1-PEO
2 0 0 # H2-PEO
3 0 0 # H-SiO_2
4 0.066 3.5 # C-PEO
5 0.17 3 # O1-SiO_2
6 0.17 3.12 # O2-SiO_2

7 0.14 2.9 # O1-PEO
8 0.17 3.12 # O2-PEO
9 0.1 4 10 # Si-SiO_2
10 0.17 3.25 # N-TFSI
11 0.25 3.55 # S-TFSI
12 0.21 2.96 # O-TFSI
13 0.066 3.5 # C-TFSO
14 0.053 2.95 # F-TFSI
15 0.166 1.506 # Li-TFSI

Bond Coeffs

1 268 1.529 # C-C PEO
2 340 1.09 # C-H1 PEO
3 320 1.41 # C-O1 PEO
4 320 1.41 # C-O2 PEO
5 553 0.945 # H-O2 SiO_2
6 300 1.65 # Si-O1 SiO_2
7 300 1.65 # Si-O2 SiO_2
8 553 0.945 # O2-H2 PEO
9 374.88 1.57 # N-S TFSI
10 637.07 1.437 # S-O TFSI
11 233.03 1.818 # S-O TFSI
12 441.92 1.323 # C-F TFSI

Angle Coeffs

1 37.5 110.7 # H1-C-C PEO
2 50 109.5 # O1-C-C PEO
3 50 109.5 # O2-C-C PEO
4 60 109.5 # C-O1-C PEO
5 55 108.5 # C-O2-H2 PEO
6 33 107.8 # H1-C-H1 PEO
7 60 110 # O1-Si-O1 SiO_2
8 60 110 # O2-Si-O1 SiO_2
9 60 110 # O2-Si-O2 SiO_2
10 20 145 # Si-O1-Si SiO_2
11 23.78 122.89 # Si-O2-H SiO_2
12 37.5 110.7 # O1-C-H1 PEO
13 35 109.5 # O2-C-H1 PEO

14 94.29 113.6 # N-S-O TFSI
15 91.3 103.5 # N-S-C TFSI
16 82.93 111.7 # S-C-F TFSI
17 80.19 125.6 # S-N-S TFSI
18 103.97 102.6 # C-S-O TFSI
19 115.8 118.5 # O-S-O TFSI
20 93.33 107.1 # F-C-F TFSI

Dihedral Coeffs

1 0.65 -0.25 0.67 0 # C-O1-C-C PEO
2 -0.356 -0.174 0.492 0 # C-C-O2-H2 PEO
3 0 0 0.3 0 # H1-C-C-H1 PEO
4 0 0 0.76 0 # C-O1-C-H1 PEO
5 0 0 0.352 0 # H1-C-O2-H2 PEO
6 0 0 0 0 # O1-Si-O1-Si SiO_2
7 0 0 0 0 # O1-Si-O2-H SiO_2
8 0 0 0 0 # Si-O1-Si-O1 SiO_2
9 0 0 0 0 # O2-Si-O2-H SiO_2
10 0 0 0.468 0 # O1-C-C-H1 PEO
11 -0.55 0 0 0 # O1-C-C-O1 PEO
12 4.319 0 0 0 # O2-C-C-O1 PEO
13 0 0 0.468 0 # O2-C-C-H1 PEO
14 0 0 0.316 0 # N-S-C-F TFSI
15 0 0 -0.004 0 # S-N-S-O TFSI
16 7.833 -2.49 -0.764 0 # S-N-S-C TFSI
17 0 0 0.347 0 # O-S-C-F TFSI

Appendix II:
FF1 including PEO, LiTFSI and Al_2O_3

Masses

1 1.008 # H1-PEO
2 1.008 # H2-PEO
3 12.011 # C-PEO
4 15.999 # O1-PEO
5 15.999 # O2-PEO
6 15.999 # O-Al_2O_3
7 26.982 # Al-Al_2O_3
8 14.007 # N-TFSI
9 32.065 # S-TFSI
10 15.999 # O-TFSI
11 12.011 # C-TFSO
12 18.998 # F-TFSI
13 6.941 # Li-TFSI

Pair Coeffs

1 0.03 2.5 # H1-PEO
2 0 0 # H2-PEO
3 0.066 3.5 # C-PEO
4 0.14 2.9 # O1-PEO
5 0.17 3.12 # O2-PEO
6 0.155 2.8 # O-Al_2O_3
7 0.155 2.2 # Al-Al_2O_3
8 0.17 3.25 # N-TFSI

9 0.25 3.55 # S-TFSI
10 0.21 2.96 # O-TFSI
11 0.066 3.5 # C-TFSO
12 0.053 2.95 # F-TFSI
13 0.166 1.506 # Li-TFSI

Bond Coeffs

1 268 1.529 # C-C PEO
2 340 1.09 # C-H1 PEO
3 320 1.41 # C-O1 PEO
4 320 1.41 # C-O2 PEO
5 553 0.945 # O2-H2 PEO
6 0.0 0.0 # Al-O Al_2O_3
7 374.88 1.57 # N-S TFSI
8 637.07 1.437 # S-O TFSI
9 233.03 1.818 # S-O TFSI
10 441.92 1.323 # C-F TFSI

Angle Coeffs

1 37.5 110.7 # H1-C-C PEO
2 50 109.5 # O1-C-C PEO
3 50 109.5 # O2-C-C PEO
4 60 109.5 # C-O1-C PEO
5 55 108.5 # C-O2-H2 PEO
6 33 107.8 # H1-C-H1 PEO
7 0.0 0.0 # Al-O-Al Al_2O_3
8 0.0 0.0 # O-Al-O Al_2O_3
9 37.5 110.7 # O1-C-H1 PEO
10 35 109.5 # O2-C-H1 PEO
11 94.29 113.6 # N-S-O TFSI
12 91.3 103.5 # N-S-C TFSI
13 82.93 111.7 # S-C-F TFSI
14 80.19 125.6 # S-N-S TFSI
15 103.97 102.6 # C-S-O TFSI
16 115.8 118.5 # O-S-O TFSI
17 93.33 107.1 # F-C-F TFSI

Dihedral Coeffs

1 0.65 -0.25 0.67 0 # C-O1-C-C PEO
2 -0.356 -0.174 0.492 0 # C-C-O2-H2 PEO
3 0 0 0.3 0 # H1-C-C-H1 PEO
4 0 0 0.76 0 # C-O1-C-H1 PEO
5 0 0 0.352 0 # H1-C-O2-H2 PEO
6 0 0 0 0 # O-Al-O-Al Al_2O_3
7 0 0 0.468 0 # O1-C-C-H1 PEO
8 -0.55 0 0 0 # O1-C-C-O1 PEO
9 4.319 0 0 0 # O2-C-C-O1 PEO
10 0 0 0.468 0 # O2-C-C-H1 PEO
11 0 0 0.316 0 # N-S-C-F TFSI
12 0 0 -0.004 0 # S-N-S-O TFSI
13 7.833 -2.49 -0.764 0 # S-N-S-C TFSI
14 0 0 0.347 0 # O-S-C-F TFSI

Appendix III: FF1 including PEO, LiTFSI and Al_2O_3

Masses

1 1.008 # H1-PEO
2 1.008 # H2-PEO
3 12.011 # C-PEO
4 15.999 # O1-PEO
5 15.999 # O2-PEO
6 15.999 # O-Al_2O_3
7 26.982 # Al-Al_2O_3
8 14.007 # N-TFSI
9 32.065 # S-TFSI
10 15.999 # O-TFSI
11 12.011 # C-TFSO
12 18.998 # F-TFSI
13 6.941 # Li-TFSI

Pair Coeffs

1 0.03 2.5 # H1-PEO
2 0 0 # H2-PEO
3 0.066 3.5 # C-PEO
4 0.14 2.9 # O1-PEO
5 0.17 3.09 # O2-PEO
6 0.155 2.8 # O-Al_2O_3
7 0.155 2.2 # Al-Al_2O_3
8 0.17 3.25 # N-TFSI

9 0.25 3.55 # S-TFSI
10 0.17 2.96 # O-TFSI
11 0.066 3.5 # C-TFSO
12 0.053 2.95 # F-TFSI
13 0.0005 2.87 # Li-TFSI

Bond Coeffs

1 268 1.529 # C-C PEO
2 340 1.09 # C-H1 PEO
3 320 1.41 # C-O1 PEO
4 320 1.41 # C-O2 PEO
5 553 0.945 # O2-H2 PEO
6 0.0 0.0 # Al-O Al_2O_3
7 434 1.67 # N-S TFSI
8 700 1.44 # S-O TFSI
9 340 1.77 # S-O TFSI
10 367 1.36 # C-F TFSI

Angle Coeffs

1 37.5 110.7 # H1-C-C PEO
2 50 109.5 # O1-C-C PEO
3 50 109.5 # O2-C-C PEO
4 60 109.5 # C-O1-C PEO
5 55 108.5 # C-O2-H2 PEO
6 33 107.8 # H1-C-H1 PEO
7 35 109.5 # O1-C-H1 PEO
8 35 109.5 # O2-C-H1 PEO
9 0.0 0.0 # Al-O-Al Al_2O_3
10 0.0 0.0 # O-Al-O Al_2O_3
11 120 107 # N-S-O TFSI
12 100 103 # N-S-C TFSI
13 50 109.5 # S-C-F TFSI
14 70 126.4 # S-N-S TFSI
15 74 108.9 # C-S-O TFSI
16 104 119 # O-S-O TFSI
17 77 109.1 # F-C-F TFSI

Dihedral Coeffs

1 0.65 -0.25 0.67 0 # C-O1-C-C PEO
2 -0.356 -0.174 0.492 0 # C-C-O2-H2 PEO
3 0 0 0.3 0 # H1-C-C-H1 PEO
4 0 0 0.76 0 # C-O1-C-H1 PEO
5 0 0 0.352 0 # H1-C-O2-H2 PEO
6 0 0 0.468 0 # O1-C-C-H1 PEO
7 -0.55 0 0 0 # O1-C-C-O1 PEO
8 4.319 0 0 0 # O2-C-C-O1 PEO
9 0 0 0.468 0 # O2-C-C-H1 PEO
10 0 0 0 0 # O-Al-O-Al Al_2O_3
11 0 0 0 0 # N-S-C-F TFSI
12 0 0 0 0 # S-N-S-O TFSI
13 0.4 4.9 0 0 # S-N-S-C TFSI
14 0 0 0 0 # O-S-C-F TFSI

Bibliography

[1] Samuel Asumadu Sarkodie, Phebe Asantewaa Owusu, and Thomas Leirvik. "Global effect of urban sprawl, industrialization, trade and economic development on carbon dioxide emissions". In: *Environmental Research Letters* 15.3 (2020), p. 034049.

[2] Sonia I Seneviratne et al. "No pause in the increase of hot temperature extremes". In: *Nature Climate Change* 4.3 (2014), pp. 161–163.

[3] Yukiko Hirabayashi et al. "Global flood risk under climate change". In: *Nature climate change* 3.9 (2013), pp. 816–821.

[4] Jofre Carnicer et al. "Widespread crown condition decline, food web disruption, and amplified tree mortality with increased climate change-type drought". In: *Proceedings of the National Academy of Sciences* 108.4 (2011), pp. 1474–1478.

[5] Daniele De Rigo et al. "Forest fire danger extremes in Europe under climate change: variability and uncertainty". PhD thesis. Publications Office of the European Union, 2017.

[6] GV Alekseev et al. "Climate change in the Arctic: causes and mechanisms". In: *IOP Conference Series: Earth and Environmental Science*. Vol. 606. 1. IOP Publishing. 2020, p. 012002.

[7] Qinglong You et al. "Warming amplification over the Arctic Pole and Third Pole: Trends, mechanisms and consequences". In: *Earth-Science Reviews* 217 (2021), p. 103625.

[8] Lee Chapman. "Transport and climate change: a review". In: *Journal of transport geography* 15.5 (2007), pp. 354–367.

[9] Payam Nejat et al. "A global review of energy consumption, CO2 emissions and policy in the residential sector (with an overview of the top ten CO2 emitting countries)". In: *Renewable and sustainable energy reviews* 43 (2015), pp. 843–862.

[10] Manh-Kien Tran et al. "A review of range extenders in battery electric vehicles: Current progress and future perspectives". In: *World Electric Vehicle Journal* 12.2 (2021), p. 54.

[11] Sara Bellocchi et al. “On the role of electric vehicles towards low-carbon energy systems: Italy and Germany in comparison”. In: *Applied energy* 255 (2019), p. 113848.

[12] Moez Krichen et al. “A Survey on energy storage: Techniques and challenges”. In: *Energies* 16.5 (2023), p. 2271.

[13] Nicola Armaroli and Vincenzo Balzani. “Towards an electricity-powered world”. In: *Energy & Environmental Science* 4.9 (2011), pp. 3193–3222.

[14] M Rosa Palacın and Anne de Guibert. “Why do batteries fail?” In: *Science* 351.6273 (2016), p. 1253292.

[15] Carola Schultz et al. “Investigation of the decomposition of organic solvent-based lithium ion battery electrolytes with liquid chromatography-mass spectrometry”. In: *Spectrosc. Eur* 28.5 (2016), pp. 21–24.

[16] Roberta Cappabianca et al. “An Overview on Transport Phenomena within Solid Electrolyte Interphase and Their Impact on the Performance and Durability of Lithium-Ion Batteries”. In: *Energies* 16.13 (2023), p. 5003.

[17] Steven Chu and Arun Majumdar. “Opportunities and challenges for a sustainable energy future”. In: *nature* 488.7411 (2012), pp. 294–303.

[18] Jordi Cabana et al. “Beyond intercalation-based Li-ion batteries: the state of the art and challenges of electrode materials reacting through conversion reactions”. In: *Advanced materials* 22.35 (2010), E170–E192.

[19] J-M Tarascon and Michel Armand. “Issues and challenges facing rechargeable lithium batteries”. In: *nature* 414.6861 (2001), pp. 359–367.

[20] E Peter Roth and Christopher J Orendorff. “How electrolytes influence battery safety”. In: *The Electrochemical Society Interface* 21.2 (2012), p. 45.

[21] Mario Joost et al. “Ionic mobility in ternary polymer electrolytes for lithium-ion batteries”. In: *Electrochimica Acta* 86 (2012), pp. 330–338.

[22] Yinghua Zhu et al. “High electrochemical stability of a 3D cross-linked network PEO@ nano-SiO 2 composite polymer electrolyte for lithium metal batteries”. In: *Journal of Materials Chemistry A* 7.12 (2019), pp. 6832–6839.

[23] Languang Lu et al. “A review on the key issues for lithium-ion battery management in electric vehicles”. In: *Journal of power sources* 226 (2013), pp. 272–288.

[24] Bruno Scrosati, Jurgen Garche, and Werner Tillmetz. *Advances in battery technologies for electric vehicles.* Woodhead Publishing, 2015.

[25] Xin Shen et al. “How does external pressure shape Li dendrites in Li metal batteries?” In: *Advanced Energy Materials* 11.10 (2021), p. 2003416.

[26] Hessam Ghassemi et al. “Real-time observation of lithium fibers growth inside a nanoscale lithium-ion battery”. In: *Applied Physics Letters* 99.12 (2011), p. 123113.

[27] Doron Aurbach et al. “A short review of failure mechanisms of lithium metal and lithiated graphite anodes in liquid electrolyte solutions”. In: *Solid state ionics* 148.3-4 (2002), pp. 405–416.

[28] Xue-Qiang Zhang, Xin-Bing Cheng, and Qiang Zhang. “Advances in interfaces between Li metal anode and electrolyte”. In: *Advanced Materials Interfaces* 5.2 (2018), p. 1701097.

[29] Jens Steiger, Dominik Kramer, and Reiner Mönig. “Mechanisms of dendritic growth investigated by in situ light microscopy during electrodeposition and dissolution of lithium”. In: *Journal of Power Sources* 261 (2014), pp. 112–119.

[30] Yu Wang et al. “Challenges and Opportunities to Mitigate the Catastrophic Thermal Runaway of High-Energy Batteries”. In: *Advanced Energy Materials* 13.15 (2023), p. 2203841.

[31] Michel Armand and J-M Tarascon. “Building better batteries”. In: *nature* 451.7179 (2008), pp. 652–657.

[32] John B Goodenough and Youngsik Kim. “Challenges for rechargeable Li batteries”. In: *Chemistry of materials* 22.3 (2010), pp. 587–603.

[33] Steven Chu, Yi Cui, and Nian Liu. “The path towards sustainable energy”. In: *Nature materials* 16.1 (2017), pp. 16–22.

[34] Yu Miao et al. “Current Li-ion battery technologies in electric vehicles and opportunities for advancements”. In: *Energies* 12.6 (2019), p. 1074.

[35] Kazuo Murata, Shuichi Izuchi, and Youetsu Yoshihisa. “An overview of the research and development of solid polymer electrolyte batteries”. In: *Electrochimica acta* 45.8-9 (2000), pp. 1501–1508.

[36] Juchuan Li et al. “Solid electrolyte: the key for high-voltage lithium batteries”. In: *Advanced Energy Materials* 5.4 (2015), p. 1401408.

[37] Douglas R MacFarlane, Junhua Huang, and Maria Forsyth. “Lithium-doped plastic crystal electrolytes exhibiting fast ion conduction for secondary batteries”. In: *Nature* 402.6763 (1999), pp. 792–794.

[38] Noriaki Kamaya et al. “A lithium superionic conductor”. In: *Nature materials* 10.9 (2011), pp. 682–686.

[39] Jingnan Feng et al. “PEO based polymer-ceramic hybrid solid electrolytes: a review”. In: *Nano Convergence* 8 (2021), pp. 1–12.

[40] Shangshu Qian et al. “Designing ceramic/polymer composite as highly ionic conductive solid-state electrolytes”. In: *Batteries & Supercaps* 4.1 (2021), pp. 39–59.

[41] Wahid Zaman et al. “Visualizing percolation and ion transport in hybrid solid electrolytes for Li–metal batteries”. In: *Journal of Materials Chemistry A* 7.41 (2019), pp. 23914–23921.

[42] Long Chen and Li–Zhen Fan. “Dendrite-free Li metal deposition in all-solid-state lithium sulfur batteries with polymer-in-salt polysiloxane electrolyte”. In: *Energy Storage Materials* 15 (2018), pp. 37–45.

[43] Phuoc Anh Le et al. “A Mini Review of Current Studies on Metal-Organic Frameworks-Incorporated Composite Solid Polymer Electrolytes in All-Solid-State Lithium Batteries”. In: *Available at SSRN 4449680* ().

[44] Guo-Rui Zhu et al. “Non-flammable solvent-free liquid polymer electrolyte for lithium metal batteries”. In: *Nature Communications* 14.1 (2023), p. 4617.

[45] Zhonghui Gao et al. “Promises, challenges, and recent progress of inorganic solid-state electrolytes for all-solid-state lithium batteries”. In: *Advanced materials* 30.17 (2018), p. 1705702.

[46] Jianneng Liang et al. “Recent progress on solid-state hybrid electrolytes for solid-state lithium batteries”. In: *Energy Storage Materials* 21 (2019), pp. 308–334.

[47] Alexis Maurel et al. “Poly (ethylene oxide)- LiTFSI solid polymer electrolyte filaments for fused deposition modeling three-dimensional printing”. In: *Journal of The Electrochemical Society* 167.7 (2020), p. 070536.

[48] Hideyuki Morimoto et al. “Preparation of lithium ion conducting solid electrolyte of NASICON-type Li1+ xAlxTi2- x (PO4) 3 (x= 0.3) obtained by using the mechanochemical method and its application as surface modification materials of LiCoO2 cathode for lithium cell”. In: *Journal of Power Sources* 240 (2013), pp. 636–643.

[49] Dorsasadat Safanama et al. “Structural evolution of NASICON-type Li 1+ x Al x Ge 2- x (PO 4) 3 using in situ synchrotron X-ray powder diffraction”. In: *Journal of Materials Chemistry A* 4.20 (2016), pp. 7718–7726.

[50] Ramaswamy Murugan, Venkataraman Thangadurai, and Werner Weppner. “Fast lithium ion conduction in garnet-type Li7La3Zr2O12”. In: *Angewandte Chemie International Edition* 46.41 (2007), pp. 7778–7781.

[51] Woo Ju Kwon et al. “Enhanced Li+ conduction in perovskite Li 3x La 2/3- x 1/3- 2x TiO 3 solid-electrolytes via microstructural engineering”. In: *Journal of materials chemistry A* 5.13 (2017), pp. 6257–6262.

[52] Mouad Dahbi et al. “Comparative study of EC/DMC LiTFSI and LiPF6 electrolytes for electrochemical storage”. In: *Journal of Power Sources* 196.22 (2011), pp. 9743–9750.

[53] Fausto Croce et al. “Nanocomposite polymer electrolytes for lithium batteries”. In: *Nature* 394.6692 (1998), pp. 456–458.

[54] Bruno Scrosati. “New approaches to developing lithium polymer batteries”. In: *The Chemical Record* 1.2 (2001), pp. 173–181.

[55] Long Chen et al. “PEO/garnet composite electrolytes for solid-state lithium batteries: From “ceramic-in-polymer” to “polymer-in-ceramic””. In: *Nano Energy* 46 (2018), pp. 176–184.

[56] Zhihua Zhang et al. “Interface re-engineering of Li10GeP2S12 electrolyte and lithium anode for all-solid-state lithium batteries with ultralong cycle life”. In: *ACS applied materials & interfaces* 10.3 (2018), pp. 2556–2565.

[57] Trang Thi Vu et al. “Hybrid electrolytes for solid-state lithium batteries: Challenges, progress, and prospects”. In: *Energy Storage Materials* (2023), p. 102876.

[58] Guan Xi et al. “Polymer-based solid electrolytes: material selection, design, and application”. In: *Advanced Functional Materials* 31.9 (2021), p. 2007598.

[59] B Scrosati, F Croce, and L Persi. “Impedance spectroscopy study of PEO-based nanocomposite polymer electrolytes”. In: *Journal of the Electrochemical Society* 147.5 (2000), p. 1718.

[60] Xiaorong Zhang et al. “Li6. 4La3Zr1. 4Ta0. 6O12 Reinforced Polystyrene-Poly (ethylene oxide)-Poly (propylene oxide)-Poly (ethylene oxide)-Polystyrene pentablock copolymer-based composite solid electrolytes for solid-state lithium metal batteries”. In: *Journal of Power Sources* 542 (2022), p. 231797.

[61] Z Jiang, B Carroll, and KM Abraham. “Studies of some poly (vinylidene fluoride) electrolytes”. In: *Electrochimica Acta* 42.17 (1997), pp. 2667–2677.

[62] Xue Zhang et al. “Synergistic coupling between Li6. 75La3Zr1. 75Ta0. 25O12 and poly (vinylidene fluoride) induces high ionic conductivity, mechanical strength, and thermal stability of solid composite electrolytes”. In: *Journal of the American Chemical Society* 139.39 (2017), pp. 13779–13785.

[63] Zhenguang Li et al. “Ion-conductive and thermal properties of a synergistic poly (ethylene carbonate)/poly (trimethylene carbonate) blend electrolyte”. In: *Macromolecular rapid communications* 39.14 (2018), p. 1800146.

[64] Guomin Mao et al. “Structure of liquid PEO-LiTFSI electrolyte”. In: *Physical review letters* 84.24 (2000), p. 5536.

[65] Reem Alfinaikh. “Preparation and Characterization of Poly (Ethylene Oxide)(MW 35K and 100K)/Silica Nanoparticle Composites”. In: (2017).

[66] Jeremy Lee et al. “Free-standing PEO/LiTFSI/LAGP composite electrolyte membranes for applications to flexible solid-state lithium-based batteries”. In: *Journal of The Electrochemical Society* 166.2 (2019), A416.

[67] S Das and A Ghosh. “Ionic conductivity and dielectric permittivity of PEO-LiClO4 solid polymer electrolyte plasticized with propylene carbonate”. In: *AIP Advances* 5.2 (2015).

[68] Zhigang Xue, Dan He, and Xiaolin Xie. “Poly (ethylene oxide)-based electrolytes for lithium-ion batteries”. In: *Journal of Materials Chemistry A* 3.38 (2015), pp. 19218–19253.

[69] Jonas Mindemark et al. “Beyond PEO—Alternative host materials for Li+-conducting solid polymer electrolytes”. In: *Progress in Polymer Science* 81 (2018), pp. 114–143.

[70] Zlatka Gadjourova et al. “Ionic conductivity in crystalline polymer electrolytes”. In: *Nature* 412.6846 (2001), pp. 520–523.

[71] K Zaghib et al. “Electrochemical study of Li4Ti5O12 as negative electrode for Li-ion polymer rechargeable batteries”. In: *Journal of Power Sources* 81 (1999), pp. 300–305.

[72] Karim Zaghib and Kimio Kinoshita. “Advanced materials for negative electrodes in Li-polymer batteries”. In: *Journal of power sources* 125.2 (2004), pp. 214–220.

[73] Graham S MacGlashan, Yuri G Andreev, and Peter G Bruce. “Structure of the polymer electrolyte poly (ethylene oxide) 6: LiAsF6”. In: *Nature* 398.6730 (1999), pp. 792–794.

[74] Jean-Christophe Daigle et al. “Lithium battery with solid polymer electrolyte based on comb-like copolymers”. In: *Journal of Power Sources* 279 (2015), pp. 372–383.

[75] Pierre Hovington et al. “New lithium metal polymer solid state battery for an ultrahigh energy: nano C-LiFePO4 versus nano Li1. 2V3O8”. In: *Nano letters* 15.4 (2015), pp. 2671–2678.

[76] Hui Yang and Nianqiang Wu. “Ionic conductivity and ion transport mechanisms of solid-state lithium-ion battery electrolytes: A review”. In: *Energy Science & Engineering* 10.5 (2022), pp. 1643–1671.

[77] Nicola Molinari, Jonathan P Mailoa, and Boris Kozinsky. “Effect of salt concentration on ion clustering and transport in polymer solid electrolytes: a molecular dynamics study of PEO–LiTFSI”. In: *Chemistry of Materials* 30.18 (2018), pp. 6298–6306.

[78] Eliana Quartarone, Piercarlo Mustarelli, and Aldo Magistris. “PEO-based composite polymer electrolytes”. In: *Solid State Ionics* 110.1-2 (1998), pp. 1–14.

[79] Tatsuo Horiba. “Lithium-ion battery systems”. In: *Proceedings of the IEEE* 102.6 (2014), pp. 939–950.

[80] Wei Yang et al. “Progress on Fe-Based Polyanionic Oxide Cathodes Materials toward Grid-Scale Energy Storage for Sodium-Ion Batteries”. In: *Small Methods* 6.9 (2022), p. 2200555.

[81] Marisa Falco et al. “UV-cross-linked composite polymer electrolyte for high-rate, ambient temperature lithium batteries”. In: *ACS Applied Energy Materials* 2.3 (2019), pp. 1600–1607.

[82] Kangqiang He et al. “Polyethylene oxide/garnet-type Li6. 4La3Zr1. 4Nb0. 6O12 composite electrolytes with improved electrochemical performance for solid state lithium rechargeable batteries”. In: *Composites Science and Technology* 175 (2019), pp. 28–34.

[83] Nan Zhang et al. “Composite solid electrolyte PEO/SN/LiAlO 2 for a solid-state lithium battery”. In: *Journal of Materials Science* 54 (2019), pp. 9603–9612.

[84] Song Li et al. “Progress and perspective of ceramic/polymer composite solid electrolytes for lithium batteries”. In: *Advanced Science* 7.5 (2020), p. 1903088.

[85] Diddo Diddens and Andreas Heuer. “Simulation study of the lithium ion transport mechanism in ternary polymer electrolytes: the critical role of the segmental mobility”. In: *The Journal of Physical Chemistry B* 118.4 (2014), pp. 1113–1125.

[86] Rotem Marom et al. “Revisiting LiClO4 as an electrolyte for rechargeable lithium-ion batteries”. In: *Journal of the Electrochemical Society* 157.8 (2010), A972.

[87] Samuel C Levy and Per Bro. *Battery hazards and accident prevention.* Springer Science & Business Media, 1994.

[88] Shimou Chen et al. “Progress and future prospects of high-voltage and high-safety electrolytes in advanced lithium batteries: from liquid to solid electrolytes”. In: *Journal of Materials Chemistry A* 6.25 (2018), pp. 11631–11663.

[89] Eliana Quartarone and Piercarlo Mustarelli. “Electrolytes for solid-state lithium rechargeable batteries: recent advances and perspectives”. In: *Chemical Society Reviews* 40.5 (2011), pp. 2525–2540.

[90] Sanaz Ketabi and Keryn Lian. “Effect of SiO2 on conductivity and structural properties of PEO–EMIHSO4 polymer electrolyte and enabled solid electrochemical capacitors”. In: *Electrochimica Acta* 103 (2013), pp. 174–178.

[91] Berhanu W Zewde et al. “Enhanced Lithium Battery with Polyethylene Oxide-Based Electrolyte Containing Silane–Al2O3 Ceramic Filler”. In: *ChemSusChem* 6.8 (2013), pp. 1400–1405.

[92] Weimin Wang et al. “Lithium ion conducting poly (ethylene oxide)-based solid electrolytes containing active or passive ceramic nanoparticles”. In: *The Journal of Physical Chemistry C* 121.5 (2017), pp. 2563–2573.

[93] Mahmut Dirican et al. “Composite solid electrolytes for all-solid-state lithium batteries”. In: *Materials Science and Engineering: R: Reports* 136 (2019), pp. 27–46.

[94] Lizhen Fan, Ce-Wen Nan, and Shujin Zhao. “Effect of modified SiO2 on the properties of PEO-based polymer electrolytes”. In: *Solid State Ionics* 164.1-2 (2003), pp. 81–86.

[95] Nan Wu et al. “Enhanced surface interactions enable fast Li+ conduction in oxide/polymer composite electrolyte”. In: *Angewandte Chemie International Edition* 59.10 (2020), pp. 4131–4137.

[96] GB Appetecchi et al. “Transport and interfacial properties of composite polymer electrolytes”. In: *Electrochimica Acta* 45.8-9 (2000), pp. 1481–1490.

[97] Huiming Zhang et al. “A novel filler for gel polymer electrolyte with a high lithium-ion transference number toward stable cycling for lithium-metal anodes in lithium–sulfur batteries”. In: *ACS Applied Materials & Interfaces* 13.41 (2021), pp. 48622–48633.

[98] Angesh Chandra, Archana Chandra, and K Thakur. “Dielectric study of hot-pressed nanocomposite polymer electrolytes”. In: *Russian Journal of General Chemistry* 83.12 (2013), pp. 2375–2379.

[99] Guoxin Jiang et al. “Ceramic-polymer electrolytes for all-solid-state lithium rechargeable batteries”. In: *Journal of The Electrochemical Society* 152.4 (2005), A767.

[100] S Das and A Ghosh. “Ion conduction and relaxation in PEO-LiTFSI-Al2O3 polymer nanocomposite electrolytes”. In: *Journal of Applied Physics* 117.17 (2015).

[101] F Croce et al. “Role of the ceramic fillers in enhancing the transport properties of composite polymer electrolytes”. In: *Electrochimica Acta* 46.16 (2001), pp. 2457–2461.

[102] RF Samsinger et al. “Influence of the processing on the ionic conductivity of solid-state hybrid electrolytes based on glass-ceramic particles dispersed in PEO with LiTFSI”. In: *Journal of The Electrochemical Society* 167.12 (2020), p. 120538.

[103] Felix Lee et al. “Capacity retention of lithium sulfur batteries enhanced with nano-sized TiO 2-embedded polyethylene oxide”. In: *Journal of Materials Chemistry A* 5.14 (2017), pp. 6708–6715.

[104] Thomas Stergiopoulos et al. “Binary polyethylene oxide/titania solid-state redox electrolyte for highly efficient nanocrystalline TiO2 photoelectrochemical cells”. In: *Nano letters* 2.11 (2002), pp. 1259–1261.

[105] Inna Gurevitch et al. “Nanocomposites of titanium dioxide and polystyrene-poly (ethylene oxide) block copolymer as solid-state electrolytes for lithium metal batteries”. In: *Journal of The Electrochemical Society* 160.9 (2013), A1611.

[106] Yuanyuan Shi et al. “Atomic-scale Al2O3 modified PEO-based composite polymer electrolyte for durable solid-state Li- S batteries”. In: *Journal of Electroanalytical Chemistry* 881 (2021), p. 114916.

[107] Y Liu, JY Lee, and L Hong. “In situ preparation of poly (ethylene oxide)–SiO2 composite polymer electrolytes”. In: *Journal of Power Sources* 129.2 (2004), pp. 303–311.

[108] Joon-Ho Shin, Fabrizio Alessandrini, and Stefano Passerini. “Comparison of Solvent-Cast and Hot-Pressed P (EO) 20LiN (SO 2 CF 2 CF 3) 2 Polymer Electrolytes Containing Nanosized SiO2”. In: *Journal of The Electrochemical Society* 152.2 (2004), A283.

[109] Huan-Ming Xiong et al. “Elucidating the conductivity enhancement effect of nano-sized SnO2 fillers in the hybrid polymer electrolyte PEO–SnO2–LiClO4”. In: *Solid State Ionics* 159.1-2 (2003), pp. 89–95.

[110] Jin-Kyung Lee et al. “Enhanced ionic conductivity in PEO-LiClO 4 hybrid electrolytes by structural modification”. In: *Journal of electroceramics* 17 (2006), pp. 941–944.

[111] Constantin Bubulinca et al. “Development of All-Solid-State Li-Ion Batteries: From Key Technical Areas to Commercial Use”. In: *Batteries* 9.3 (2023), p. 157.

[112] Arumugam Manthiram, Xingwen Yu, and Shaofei Wang. “Lithium battery chemistries enabled by solid-state electrolytes”. In: *Nature Reviews Materials* 2.4 (2017), pp. 1–16.

[113] Fausto Croce et al. “Physical and chemical properties of nanocomposite polymer electrolytes”. In: *The Journal of Physical Chemistry B* 103.48 (1999), pp. 10632–10638.

[114] Nyalaliska W Utomo et al. “Structure and Evolution of Quasi-Solid-State Hybrid Electrolytes Formed Inside Electrochemical Cells”. In: *Advanced Materials* 34.32 (2022), p. 2110333.

[115] W Krawiec et al. “Polymer nanocomposites: a new strategy for synthesizing solid electrolytes for rechargeable lithium batteries”. In: *Journal of Power Sources* 54.2 (1995), pp. 310–315.

[116] PARD Jayathilaka et al. “Effect of nano-porous Al2O3 on thermal, dielectric and transport properties of the (PEO) 9LiTFSI polymer electrolyte system”. In: *Electrochimica acta* 47.20 (2002), pp. 3257–3268.

[117] MAKL Dissanayake et al. “Effect of concentration and grain size of alumina filler on the ionic conductivity enhancement of the (PEO) 9LiCF3SO3: Al2O3 composite polymer electrolyte”. In: *Journal of Power Sources* 119 (2003), pp. 409–414.

[118] SH Chung et al. “Enhancement of ion transport in polymer electrolytes by addition of nanoscale inorganic oxides”. In: *Journal of power sources* 97 (2001), pp. 644–648.

[119] F Capuano, F Croce, and B Scrosati. “Composite polymer electrolytes”. In: *Journal of the Electrochemical Society* 138.7 (1991), p. 1918.

[120] Nicola Boaretto et al. “Lithium solid-state batteries: State-of-the-art and challenges for materials, interfaces and processing”. In: *Journal of Power Sources* 502 (2021), p. 229919.

[121] Yasuhide Matsuo and Jun Kuwano. “Ionic conductivity of poly (ethylene glycol)-LiCF3SO3-ultrafine SiO2 composite electrolytes: Effects of addition of the surfactant lithium dodecylsulfate”. In: *Solid State Ionics* 79 (1995), pp. 295–299.

[122] Cai Shen et al. “Unraveling the mechanism of ion and electron migration in composite solid-state electrolyte using conductive atomic force microscopy”. In: *Energy Storage Materials* 39 (2021), pp. 271–277.

[123] Lu Han et al. “Recent developments and challenges in hybrid solid electrolytes for lithium-ion batteries”. In: *Frontiers in Energy Research* 8 (2020), p. 202.

[124] James A Isaac, Didier Devaux, and Renaud Bouchet. “Dense inorganic electrolyte particles as a lever to promote composite electrolyte conductivity”. In: *Nature Materials* 21.12 (2022), pp. 1412–1418.

[125] Marshall C Tekell et al. “Ionic Conductivity and Mechanical Reinforcement of Well-Dispersed Polymer Nanocomposite Electrolytes”. In: *ACS Applied Materials & Interfaces* (2023).

[126] Susan K Fullerton-Shirey et al. “Influence of thermal history and humidity on the ionic conductivity of nanoparticle-filled solid polymer electrolytes”. In: *Journal of Polymer Science Part B: Polymer Physics* 49.21 (2011), pp. 1496–1505.

[127] Youngwoo Choo et al. “Diffusion and migration in polymer electrolytes”. In: *Progress in Polymer Science* 103 (2020), p. 101220.

[128] Diddo Diddens, Andreas Heuer, and Oleg Borodin. “Understanding the lithium transport within a rouse-based model for a PEO/LiTFSI polymer electrolyte”. In: *Macromolecules* 43.4 (2010), pp. 2028–2036.

[129] Daniel J Brooks et al. “Atomistic description of ionic diffusion in PEO–LiTFSI: Effect of temperature, molecular weight, and ionic concentration”. In: *Macromolecules* 51.21 (2018), pp. 8987–8995.

[130] Jiaqi Wang et al. “Lithium ion transport in solid polymer electrolyte filled with alumina nanoparticles”. In: *Energy Advances* 1.5 (2022), pp. 269–276.

[131] Ben Hanson, Victor Pryamitsyn, and Venkat Ganesan. “Mechanisms underlying ionic mobilities in nanocomposite polymer electrolytes”. In: *ACS Macro Letters* 2.11 (2013), pp. 1001–1005.

[132] Santosh Mogurampelly and Venkat Ganesan. “Effect of nanoparticles on ion transport in polymer electrolytes”. In: *Macromolecules* 48.8 (2015), pp. 2773–2786.

[133] Santosh Mogurampelly and Venkat Ganesan. “Influence of nanoparticle surface chemistry on ion transport in polymer nanocomposite electrolytes”. In: *Solid State Ionics* 286 (2016), pp. 57–65.

[134] Santosh Mogurampelly et al. “Influence of nanoparticle-ion and nanoparticle-polymer interactions on ion transport and viscoelastic properties of polymer electrolytes”. In: *The Journal of Chemical Physics* 144.15 (2016).

[135] Qin Li and Haleh Ardebili. “Atomistic investigation of the nanoparticle size and shape effects on ionic conductivity of solid polymer electrolytes”. In: *Solid State Ionics* 268 (2014), pp. 156–161.

[136] Ji Hu et al. “Composite polymer electrolytes reinforced by hollow silica nanotubes for lithium metal batteries”. In: *Journal of Membrane Science* 618 (2021), p. 118697.

[137] Gabriel R Schleder et al. “From DFT to machine learning: recent approaches to materials science–a review”. In: *Journal of Physics: Materials* 2.3 (2019), p. 032001.

[138] Igor L Markov. “Limits on fundamental limits to computation”. In: *Nature* 512.7513 (2014), pp. 147–154.

[139] Martin O Steinhauser and Stefan Hiermaier. “A review of computational methods in materials science: examples from shock-wave and polymer physics”. In: *International journal of molecular sciences* 10.12 (2009), pp. 5135–5216.

[140] Lara Kathleen Smetana and Randy L Bell. “Computer simulations to support science instruction and learning: A critical review of the literature”. In: *International Journal of Science Education* 34.9 (2012), pp. 1337–1370.

[141] Syi Su and Chung-Liang Shih. “Modeling an emergency medical services system using computer simulation”. In: *International journal of medical informatics* 72.1-3 (2003), pp. 57–72.

[142] Deborah Dowling. “Experimenting on theories”. In: *Science in context* 12.2 (1999), pp. 261–273.

[143] Jorge Trindade, Carlos Fiolhais, and Leandro Almeida. “Science learning in virtual environments: a descriptive study”. In: *British Journal of Educational Technology* 33.4 (2002), pp. 471–488.

[144] Fabrice Wendling et al. “Computational models of epileptiform activity”. In: *Journal of neuroscience methods* 260 (2016), pp. 233–251.

[145] Meili Kang et al. “A Review of the Ethical Use of Animals in Functional Experimental Research in China Based on the “Four R” Principles of Reduction, Replacement, Refinement, and Responsibility”. In: *Medical Science Monitor: International Medical Journal of Experimental and Clinical Research* 28 (2022), e938807–1.

[146] Zheng Chen et al. “Multiscale modeling and simulations of responsive polymers”. In: *Current Opinion in Chemical Engineering* 23 (2019), pp. 21–33.

[147] Kenneth G Wilson. “Grand challenges to computational science”. In: *Future Generation Computer Systems* 5.2-3 (1989), pp. 171–189.

[148] VR Voller and F Porte-Agel. “Moore’s law and numerical modeling”. In: *Journal of Computational Physics* 179.2 (2002), pp. 698–703.

[149] Frank Hopfgartner et al. “Evaluation-as-a-service for the computational sciences: Overview and outlook”. In: *Journal of Data and Information Quality (JDIQ)* 10.4 (2018), pp. 1–32.

[150] Michael Frank, Dimitris Drikakis, and Vassilis Charissis. “Machine-learning methods for computational science and engineering”. In: *Computation* 8.1 (2020), p. 15.

[151] Scott A Hollingsworth and Ron O Dror. “Molecular dynamics simulation for all”. In: *Neuron* 99.6 (2018), pp. 1129–1143.

[152] Ali Gooneie, Stephan Schuschnigg, and Clemens Holzer. “A review of multiscale computational methods in polymeric materials”. In: *Polymers* 9.1 (2017), p. 16.

[153] Dirk P Kroese et al. “Why the Monte Carlo method is so important today”. In: *Wiley Interdisciplinary Reviews: Computational Statistics* 6.6 (2014), pp. 386–392.

[154] Xiaocong He. “A review of finite element analysis of adhesively bonded joints”. In: *International Journal of Adhesion and Adhesives* 31.4 (2011), pp. 248–264.

[155] Aravindhan Ganesan, Michelle L Coote, and Khaled Barakat. “Molecular dynamics-driven drug discovery: leaping forward with confidence”. In: *Drug discovery today* 22.2 (2017), pp. 249–269.

[156] Mohammed N Al-Qattan, Pran Kishore Deb, and Rakesh K Tekade. “Molecular dynamics simulation strategies for designing carbon-nanotube-based targeted drug delivery”. In: *Drug discovery today* 23.2 (2018), pp. 235–250.

[157] Luciano da Fontoura Costa et al. “Analyzing and modeling real-world phenomena with complex networks: a survey of applications”. In: *Advances in Physics* 60.3 (2011), pp. 329–412.

[158] Filip Lievens and Britt De Soete. “Simulations”. In: (2012).

[159] Robert C Bishop. “Metaphysical and epistemological issues in complex systems”. In: *Philosophy of complex systems*. Elsevier, 2011, pp. 105–136.

[160] Wilfred F van Gunsteren et al. “Validation of molecular simulation: an overview of issues”. In: *Angewandte Chemie International Edition* 57.4 (2018), pp. 884–902.

[161] Erik Van Der Giessen et al. “Roadmap on multiscale materials modeling”. In: *Modelling and Simulation in Materials Science and Engineering* 28.4 (2020), p. 043001.

[162] Jarosaw Meller et al. “Molecular dynamics”. In: *Encyclopedia of life sciences* 18 (2001).

[163] Miguel A González. “Force fields and molecular dynamics simulations”. In: *École thématique de la Société Française de la Neutronique* 12 (2011), pp. 169–200.

[164] Loup Verlet. “Computer” experiments” on classical fluids. I. Thermodynamical properties of Lennard-Jones molecules”. In: *Physical review* 159.1 (1967), p. 98.

[165] Robert E Rudd and Jeremy Q Broughton. “Coarse-grained molecular dynamics and the atomic limit of finite elements”. In: *Physical review B* 58.10 (1998), R5893.

[166] Libero J Bartolotti and Ken Flurchick. “An introduction to density functional theory”. In: *Reviews in computational chemistry* (1996), pp. 187–216.

[167] Thomas R Mattsson et al. “First-principles and classical molecular dynamics simulation of shocked polymers”. In: *Physical Review B* 81.5 (2010), p. 054103.

[168] Oleg Borodin. “Polarizable force field development and molecular dynamics simulations of ionic liquids”. In: *The Journal of Physical Chemistry B* 113.33 (2009), pp. 11463–11478.

[169] Luca Monticelli and D Peter Tieleman. “Force fields for classical molecular dynamics”. In: *Biomolecular simulations: Methods and protocols* (2013), pp. 197–213.

[170] Benjamin J Cowen and Mohamed S El-Genk. “On force fields for molecular dynamics simulations of crystalline silica”. In: *Computational Materials Science* 107 (2015), pp. 88–101.

[171] Alex D MacKerell Jr et al. “All-atom empirical potential for molecular modeling and dynamics studies of proteins”. In: *The journal of physical chemistry B* 102.18 (1998), pp. 3586–3616.

[172] Kolawole Sonibare, Lasantha Rathnayaka, and Liqun Zhang. “Comparison of CHARMM and OPLS-aa forcefield predictions for components in one model asphalt mixture”. In: *Construction and Building Materials* 236 (2020), p. 117577.

[173] David A Pearlman et al. “AMBER, a package of computer programs for applying molecular mechanics, normal mode analysis, molecular dynamics and free energy calculations to simulate the structural and energetic properties of molecules”. In: *Computer Physics Communications* 91.1-3 (1995), pp. 1–41.

[174] Emiliano Stendardo et al. “Extension of the AMBER force-field for the study of large nitroxides in condensed phases: an ab initio parameterization”. In: *Physical Chemistry Chemical Physics* 12.37 (2010), pp. 11697–11709.

[175] William L Jorgensen, David S Maxwell, and Julian Tirado-Rives. “Development and testing of the OPLS all-atom force field on conformational energetics and properties of organic liquids”. In: *Journal of the American Chemical Society* 118.45 (1996), pp. 11225–11236.

[176] Huai Sun. “COMPASS: an ab initio force-field optimized for condensed-phase applications overview with details on alkane and benzene compounds”. In: *The Journal of Physical Chemistry B* 102.38 (1998), pp. 7338–7364.

[177] José N Canongia Lopes and Agılio AH Pádua. “Molecular force field for ionic liquids III: Imidazolium, pyridinium, and phosphonium cations; chloride, bromide, and dicyanamide anions”. In: *The Journal of Physical Chemistry B* 110.39 (2006), pp. 19586–19592.

[178] Wei Shi and Edward J Maginn. “Molecular simulation of ammonia absorption in the ionic liquid 1-ethyl-3-methylimidazolium bis (trifluoromethylsulfonyl) imide ([emim][Tf2N])”. In: *AIChE journal* 55.9 (2009), pp. 2414–2421.

[179] Chan-En Fang et al. “Revised atomic charges for OPLS force field model of poly (ethylene oxide): Benchmarks and applications in polymer electrolyte”. In: *Polymers* 13.7 (2021), p. 1131.

[180] Alexandar T Tzanov, Michel A Cuendet, and Mark E Tuckerman. “How accurately do current force fields predict experimental peptide conformations? An adiabatic free energy dynamics study”. In: *The Journal of Physical Chemistry B* 118.24 (2014), pp. 6539–6552.

[181] Michael J Robertson, Julian Tirado-Rives, and William L Jorgensen. “Improved peptide and protein torsional energetics with the OPLS-AA force field”. In: *Journal of chemical theory and computation* 11.7 (2015), pp. 3499–3509.

[182] Shirley WI Siu, Kristyna Pluhackova, and Rainer A Böckmann. “Optimization of the OPLS-AA force field for long hydrocarbons”. In: *Journal of Chemical theory and Computation* 8.4 (2012), pp. 1459–1470.

[183] In-Chul Yeh and Gerhard Hummer. “System-size dependence of diffusion coefficients and viscosities from molecular dynamics simulations with periodic boundary conditions”. In: *The Journal of Physical Chemistry B* 108.40 (2004), pp. 15873–15879.

[184] Thomas E Gartner III and Arthi Jayaraman. “Modeling and simulations of polymers: a roadmap”. In: *Macromolecules* 52.3 (2019), pp. 755–786.

[185] A. P. Thompson et al. “LAMMPS - a flexible simulation tool for particle-based materials modeling at the atomic, meso, and continuum scales”. In: *Comp. Phys. Comm.* 271 (2022), p. 108171. DOI: `10.1016/j.cpc.2021.108171`.

[186] Sunhwan Jo et al. “CHARMM-GUI: a web-based graphical user interface for CHARMM”. In: *Journal of computational chemistry* 29.11 (2008), pp. 1859–1865.

[187] Bernard R Brooks et al. “CHARMM: the biomolecular simulation program”. In: *Journal of computational chemistry* 30.10 (2009), pp. 1545–1614.

[188] Jumin Lee et al. “CHARMM-GUI input generator for NAMD, GROMACS, AMBER, OpenMM, and CHARMM/OpenMM simulations using the CHARMM36 additive force field”. In: *Biophysical journal* 110.3 (2016), 641a.

[189] Yeol Kyo Choi et al. “CHARMM-GUI polymer builder for modeling and simulation of synthetic polymers”. In: *Journal of chemical theory and computation* 17.4 (2021), pp. 2431–2443.

[190] Yeol Kyo Choi et al. “CHARMM-GUI nanomaterial modeler for modeling and simulation of nanomaterial systems”. In: *Journal of chemical theory and computation* 18.1 (2021), pp. 479–493.

[191] Nathan R Kern et al. “CHARMM-GUI multicomponent assembler for modeling and simulation of complex multicomponent systems”. In: *Biophysical Journal* 121.3 (2022), 529a.

[192] Brian Doherty et al. “Revisiting OPLS force field parameters for ionic liquid simulations”. In: *Journal of chemical theory and computation* 13.12 (2017), pp. 6131–6145.

[193] William L Jorgensen and Julian Tirado-Rives. “Potential energy functions for atomic-level simulations of water and organic and biomolecular systems”. In: *Proceedings of the National Academy of Sciences* 102.19 (2005), pp. 6665–6670.

[194] Leela S Dodda et al. “1.14* CM1A-LBCC: localized bond-charge corrected CM1A charges for condensed-phase simulations”. In: *The Journal of Physical Chemistry B* 121.15 (2017), pp. 3864–3870.

[195] Leela S Dodda et al. “LigParGen web server: an automatic OPLS-AA parameter generator for organic ligands”. In: *Nucleic acids research* 45.W1 (2017), W331–W336.

[196] Yunlong Li, Shijie Wang, and Quan Wang. “A molecular dynamics simulation study on enhancement of mechanical and tribological properties of polymer composites by introduction of graphene”. In: *Carbon* 111 (2017), pp. 538–545.

[197] Kavitha Chelakara Satyanarayana et al. “Analysis of the torsion angle distribution of poly (vinylidene fluoride) in the melt”. In: *Polymer* 53.5 (2012), pp. 1109–1114.

[198] Jean Bélanger, Philippe Venne, and Jean-Nicolas Paquin. “The what, where and why of real-time simulation”. In: *Planet Rt* 1.1 (2010), pp. 25–29.

[199] Guido Van Rossum and Fred L. Drake. *Python 3 Reference Manual*. Scotts Valley, CA: CreateSpace, 2009. ISBN: 1441412697.

[200] Guido Van Rossum and Fred L Drake Jr. *Python tutorial*. Centrum voor Wiskunde en Informatica Amsterdam, The Netherlands, 1995.

[201] William Humphrey, Andrew Dalke, and Klaus Schulten. “VMD: visual molecular dynamics”. In: *Journal of molecular graphics* 14.1 (1996), pp. 33–38.

[202] Xavier Michalet. “Mean square displacement analysis of single-particle trajectories with localization error: Brownian motion in an isotropic medium”. In: *Physical Review E* 82.4 (2010), p. 041914.

[203] G Rehage, O Ernst, and J Fuhrmann. “Fickian and non-Fickian diffusion in high polymer systems”. In: *Discussions of the Faraday Society* 49 (1970), pp. 208–221.

[204] Arthur France-Lanord and Jeffrey C Grossman. “Correlations from ion pairing and the Nernst-Einstein equation”. In: *Physical review letters* 122.13 (2019), p. 136001.

[205] Zhe Li et al. “Effect of organic solvents on Li+ ion solvation and transport in ionic liquid electrolytes: a molecular dynamics simulation study”. In: *The Journal of Physical Chemistry B* 119.7 (2015), pp. 3085–3096.

[206] Henry M Woolley and Nella M Vargas-Barbosa. “Hybrid solid electrolyte-liquid electrolyte systems for (almost) solid-state batteries: Why, how, and where to?” In: *Journal of Materials Chemistry A* 11.3 (2023), pp. 1083–1097.

[207] Jelena Popovic et al. “Polymer-based hybrid battery electrolytes: theoretical insights, recent advances and challenges”. In: *Journal of Materials Chemistry A* 9.10 (2021), pp. 6050–6069.

[208] P Sánchez-Soto et al. “Effect of molecular mass on the melting temperature, enthalpy and entropy of hydroxy-terminated PEO”. In: *Journal of thermal analysis and calorimetry* 67.1 (2002), pp. 189–197.

[209] Akira Koyama et al. “Molecular dynamics simulation of polymer crystallization from an oriented amorphous state”. In: *Physical Review E* 65.5 (2002), p. 050801.

[210] Vaidyanathan Sethuraman, Santosh Mogurampelly, and Venkat Ganesan. “Multiscale Simulations of Lamellar PS–PEO Block Copolymers Doped with LiPF6 Ions”. In: *Macromolecules* 50.11 (2017), pp. 4542–4554.

[211] Rafael C Howell, Thomas Proffen, and Steven D Conradson. “Pair distribution function and structure factor of spherical particles”. In: *Physical Review B* 73.9 (2006), p. 094107.

[212] Oleg Borodin and Grant D Smith. “Mechanism of ion transport in amorphous poly (ethylene oxide)/LiTFSI from molecular dynamics simulations”. In: *Macromolecules* 39.4 (2006), pp. 1620–1629.

[213] Patrik Johansson, Jörgen Tegenfeldt, and Jan Lindgren. “Modelling amorphous lithium salt–PEO polymer electrolytes: ab initio calculations of lithium ion–tetra-, penta-and hexaglyme complexes”. In: *Polymer* 40.15 (1999), pp. 4399–4406.

[214] Deya Das et al. “Effect of crystallinity on Li adsorption in polyethylene oxide”. In: *Chemistry of Materials* 30.24 (2018), pp. 8804–8810.

[215] V Kuppa and E Manias. “Computer simulation of PEO/layered-silicate nanocomposites: 2. Lithium dynamics in PEO/Li+ montmorillonite intercalates”. In: *Chemistry of Materials* 14.5 (2002), pp. 2171–2175.

[216] E Hackett, E Manias, and EP Giannelis. “Computer simulation studies of PEO/layer silicate nanocomposites”. In: *Chemistry of Materials* 12.8 (2000), pp. 2161–2167.

[217] Qianwen Huang et al. “Solvation Structure and Dynamics of Li+ in Ternary Ionic Liquid–Lithium Salt Electrolytes”. In: *The Journal of Physical Chemistry B* 123.2 (2018), pp. 516–527.

[218] Peibin Kang et al. “Dynamical ion association and transport properties in PEO–LiTFSI electrolytes: effect of salt concentration”. In: *The Journal of Physical Chemistry B* 126.24 (2022), pp. 4531–4542.

[219] Chuting Deng et al. “Role of molecular architecture on ion transport in ethylene oxide-based polymer electrolytes”. In: *Macromolecules* 54.5 (2021), pp. 2266–2276.

[220] Suriani Ibrahim et al. “Conductivity and dielectric behaviour of PEO-based solid nanocomposite polymer electrolytes”. In: *Solid state communications* 152.5 (2012), pp. 426–434.

[221] Didier Devaux et al. “Mechanism of ion transport in PEO/LiTFSI complexes: Effect of temperature, molecular weight and end groups”. In: *Solid State Ionics* 227 (2012), pp. 119–127.

[222] Mojca Pavlin, Tomaz Slivnik, and Damijan Miklavcic. “Effective conductivity of cell suspensions”. In: *IEEE transactions on bio-medical engineering* 49 (Feb. 2002), pp. 77–80. DOI: `10.1109/10.972843`.

[223] X Chelsea Chen et al. “Study of segmental dynamics and ion transport in polymer–ceramic composite electrolytes by quasi-elastic neutron scattering”. In: *Molecular Systems Design & Engineering* 4.2 (2019), pp. 379–385.

[224] Gang Chen et al. “Mechanical and dynamic properties of resin blend and composite systems: A molecular dynamics study”. In: *Composite Structures* 190 (2018), pp. 160–168.

[225] Yunqi Shao et al. “Transference Number in Polymer Electrolytes: Mind the Reference-Frame Gap”. In: *Journal of the American Chemical Society* 144.17 (May 2022), pp. 7583–7587. ISSN: 0002-7863. DOI: `10.1021/jacs.2c02389`. URL: `https://doi.org/10.1021/jacs.2c02389` (visited on 08/04/2023).

[226] Irune Villaluenga et al. “Negative Stefan-Maxwell Diffusion Coefficients and Complete Electrochemical Transport Characterization of Homopolymer and Block Copolymer Electrolytes”. In: *Journal of The Electrochemical Society* 165.11 (Aug. 2018), A2766. ISSN: 1945-7111. DOI: `10.1149/2.0641811jes`. URL: `https://iopscience.iop.org/article/10.1149/2.0641811jes/meta` (visited on 08/04/2023).

[227] RW Hockney and JW Eastwood. “The particle-mesh force calculation”. In: *Computer Simulation Using Particles, Adam Hilger, Bristol and New York, NY, USA* (1989), pp. 120–165.

[228] Andrew I Jewett et al. “Moltemplate: A tool for coarse-grained modeling of complex biological matter and soft condensed matter physics”. In: *Journal of molecular biology* 433.11 (2021), p. 166841.

[229] J. Wang. “Private communication with J. Wang”. In: 2023.

[230] Hellen Papananou et al. “Tuning polymer crystallinity via the appropriate selection of inorganic nanoadditives”. In: *Polymer* 157 (2018), pp. 111–121.

[231] Miguel I Delgado Rosero, Nori M Jurado Meneses, and Ramiro Uribe Kaffure. “Thermal properties of composite polymer electrolytes poly (ethylene oxide)/sodium trifluoroacetate/aluminum oxide (PEO) 10CF3COONa+ x wt.% Al2O3”. In: *Materials* 12.9 (2019), p. 1464.

[232] Lorena S Grundy et al. “Electrochemical Characterization of PEO/LiTFSI Electrolytes Near the Solubility Limit”. In: *Macromolecules* 55.20 (2022), pp. 9030–9038.